FACULTY OF SCIENCE
UNIVERSITY OF COPENHAGEN

Collective Rayleigh scattering in a Bose Einstein condensate

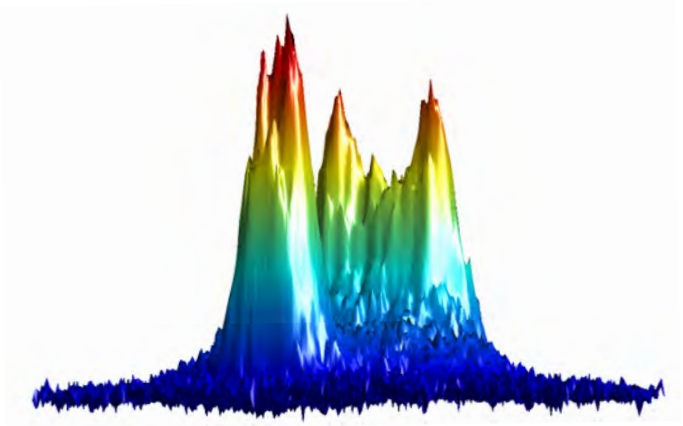

PhD thesis

Andrew Hilliard

Danish National Research Foundation
Center for Quantum Optics – Quantop
Niels Bohr Institute

Academic supervisors: Eugene S. Polzik
Jörg Helge Müller

October, 2008

Collective Rayleigh scattering in a Bose Einstein condensate

Andrew Hilliard

This thesis is submitted in partial fulfilment of the requirements for the Ph.D. degree at University of Copenhagen.
Version 1

Abstract

This thesis describes the construction of a machine to generate Bose Einstein condensates in ^{87}Rb and the first experiments performed with this machine on superradiant Rayleigh scattering.

Bose Einstein condensates of ^{87}Rb are produced by evaporatively cooling atoms in a magnetic trap of the quadrupole-Ioffe configuration. The atoms are loaded into the magnetic trap in a region of ultra-high vacuum from a double Magneto-Optical trap set-up. The evaporative cooling is achieved by selectively driving radio-frequency transitions to untrapped magnetic substates. During the evaporation, the magnetic trap is relaxed so that density dependent heating does not substantially reduce the number of atoms in the condensate. With a duty cycle of about a minute, we produce pure, prolate condensates containing up to a few million atoms.

The application of an off-resonant beam of light along the long axis of the condensate leads to a form of collective Rayleigh scattering analogous to the superradiance that occurs in electronically inverted samples. One can think of this process as the amplification of quantum noise: photons are spontaneously scattered out of the pump beam, and due to the extended optical depth along the long axis of the BEC, the modes that propagate along this axis see the most gain. In the end-pumped geometry, the strongest superradiant mode is the one where photons are back-scattered by the atoms. The overlap of stationary and recoiling atoms recoil produces a density modulation - a Bragg grating - which amplifies the back-scattering. We have performed a systematic study of the effects of pump detuning on the process while keeping the single particle scattering rate constant. In this way, we move between the case where the pump beam functions as a reservoir of photons to the situation where superradiance is clamped by a lack of photons in the pump beam. Our experimental results are strongly supported by simulations of the system based on 1D Maxwell-Schrödinger equations. We demonstrate that the dynamics result from the structures that build up in the light and matter fields along the long axis of the condensate. In particular, we find that the emission of the first superradiant pulse may be understood in terms of the overlap of light and matter wave gratings. Finally, the random nature of the spontaneous scattering that initiates the collective scattering is manifest at later times in the distribution of arrival times and photon numbers of the first superradiant pulse.

Sammendrag

I denne afhandling, beskrives konstruktionen af en maskine, der skaber Bose Einstein kondensater i ^{87}Rb og de første forsøg udført med denne maskine i superradiant Rayleigh spredning.

Bose Einstein kondensater i ^{87}Rb produceres ved fordampningskøling i en magnetfælde i en kvadrupol-Ioffe-konfiguration. I et område med ultra-højt vakuum fyldes magnetfælden med atomer fra en dobbel Magneto-Optisk-fælde opstilling. Fordampningskøling udføres ved at drive radio-frekvens overgange til ikke-fangede magnetiske tilstande. Under fordampningsforløbet forminskes magnetfældens stejlhed så tæthedsafhængig opvarmning ikke forårsager en kritisk reduktion i det endelige antal atomer i kondensatet. Med en repetitions-rate på omtrent et minut, kan vi producere rene, aflange kondensater, som indeholder op til nogle få millioner atomer.

Ved brug af en ikke-resonant laserstråle langs kondensatets lange akse opstår der en form for kollektiv Rayleigh spredning, der er lig superradians i elektronisk inverterede atomare ensembler. Man kan betragte denne process som forstærkningen af kvante-støj: fotoner bliver spontant spredt ud af pumpestrålen og på grund af den store optiske tæthed langs kondensatets lange akse, oplever lys-modes som bevæger sig langs denne akse den største forstærkning. I den ende-pumpede geometri er den kraftigste superradians-mode den, hvor fotoner bliver spredt tilbage af atomerne. Overlappet af stationære atomer og atomer med rekyl skaber en tæthedsmodulation - et Bragg gitter - der forstærker tilbage-spredningen af fotoner. Vi har udført en systematisk undersøgelse af indflydelsen af pumpestrålens detuning på dynamikken for en konstant enkelt-atom-sprednings-rate. På denne måde, skifter vi mellem, situationen hvor pumpestrålen optræder som et foton-reservoir, til situationen hvor processen stoppes på grund af mangel på fotoner i pumpestrålen. Vores eksperimentelle resultater understøttes kraftigt af simulationer af systemet, som bygger på 1D Maxwell-Schrödinger ligninger. Vi viser, at dynamikken opstår på grund af strukturer, der bliver dannet i lys- og stof-felterne langs kondensatets lange akse. Desuden finder vi, at emission af den første superradiante puls kan forstås ud fra overlappet af lys- og stof-bølger. Endeligt påviser vi, at den tilfældige karakter af den spontane spredning, som igangsætter processen, viser sig i den senere dynamik i fordelingen af ankomst tidspunkter af og foton-tal i den første superradiante puls.

Acknowledgements

The work described in this thesis was carried out at the Danish National Research Centre for Quantum Optics - Quantop - at the Niels Bohr Institute, over a period of a little over four and a half years. I began my PhD in January 2004 in the nascent BEC laboratory under the supervision of Professor Eugene Polzik and then associate research professor, Jörg Helge Müller. As the only PhD student directly involved in the lab for the first three and a half years, I have had the opportunity to build up the laboratory from bare optical table to the point where BECs are routinely produced and probed. It has been a long, and at times, difficult process to build up the lab, but also a rewarding one. I am very grateful for the experience and I would like to thank Eugene for giving me the opportunity, and his guidance throughout my PhD. More generally, I am grateful to have had a workplace as good as Quantop: from the competent and social group members, to the privilege of being able to carry out research with a good level of funding. Clearly, Eugene deserves a lot of credit for creating such a group. Throughout my time at Quantop, I have worked most closely with my other supervisor, Jörg Helge Müller, and I would like to thank him for his guidance, his good humour, and for being a tremendous source of knowledge on all things experimental and many other areas of physics.

I would also like to thank my fellow lab workers. Christina Olausson joined the lab at the end of 2004 to earn some practical points towards her Bachelor's degree, and then stayed on in the lab for her Master's thesis. We enjoyed a good collaboration and she was a fun and positive person to have around the lab, and in the group as a whole. Franziska Kaminksi joined the lab as a PhD student in April 2007 and has been a pleasure to work with and have around the group. Likewise, Rodolphe le Targat joined the group as a post-doc in September that year, with good humour, an attention to detail and firm ideas on the correct positioning of irises! The experimental results on superradiant scattering are a result of the collaboration between Franziska, Rodolphe and myself in the latter half of 2007 and first month or two of 2008. Together with PhD student Nir Kampel, who is the most recent addition to the lab, Franziska and Rodolphe are the new generation of lab workers and I wish them well and look forward to having my publication list grow as a result of their work!

I would like to acknowledge others who made contributions to the laboratory.

They are Aśka Dolińska, Niels Kjærgaard, Jonas Meyer Petersen, Patrick Windpassinger, and Marco Koschorreck. Furthermore, I thank Todd Meyrath for his advice on the construction of the magnetic trap coils.

It is important to recognise the contribution made by technical staff at the Niels Bohr Institute. First and foremost, I would like to thank the staff in the various mechanical workshops who have managed to make what I wanted rather than what I implied in my technical drawings. Top of this list is Niels Lindegaard, who got more than his fair share of big and small projects for the BEC lab - among other things, various incarnations of the magnetic trap coils. I would also like to thank the electronics staff, and in particular, Bjørn Rasmussen and Axel Boisen. In terms of IT support, I thank Jimmy Hansen for his help with various ailing computers and their power supplies. Finally, I would like to thank Björn Nilsson, who (after the appropriate pre-emptory phone call or email!) has always been incredibly helpful and quick to respond.

I would also like to thank the administrative staff at the Niels Bohr Institute on Blegdamsvej. In particular, I thank Charlotte Hviid, our group secretary and Toke Nordbo, the PhD coordinator. I would also like to thank Ulla Holm who has been extremely helpful with residency permits and more generally, helping me as a foreigner through local bureaucracy.

As I mentioned above, Quantop has been a very good place to work, mainly for the people who have worked here. I have enjoyed the friendly and fun atmosphere, exemplified by ritual coffee breaks. I would like to thank all the past and present members of Quantop at the Niels Bohr Institute - it's been a blast.

Finally, I would like to thank friends and family for their support during my stay in Denmark. I have received many guests during my time here, and most of my family and friends from New Zealand have made it over here at some stage. In terms of locals, I would like to thank Solveig and her family, and Gitte and Keld Velling for their support. Thanks to Shlomy for music and friendship over the last few years, and Søren and Pernille, at whose apartment I was always welcome. Finally, I would like to thank Charlotte for her wonderful company and support in the last half year - it has made the writing process far more pleasant!

Contents

Chapter 1

Introduction

The coherent control of the interaction between light and matter is the cornerstone of many physical realizations of Quantum Information Processing (QIP). By coherent control of an interaction, we mean that the coupling between the two interacting systems can be precisely controlled by experimental parameter(s) and that it is much stronger than the couplings to their respective environments. Such a capability provides the tools for the generation of arbitrary quantum states of the individual systems or the combined system, and this has important applications such as quantum repeaters, or more generally, extended quantum networks. In this setting, the quantum interface between light and atoms is critical, because it links natural information carriers - photons - with atoms that can be used to store and process information [1]. On a technical level, the preparation of quantum states requires measurements at the quantum limit, where the effect of the interaction is studied in both the atoms and the light. Such an approach is more nuanced than, for instance, spectroscopy on an atomic sample where the light is regarded as a probe that exerts no significant effect on the atoms; or alternatively, the optical pumping of an atomic sample, where one's only focus is the atomic state after the process. In quantum state engineering in light and atoms, one is interested in both the action of the atoms on the light, and the action of the light on the atoms.

Until recently, the standard approach was to place atoms in high finesse optical cavities to increase the strength of the atom-light interaction, but recently the coupling of light to atomic ensembles has emerged as a viable alternative. The latter approach is appealing because it does not suffer from the same technical difficulties as cavity Quantum Electrodynamics (QED), such as placing optical cavities in ultra-high vacuum. In such an approach, the strength of the coupling is increased by a factor which depends on the finesse of the optical resonator. The analogous quantity in the coupling of light and atomic ensembles is the resonant optical depth of the atomic sample $OD = \sigma_{\text{abs}}\tilde{n}$, where the first factor is the absorption cross section, and the second is the column density of the sample. In both cases, the interaction is en-

gineered so as to favour the coupling to a limited number of field modes - in contrast to the case of an isolated atom in free space where the coupling is nearly isotropic; this is achieved through modified boundary conditions in the case of optical cavities, and phase-matching the coupling of many atoms in the ensemble approach.

The interaction between light and atomic ensembles may be divided into two main categories: single quadrature or Quantum Non-Demolition (QND) type coupling, and two quadrature coupling such as beam-splitter and two mode squeezing interactions. By quadratures, we mean the canonical operators X and P from a quantum mechanical harmonic oscillator - a formalism that may be advantageously applied to any bosonic system such as a light field or the collective angular momentum operators of an ensemble of atoms [2]. These two categories may be expressed by the following effective Hamiltonians:

$$H_{\mathrm{I}} = \alpha_{\mathrm{X}} X_1 X_2, \tag{1.1}$$

$$H_{\mathrm{II}} = \alpha_{\mathrm{X}} X_1 X_2 + \alpha_{\mathrm{P}} P_1 P_2, \tag{1.2}$$

where (1.1) describes single quadrature coupling, (1.2) describes two mode coupling, and the indices 1 and 2 of the operators refer to the respective bosonic fields. The coupling constants can be expressed as $\alpha_{\mathrm{X,P}} \propto \sqrt{OD \cdot R}$, where R denotes the single particle scattering rate. Strong coupling is characterized by $OD \cdot R \gtrsim 1$. In the context of a single mode light field interacting with an ensemble of spin polarized atoms, H_{I} describes the coupled polarization rotation of the light field by the atomic ensemble and precession of the macroscopic Zeeman coherences due to light shifts, where X_1 represents one of the Stokes operators for light, and X_2 represents the collective spin projection onto the direction of light propagation [3, 4]. In the high and low detuning limits in light coupling to a Λ-shaped atomic level scheme, H_{II} can be used to model respectively the Raman and Electromagnetically Induced Transparency (EIT) protocols. Standard experimental realizations of both of these categories have made use of vapour gas cells, but increasingly ultra-cold atomic samples are becoming popular, given the value of high optical depth of the atomic ensemble to the coupling strength.

A case in point is a Bose-Einstein condensate: with the realization of Bose-Einstein condensation in dilute atomic samples in 1995, a new era began in atom optics. Since the first demonstrations [5, 6, 7], the growth of the field has been remarkable. Part of the appeal of a Bose Einstein condensate (BEC) in a dilute gas is that it is a many body quantum system where one can tune the degree of atom-atom interactions effectively by a variety of methods, whether it be through the atom number, the trapping potential, or by altering the scattering properties through applied electromagnetic fields. In the context of light coupling to atomic ensembles, a BEC provides an atomic sample with unique coherence properties. This has clear benefits in terms of decoherence times, but also adds some complexity to the atom-light interaction as compared to vapour cells.

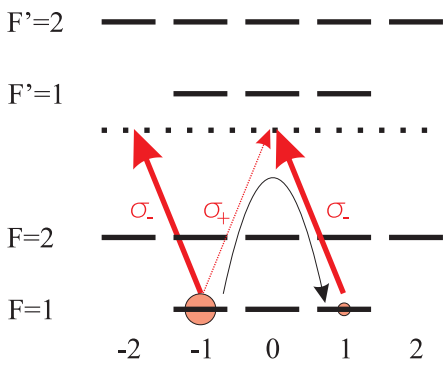

FIGURE 1.1: Protocol for storing a weak pulse of light in the ground state coherence of an ensemble of ^{87}Rb atoms. The atomic sample is dressed by a strong beam of light with σ_- polarization, and the weak beam has the opposite polarization; both are detuned by some amount from the D1 line excited states.

We can illustrate this in the context of a quantum memory scheme based on a Raman interaction. Figure 1.1 shows a memory protocol where a weak quantum field with left hand circular polarization σ_+ is incident on an ensemble of ^{87}Rb atoms held in the lower hyperfine sublevel $|F=1,m_F=-1\rangle$; the atoms are dressed by a strong classical light field in the opposite polarization [8, 9]. The Raman channel allows the transfer of a small proportion of the atoms into the $|F=1,m_F=1\rangle$ state: this is an example of a light-atom interface well described by an $H_{\rm II}$ effective Hamiltonian. In the cited references it is shown that quantum properties of the weak light field are transferred with a given fidelity to the coherence between the coupled ground states. Given that the optical depth is the figure of merit, the light is applied along the longest axis of the sample so as to attain the strongest coupling.

However, if one applies such a protocol to a trapped Bose Einstein condensate, a process other than the intended memory scheme can dominate: the spontaneous scattering due to the strong beam induces a process that is closely related to the superradiance of electronically inverted samples first described by Dicke [10]. This collective Rayleigh scattering is a process whereby initially unoccupied modes of the electromagnetic field become weakly populated by spontaneous Rayleigh scattering, and then amplified along the direction of highest optical depth. The superradiance arises because of the long-lived coherence between different motional states of the condensate, and in fact it can be described by a two-mode squeezing Hamiltonian with the form of equation (1.2). Typically, condensates are produced in anisotropic harmonic potentials, so they are cigar shaped, and the transverse modes that dominate are those that propagate along the long axis of the BEC - these are the so-called endfire modes. While an atom returns to its initial internal state after a scattering event, conservation of momentum requires that the atom recoils, and in fact this

recoil plays a significant role in the dynamics: the overlap of recoiling and stationary wavefunctions leads to a modulation of the atomic density distribution. For the case of an end-pumped sample, so that the strong beam propagates along the long axis of the condensate, the overlap of the mother condensate and one recoiling order leads to a modulation with spatial period $\lambda/2$, where λ is the wavelength of the incident light. Similarly, the scattered light interferes with the incident light, leading to an intensity modulation - again with spatial period $\lambda/2$. In this way, the dynamics is determined by the overlap of the light and matter-wave *gratings*, and in general, these vary in amplitude and phase over the length of the BEC. As such, this four wave mixing is an example of the quantum state engineering mentioned above, where the light and atomic systems exert a comparable effect on each other.

Superradiant Rayleigh scattering is the primary topic of this thesis. Our goal is to explore the process in order to provide a foundation for later work on quantum memories and in general, the probing of the condensate by off-resonant light. The experimental work was performed over a four year period, from January 2004 to February 2008. However, nearly the first three years were spent building the machine to produce Bose Einstein condensates, and this is the subject of the next two chapters. Chapter 2 introduces some fundamental results relating to Bose-Einstein condensation in dilute gases. The first half of chapter 3 describes the more applied background for the realization of Bose-Einstein condensation in ^{87}Rb: the relevant atomic properties and the cooling and trapping techniques are described. The second half of chapter 3 describes the practical details in the experimental realization, culminating in the demonstration of Bose-Einstein condensation. Chapter 4 is a presentation of the methods we use to probe the atoms; a significant portion of the chapter is devoted to absorption imaging. Chapter 5 provides an introduction to superradiance, and a presentation of the 1D Maxwell-Schrödinger equations we use to simulate the process. Where possible in the later chapters, we point out similarities between the superradiance of inverted samples, and the superradiant scattering we observe. Chapter 6 contains a study of the dynamics of superradiant Rayleigh scattering, where the main results relate to a systematic study of the effects pump beam detuning and depletion on the dynamics [11, 12]. We compare the experimental data with simulations of the 1D Maxwell-Schrödinger equations and find good agreement, but more generally, the simulations give great insight into the longitudinal structure that builds up in the light and matter waves. The most remarkable feature is the formation of resonator structures within the BEC. Chapter 7 presents two results associated with fluctuations in superradiance: given that the process is initiated by spontaneous scattering, superradiant light scattering may be thought of as the amplification of quantum noise [13]. The final section of chapter 7 is devoted to a first attempt to observe correlations in the number of diffracted atoms and scattered photons. Finally, chapter 8 presents a brief summary of the thesis and an outlook for the experiment.

Chapter 2

BEC theory

2.1 Introduction

When the number of Bosons in a particular state becomes so large that it is comparable to the total number of particles in the system, this state is called a Bose-Einstein condensate. The name comes from the physicists who predicted the phenomenon [14, 15], and the analogy of vapour condensing on a cold surface: the microscopic arrangement of particles in the system and hence the ensemble's physical properties change dramatically. Since the realization of Bose-Einstein condensation in dilute alkali gases in 1995 [5, 6, 7], BEC has become an incredibly active field of research with great interplay between theory and experiments. Developments in experimental atomic physics have meant that BECs can be produced with a wide variety of properties such as particle number, geometry, dimensionality, density and inter-atomic interaction strength, and that these properties can be explored with great precision. Furthermore, beyond being of fundamental interest, a BEC is a very attractive and useful atomic sample for its high density and unique coherence properties within the fields of quantum optics, and more recently, quantum information.

In this chapter, we introduce the ideas necessary for a general understanding of the realization of Bose-Einstein condensation in dilute gases, and the rudiments of the mathematical description of trapped BECs. The physics we describe here is one step removed from that of the realization - the trapping and cooling to degeneracy of ^{87}Rb will be described in chapter 3. We begin with the thermodynamics of a non-interacting Bose gas, with the goals of getting estimates for the critical temperature at which Bose-Einstein condensation begins and other thermodynamic quantities that inform our experimental practices. In particular, we explore how the velocity distributions of thermal clouds and BECs differ, which is an important experimental signature of Bose-Einstein condensation. We subsequently give a brief introduction to the microscopic description of an interacting Bose gas, formulated in the language of second quantization. We then show how a *mean-field* description of the condensed

state arises through an approximation of the field operators. The mean-field description of the condensed state leads to the Gross-Pitaevskii equation (GPE). This is a Schrödinger equation with a non-linear term that describes interactions between the atoms at the mean field level. This brief summary draws primarily on [16, 17, 18].

2.2 The non-interacting Bose gas

The mean occupation number n_s of the single particle state s is given by the Bose distribution:

$$n_s = n(\varepsilon_s) = \frac{1}{\exp((\varepsilon_s - \mu)/k_B T) - 1}, \tag{2.1}$$

where μ is the chemical potential, k_B Boltzmann's constant, T the temperature and ε_s denotes the energy of the single particle state for the given trapping potential. The total number of particles can then be expressed as:

$$N = \sum_{s=0}^{\infty} n_s = N_0 + \sum_{s=1}^{\infty} n_s, \tag{2.2}$$

where in the last equality we break up the sum to explicitly include the occupation of the lowest energy state, and write N_0 for the ground state occupation number. Typically the sum over the excited states on the right hand side of equation (2.2) is replaced by an integral because analytic solutions are difficult to calculate for discrete energy levels. If the energy eigenvalues of the system are close together compared to the energy in the system - i.e., $k_B T \gg \varepsilon_s$ - then the discrete levels may be well-approximated by a continuum. We can rewrite (2.2) using this approximation:

$$N = N_0 + N_{\text{ex}} = N_0 + \int_0^{\infty} d\varepsilon g(\varepsilon) n(\varepsilon), \tag{2.3}$$

where $g(\varepsilon)$ is the density of states. The strategy then is to evaluate the number of bosons in excited states N_{ex} using this method and then to infer the occupation number N_0 from equation (2.2).

In order to proceed, we require an expression for the density of states, and this means that we must choose the form of the potential used to trap the bosons. In essentially all experiments used to generate BECs, the trapping potentials can be regarded as being (at some level of approximation) harmonic, defined by:

$$V(\mathbf{x}) = \frac{1}{2} M(\omega_1^2 x_1^2 + \omega_2^2 x_2^2 + \omega_3^2 x_3^2), \tag{2.4}$$

where M is the mass of a particle and ω_i is the classical oscillation frequency along direction i. If we neglect the zero-point motion of the atoms, and make the continuum approximation described above, we find the density of states for a three dimensional harmonic oscillator to be:

$$g(\varepsilon) = \frac{\varepsilon^2}{2\hbar^3 \bar{\omega}^3}, \tag{2.5}$$

where $\bar{\omega} = (\omega_1\omega_2\omega_3)^{1/3}$ is the geometric mean of the trap frequencies .

2.2.1 Critical temperature

The highest temperature at which there is a macroscopic population in the lowest energy state is called the critical temperature T_c. Alternatively, we may obtain T_c (or at least an upper bound for T_c) by finding the lowest temperature at which all of the particles may be accommodated in the excited states. At T_c, the chemical potential is very small, slightly negative, and, in principle, the chemical potential must be set such that equation (2.3) is satisfied. However, another advantage of the approach of using the occupancies of the excited states to infer N_0 is that the exact value of μ affects $N_{\rm ex}$ very weakly (the excited state energies $\varepsilon \gg \mu T_c$), whereas it has a very strong effect on the value of $N_0 = 1/(\exp(-\mu/k_BT_c) - 1)$. Thus, to a good approximation we may set $\mu = 0$ and find T_c from:

$$\begin{aligned} N = N_{\rm ex}(T_c, \mu = 0) &= \int_0^\infty d\varepsilon g(\varepsilon) n(\varepsilon) \\ &= \frac{1}{2\hbar^3\bar{\omega}^3}\int_0^\infty d\varepsilon \frac{\varepsilon^2}{\exp(\varepsilon/k_BT) - 1} \\ &= \frac{1}{2\hbar^3\bar{\omega}^3}\Gamma(3)\zeta(3)(kT_c)^3. \end{aligned} \tag{2.6}$$

The integral is solved by expanding the Bose distribution in powers of $\exp(-\varepsilon_s/k_BT)$ and recognizing the gamma function $\Gamma(\alpha) = \int_0^\infty dx x^{\alpha-1}e^{-x}$, and $\zeta(\alpha) = \sum_{m=1}^\infty m^{-\alpha}$ as the Riemann Zeta function. Rearranging, and noting $\Gamma(3) = 2$, $\zeta(3) = 1.202$, we find:

$$k_BT_c = \hbar\bar{\omega}\left(\frac{N}{\zeta(3)}\right)^{1/3} \approx 0.94\hbar\bar{\omega}N^{1/3}. \tag{2.7}$$

To put an approximate value to this, equation (2.7) leads to a critical temperature of ~ 250 nK for standard experimental values ($N \sim 10^6$ and $\bar{f} = \bar{\omega}/2\pi \sim 50$ Hz). Corrections such as the effects of finite particle number and collisions between atoms modify this result by only a few percent [19].

There is an additional way to quantify the conditions under which a BEC is formed, namely through the phase-space density, which is defined as:

$$\rho = n\lambda_T^3 = n\left(\frac{2\pi\hbar^2}{Mk_BT}\right)^{3/2}, \tag{2.8}$$

where n is the particle density, and λ_T is the thermal de Broglie wavelength. It is instructive to consider the phase space density at the centre of a trapped cloud, around the critical temperature. As we shall see in section 2.2.3, the density distribution of a thermal cloud in a harmonic trap is Gaussian, so if we consider a small central volume V of the cloud where the density distribution is essentially flat, then the density in this region takes the very simple form of $n = N/V$, i.e., we approximate the

central portion of the cloud with a uniform gas. With this approximation, equation (2.8) becomes $\rho = N(\lambda_T^3/V)$. From this equation, it is clear that the phase space density quantifies the ratio between the physical extent of the particle wavefunctions and the volume they occupy. The equivalent result to equation (2.7) for a uniform gas is $k_B T_c = (2\pi\hbar^2/m)(n/\zeta(3/2))^{3/2}$. Inserting this into equation (2.8), we find that at the critical temperature, the phase space density at the centre of the cloud is $\rho = \zeta(3/2) \approx 2.612$. This suggests the intuitive idea that condensation begins when the wavefunctions of different particles begin to overlap.

2.2.2 Condensate fraction

Under the approximation $\mu = 0$, the result of equation (2.6) may be used to calculate the number of particles in the condensate below the critical temperature. We have:

$$N_{\rm ex}(T, \mu = 0) = N\left(\frac{T}{T_c}\right)^3, \tag{2.9}$$

and the number of particles in the condensate is given by:

$$N_0 = N - N_{\rm ex} = N\left[1 - \left(\frac{T}{T_c}\right)^3\right]. \tag{2.10}$$

2.2.3 Position and momentum distributions

The density and velocity distributions of trapped Bose Einstein condensates are the main features that are experimentally accessible; for this reason we now give a brief summary of what is expected from quantum mechanics for the condensed state and from statistical mechanics for the particles in excited states, when interactions between particles are neglected.

The wavefunction of the condensed state in the absence of interactions is simply N times the single particle wavefunction, which in a harmonic potential is Gaussian. The total density is thus:

$$n(\mathbf{x}) = N\,|\phi_0(\mathbf{x})|^2, \tag{2.11}$$

and the single particle wavefunctions are given by:

$$\phi_0(\mathbf{x}) = \frac{1}{\pi^{3/4}\sqrt{\sigma_1\sigma_2\sigma_3}} e^{-x_1^2/2\sigma_1^2} e^{-x_2^2/2\sigma_2^2} e^{-x_3^2/2\sigma_3^2}, \tag{2.12}$$

where $\sigma_i^2 = \hbar/M\omega_i$ defines the widths in the three directions. The momentum distribution is given by the Fourier transform of equation (2.12). Because the Fourier transform of a Gaussian is also a Gaussian, $\phi_0(\mathbf{p})$ has the same form as equation (2.12) except that the widths are given by $\varsigma_i^2 = \hbar^2/\sigma_i^2 = \hbar M\omega_i$. This relationship

is the content of the Heisenberg uncertainty principle for canonical variables x and p: in this setting the uncertainty principle is essentially a Cauchy-Scwharz inequality applied to Fourier transform pairs. Thus, wavefunctions that are tightly confined in space will have correspondingly larger widths in momentum space, meaning that clouds released from anisotropic traps will expand differently along the different axes of the trap.

In principle, the density distribution of trapped atoms may be found by evaluating:

$$n(\mathbf{x}) = \sum_s n_s \, |\phi_s(\mathbf{x})|^2 , \tag{2.13}$$

where the density distribution of each state is weighted by its occupation number, given by the Bose distribution (2.1). Such an approach requires knowledge of the wavefunctions of the given potential and is difficult to work with in general. However, there exists an alternative, semi-classical approach that works well for the excited states and reproduces the results for N_0, $N_{\rm ex}$, and T_c that we calculated above [16]. The approach relies on replacing the discrete energy eigenvalues ε_s and eigenstates $\phi_s(\mathbf{x})$ in equation (2.13) with the energy of a free particle in a potential:

$$\varepsilon(\mathbf{p},\mathbf{x}) = p^2/2M + V(\mathbf{x}). \tag{2.14}$$

In this way, the gas is treated as uniform, where the particle's energy is determined by its kinetic energy and the local value of the potential. The approach is valid when the spatial de Broglie wavelength of the particle is small compared to interval over which the potential varies significantly. Using (2.14), the Bose distribution can be modified such that:

$$n(\mathbf{p},\mathbf{x}) = \frac{1}{\exp((\varepsilon(\mathbf{p},\mathbf{x}) - \mu)/k_B T) - 1}, \tag{2.15}$$

where $n(\mathbf{p},\mathbf{x}) d\mathbf{p} d\mathbf{x}/(2\pi\hbar)^3$ yields the number of particles in a phase-space volume element [20]. Thus, we can obtain in-trap position and momentum distributions for the excited states by integrating equation (2.15) over $\mathbf{p}$ and $\mathbf{x}$ respectively. For example:

$$n_{\rm ex}(\mathbf{x}) = \int \frac{d\mathbf{p}}{(2\pi\hbar)^3} \frac{1}{\exp((\varepsilon(\mathbf{p},\mathbf{x}) - \mu)/k_B T) - 1}. \tag{2.16}$$

To solve the integral, we define $z(\mathbf{x}) = \exp(\mu - V(\mathbf{x})/k_B T)$, adopt spherical polar coordinates so that $d\mathbf{p} = p^2 \sin\theta \, dp \, d\theta \, d\phi$, and make the substitution $y = p^2/2Mk_B T$ so that (2.16) becomes:

$$n_{\rm ex}(\mathbf{x}) = \frac{2}{\sqrt{\pi}\lambda_T^3} \int dy \frac{y^{1/2}}{z^{-1}\exp(y) - 1}. \tag{2.17}$$

This integral is similar to that found in (2.6), and again one expands the denominator of the integrand in a power series $1/(z^{-1}e^y - 1) = ze^{-y}/(1 - ze^{-y}) = \sum_{n=1}^{\infty} z^n e^{-ny}$.

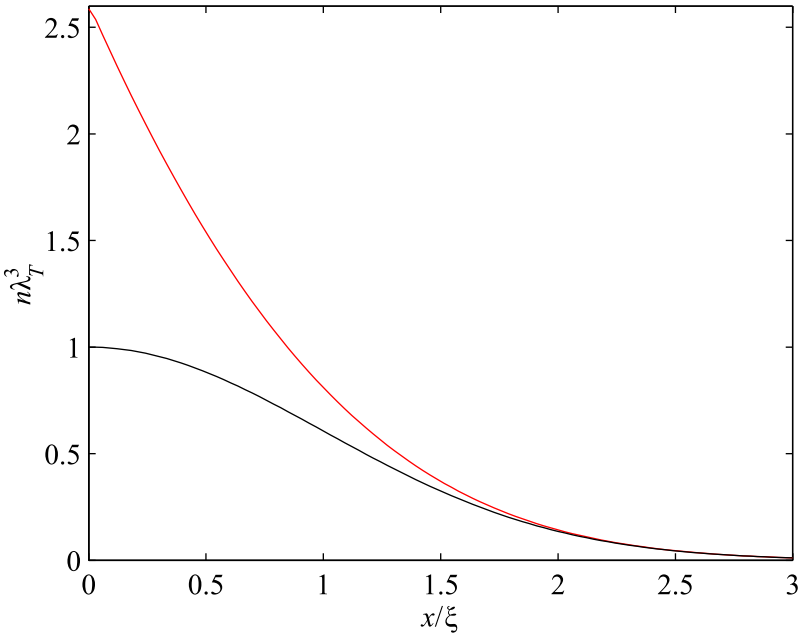

FIGURE 2.1: The density distribution along one axis of a thermal cloud trapped in a harmonic potential. $g_{3/2}(z(x))$ (red) and a Gaussian (black) are plotted. The Gaussian corresponds to the first term of the Bose function.

The result is:

$$n_{\text{ex}}(\mathbf{x}) = \frac{g_{3/2}(z(\mathbf{x}))}{\lambda_T^3}, \tag{2.18}$$

where

$$g_\gamma(z) = \sum_{m=1}^{\infty} \frac{z^m}{m^\gamma}, \tag{2.19}$$

is the Bose function. When $z = 1$ (i.e., $V = 0$ and $\mu = 0$), the Bose function reduces to the Riemann Zeta function $\zeta(\gamma)$ in agreement with the results of section 2.2.1. Equation (2.18) gives the density distribution of the excited states for a given trapping potential. The first term of the series expansion corresponds to the result if we had considered the Boltzmann distribution rather than the Bose distribution. In the case of a harmonic potential, and setting $\mu = 0$, $z(\mathbf{x}) = \exp(-M(\omega_1^2 x_1^2 + \omega_2^2 x_2^2 + \omega_3^2 x_3^2)/2k_B T)$, we find the expected Gaussian density distribution for a gas at high temperature. As such, the terms $m \geq 2$ in equation (2.19) show how the Gaussian density distribution at high $k_B T$ is modified by Bose-Einstein statistics at low temperatures. Indeed, the density of a Bose gas is larger than that of a classical ideal gas by a factor of $g_{3/2}(z)/z$ [21], as may be seen in figure 2.1.

The momentum distribution may be found by the same method, except that in equation (2.16) we integrate over $d\mathbf{x}$. Due to the fact that the kinetic energy and potential terms are both quadratic in a harmonic oscillator, the integral over $\mathbf{x}$ yields (up to a constant factor) the same result as equation (2.18). Thus for zero chemical potential, $z(\mathbf{p}) = \exp(p^2/2Mk_BT)$, and the momentum distribution is Gaussian, with corrections given by the higher order terms of the Bose function. The crucial factor to note however, is that the momentum distribution in-trap is isotropic, in stark contrast to that of the condensate.

In summary, the in-trap density and momentum distributions of condensed and excited non-interacting particles show considerable differences. The density distributions in both cases reflect the shape of the trap: the higher the trapping frequency in a given direction, the narrower the density distribution along this direction. However, the widths of the Bose-condensed and thermal clouds differ considerably: even at T_c the characteristic width of the ground state wavefunctions in a harmonic trap $\sigma_i = \sqrt{\hbar/M\omega_i}$ is much smaller than the corresponding widths of the Boltzmann distribution $\xi_i = \sqrt{k_BT/M\omega_i^2}$. The ratio of the two widths is $\xi_i/\sigma_i = \sqrt{k_BT/\hbar\omega_i}$, and the same result holds for the ratio of the widths of the momentum distributions. For standard experimental parameters (see section 2.2.1), this ratio is of order 10, meaning that the different cases are easy to differentiate. Thus the picture that emerges is that the BEC will appear as a narrow peak at the centre of both the density and momentum distributions. In the case of the density distribution, the condensate shares the same aspect ratio as the thermal cloud, determined by the trapping potential; whereas in the momentum distribution, the condensate will reflect the uncertainty principle and show the inverse aspect ratio, and the momentum distribution of the thermal cloud will be isotropic.

2.3 Theory of the condensed state

Given the extremely high density in a BEC, collisions between particles become important and must be taken into account in the condensed state's description. Our main goal in this section is to present the Gross-Pitaevskii equation, the analogue of the Schrödinger equation for the condensed state that has an additional, non-linear term that describes the effects of collisions between the particles at the mean field level. With this equation, we obtain the density distribution of the condensed state that differs from that obtained in the non-interacting case. However, we first sketch how the Gross-Pitaevskii equation is obtained and the conditions under which it is valid.

2.3.1 Field theoretic description of the condensed state

The many-body Hamiltonian describing the condensed state in position space in second quantization is given by [17]:

$$\begin{aligned}\hat{H} = &\int d\mathbf{x}\hat{\Psi}^\dagger(\mathbf{x})\left[-\frac{\hbar^2}{2M}\nabla^2 + V(\mathbf{x})\right]\hat{\Psi}(\mathbf{x}) \\ &+ \frac{1}{2}\int d\mathbf{x}d\mathbf{x}'\hat{\Psi}^\dagger(\mathbf{x})\hat{\Psi}^\dagger(\mathbf{x}')U(\mathbf{x}-\mathbf{x}')\hat{\Psi}(\mathbf{x}')\hat{\Psi}(\mathbf{x}),\end{aligned} \tag{2.20}$$

where $\hat{\Psi}(\mathbf{x})$ and $\hat{\Psi}^\dagger(\mathbf{x})$ are the bosonic field operators that create and annihilate respectively a particle at position $\mathbf{x}$, and $U(\mathbf{x}-\mathbf{x}')$ is the potential of the two body interaction. The field operators may be decomposed as $\hat{\Psi}(\mathbf{x}) = \sum_s \Psi_s(\mathbf{x})\hat{b}_s$ such that the position dependence is absorbed into the single particle wavefunctions $\Psi_s(\mathbf{x})$, leaving the bosonic creation and annihilation operators defined in Fock space by:

$$\hat{b}_s^\dagger|n_0,n_1,\ldots,n_s,\ldots\rangle = \sqrt{n_s+1}|n_0,n_1,\ldots,n_s+1,\ldots\rangle, \tag{2.21a}$$

$$\hat{b}_s|n_0,n_1,\ldots,n_s,\ldots\rangle = \sqrt{n_s}|n_0,n_1,\ldots,n_s-1,\ldots\rangle, \tag{2.21b}$$

where n_s is the eigenvalue of the number operator defined by:

$$\hat{n}_s = \hat{b}_s^\dagger\hat{b}_s. \tag{2.22}$$

The bosonic creation and annihilation operators satisfy the commutation relations:

$$[\hat{b}_s,\hat{b}_t^\dagger] = \delta_{s,t}, \qquad [\hat{b}_s,\hat{b}_t] = 0, \qquad [\hat{b}_s^\dagger,\hat{b}_t^\dagger] = 0. \tag{2.23}$$

The corresponding commutation relations for the position space field operators are given by:

$$[\hat{\Psi}(\mathbf{x}),\hat{\Psi}^\dagger(\mathbf{x}')] = \delta(\mathbf{x}-\mathbf{x}'), \quad [\hat{\Psi}(\mathbf{x}),\hat{\Psi}(\mathbf{x}')] = 0, \quad [\hat{\Psi}^\dagger(\mathbf{x}),\hat{\Psi}^\dagger(\mathbf{x}')] = 0. \tag{2.24}$$

As we have seen, Bose-Einstein condensation occurs when the occupation number n_s of a particular state becomes commensurate with the number of particles in the system. Here, we only consider the case where $s = 0$, i.e., when the condensate forms in the ground state of the system. In this case, $n_0 = N_0 \simeq N$, and the ratio N_0/N remains finite in the thermodynamic limit where $N \to \infty$. Accordingly, N_0 is generally a very large number, so that $N_0 \simeq N_0 \pm 1$ and the physical states corresponding to these occupation numbers are approximately the same, provided one assumes that a coherent state is an appropriate description of the condensed state. Formally, one can replace the operators $\hat{b}$ and $\hat{b}^\dagger$ by their approximate eigenvalues so that $\hat{b} = \hat{b}^\dagger = \sqrt{N}$. It corresponds to representing the field operators by their approximate mean values plus a perturbation that retains the operator character. Thus, the field operators may be expressed in the Heisenberg representation:

$$\hat{\Psi}(\mathbf{x},t) = \psi(\mathbf{x},t) + \delta\hat{\Psi}(\mathbf{x},t), \tag{2.25}$$

where $\psi(\mathbf{x},t) \equiv \left\langle \hat{\Psi}(\mathbf{x},t) \right\rangle$ is the mean value of the field operator, and $\delta\hat{\Psi}(\mathbf{x},t)$ represents the deviations from this mean. $\psi(\mathbf{x},t)$ is called the condensate wavefunction or *order parameter* and has the same interpretation as a many-body wavefunction from standard first quantization quantum mechanics. The condensate wavefunction is normalized such that:

$$\int d\mathbf{x} n_0(\mathbf{x},t) = \int d\mathbf{x} |\psi(\mathbf{x},t)|^2 = N_0. \tag{2.26}$$

The dynamics of the condensate are obtained from the Heisenberg equation of motion for the field operator:

$$\begin{aligned} i\hbar\frac{\partial\hat{\Psi}(\mathbf{x},t)}{\partial t} &= [\hat{\Psi},\hat{H}] \\ &= \left[-\frac{\hbar^2}{2M}\nabla^2 + V(\mathbf{x}) + \int d\mathbf{x}\hat{\Psi}^\dagger(\mathbf{x},t)U(\mathbf{x}-\mathbf{x}')\hat{\Psi}(\mathbf{x}',t)\right]\hat{\Psi}(\mathbf{x},t) \end{aligned} \tag{2.27}$$

If we now substitute equation (2.25) into equation (2.27) and select the mean field component we obtain the Schrödinger equation for the condensate wavefunction.

$$i\hbar\frac{\partial\psi(\mathbf{x},t)}{\partial t} = \left[-\frac{\hbar^2}{2M}\nabla^2 + V(\mathbf{x}) + \int d\mathbf{x}\psi(\mathbf{x},t)U(\mathbf{x}-\mathbf{x}')\psi(\mathbf{x}',t)\right]\psi(\mathbf{x},t) \tag{2.28}$$

However, in order to continue we require an expression for the interaction term $U(\mathbf{x}-\mathbf{x}')$.

2.4 Interactions in a dilute gas

It is an important feature of most experimentally produced BECs that while their density is very high, they are still dilute gases in the sense that the length a that characterizes collisions between particles is much smaller than the mean inter-particle spacing, which is of order $\Delta x \simeq (1/n)^{1/3}$. Approximate values for these quantities are $a \sim 100a_0 \simeq 5$ nm where a_0 is the Bohr radius and which gives the approximate size of an atom; and $\Delta x \simeq 100$ nm for density $n = 10^{14}$ cm^{-3}. As such, two body collisions dominate.

At the low temperatures described in section 2.2.1 where BECs form, the main form of scattering that occurs is isotropic. That is, *s-wave* scattering predominates, corresponding to the $l = 0$ term in a partial-wave expansion of the scattered wave [22]. The inter-atomic potential is given by the lowest order van der Waals interaction - an induced dipole-dipole interaction - that has the form $U \sim \alpha/r^6$ as the separation between atoms $r \to \infty$, where α is a constant. In this limit, the scattering is characterized by a single parameter, the *scattering length* a, and the scattered wavefunction describing the relative motion, having transformed into the centre of mass frame, can be written as:

$$\psi(r) = C\frac{\sin(k(r-a))}{r}, \tag{2.29}$$

where C is a constant. If the scattering length is negative, ψ is drawn closer to the origin - the interaction is attractive. If the scattering length is positive, then the relative wavefunction is pushed away from the origin, i.e., the interaction is repulsive, and the wavefunction (at large r) is equivalent to one that would arise from scattering from a hard sphere potential of radius a [18]. While the colliding particles are 'close' to each other, that is for $r < a$, the wavefunctions undergo rapid oscillations that depend on the exact nature of the full potential U. However, under the condition that two-body, low energy collisions between atoms predominate, the true potential $U(\mathbf{x}-\mathbf{x}')$ may be replaced by an effective interaction between bosons that is exact in the limit of large separation. This is given by:

$$U_0(\mathbf{x}-\mathbf{x}') = \frac{4\pi\hbar^2 a}{M}\delta(\mathbf{x}-\mathbf{x}'). \tag{2.30}$$

2.5 The Gross-Pitaevskii equation

Upon substitution of equation (2.30) into equation (2.28), and suppressing the time dependence, we obtain the time-independent Gross-Pitaevskii equation :

$$-\frac{\hbar^2}{2M}\nabla^2\psi(\mathbf{x}) + V(\mathbf{x})\psi(\mathbf{x}) + U_0\left|\psi(\mathbf{x})\right|^2\psi(\mathbf{x}) = \mu\psi(\mathbf{x}). \tag{2.31}$$

Equation (2.31) is the Schrödinger equation for the mean field of the condensed state where interactions between atoms are described through a nonlinear, density dependent term [23, 24]. The eigenvalue on the right hand side of equation (2.31) is the chemical potential rather than the energy.

2.5.1 The Thomas Fermi approximation

For a sufficiently large cloud, the mean field interaction term in equation (2.31) becomes large due to its non-linearity. If the scattering length is positive then the effective interaction between particles is repulsive and the density distribution becomes broader as particles in the high-density centre of the cloud seek to lower their energy. In this case, the kinetic energy term in equation (2.31) becomes small relative to the potential and mean-field terms and may be neglected. Then equation (2.31) becomes:

$$\left[V(\mathbf{x}) + U_0\left|\psi(\mathbf{x})\right|^2\right]\psi(\mathbf{x}) = \mu\psi(\mathbf{x}), \tag{2.32}$$

which has the solution:

$$n(\mathbf{x}) = \left|\psi(\mathbf{x})\right|^2 = \frac{\mu - V(\mathbf{x})}{U_0}. \tag{2.33}$$

Given the density cannot become negative, the wavefunction must vanish when $\mu - V(\mathbf{x}) \leq 0$. Thus, a cloud in the Thomas Fermi approximation in a harmonic potential has the form of an inverted parabola:

$$n(\mathbf{x}) = \begin{cases} \left[\mu - \frac{1}{2}M(\omega_1^2 x_1^2 + \omega_2^2 x_2^2 + \omega_3^2 x_3^2)\right]/U_0 & x_i \leq \sqrt{\frac{2\mu}{M\omega_i^2}}, \\ 0 & \text{elsewhere.} \end{cases} \tag{2.34}$$

Chapter 3

Realization

3.1 Introduction

In this chapter, we describe the important elements in our realization of Bose-Einstein condensation in ^{87}Rb. The path we have taken to generate BEC in ^{87}Rb is reasonably well-trodden, so essentially all of the material presented here can be found in other publications. Nonetheless, a coherent description of the diverse physics and techniques that goes into the realization is valuable both for the author and new students entering the lab. As such, the style of this chapter will be part tutorial and part 'distilled experience from the lab'.

To get an idea of the general set-up of the experiment, it actually helps to start at the final phase of BEC generation: evaporative cooling in a magnetic trap. Evaporative cooling is a multi-step process in which the hottest atoms are selectively removed from the trap, whereupon, due to elastic collisions between the atoms, a new 'thermal tail' appears in the Maxwell Boltzmann distribution of the sample. When the process is repeated many times, or continuously in practice, the atoms that carry more than the mean energy are removed from the sample, leading to a reduction in its temperature - at the expense of discarding some fraction of the atoms. Evaporative cooling works very efficiently when one reaches high densities, but if one doesn't start with the appropriate initial conditions, no amount of optimization will be enough to achieve BEC. One needs to begin with samples of high enough density such that the elastic collision rate increases throughout the cooling, despite the losses associated with evaporation and collisions with background gas molecules. This leads to several practical requirements: a tight trap and a large number of atoms in the sample at the start of evaporation, so that one can achieve high initial densities, and a very good level of vacuum so that the lifetime of the trap is sufficient. For the latter reasons, vacuum chambers for BEC experiments are generally divided into two parts that are kept at different levels of vacuum. In the first part, *the loading chamber*, the goal is to accumulate as many atoms at as low a temperature as possible. In our case,

we run a 2D MOT from a background vapour of ^{87}Rb at $\sim 10^{-9}$ torr, produced by dispensers inside the chamber. This level of background pressure is not compatible with the stringent vacuum requirements described above - hence the need for a dedicated chamber for this purpose. The atoms are transferred by radiation pressure to the second chamber - *the science chamber* - where the evaporation takes place. The atoms are caught in a standard 3D MOT in the science chamber, which is held by differential pumping at the required level of vacuum, on the order of 10^{-11} torr. When a sufficient number of atoms has been loaded into the science MOT, the trapping light is extinguished and the magnetic trap is turned on, whereupon we evaporatively cool the atoms by selectively driving radio-frequency (RF) transitions to untrapped states.

As such, there are several phases in an experimental run to produce a BEC, each requiring its own techniques and equipment. The chapter begins with a brief description of some of the relevant properties of ^{87}Rb. Subsequently, we present an introduction to the cooling and trapping physics we make use of in the experiment. We give a very brief introduction in section 3.4 to absorption imaging and the different cloud shapes we observe by this method. This leads to a description of the main components of the laboratory. The chapter concludes with the experimental demonstration of Bose-Einstein condensation.

3.2 Properties of Rubidium 87

Of the many groups around the world that produce Bose Einstein condensates, by far and away the most common atomic species used is ^{87}Rb. There are several reasons for this, but the most obvious are that the wavelengths of the main resonance lines are accessible by inexpensive lasers, that the vapour pressure at room temperature allows loading of Magneto-Optical traps (MOTs) from background vapour, and the fact that it has reasonably favourable collisional properties. Furthermore, it is a species for which the path to BEC is well known. ^{87}Rb was the first species to be condensed [5]; followed very closely by Sodium (^{23}Na) [6]. Subsequently the following species have been condensed: Lithium (^{7}Li) [7, 25], Hydrogen (^{1}H) [26], the other bosonic isotope of Rubidium (^{85}Rb), metastable triplet Helium (^{4}He*) [27, 28], Potassium (^{41}K) [29], Caesium (^{133}Cs) [30], Ytterbium (^{174}Yb) [31], and Chromium (^{52}Cr) [32]. As such, the alkali earths - the left-most column of the periodic table with a single unbound electron in the outermost shell - have predominated, but atoms with other configurations are now becoming more popular in the search for atoms with different (collisional) properties. Here we summarize the properties of ^{87}Rb that are important in the realization of Bose-Einstein condensation. An excellent resource for the properties of ^{87}Rb is reference [33].

The first point to note that ^{87}Rb is a boson comprised of an even number of fermions - it has integer total spin: 37 protons and electrons each, and 50 neutrons.

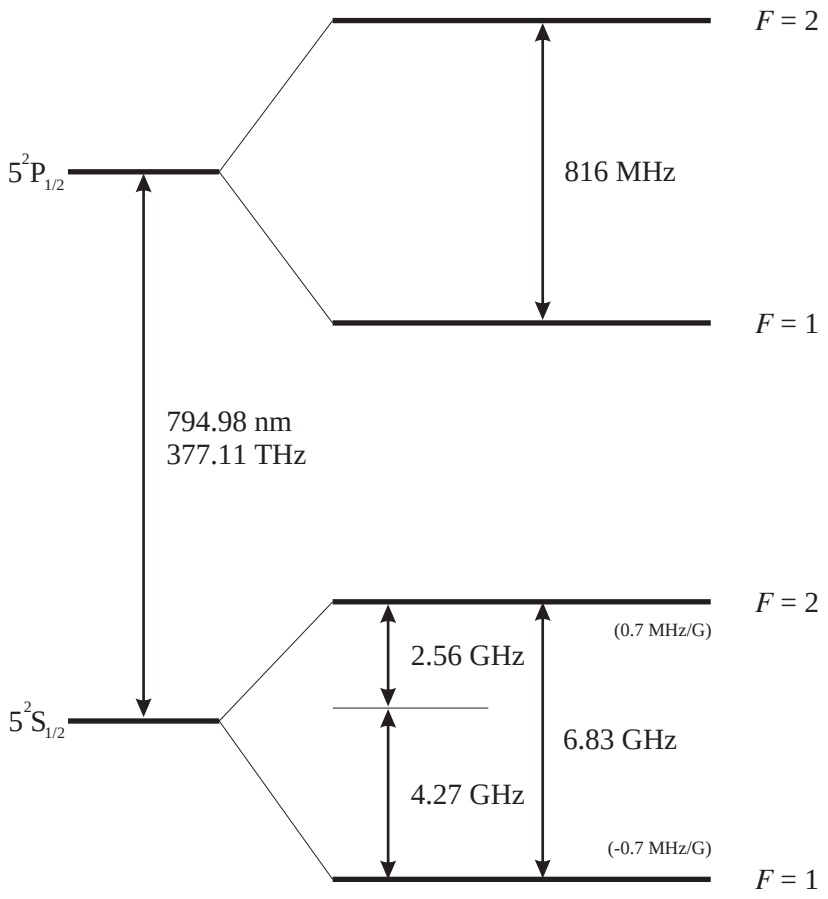

FIGURE 3.1: D1 line of ^{87}Rb: $5^2S_{1/2} \rightarrow 5^2P_{1/2}$. The Zeeman shift for low applied magnetic field between adjacent magnetic sublevels is shown for the two ground states.

As long as the energies involved in the generation of the condensate are considerably smaller than the ionization or binding energies of the atom, the fact that it has internal structure will not affect its 'bosonic properties'.

The atomic mass of ^{87}Rb is 1.443×10^{-25} kg. The vapour pressure at 25°C is 3.0×10^{-7} torr; it turns out that this value means that a good sized MOT can be loaded efficiently from a background vapour that is still compatible with Ultra High Vacuum (UHV - corresponding to pressures lower than $\sim 10^{-9}$ torr). If one compares this value with that for Sodium - 2.2×10^{-11} torr - it is understandable that BEC experiments in Sodium require ovens and Zeeman-slowers to produce the atom flux necessary to load large MOTs.

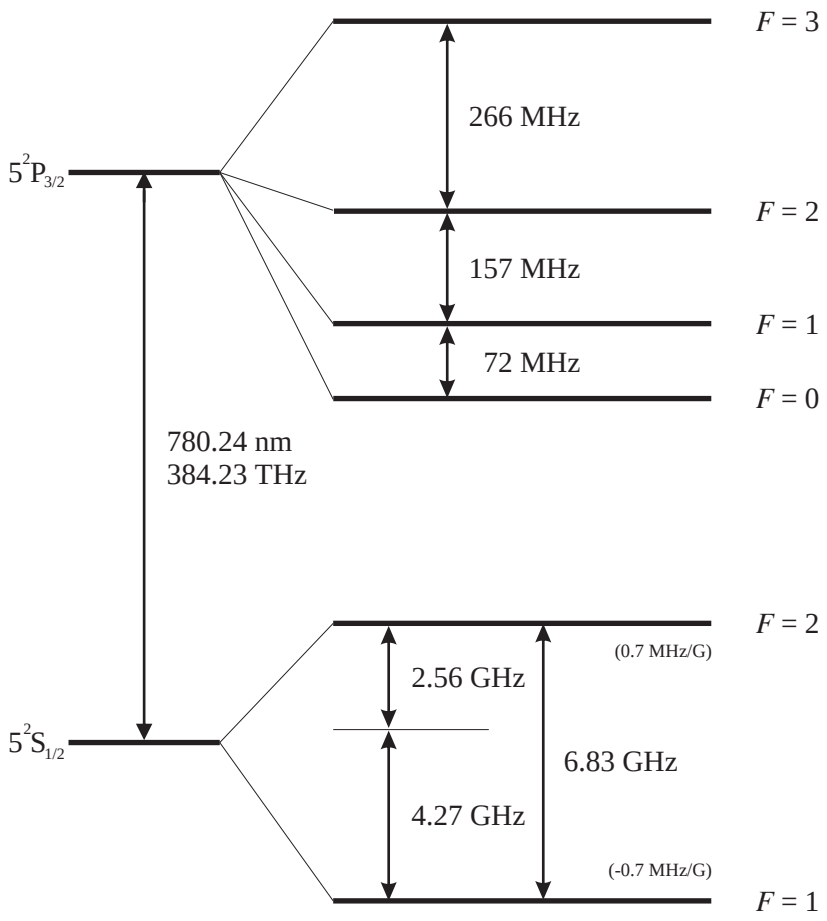

FIGURE 3.2: D2 line of ^{87}Rb: $5^2S_{1/2} \rightarrow 5^2P_{3/2}$. The Zeeman shift for low applied magnetic field between adjacent magnetic sublevels is shown for the two ground states.

3.2.1 Optical transitions

The most frequently used optical resonance lines of ^{87}Rb are shown in figures 3.1 and 3.2. ^{87}Rb has nuclear spin $I = 3/2$, and the coupling of this with the electron spin $S = 1/2$ leads to two ground states, corresponding to total angular momentum $F = I \pm S = 1,2$. In general, the coupling of nuclear spin and the angular momentum of the electron $\mathbf{J} = \mathbf{L} + \mathbf{S}$ - the hyperfine interaction $\propto \mathbf{I} \cdot \mathbf{J}$ - leads to a splitting of the energy levels. The fine structure splitting - the coupling of the electron spin with the orbital angular momentum $\propto \mathbf{S} \cdot \mathbf{L}$ - means that the $L = 0 \rightarrow L = 1$ transition D-line is a doublet, and in fact the splitting is so large that the lines are generally treated separately. Figure 3.1 shows the D1 line, $5^2S_{1/2} \rightarrow 5^2P_{1/2}$, at 795 nm; and figure 3.2 shows the D2 line, $5^2S_{1/2} \rightarrow 5^2P_{3/2}$, at 780 nm. In terms of optical transitions, the closest one can come to a two-level atom in ^{87}Rb is the *cycling transition*

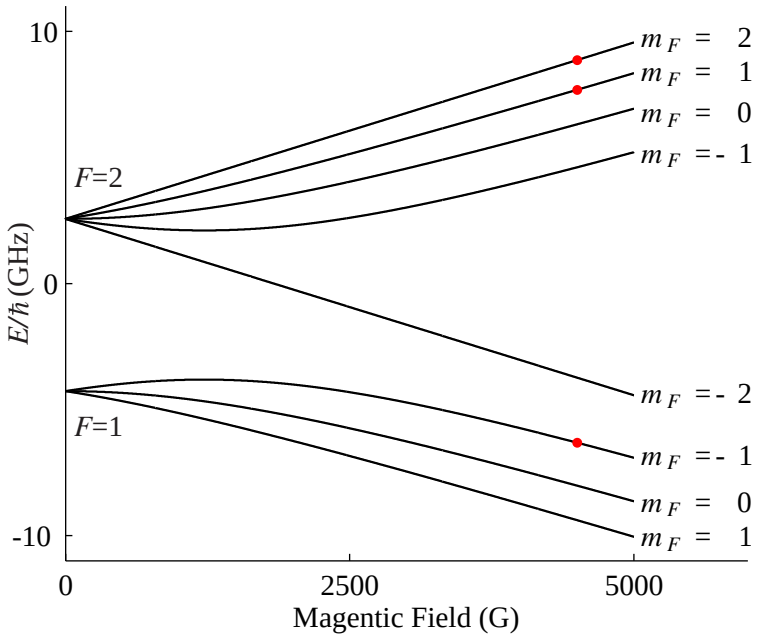

FIGURE 3.3: The Zeeman shift versus applied magnetic field is shown for the two ground states of ^{87}Rb. The red dots denote the magnetic sublevels $F = 2, m_F = 2$, $F = 2, m_F = 1$, and $F = 1, m_F = -1$ that are weak-field seeking states which therefore can be trapped in a magnetic field minimum [34].

$F = 2, m_F = \pm 2 \rightarrow F = 3, m_F = \pm 3$ in the D2 line, in the sense that it is a closed transition: if an atom is in the $F = 3$ excited state, according to selection rules for electric dipole transitions, it can only decay to the $F = 2$ ground state. Thus if one wants to scatter as many photons in as simple a configuration as possible, the cycling transition is the most appropriate, and it is used heavily in the laser cooling and imaging of ^{87}Rb.

3.2.2 Response to a magnetic field

The application of an external magnetic field breaks the degeneracy of the magnetic sublevels. Figure 3.3 shows how the energy levels are perturbed as a function of applied magnetic field. The curves in figure 3.3 are calculated from a diagonalization of the Hamiltonian:

$$H = A_{\mathrm{hfs}} \mathbf{I} \cdot \mathbf{J} + \mu_{\mathrm{B}} (g_J J_z + g_I I_z) B_z, \tag{3.1}$$

where the applied magnetic field has been chosen to be along the z direction. Equation (3.1) is valid for the ground state $L = 0$ provided that the perturbation of the energy levels is small compared to the fine structure splitting[1]. Of interest are the three states that show an (initial) increase in their energy versus applied magnetic field: these are the *weak-field seeking states*. As it is only possible to generate a local magnetic field minimum in a current free region [35], these are the states that can be magnetically trapped; they are identified with red dots in figure 3.3 and are the states: $F = 2, m_F = 2$, $F = 2, m_F = 1$, and $F = 1, m_F = -1$. For low magnetic field values, F is a good quantum number and the change in internal state energy is well described by the relation:

$$\Delta E = m_F g_F \mu_{\mathrm{B}} B, \tag{3.2}$$

where $g_F \approx 1/2$ is the hyperfine Landé g-factor (with correction at the per mil level), and $\mu_{\mathrm{B}} = 1.4$ MHz/G is the Bohr magneton. The maximum magnetic field values we deal with are at the level of a few hundred Gauss, so this approximation is more than adequate.

3.3 Cooling and trapping physics

3.3.1 Laser cooling and the Magneto-Optical trap

We now give a brief introduction to laser cooling and the Magneto-Optical trap (MOT). There are a number of excellent texts on the subject, and the reader is referred to these for a comprehensive presentation of the material [36, 37, 38, 39].

The main idea behind laser cooling is that light exerts a mechanical effect on atoms. A photon carries momentum $\hbar k_l$, where $k_l = 2\pi/\lambda$ is the wavenumber of the light, and when a photon is absorbed and re-emitted by an atom, the motion of the atoms changes so as to conserve momentum. While $\hbar k_l$ is very small compared to the momenta of atoms at room temperature, many absorption and re-emission events arranged in the right way can have a significant effect on an atom's momentum on a short (ms or less) time scale. As is evident in section 2.2.3, to cool an atomic sample means to make its momentum distribution narrower - we require a momentum (or velocity) dependent force. Likewise, to trap the atoms we require a position dependent force.

The force from a beam of light on a two-level atom that is often the starting point for a heuristic discussion of Doppler cooling is given by:

$$F_{\mathrm{sp}} = \hbar k_l \Gamma \rho_{ee} = \hbar k_l \Gamma \frac{s_0/2}{1 + s_0 + (2\delta/\Gamma)^2}. \tag{3.3}$$

[1] The fine splitting is ≈ 7.3 THz, and it is evident from figure 3.3 that the perturbations are on the order of the hyperfine splitting ~ 10 GHz, so the condition is satisfied.

That is, the force on a two level atom is simply given by the momentum of a photon multiplied by the spontaneous emission rate - the decay rate of the excited state Γ multiplied by the probability ρ_{ee} that the atom is in the excited state. The population of the excited state is given in terms of the *on-resonance saturation parameter* $s_0 = 2|\Omega|^2/\Gamma^2 = I/I_s$, where Ω is the Rabi frequency, and I_s is the *saturation intensity*; and the detuning $\delta = \omega_l - \omega_0$. Note that for red detunings $\omega_0 < \omega_l$, and $\delta < 0$. Equation (3.3) does not include the dipole force because at the relatively low detunings considered the absorption and emission of real photons predominates over the dispersive interaction. Furthermore, (3.3) assumes that the direction of re-emission is arbitrary so that on average over many events, the momentum kick from the absorbtion of a laser beam photon is always in the same direction, whereas the net momentum change to the atom from the re-emission of photons is zero.

The required velocity and position dependent forces are realized by changing the effective detuning δ in the force of equation 3.3.

The velocity dependence comes about through the Doppler shift so that the detuning becomes $\delta_D(\vec{v}) = \delta - \vec{k_l} \cdot \vec{v}$. With the choice of red detuning, an atom moving 'towards the beam' will be Doppler shifted closer to resonance and hence the scattering rate will increase, leading to a force opposing the atom's motion. Conversely, if the atom is moving 'away from the beam', the Doppler shift will be negative, and the force on the atom will be lower than that on a stationary atom. By introducing a counter-propagating beam, it is thus possible to damp the motion of an atom in one dimension, provided the atom's velocity is not so large that the concomitant Doppler shift is greater than Γ. This capture velocity is of order $\Gamma/k_l \approx 5$ ms^{-1} for the D2 line of ^{87}Rb .

The position dependent force can be effected by introducing a magnetic field gradient, so that the detuning is modified by a Zeeman energy term like 3.2 (expressed as a frequency): $\delta_{\mathrm{MOT}}(\vec{v}, z) = \delta - \vec{k_l} \cdot \vec{v} + \mu B' z$, where the magnetic field is applied along the z direction. It is important to reinforce that our goal is not to magnetically trap the atom by this arrangement, but to modify the internal energy structure of the atom via the Zeeman effect with the result that the further away from zero magnetic field it ventures, the closer to resonance it is pushed, and hence the higher the restoring force it experiences.

At this point in a serious discussion of laser cooling and trapping, one needs to introduce the rudiments of the multi-level structure of neutral atoms, and the polarization of the light. Given the brevity of this treatment we simply mention that the cooling and trapping in one dimension can be extended to three dimensions by introducing six counter-propagating laser beams: forwards and backwards, up and down, left and right; and by introducing a 3D quadrupole magnetic field. The beams are red detuned, and with polarizations such that they address the correct magnetic sublevels, because as we saw in section 3.2.2, the Zeeman shift depends on both the sign of the local magnetic field, and the response of the given magnetic substate. The

optical transition used for cooling in ^{87}Rb is the cycling transition on the D2 line (see figure 3.2); this is called *trap light*. This transition is closed, but due to the finite probability of driving the $F = 2 \rightarrow F = 1, 2$ transitions, atoms can accumulate in the lower hyperfine ground level $F = 1$. For this reason, we require *repump light* tuned close to $F = 1 \rightarrow F = 2$ or $F = 1 \rightarrow F = 3$ so that atoms are optically pumped into the $F = 2$ ground state manifold, and can continue to be cooled. In the absence of the repump light, a ^{87}Rb MOT disappears within a matter of several milliseconds.

It turns out that the magnetic sublevel structure plays a crucial role in additional cooling mechanisms that are more sophisticated than that of Doppler cooling outlined above. In general, these *polarization gradient* cooling schemes take into account the intensity and polarization modulation that occurs when two counter-propagating laser beams overlap, and the way this affects optical pumping. A simple and very useful result from a treatment of these mechanisms is that the temperature of an atomic sample is given by [40]: $k_B T \propto \hbar\Omega^2/|\delta|$. Thus, to lower the temperature of an ensemble of atoms in such a scheme, we need to reduce the optical intensity, and increase the detuning. However, the obtainable temperatures are still limited by the random momentum kicks inherent in the schemes: $k_B T = \hbar^2 k_l^2/(2M)$; although it should be noted that more sophisticated schemes can approach or beat this value [41, 42, 43].

Moreover, as noted in section 2.2, the quantity we should focus on in order to generate a BEC is the phase space density. A significant complication in laser cooling is that as the atomic sample becomes very dense, the light scattered by one atom in the cooling process is re-absorbed by another, leading to a repulsion between the two [44]. There are several schemes designed to circumvent this by limiting the amount of time an atom spends in the $F = 2$ manifold and hence reducing the light scattered on the cycling transition; this is achieved by reducing the intensity of repump, either at some stage in the experimental sequence (as we do), or spatially (the *dark-spot MOT* [45]). Nonetheless, we require subsequent forms of trapping and cooling that do not have intrinsic mechanisms that prevent us from cooling bosonic atoms to degeneracy: magnetic trapping and evaporative cooling.

3.3.2 Magnetic trapping

As we saw in section 3.2.2, a neutral atom that shows an increase in internal energy with applied magnetic field can be trapped at the local minimum of an applied magnetic field. Rewriting equation (3.2) to include the vector character, we obtain:

$$V(\mathbf{r}) = -\vec{\mu} \cdot \mathbf{B}(\mathbf{r}), \tag{3.4}$$

where $|\vec{\mu}| = \mu = m_F g_F \mu_B$. Such a potential leads in general to precessional motion about the direction of the local magnetic field, and as it moves, the atom attempts to align its magnetic moment with this field. As such, the ability to trap a neutral atom

in an magnetic 'bowl' depends on how well the atom can *adiabatically* follow the field. As an atom travels through an inhomogeneous magnetic field, it experiences an effective time dependent magnetic field, and this can induce transitions to other magnetic sublevels which in general will have a different response to the magnetic field; as is evident in figure 3.3, these other magnetic sublevels will most likely be untrapped or anti-trapped states. Such a process is called a *Majorana spin flip*. It is important to note that it is the directional change in the magnetic field that is critical. This condition for adiabatic motion can be expressed as:

$$\omega_L \gg \left| \frac{d\mathbf{B}/dt}{\mathbf{B}} \right|, \tag{3.5}$$

where ω_L is the Larmor precession rate [36]. If this condition is satisfied, then the atom experiences a potential proportional to the modulus of the field $V(\mathbf{r}) = \mu\,|\mathbf{B}(\mathbf{r})|$.

The depth of a magnetic trap expressed as a temperature can be estimated from the relation that follows from equation (3.2): $T = \mu\Delta B/k_B$. For standard laboratory magnetic fields ($\sim$ 500 G), this leads to an order of magnitude estimate of 10 mK. Thus, it is clear that the atoms need to be pre-cooled before a significant number can be trapped magnetically, and this is provided by the laser cooling methods outlined above.

There are two geometries of magnetic trap we need to discuss: the quadrupole trap, and the Ioffe Pritchard tap.

The quadrupole trap

The standard way of generating a quadrupole field is to pass opposite currents through two coaxial coils placed a certain distance apart - two coils in anti-Helmholtz configuration. A 3D quadrupole field close to the symmetry axis of the two coils may be written as:

$$\mathbf{B}(\mathbf{r}) = B'(x\,\hat{\mathbf{x}} + y\,\hat{\mathbf{y}} - 2z\,\hat{\mathbf{z}}), \tag{3.6}$$

and its modulus is given by:

$$|\mathbf{B}(\mathbf{r})| = B'\sqrt{x^2 + y^2 + 4z^2}, \tag{3.7}$$

where B' is (colloquially) referred to as the magnetic field gradient, and the shared axis of the coils lies along z. Thus, along any direction, the field increases linearly. Evidently, the field minimum of the quadrupole trap is zero, and this leads to violations of the adiabaticity condition of equation (3.5). To put it loosely, the atom cannot follow the direction of the local magnetic field if the field is zero. More formally, one can consider orbits of atoms in the trap and show that both classically and quantum mechanically, the adiabaticity condition of (3.5) is violated for low-lying orbits - those based around the minimum of the trap [36]. As we saw in section 2.2.3, the colder a cloud becomes, the higher the density at the centre of the trap, and thus,

the quadrupole trap 'starts to leak' as we cool the sample. For this reason, we require a trap that has a non-zero minimum, and we choose a Ioffe-Pritchard configuration.

The Ioffe-Pritchard trap

The components of the magnetic field in a Ioffe-Pritchard (IP) trap are given by [21]:

$$\begin{pmatrix} B_x \\ B_y \\ B_z \end{pmatrix} = B_0 \begin{pmatrix} 0 \\ 0 \\ 1 \end{pmatrix} + B' \begin{pmatrix} x \\ -y \\ 0 \end{pmatrix} + \frac{B''}{2} \begin{pmatrix} -xz \\ -yz \\ z^2 - \frac{1}{2}(x^2+y^2) \end{pmatrix}, \tag{3.8}$$

and the magnetic field strength is given by:

$$|\mathbf{B}(\mathbf{r})| = \sqrt{\left(B'x - \frac{B''}{2}xz\right)^2 + \left(-B'y - \frac{B''}{2}yz\right)^2 + \left(B_0 + \frac{B''}{2}z^2 - \frac{B''}{4}(x^2+y^2)\right)^2}. \tag{3.9}$$

In standard realizations of a Ioffe-Pritchard trap, $|B'| \gg |B''|^{1/2}$, so that the confinement in the radial directions due to the magnetic field gradient $|B'|$ is much stronger than the harmonic component, and the cloud is generally prolate, with its long axis along the direction of harmonic confinement. In this limit, we ignore the radial harmonic dependence and the bias field B_0 to give a field that is linear in the radial direction and harmonic in the axial direction:

$$|\mathbf{B}(\mathbf{r})| = \sqrt{(B'\rho)^2 + \left(\frac{B''}{2}\right)^2 z^4}, \tag{3.10}$$

where $\rho^2 = x^2 + y^2$. As we shall see in section 3.3.3, a linear potential is advantageous in evaporative cooling.

In the limit of a cold cloud, we can obtain an approximate expression for the field magnitude about the centre of the trap using the standard binomial approximation $(1+x)^n \approx (1+nx)$ for small x:

$$|\mathbf{B}(\mathbf{r})| = B_0 + \frac{\rho^2}{2}\left(\frac{B'^2_\rho}{B_0} - \frac{B''_z}{2}\right) + \frac{B''}{2}z^2. \tag{3.11}$$

In this limit, the field magnitude is harmonic, and we can express the trapping potential as:

$$V(\mathbf{r}) = \mu B_0 + \frac{1}{2}M\omega_\rho^2\rho^2 + \frac{1}{2}M\omega_z^2 z^2, \tag{3.12}$$

where the trap frequencies are given by:

$$\omega_\rho^2 = \frac{\mu}{M}\left(\frac{B'^2_\rho}{B_0} - \frac{B''}{2}\right) \quad \text{and} \quad \omega_z^2 = \frac{\mu}{M}B''. \tag{3.13}$$

It is worth noting that the radial confinement can be modified significantly by the value of the bias field, although the extent to which one can exploit this depends on the experimental realization. For instance, in a Ioffe-Pritchard trap where the bias field and axial confinement are generated by a pair of Helmholtz coils, the bias field can be modified very simply by changing the current through these coils.

3.3.3 Evaporative cooling

The main idea of evaporative cooling is to remove particles from a system in (approximate) thermal equilibrium that have energy greater than the mean of the system. In this way, energy of the system is lowered disproportionately to the number of particles lost from the system. The obligatory real-life analogy is the cooling of a cup of coffee: the hottest molecules have sufficient energy to break away from the surface of the coffee, carrying away more than their fair share of the energy in the system. The idea is illustrated in figure 3.4, which shows two Maxwell-Boltzmann (MB) distributions. The use of classical statistics is justified as the effects of quantum statistics are negligible for all but the very end of the evaporation (see (2.19)); and the energies are such that it is sufficient to consider only *s*-wave collisions. The distribution initially (dashed line) has mean energy $\bar{\varepsilon}_i$. Subsequently, all particles with energy greater than the *truncation energy* ε_t are removed from the distribution. After some later time when collisions have re-established quasi-equilibrium, a new, narrower Maxwell-Boltzmann distribution (solid line) is shown with mean energy $\bar{\varepsilon}_f$. Numerical simulations have shown that only a few elastic collisions are required per atom to establish quasi-equilibrium[2] [47] . Note that some of the hottest particles in the new distribution will also be removed from the trap, but at some point this will stop as the number of particles with energies greater than ε_t becomes negligible. The process of systematically lowering the level of ε_t to cause continued cooling is called *forced evaporative cooling*, and is the standard method used to experimentally cool atoms to degeneracy.

Even in this simplified description, questions arise regarding the optimal value of the truncation energy ε_t, and the time scales involved - how quickly one should lower the truncation energy. From the above example it is perhaps apparent that a large initial value of ε_t compared to $\bar{\varepsilon}_i$, followed by an arbitrarily slow reduction of it will be advantageous: in this way, one gets the most out of a given cut by removing hot atoms generated by re-thermalization, rather than through the *spilling* of atoms (to continue the cup of coffee analogy). However, a finite time scale is imposed in experiments by losses, namely 'undesirable' or 'bad' collisions.

There are three types of collisions that need to be considered: those between background gas atoms and trapped atoms, inelastic two-body collisions, and three-

[2] Although this number can be an order or two larger to establish the extremities of the distribution [46].

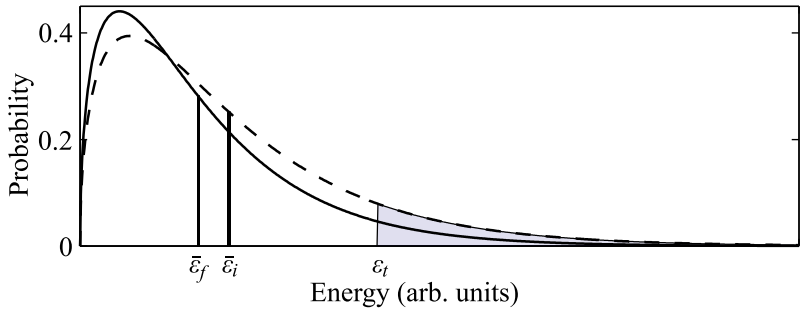

FIGURE 3.4: Maxwell-Boltzmann distributions illustrating evaporative cooling: an operation is performed on a system of particles of mean energy $\bar{\varepsilon}_i$ that causes all particles with energy greater than some truncation energy ε_t to be ejected; the particles are allowed to thermalize via elastic collisions, leading to a new and narrower Maxwell-Boltzmann distribution with mean $\bar{\varepsilon}_f < \bar{\varepsilon}_i$ [34].

body collisions. Background gas collisions depend on the quality of the vacuum of the chamber in which the atoms are trapped: such collisions lead to loss of atoms from the trap and are essentially independent of the sample density. The required vacuum level depends very much on the type of trap one uses - the tighter the trap, the higher the elastic collision rate and thus the quicker one can evaporate the atomic sample to BEC, meaning that the vacuum requirements are not as stringent. Inelastic two body collisions lead to a change in the internal state of the atom, which in a magnetic trap generally leads to a loss of atoms. Furthermore, because the per atom rate scales with the density, inelastic scattering also heats the sample because it primarily affects the coldest atoms at the centre of the trap. However, two-body inelastic collisions are significantly suppressed in the *doubly polarized state* $|F = I + 1/2, m_F = F\rangle$ and in the *maximally stretched state* $|F = I - 1/2, m_F = -F\rangle$ in ^{87}Rb [3]. An upper bound for the two-body inelastic collision rate constant for the $|1,-1\rangle$ state in ^{87}Rb was measured to be $G_2 = 1.6 \times 10^{-16}\text{cm}^3\text{s}^{-1}$ [48], which leads to a rate $\Gamma_{2\text{B loss}} = G_2 n_0$ that is considerably smaller than the elastic collision rate at all times in the evaporation. Three-body recombination is the process whereby three atoms collide to form a molecule (dimer), with the third carrying away the remaining energy. Like inelastic binary collisions, it leads to both trap loss and heating, but because the per atom rate scales with the density squared, the effects can be severe towards the end of evaporation. The rate constants in $|1,-1\rangle$in ^{87}Rb for condensed and non-condensed atoms respectively are $G_3^{\text{c}} = 5.8(1.9) \times 10^{-30}\text{cm}^6\text{s}^{-1}$ and $G_3^{\text{nc}} = 4.3(1.8) \times 10^{-29}\text{cm}^6\text{s}^{-1}$ [48]. The fact that the rate for condensed atoms is lower (by approximately a factor of 3!) than for thermal atoms has been used as

[3] There are several dipolar processes that can occur; see pp. 125-130 in [16] for details.

evidence of anti-bunching in Bose-condensed samples [48]. While three body recombination can be a significant problem in ^{87}Rb in the last phase of evaporative cooling, the problem can be circumvented somewhat by relaxing the trap at some point in the evaporation. Finally, the effects of all of the three collision processes can be considerably more serious when the density and dimensions of the cloud become such that the scattering products cannot leave the cloud without colliding with other atoms, leading to so-called collisional avalanches [49].

The optimal evaporation sequence is found by maximizing the following quantity for each step in the evaporation process [50]:

$$\gamma = \frac{d\ln\rho}{d\ln N} \approx \frac{\ln(\rho_f/\rho_i)}{\ln(N_f/N_i)}, \tag{3.14}$$

where ρ is the phase space density defined in (2.8), and N the number of atoms. The extreme right hand side gives the expression when using finite steps. In general, logarithmic derivatives like (3.14) appear in treatments of evaporative cooling, because the relevant quantities (atom number, temperature, density) change by a constant factor in a given time interval. We now sketch an argument from reference [50] that gives approximate results and identifies the main ideas necessary to understand evaporative cooling; a comprehensive modelling of evaporative cooling, where the different collisions and loss mechanisms are included, is possible [46, 51, 52], and one of these models is applied to our apparatus in reference [34].

Consider the situation represented in figure 3.4. Let us assume the atoms are confined in a power law potential $U(\mathbf{r}) \propto r^\delta$, where δ is defined such that the volume of the gas scales as T^δ: $\delta = 3/2$ for a 3D harmonic potential and $\delta = 3$ for a 3D linear potential. The total energy of the system before evaporation is given by $E = \bar{\varepsilon}N$, and - after a change in the truncation energy - the energy is $E = \bar{\varepsilon}N + (1+\alpha)\bar{\varepsilon}dN$. For particle loss, dN is negative. Through some algebra, one arrives at:

$$\alpha = \frac{d\ln\bar{\varepsilon}}{d\ln N} = \frac{\dot{\bar{\varepsilon}}/\bar{\varepsilon}}{\dot{N}/N} = \frac{\dot{T}/T}{\dot{N}/N}. \tag{3.15}$$

where the final equality follows because the mean energy of a classical particle in a 3D trap is given by $\bar{\varepsilon} = (\delta + 3/2)k_BT$. To avoid carrying factors of k_BT in calculations, we define the dimensionless *truncation parameter* $\eta = \varepsilon_t/(k_BT)$. In the following treatment where the use of a truncated MB distribution is valid, α has a simple representation:

$$\alpha = \frac{\eta + \kappa}{\delta + 3/2} - 1, \tag{3.16}$$

where κ is a small number between 0 and 1, describing how different the energy of evaporated particles is from η. Table 3.1 lists the exponents relating various quantities relevant in evaporative cooling to the number of atoms.

The main goal of the argument is to understand how the evaporation rate depends on the elastic collision rate and the truncation parameter. Luiten *et al.* showed

Quantity Z	**Exponent** x
Number of atoms, N	1
Temperature, T	α
Volume, V	$\delta\alpha$
Density, n	$1-\delta\alpha$
Phase space density, ρ	$1-\alpha(\delta+3/2)$
Elastic collision rate, $\Gamma_{\rm el}$	$1-\alpha(\delta-1/2)$

TABLE 3.1: Scaling laws for evaporative cooling in a potential $U(\mathbf{r}) \propto r^{\delta}$. Quantities scale as $(\dot{Z}/Z) = (\dot{N}/N)^{x}$ [50].

in [46] that the energy distribution of evaporating particles is very well described by a truncated Maxwell-Boltzmann distribution. For this reason, we may argue using a standard MB distribution to quantify the rate of scattering into the high-energy tail of the distribution: i.e., those atoms removed from the trap due to its finite height. In the limit of high η, it is highly probable an atom with energy greater than ε_t that undergoes a collision will be knocked out of the tail. In order to maintain the temperature, there must be a corresponding scattering into the tail; this is detailed balance. As such, the rate at which atoms are scattered into the tail and hence removed from the system may be obtained from the collision rate of atoms with energies $\varepsilon > \varepsilon_t$. The probability of being in the tail is found by integrating the MB distribution:

$$P(\tilde{\varepsilon} > \eta) = \int_{\eta}^{\infty} \frac{2}{\sqrt{\pi}} \sqrt{\tilde{\varepsilon}} \mathrm{e}^{-\tilde{\varepsilon}} d\tilde{\varepsilon} \approx \frac{2}{\sqrt{\pi}} \sqrt{\eta} \mathrm{e}^{-\eta}, \tag{3.17}$$

where $\tilde{\varepsilon} = \varepsilon/(k_B T)$, and the final approximate equality is valid for $\eta \gtrsim 4$ [53]. The velocity v_η of atoms with energy $\eta k_B T$ is $\bar{v}\sqrt{\pi\eta}/2$, with the mean velocity given by $\bar{v} = \sqrt{8k_B T/(\pi M)}$. The evaporative cooling rate is then given by product of the elastic scattering rate and the number of atoms in the tail:

$$\Gamma_{\rm ev} = n_0 \sigma_{\rm el} v_\eta P(\varepsilon > \eta) N = n_0 \sigma_{\rm el} \bar{v} \eta \mathrm{e}^{-\eta} N = \frac{N}{\tau_{\rm ev}}, \tag{3.18}$$

where $\sigma_{\rm el} = 8\pi a^2$ is the two body elastic collision cross-section, consistent with equation (2.30), and $\tau_{\rm ev}$ is the evaporation time constant. The mean elastic collision rate of the sample is given by:

$$\Gamma_{\rm el} = \frac{1}{\tau_{\rm el}} = \sqrt{2} n_0 \sigma_{\rm el} \bar{v}, \tag{3.19}$$

so that the ratio $\tau_{\rm ev}/\tau_{\rm el} = \sqrt{2}\mathrm{e}^{\eta}/\eta$ is seen to increase exponentially with the truncation energy, confirming the conclusions from the heuristic example above. Such an expression is in fact valid for any potential in the limit of large η, where n_0 is the

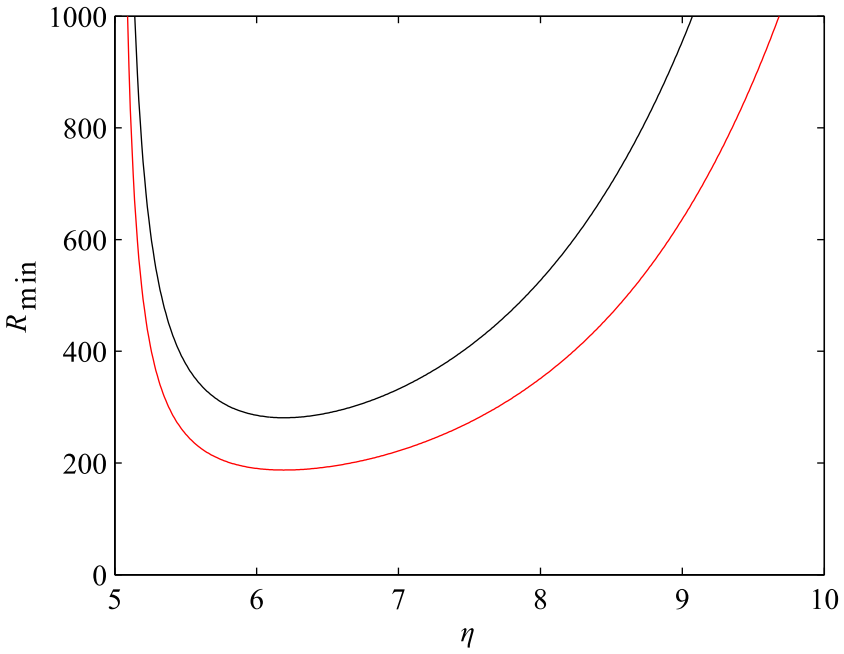

FIGURE 3.5: An estimate of the minimum ratio of good to bad collisions required to sustain runaway evaporative cooling for a 3D harmonic potential (black) and 3D linear potential (red). $R_{\min}$ as given in (3.20), and $\kappa = 1$ in the calculation of α.

peak density, because evaporation occurs locally such that each volume element can be regarded as a square well [46], in keeping with the discussion of section 2.2.1. Clearly, the elastic collision rate changes as the sample is cooled - it increases as the density increases, but reduces as the mean velocity of the atoms decreases.

It is evident from the above results that in order for evaporation to be effective, the elastic collision rate must exceed the loss rate, for which the loss due to collisions with background gas molecules is the dominant component for all but the very end of the evaporation. This condition is called *runaway evaporative cooling*, and it requires that the ratio of good to bad collisions, $R = \Gamma_{\rm el}/\Gamma_{\rm loss}$, fulfill:

$$R \geq R_{\min} = \frac{\lambda}{\alpha(\delta - 1/2) - 1}, \tag{3.20}$$

where $\lambda = \Gamma_{\rm el}/\Gamma_{\rm ev}$. Equation (3.20) is plotted in figure 3.5 for a linear and harmonic potential. It is evident that a linear potential is preferable, essentially because a cloud is more compressed in a linear potential, and hence the density and elastic collision rate are higher.

By the same methods that led to (3.20), one may obtain an expression for equation (3.14), i.e., the relative increase in the phase space density with decreasing atom

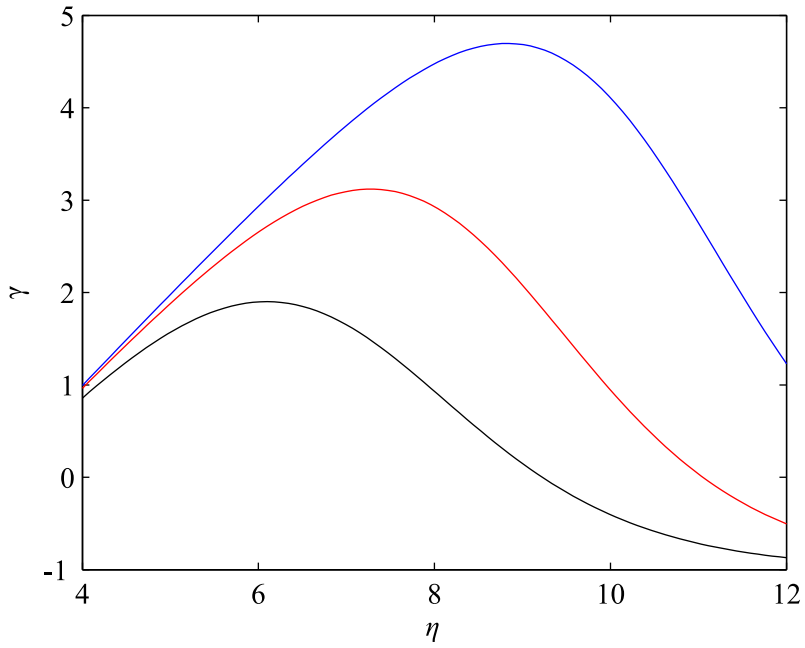

FIGURE 3.6: The value of γ as a function of η in a 3D harmonic potential for three values of the ratio of good to bad collisions: $R = 250$ (black), 500 (red), 5500 (blue).

number:

$$\gamma = -\frac{d\ln\rho}{d\ln N} = \frac{\alpha(\delta+1/2)}{1+\lambda/R} - 1. \tag{3.21}$$

Equation (3.21) is plotted in figure 3.6, for three values of the ratio of good to bad collisions. The first point to note is that the value of R guides the choice of truncation parameter. For values of $R \sim R_{\min}$, the efficiency of evaporative cooling is maximized by choosing $\eta \approx 6$. If however R is considerably larger than $R_{\min}$, it is advantageous to choose a larger η. In general, the figure shows that one should tailor the truncation parameter to the value of R, which, as discussed above, changes as the sample becomes colder.

To summarize, the above discussion demonstrates that to generate a BEC through evaporative cooling, it is crucial that initially we have a sufficient number of atoms in the trap, combined with a vacuum level such that the ratio of good to bad collisions is at least on the order of several hundred. It is clear that the larger our initial clouds, the easier the rest of the process becomes.

Forced evaporative cooling by RF transitions

Forced evaporative cooling may be implemented by driving radio-frequency (RF) transitions to untrapped states in the hottest atoms in the trap. The technique makes

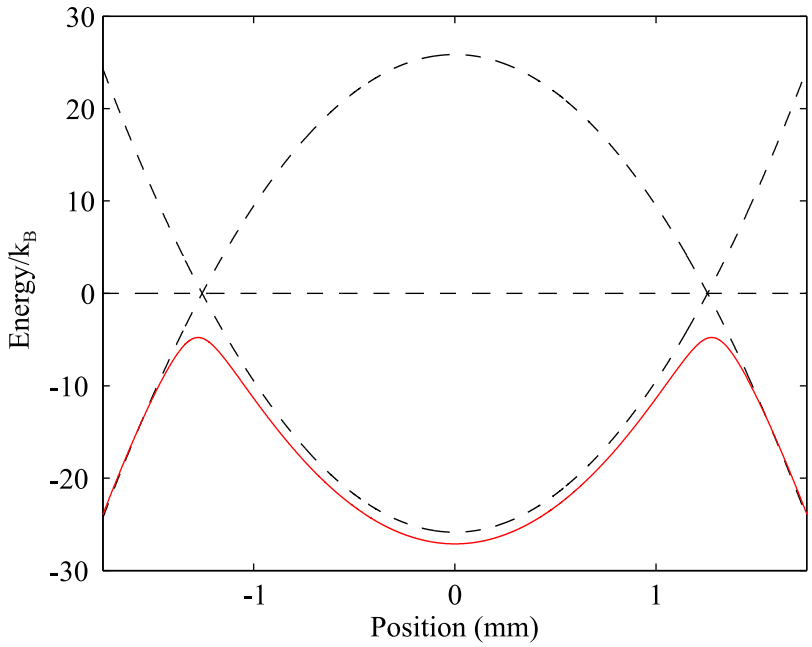

FIGURE 3.7: The effect of RF radiation on the trapped state $|F=1,m_F=-1\rangle$. The Zeeman energies of the three states $|F=1,m_F=-1\rangle$, $|F=1,m_F=0\rangle$, and $|F=1,m_F=1\rangle$ are shown as dashed lines. The state $|F=1,m_F=-1\rangle$, dressed by the RF field is shown in red. The transitions induced by the RF field lead to a mixing of the sublevels, so that an atom moving in the potential will be adiabatically transferred to an untrapped state if it crosses the position defined by the resonance condition [34].

use of the fact that the hottest atoms spend most time in the wings of the spatial distribution. If the cloud is bathed in RF radiation of frequency $\omega_{\rm rf}$ then due to the Zeeman shift of the atoms in the trap, there will be a spatially dependent resonance condition given by:

$$\hbar\omega_{\rm rf} = \mu\,|B(\mathbf{r})|\,. \tag{3.22}$$

Thus, atoms in $|F=1,m_F=-1\rangle$ will be transferred to the untrapped state $|F=1,m_F=0\rangle$ or the anti-trapped state $|F=1,m_F=1\rangle$. A representation of this in terms of dressed states is shown in figure 3.7. The Zeeman energy of an atom in one of the three magnetic sublevels varies with position in the harmonic trap; when an RF field of given frequency is applied, the transitions from $|F=1,m_F=-1\rangle$ to the other magnetic substates appear as an adiabatic passage out of the trap.

Given that the relevant quantities such as temperature or phase space density change exponentially as evaporation proceeds, the frequency of the 'RF knife' must follow in a similar way if our strategy is to evaporate at a constant value of η. Thus,

the frequency $\nu = \omega/(2\pi)$ of the RF has the functional form [54]:

$$\nu(t) = (\nu_{\text{start}} - \nu_0)e^{-t/\tau} + \nu_0, \tag{3.23}$$

where ν_{start} is the frequency at which the evaporation begins, $\nu_0 = \mu B_0$ is the frequency corresponding to the bottom of the trap, and τ is the evaporation time constant. To optimize the RF evaporation experimentally, one tries several values of τ within a given frequency interval in which one approximates the elastic collision rate as being constant, and chooses the time constant that maximizes equation (3.14).

3.4 Cloud shapes in absorption imaging

All the measurements we can perform on the BEC derive from the analysis of light that has interacted with the condensate and in this section we present the most direct of such measurements: the absorption of quasi-resonant light by the condensate. This is a very brief introduction so that the methodology used to obtain the results presented in the following sections is understandable. A longer description of absorption imaging is presented in section 4.2.

The passage of light through a medium of length L may be described at some level of approximation by the Lambert-Beer law:

$$I(x,y) = I_0(x,y)e^{-OD(x,y)}, \tag{3.24}$$

where $I = I(L)$ and $I_0 = I(0)$ and the optical depth is given by

$$OD(x,y) = \int_0^L \sigma_{\text{abs}} n(x,y,z)dz = \sigma_{\text{abs}}\tilde{n}(x,y), \tag{3.25}$$

where σ_{abs} is the absorption cross section, characterizing the strength of the interaction. $\tilde{n}(x,y)$ is the column density of the sample - the density integrated along the line of sight of the imaging beam. A model to visualize the content of the Lambert-Beer law is a collection of beam-splitters, oriented such that the reflected light is directed out of the beam. In ^{87}Rb, we use the $F = 2, m_F = \pm 2 \rightarrow F' = 3, m_F = \pm 3$ cycling transition to image the atoms.

In practice, we require several raw images to generate a high quality absorption image of the BEC. A raw image consists of sending a pulse of light through the region of interest, then imaging the beam at the position of the atoms on a Charge Coupled Device (CCD) camera with some magnification M. The general procedure is to take a *shadow* image I_{sh} of the atomic distribution of interest, wait for the atoms to fully disperse, take a picture of the beam in the absence of atoms I_{bg}, then finally take a bias image I_{bia} using the same procedure but without the pulse of light. Using this data, one can invert equations (3.24) and (3.25) to obtain an expression for the

column density of the atomic distribution:

$$\tilde{n}(x,y)dxdy = \frac{A}{\sigma_{\rm abs}M^2}\ln\left(\frac{I_{\rm bg}(x,y)-I_{\rm bia}(x,y)}{I_{\rm shd}(x,y)-I_{\rm bia}(x,y)}\right), \tag{3.26}$$

where A is the area of a camera pixel. The ratio A/M^2 gives the size of a pixel in the image plane. The bias image is necessary as the raw images contain offsets that vary from pixel to pixel, and this additive noise must be removed to achieve high quality processed images.

All of the images presented in this work are absorption images taken some time after the magnetic trap was extinguished. Such images are called *time of flight* (TOF) images, and the delay between release and picture taking is on the order of tens of milliseconds. In general, such images, rather than *in situ* images of the trapped cloud, are easier to obtain from a technical point of view. Ultra-cold atomic clouds have dimensions on the micrometer scale, and are very dense so that the optical depth of trapped clouds can be on the order of several thousand. Apart from the high level of magnification this implies given that the dimensions of pixels in CCD arrays are also on the several micrometer scale, for technical reasons, absorption imaging works best at optical depths on the order of two.

3.4.1 Non-condensed clouds

We can use the semi-classical approach from section 2.2.3 to evaluate the density distributions of non-condensed clouds after time of flight. Taking in-trap momentum $\mathbf{p}$ and position $\mathbf{x_0}$ coordinates, the position distribution after time of flight may be evaluated given that the distance a particle travels in ballistic expansion must be related to its initial momentum by $\mathbf{p} = M(\mathbf{x}-\mathbf{x_0})/t$. Modifying (2.16) accordingly, and noting that $\varepsilon(\mathbf{p},\mathbf{x_0})$ is defined in (2.14), we have [21]:

$$\begin{aligned} n_{\rm ex}^{\rm tof}(\mathbf{x},t) &= \int \frac{d\mathbf{p}d\mathbf{x_0}}{(2\pi\hbar)^3}\frac{1}{\exp((\varepsilon(\mathbf{p},\mathbf{x_0})-\mu)/k_BT)-1}\delta(\mathbf{x}-\mathbf{x_0}-\frac{\mathbf{p}}{M}t) \\ &= \frac{1}{\lambda_T^3}\prod_{i=1}^{3}\sqrt{\frac{\omega_i^2}{1+\omega_i^2t^2}}\; g_{3/2}\left(\exp\left[\frac{\mu}{k_BT}-\frac{M}{2k_BT}\sum_{j=1}^{3}x_j^2\left(\frac{\omega_j^2}{1+\omega_j^2t^2}\right)\right]\right). \end{aligned} \tag{3.27}$$

As one would expect from the discussion of section 2.2.3, in the limit of long times of flight such that $t \gg \omega_i^{-1}$, the density profile becomes isotropic:

$$n_{\rm ex}^{\rm tof}(\mathbf{x},t) \propto g_{3/2}\left(\exp((\mu - Mr^2/2t^2)/k_BT)\right), \tag{3.28}$$

where $r^2 = x_1^2+x_2^2+x_3^2$. Integrating along the line of sight, the column density is given by [21]:

$$\tilde{n}_{\rm ex}(x_1,x_2) = \frac{\tilde{n}_{\rm ex}(0,0)}{g_2(1)}g_2\left(e^{1-x_1^2/2\sigma_1^2-x_1^2/2\sigma_2^2}\right). \tag{3.29}$$

Generally, a Gaussian is a perfectly adequate model for all but the very end of the evaporation. As is evident in figure 2.1, the Bose and Gaussian distributions are essentially the same in the wings, and only differ substantially towards the centre of the cloud. For this reason, if one's intention is to measure the temperature in the wings of a bi-modal cloud (i.e., one with both BEC and thermal components) then provided one chooses the fitting region appropriately, a Gaussian suffices. The rms width of a thermal cloud along a given direction after time of flight is given by:

$$\xi_i(\omega_i, T, t) = \sqrt{\frac{k_B T}{M}\left(\frac{1}{\omega_i^2} + t^2\right)}. \tag{3.30}$$

3.4.2 Condensed clouds

As we saw in sections 2.2.3 and 2.5.1, the density distribution of a BEC trapped in a harmonic potential in the limit of weak interactions is a Gaussian, and in the Thomas-Fermi regime when interactions between atoms are strong, the BEC is an inverted paraboloid. In the limit of weak interactions, the momentum distribution is also Gaussian, leading to an expansion upon release from the trap that reflects the strength of the confinement in the trap. In this case, the relevant fitting function for the column density is also Gaussian. In the Thomas-Fermi regime, the situation is not as simple, as the expansion is not purely ballistic, but rather driven initially by the repulsion between the atoms (assuming a positive scattering length).

Fortuitously, it has been shown that the density profile of a harmonically trapped BEC in the Thomas-Fermi regime remains parabolic once it has been released from the trap. In many trap geometries, and in particular in the case of a Ioffe-Pritchard magnetic trap (see section 3.3.2), trapped clouds are prolate and have cylindrical symmetry about the long axis of the trap. For an anisotropic trap where the radial trapping frequency is much greater than the axial, i.e., $\omega_\rho \gg \omega_z$, the expansion of the cloud may be expressed as a rescaling of the principle axes ρ_0 and z_0 [55, 56]:

$$\begin{aligned} \rho_0(t) &= \rho_0(0)\sqrt{1+\tau^2} \\ z_0(t) &= \frac{\rho_0(0)}{\varepsilon}\left(1 + \varepsilon^2\left[\tau \arctan\tau - \ln\sqrt{1+\tau^2}\right]\right), \end{aligned} \tag{3.31}$$

where $\tau = \omega_\rho t$ and $\varepsilon = \omega_z/\omega_\rho$. Note that $\rho_0(0)/\varepsilon = \sqrt{2\mu/(M\omega_\rho^2)}\cdot\omega_\rho/\omega_z$.

As such, the column density expression for an expanded BEC is given by integrating (2.34), appropriately modified according to equation (3.31), along the imaging line of sight. Equation (2.34) can be re-written to explicitly include the number of atoms in the cloud:

$$n_c(\mathbf{x}) = \frac{15}{8\pi}\frac{N}{\prod_{i=1}^{3} x_{i,c}}\max\left(1 - \sum_{j=1}^{3}\frac{x_j^2}{x_{j,c}^2}, 0\right). \tag{3.32}$$

	In trap		Expansion	
	Radial ρ	Axial z	Radial ρ	Axial z
Thermal cloud	$\sqrt{\frac{k_B T}{M}}\frac{1}{\omega_\rho}$	$\sqrt{\frac{k_B T}{M}}\frac{1}{\omega_z}$	$\sqrt{\frac{k_B T}{M}}t$	$\sqrt{\frac{k_B T}{M}}t$
Weakly interacting condensate	$\sqrt{\frac{\hbar}{2M}}\frac{1}{\sqrt{\omega_\rho}}$	$\sqrt{\frac{\hbar}{2M}}\frac{1}{\sqrt{\omega_z}}$	$\sqrt{\frac{\hbar}{2M}}\sqrt{\omega_\rho}t$	$\sqrt{\frac{\hbar}{2M}}\sqrt{\omega_z}t$
Thomas-Fermi condensate	$\sqrt{\frac{2\mu}{M}}\frac{1}{\omega_\rho}$	$\sqrt{\frac{2\mu}{M}}\frac{1}{\omega_z}$	$\sqrt{\frac{2\mu}{M}}t$	$\sqrt{\frac{2\mu}{M}}\frac{\pi\omega_z}{2\omega_\rho}t$

TABLE 3.2: Characteristic widths for a thermal cloud, a weakly interacting condensate, and a condensate in the Thomas-Fermi regime in trap, and after time of flight [21].

Some useful expressions linking the number of atoms and the chemical potential are:

$$N = \frac{15}{8\pi}\left(\frac{2\mu}{M\bar{\omega}^2}\right)^{3/2}\frac{\mu}{U_0}, \quad \text{or} \quad \mu^{5/2} = \frac{15\hbar^2 M^{1/2}}{2^{5/2}} N\bar{\omega}^3 a. \tag{3.33}$$

The column density is given by:

$$\tilde{n}_c(x_1,x_2) = \tilde{n}_c(0)\max\left(1 - \frac{x_1^2}{x_{1,c}^2} - \frac{x_2^2}{x_{2,c}^2}, 0\right)^{3/2}, \tag{3.34}$$

where $\tilde{n}_c(0) = 4/3x_{3,c}n_c(0) = 5N/(2\pi x_{1,c}x_{2,c})$.

3.4.3 Extracting cloud properties from time of flight images

The results of this section provide a method to extract important quantities such as the number of atoms from absorption images of expanded clouds. Having obtained a processed image of the column density via equation (3.26), one can fit with the appropriate model: a Bose distribution (equation (3.29)), or a Thomas-Fermi profile for BECs of sufficient size (equation (3.34)), or simply a 2D Gaussian for either a thermal cloud or non-interacting BEC, or indeed some combination for bimodal clouds. In this way, one makes use of the light scattering cross-section σ_{abs} to convert optical density to column density. In practice, this can lead to problems in determining the atom number, because it requires σ_{abs} to be known very precisely. This will be discussed in chapter 4.

However, there is an alternative way to infer the number of atoms from an image of an expanded cloud where one does not require detailed knowledge of the light

scattering cross section: one uses only the fitted widths to infer the value of the chemical potential, from which the total number of atoms follows via (3.33). The chemical potential is related to the widths of a Thomas Fermi profile by $x_{i,c} = \sqrt{2\mu/(M\omega_i^2)}$ (see equation (2.34)). Given that a Thomas Fermi profile expands ballistically in the radial direction ((3.31) and table 3.2), one can infer the initial in-trap width and thus the chemical potential by:

$$\mu = \frac{M}{2}\left(\frac{\omega_\rho^2}{1+\omega_\rho^2 t^2}\right)\rho_c^2. \tag{3.35}$$

A similar method can be applied for thermal clouds.

3.5 Components and construction

We now give a description of important parts of the set-up. For a list of the components used, the reader is referred to [34].

3.5.1 Vacuum chamber

The general layout of the experiment is shown in figure 3.8, where the view is from above. The experiment is mounted on an optical table parallel to the table top at centre height of 30 cm (i.e., the height above the table top at which the atoms are trapped in the MOTs and magnetic trap). To give an idea of the scale, the chamber construction is approximately 45 cm in length. The optical table was chosen to be as solid as possible in order to minimize vibrations; it has dimensions: 120 (width) x 360 (length) x 45 (depth) cm.

We begin with a brief historical introduction, because the form of the vacuum chamber was heavily influenced by a desire to re-use existing components from a previous effort in the group to magnetically trap ^{87}Rb . In fact, essentially the entire chamber excluding the science cell was to be re-used, including existing ion pumps and a Titanium Sublimation pump (where the Non-Evaporable Getter pump now sits). The loading chamber was originally intended to lie at 90° to its present orientation, such that it could accommodate a 3D MOT. The two chambers were then connected by a long narrow tube ($\sim$ 30cm long) that functioned as a differential pumping stage. This was the initial configuration of the chamber, in fact, and remained so for the first year, while the initial stages of the experiment were being built up. We had realized a MOT in the loading chamber, and were trying to transfer atoms to the science chamber MOT when the power supply to the ^{87}Rb dispensers suffered what we can euphemistically term 'catastrophic failure', and sent several more amps through the dispensers than the supply was rated for.[4] This necessitated

[4] As such, we recommend any group using dispensers invest the 50 cents or so required for a fuse between supply and dispensers.

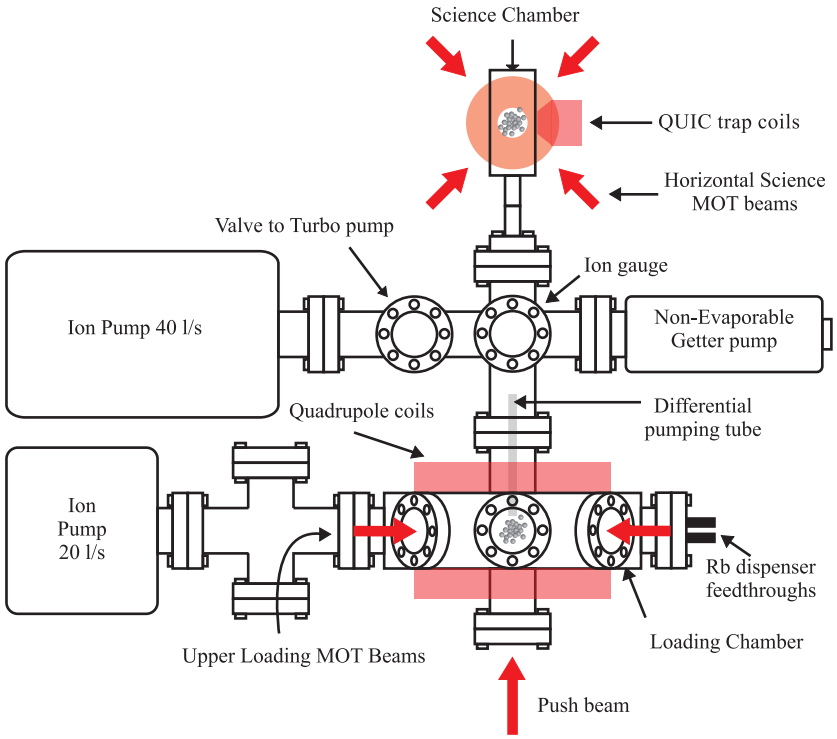

FIGURE 3.8: Schematic drawing of the vacuum chamber, looking from above. The chamber is divided into two regions with different pressures: the loading chamber and the science chamber. The pressure difference is maintained by differential pumping. Atoms from the 2D MOT in the loading chamber are pushed with radiation pressure to a 3D MOT in the science chamber. The entire chamber construction is approximately 45 cm in length [34].

a new bake-out, and at that time we chose to modify the chamber set-up, because the indicators of pressure had not been overwhelmingly positive in this configuration. In particular, the narrow tube connecting the chambers was very delicate, and several coatings of Vacseal® (a brush-on sealant compatible with vacuum) had been applied, with ambiguous results.

This led to the present configuration shown in figure 3.8. The loading chamber was turned onto its side, and a graphite tube, of internal diameter 5 mm and 85 mm in length, was inserted as the differential pumping stage. Even though this addressed the main concern with the previous chamber, it is a time-consuming process to bake out a chamber to the necessary ultra-high vacuum conditions, and we decided to buy new ion pumps and replace the Titanium Sublimation pump - which we had never observed to have any effect - with a Non-Evaporable Getter (NEG) pump. The NEG pump is a passive pump, that is activated (by a heater) in the baking process: it pumps primarily hydrogen and water.

Except for the science cell, the vacuum chamber is made of stainless steel. The

loading chamber has AR coated windows built into flanges that have clear diameter 37 mm. The science chamber is a rectangular glass cell with good optical properties and external dimensions 31x31x100 mm. The cell walls are approximately 3mm thick, and are anti-reflection (AR) coated on the external surfaces. The assembled system was baked out at an ultimate temperature of 240°C for a few weeks with a turbo pump attached. In the latter stages of the bake-out, the ion pumps were turned on and the NEG pump activated. The reader is referred to reference [54] for a thorough description of good Ultra-High Vacuum (UHV) practices. The pressures can be inferred - to a certain level - from the current passing in the ion pumps. After the bake-out, the loading chamber ion pump (20 l/s) and the science chamber ion pump (40 l/s) showed their offset currents, implying an upper bound for the pressure in the two chambers of 10^{-9} mbar. Ion gauges in the science chamber end and in the turbo-pump indicated a pressure of 10^{-11} mbar. However, pressure readings of this type are not entirely reliable, because the gauge itself functions as an ion pump of sorts. The ultimate figure of merit for the level of vacuum is the lifetime of a trapped sample.

The lifetime of a thermal cloud in the quadrupole magnetic trap was measured by taking absorption images (see 3.4) after variable hold-times. The result of such a measurement is shown in figure 3.9, showing exponential decay with fitted time constant $\tau_{\text{loss}} = 62$ s. The trap loss due to Majorana spin flips is not critical here given the temperature of the cloud: the time constant of the decay is ~ 90 s for our trap parameters [34, 57]. The life-time due to background losses is more than sufficient to generate BECs, which in our set-up takes about 45 s in the (two forms of) magnetic trap. In the evaporation, the atom number drops by approximately two orders of magnitude, so that the factor of two associated with loss due to background collisions is not at all critical.

3.5.2 Lasers

Several lasers are required to provide the light for the Magneto-Optical traps, and the subsequent probing of the atoms. As noted in section 3.3.1, we require two transitions from the D2 line (780 nm) of ^{87}Rb for laser cooling: so-called trapping and repump light. These transitions are separated by 6.8 GHz - too far to shift in frequency by standard techniques such as Acousto-Optic Modulators (AOMS) - so we require two separate lasers that are locked to these transitions: these lasers are standard External Cavity stabilized Diode Lasers (ECDL). In order to run the two MOTs, we require more trapping light than the trap ECDL can provide. We therefore use this frequency stabilized laser light from the ECDL *master* laser to inject several *slave* diodes. All these lasers are homebuilt, using laser diodes that run freely at 785 nm (at room

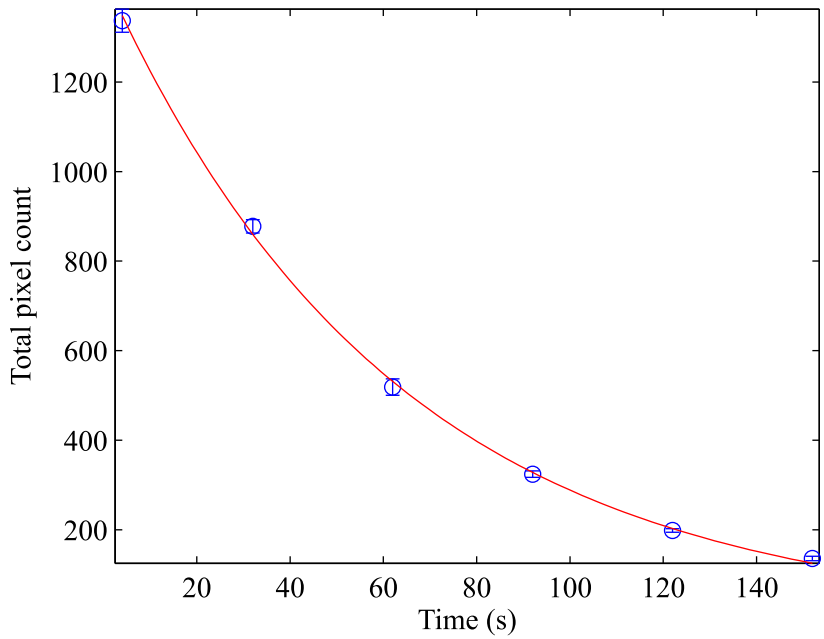

FIGURE 3.9: Measuring the life-time of a thermal cloud in the quadrupole magnetic trap: absorption images were taken for each value of hold-time. The integrated total count of the absorption image is shown as a measure of the number of atoms in the cloud. The results were fitted with a decaying exponential with time constant $\tau_{\text{loss}} = 62$ s. The errorbar limits denote the standard error of the mean of five realizations.

temperature). These diodes are inexpensive[5] - about 50 $US - although when CD players become obsolete, these diodes will certainly become more expensive and harder to procure. It should be noted that this approach is somewhat old-fashioned, with the preferred option now to use a *tapered amplifier* instead of the slaves, or indeed to just buy a commercial diode laser that provides the necessary power and essentially just requires a locking error-signal in order to work on the right line. The probing of the BEC is off-resonant to the D1 line (795 nm), and for this we use two ECDLs such that one is locked to a line in ^{85}Rb, and the other is *beat-note* locked at some frequency relative to this reference.

Figure 3.10 shows the layout of the MOT lasers on the trap table. RBS1-RBS4 are the slave diodes. After each laser one can see an anamorphic prism pair to correct for the elliptical shape of the transverse mode. Subsequently, one finds a Faraday Isolator (FI) that functions as an optical diode. Beams are split with the combination of a half-wave plate ($\lambda/2$) and a Polarizing Beam Splitter (PBS). It is worth noting that the polarization of the transmitted light is much purer than the light reflected by

[5]This is convenient as it seems to be a rite of passage for every new student in the lab to kill at least one laser diode.

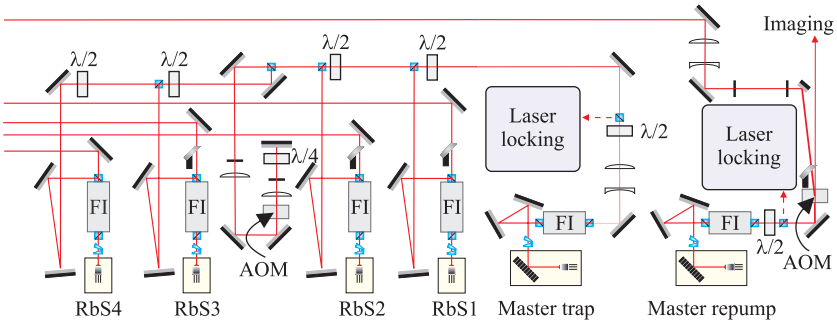

FIGURE 3.10: Schematic diagram of the layout of the lasers used in the MOTs and in imaging. Light from the frequency stabilized master trap laser is used to inject four slave diodes. RBS1 and RBS2 each provide light for an arm of the 2D MOT. RBS3 provides light for the science MOT, and RBS4 supplies the push beam, and the imaging light. Note that RBS3 and RBS4 are injected with light that is shifted in frequency by an AOM in cat's eye configuration.

a PBS: Less than 0.04% of radiation polarized vertically to the plane of incidence is contained in the transmitted light, whereas the reflected light contains 2-3% radiation polarized parallel to the plane of incidence. As such, to clean the polarization of a beam, polarizing beam splitters are always used in transmission. The lock point of the trap laser is chosen such that it has the correct frequency for the loading MOT. RBS1 and RBS2 provide light for the 2D loading MOT - one laser for each arm. The switching of these lasers is not critical, so shutters shortly after the Faraday isolators suffice to switch the light. However, the requirements for the science MOT (SMOT) and imaging are more exacting: we need to be able to change the frequency and intensity of these beams dynamically in the course of an experimental run. The AOM in cat's eye configuration between RBS2 and RBS3 allows us to change the frequency of the light that injects RBS3 and RBS4 so that we can push it to resonance (for imaging) or tens of MHz to the red (polarization gradient cooling etc.) on a millisecond timescale. Optical shuttering of these beams is achieved with single-pass AOMs further down the table (not shown in figure 3.10). The repump is optically shuttered by an AOM and a mechanical shutter, providing light for the MOTs. For imaging, the repump AOM is switched off and the zeroth order beam is sent to another AOM in order to provide a dedicated repump beam.

External Cavity Diode Lasers

As mentioned above, the lab houses four homebuilt external cavity diode lasers to provide frequency stabilized light trap and repump light for laser cooling and imaging on the D2 line, and probing on the D1 line. A picture of the laser is shown in figure 3.11. The lasers are of a fairly standard design that use a diffraction grating in Littrow configuration: i.e., the first order beam is sent back to the diode to pro-

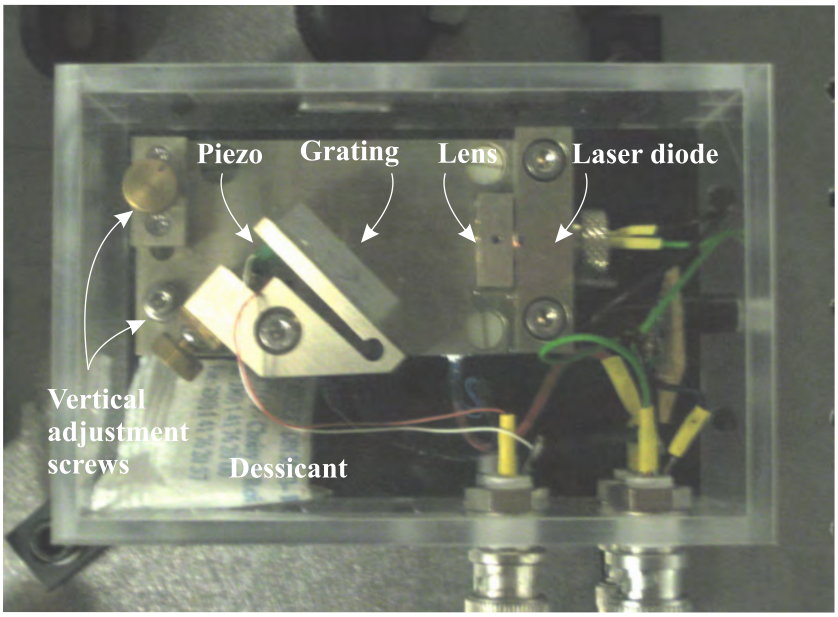

FIGURE 3.11: View from above of one of the master lasers.

vide optical feedback. The diode is held in commercially available holders, but the remaining components were machined in the technical workshops at the Niels Bohr Institute. The laser diodes are very sensitive to changes in temperature and humidity. As such, the diodes are mounted with very good thermal contact to a peltier using an alloy for the diode plate and grating mount that has a high copper content for good thermal conductivity. In turn, the peltier lies flush on a large mounting block that functions as a thermal reservoir. The lasers are cooled to about 15°C, such that they are colder than room temperature but above dew-point, so as to minimize the effects of changes in the laboratory temperature which is maintained by air conditioning. The desiccant sachet that is visible in the laser enclosure is a (token) effort to keep the humidity at a low level. The innards of the ECDLs are enclosed by Perspex, punctured only by the hole from which the light is emitted.

Each laser has its own Saturated Absorption Spectroscopy (SAS) set-up, where some light from the laser is sent through a cell with Rubidium vapour which is then detected by photodiode. 'Slow' corrections (up to several kHz) to the frequency of the laser are made by changing the angle of the grating, achieved by a piezo stack behind the grating. By driving this piezo with a triangle waveform, one can scan several hundred MHz without a mode-hop, and certainly enough to sweep across all the transitions on a given D1 or D2 line. The linewidths of the master lasers are on the order of a few hundred kHz: a beat-note measurement when the trap and repump lasers were locked to the same line yielded a result of 500kHz.

We use several techniques to lock the ECDLs. The locking set-ups for the trap

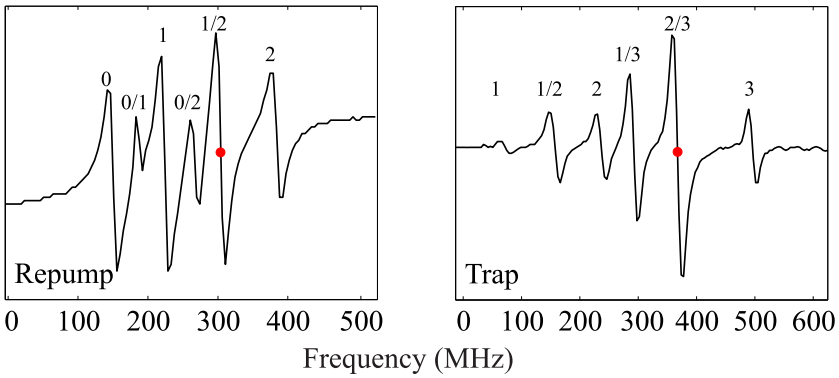

FIGURE 3.12: The spectra of the trap (left) and repump (lasers), as generated by frequency modulating light passed to saturated absorption spectroscopy set-ups and with the appropriate lock-in detection. The locking points are shown as red dots. Labels identify the peaks in such a spectrum. For instance, in the repump, the left-most peak is the $F = 1 \rightarrow F = 0$ transition. Labels like 0/1 identify *cross-over peaks* - an artifact of the spectroscopy - that lie in the middle between a pair of transitions.

and repump lasers were described in [34] but we give a brief summary. The repump is locked via standard modulation of the current at $\approx$ 4MHz. The trap laser uses a different technique: to avoid side-bands on the trap laser - which is also used for absorption imaging - only the light that is directed to the SAS set-up is frequency modulated (at $\approx$ 20kHz) and this is achieved with a double pass AOM in cat's eye configuration. With the appropriate lock-in detection, we generate dispersion-like signals that can be used to lock the lasers [58]. These dispersion signals are sent to home built lock boxes (based on Proportional Integral Differential (PID) circuits) which provide the appropriate feedback signals for the piezo and current controllers. The dispersion signals for the trap and repump lasers that we observe when the piezo is scanned are shown in figure 3.12.

The probe lasers at 795nm provide light for the interrogation of the atoms. For this application, power is not an issue but it is important that we can tune the frequency of the probe light by an arbitrary amount from the resonance lines of the atoms. The first probe laser, Probe 1, is FM locked, typically to a line in ^{85}Rb, some 2.7 GHz away from the nearest line in ^{87}Rb. In an initial set-up, consisting of Probe 1 locked on resonance and shifted away by a few hundred MHz with an AOM, we experienced difficulties in light leaking through the zeroth order of the AOM and indeed stray light reflecting from walls and leaking in through the cladding of an optical fibre. For this reason, and the desire to have freedom in the detuning of the probe light, we introduced a second ECDL, Probe 2, which we lock via its beat-note with Probe 1. The beat signal is detected on a photodiode of sufficient bandwidth, amplified, then sent to a home-built piece of equipment that generates an error signal.

This *phase lock box* was designed by Jürgen Appel, and details regarding its design may be found in [59]. Briefly, the beat signal is digitized, divided by a user-defined number and compared with a digitized reference signal. The box generates an error signal that is sent to the PID lockboxes. As the name suggests, the phase lock box is capable of phase-locking the two lasers but to date we have not made use of this capability.

The stability of the ECDL lasers is reasonable. In general, once a laser is properly set-up, it will run without significant adjustment for a period ranging from a month to several months. By significant, we mean manually changing the vertical tilt the grating, but for an experienced worker in the lab this takes on the order of 10 minutes. More frequently, a slight tweak of the laser temperature is required to bring the desired spectrum back to the middle of the ramp. Often, large changes in outside temperature or humidity (e.g., the first hot period in summer) - despite the air-conditioning of the laboratory - will force an adjustment of the grating. The main instability seems to be of a mechanical nature, namely the vertical alignment of the grating. There are two screws used to control the vertical tilt of the grating. We found that with a single screw, the acoustic stability left something to be desired. The main problem is that the material is reasonably soft, as indeed it must be to tilt the grating. However, it is our impression that screws maintaining the tilt of the grating slip on the mentioned time period. For this reason, one should not over-tighten these screws when setting up the laser: it will improve the acoustic stability up to a point, but the injection of the laser will be lost much more quickly. Furthermore, it is our impression that the material has some kind of 'memory', so that an aggressive alignment leads to worse long-term stability.

Slave lasers

The slave lasers are simply laser diodes secured in a cooled and sealed mount, similar to the ECDLs but without the grating. RBS1 and RBS2 are each injected with approximately 1 mW of light. RBS3 and RBS4 require a little more in steady state operation because they are injected with light that passes through a double pass AOM, and when the frequency of the AOM is changed, its efficiency changes leading to a variation in the diffracted power. Furthermore, it is difficult to avoid some beam-steering despite the cat's eye configuration, and this, combined with narrow apertures to block unwanted diffracted orders propagating through the system, leads to a slight variation in the injection as the frequency is changed. Given that the AOM is pushed both ways in the course of an experimental run - tens of MHz to the red for sub-doppler cooling and on-resonance or to the blue for imaging - the best procedure is optimize the AOM alignment at roughly in the middle of these two extremes. Subsequently, one optimizes injection for each laser using approximately the central frequency it runs at during the experiment (somewhat red for RBS3, the SMOT laser;

and somewhat blue for RBS4, the push beam and imaging beam). It is a good practice to spend half an hour or so to inject the slaves and check the alignment of the cat's eye AOM on a weekly basis, although this is more of a pre-emptive tactic. Note that the lasers are injected from the side port so that the output light from a diode is transmitted through the polarizing beam splitter cubes of the Faraday isolator in order to ensure the polarization of the light is pure. As described in [34], injection is checked by modulating the current of the slaves and looking at the response of the frequency of the laser by its scattering from a Rubidium cell, given that at an earlier stage these signals were 'calibrated' by simultaneously sending the light to a wavemeter. Nonetheless, this method is could be improved upon, for instance by the introduction of a monitor-cavity.

Laser spectra

Provided the ECDLs are properly set up and are well locked, and the slaves are properly injected, the spectral purity of the light is more than adequate for producing BECs. This is largely due to the fact that laser cooling is not very sensitive to the linewidths of the trapping and repump light. Nonetheless, there are two main areas where one needs to be vigilant.

The first area where care must be taken is light leaking from unwanted AOM diffraction orders, as spurious light on the order of hundreds of MHz away from the intended frequency can be very problematic. For single-pass AOMs, it is then a simple matter of picking out the desired diffraction order provided one has enough distance between AOM and iris. If one does not take care with this, it is a common problem that light from the zeroth order leaks into the first order beam, and this can certainly upset laser cooling, not to mention more sensitive applications such as imaging and probing. Double pass AOMs can be more problematic, as one relies on polarization optics to separate incoming and outgoing light. For this reason, it is wise invest in high quality polarization optics such as zero-order quarter-wave plates for this application and to take great care in the alignment. Nonetheless, it is straightforward to check that there are not spurious diffraction orders in the beam by performing a beat-measurement with another (spectrally pure) beam. The output of the cat's eye (set for resonant absorption imaging) was measured by this method to be 40 dB greater than the nearest diffraction order. Similarly, the central frequency of the imaging beam, having passed through its single pass AOM, was measured to be 43 dB greater than any other component.

The second problem area is the broad background characteristic of diode lasers. This background is not filtered by the diffraction grating in the ECDLs because the output beam is the zeroth order beam. That is, there is no frequency selective component in the outcoupling of the light, only in defining which longitudinal mode sees the most gain. Thus, the broad background, i.e., spontaneous emission by the diode,

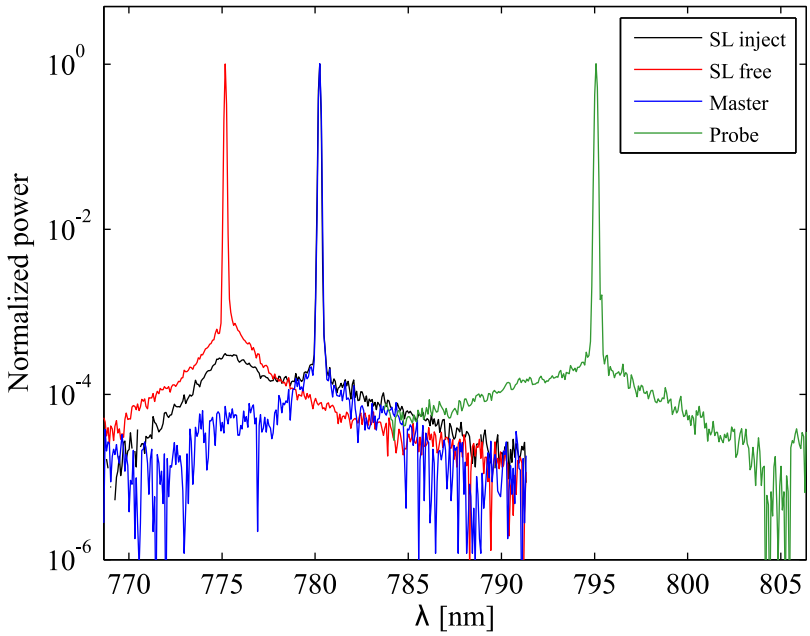

FIGURE 3.13: Large scale spectra of several diode lasers. The spectra were obtained by scanning spatially filtered beams that had been directed onto a diffraction grating across a slit. Each point corresponds to the power in a frequency window of $\approx$ 130GHz window. Different sensitivity settings were used for the peaks and background. The resolution was limited by the spot size of the beam, which for practical reasons was focused onto the slit. The four traces correspond to RBS4 injected and free-running, the trap master laser, and Probe 1. The trap master and RBS4 when injected overlap except for the hump in the injected RBS4 signal where the diode is free-running at 775nm.

is allowed to propagate through the system, unless one introduces additional filtering. This background was measured by shining spatially filtered light from a given laser onto a diffraction grating: the diffracted light was scanned across a narrow slit by a mirror mounted on a stepper motor and the transmitted light was measured on a photodiode. By performing the same measurement for the D1 and D2 lines, we calibrated the wavelength of the diffracted light with the position of the stepper motor. The result is shown in figure 3.13, and confirms the presence of broad backgrounds on all of the lasers. Another element of concern is the hump present in the injected RBS4 spectrum, centred at the diode's free running wavelength of 795 nm. By numerical integration of the injected slave signal, the central peak comprised 97.7% of the total signal, implying an upper bound of 2.3% for the non-resonant background component.

AOMs, switching and shutters

As described above, acousto-optic modulators are employed in single-pass to function largely as optical shutters, and in double-pass to provide dynamic control of the frequency of a beam. Typically, we focus weakly into AOMs to obtain reasonably small waists at the point of diffraction - and hence short switching times - without costing too much in efficiency due to the increased spread in wavevectors inherent in a focused Gaussian beam.

The frequency sources for the AOMs are homebuilt Voltage Controlled Oscillators (VCO). The VCO signal is sent to an RF attenuator and then a digital switch, from which the signal is amplified by an RF amplifier, and then sent to the AOM. The cat's eye VCO is computer controlled: it accepts an analogue signal (0-10V) and the output frequency - typically 100-200 MHz - can be varied by $\pm 20\%$. The VCOs can change their offset slightly on a weekly basis, so it is good practice to check them with a frequency counter on this time scale. Given that the frequencies of the SMOT and push beam light depend on the values of three different AOMs (that used in the trap lock, the cat's eye, and each beam's respective single-pass AOM), such off-sets can add up and affect the performance of the loading of the SMOT. Via an applied current, the RF attenuator controls the amplitude of the signal to be amplified and hence the ultimate signal that drives the AOM. Typically, this is controlled manually (set so as to optimize the diffraction efficiency), but in some cases, such as the SMOT trap and repump beams, we require dynamic control, in which case the control current is derived from an analogue signal from the control computer. Extinction of the RF signal and the switching times are inadequate with only the RF attenuators, so we use digital switches. We achieve rise times of less than 100 ns and extinction ratios of -40 dB.

This extinction ratio is reasonable, but we require mechanical shutters to do the job properly. The shutters are homebuilt, based on telephone relays and driven by digital signals derived from the computer. The shutter itself is formed from stiff black cardboard, augmented by a segment of copper foil where the light is blocked. Despite this modest technology, the shutters work reasonably well, yielding rise and fall times of 1-2 ms where the exact time depends on how small the beam is. Each shutter has a delay on the order of a few milliseconds that depends on how far the shutter must move before it clips the beam. The shutter is mounted to a plate that is sandwiched between layers of shock-absorbing material. We use 1/2" diameter hemispheres made of a proprietary viscoelastic polymer called Sorbothane® as the shock absorber. The shutter holders work very well: the acoustic effect of a shutter closing or opening is only weakly visible on the laser lock signals, and never come close to driving the laser out of lock.

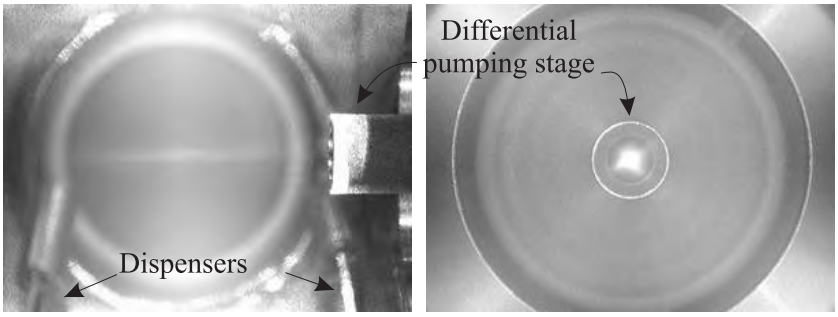

FIGURE 3.14: Pictures of the 2D loading MOT from above (left) and from in front, looking down towards the science chamber.

3.5.3 Magneto-Optical traps and push beam

Loading MOT

The loading MOT is comprised of two retro-reflected beams and a 3D quadrupole field. The beams are approximately 20 mm in diameter and each has 60 mW of power, at a detuning 28 MHz to the red of the $F = 2 \rightarrow F = 3$ transition. The beams come directly from the slave lasers RBS1 and RBS2 - they are not spatially filtered. A few milliwatts of repump power is added in each arm. Fortunately, the transverse mode appears reasonably clean straight from the slave and anamorphic prism pair. The quadrupole field is generated by two coils run at 4 A, consisting of 99 windings each, wound with 1.6 mm wire on spools made from teflon laced with 25% glass-fibre. Teflon is used so as to avoid eddy currents in the holder, and the glass fibre increases the maximum temperature the teflon can sustain without becoming soft. The coils lie flat against the loading chamber so that the symmetry axis is along the line connecting the two chambers.

Push beam

The push beam is weakly divergent, carrying 3 mW of optical power, detuned by -31 MHz from the $F = 2 \rightarrow F = 3$ transition. The beam has a diameter of 2 mm at the position of the loading MOT, and increases in diameter by about a factor of three at the position of the science MOT. The beam is chosen to be diverging so as to limit its effect on the science MOT.

Science MOT

The science MOT is a standard six beam Magneto-Optical trap that uses the quadrupole coils of the magnetic trap to produce the required magnetic field. We use six individual beams (each beam pair is taken from the two ports of a polarizing beamsplitter) rather than three retro-reflected beams, because the atomic cloud casts a significant

shadow on the beams. Each beam is about 15 mm in diameter and carries about 2 mW of power, detuned by -14.5 MHz from the $F = 2 \rightarrow F = 3$ transition; the light is not spatially filtered. Approximately 7 mW of repump power is added in one of the two horizontal beam pairs but the reason for this is historical: at an earlier stage we used the repump MOT beams to optically pump the cold atomic clouds into $F = 2$ prior to imaging, and with this arrangement we avoided repump light in the (vertical) imaging beam path.

The science MOT has three pairs of magnetic compensation coils which are typically used to generate fields on the order of half a Gauss.

3.5.4 QUIC magnetic trap

We realize the Ioffe-Pritchard trap described in section 3.3.2 by a three coil construction known as the Quadrupole Ioffe Configuration (QUIC) trap [60]. A diagram to illustrate the main elements of the arrangement is shown in figure 3.15. The QUIC trap is based on a simple idea: The Ioffe coil is set such that the linear component of its axial field cancels the linear component of the quadrupole field along the symmetry axis of the Ioffe coil. In this way, only the constant, quadratic and higher order terms remain, and the total magnetic field along this direction (the z direction in figure 3.15) becomes approximately harmonic about a non-zero minimum. In the two remaining directions, x and y, the effect of the Ioffe coil is to equalize the linear components of the quadrupole field. This point may be easily understood given the magnetic field gradient along the symmetry axis of a single coil has twice the magnitude and the opposite sign as the radial components; this is evident in the expression for a quadrupole field in (3.6), or indeed by just noting $\nabla \cdot \mathbf{B} = 0$ in this region and using a symmetry argument [61]. In any case, given we choose $B'_{I,z} = -B'_{Q,z}$ and given $B'_{Q,y} = -2B'_{Q,x} = -2B'_{Q,z}$ and $B'_{I,z} = -2B'_{I,x} = -2B'_{I,y}$, it follows that the total field gradient is the same along any direction perpendicular to the symmetry axis of the Ioffe coil. Thus, we obtain the Ioffe-Pritchard field geometry of equation (3.8) in which to trap the atoms.

The QUIC trap has its advantages and its disadvantages. Beyond the apparent simplicity of requiring only three coils, the QUIC trap has the advantage that initially the atoms can be trapped in a pure quadrupole potential, and then be transferred to a full IP trap as the current to the Ioffe coil is increased. The total field for different stages of the transfer is shown in figure 3.16. This means that the quadrupole coils can supply the (considerably weaker) field for the SMOT, making it easier to ensure the overlap between MOT and magnetic trap is good. If it is advantageous, one can begin to evaporate in the quadrupole trap, making use of the increased collision rate in that configuration (see section 3.3.3). A more neutral point is that the centre of the IP trap is displaced from that of the quadrupole - in our trap by about eight millimetres, as can be seen in figure 3.16. This can be considered advantageous as it draws the

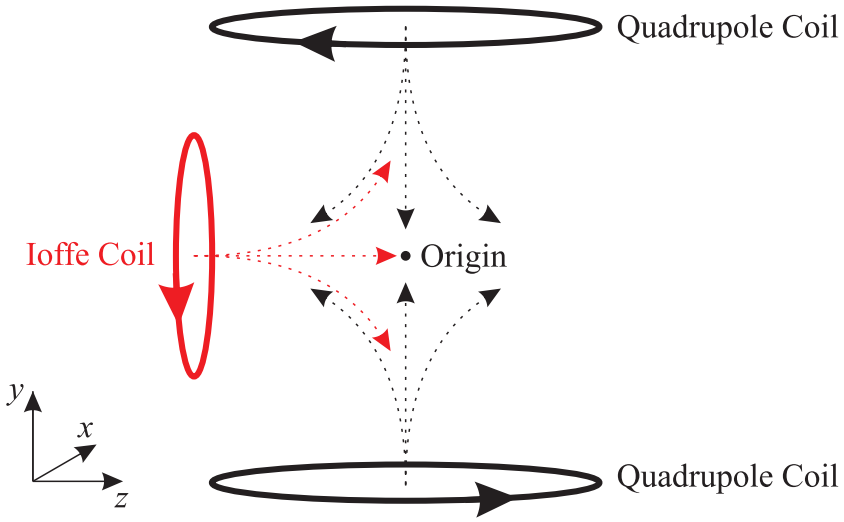

FIGURE 3.15: A cartoon of the basic idea of the QUIC, and more generally, any magnetic trap. The fields from different coils are arranged so as to produce a local minimum at a particular point between the coils. In the QUIC trap, a third coil - the Ioffe coil - is added to a standard quadrupole or anti-Helmholtz pair of coils. The linear component of the axial field produced by the Ioffe coil cancels the linear component along the same axis of the field produced by the quadrupole coils. The field lines are represented by dashed lines and arrows. The arrows superimposed on the coils indicate the direction of current flow.

cloud away from the line of sight to the loading chamber, and this may improve the lifetime in the IP trap. On the other hand, the eight millimetre shift draws the cloud much closer to the cell wall, which can be problematic in terms of stray reflections from the cell wall so close to the BEC. In general, however, the biggest disadvantage of the QUIC trap is the reduction in optical access due to the presence of the Ioffe coil. For this reason, given our desire to probe along the long axis of the BEC (i.e., the symmetry axis of the Ioffe coil), we designed the Ioffe coil with a small hole through which to pass a beam.

It is common in a QUIC trap to use the same current - from the same supply - in all three coils in the full IP configuration. The point about the same supply is important: any magnetic trap requires the cancellation of large magnetic fields to produce the correct trap geometry, and any current supply has some level of noise on the current it produces; by using the same supply for all three coils, one has the same noise on all the coils. Clearly, one wants as quiet a supply as possible, but it is important to note that with a common current, the trap will just shake and change its geometry slightly, whereas the consequences can be much more severe if each coil or pair of coils has its own (noisy) supply. The greatest fear is that due to some non-ideal feature, the trap bottom crosses zero magnetic field, and all the atoms are

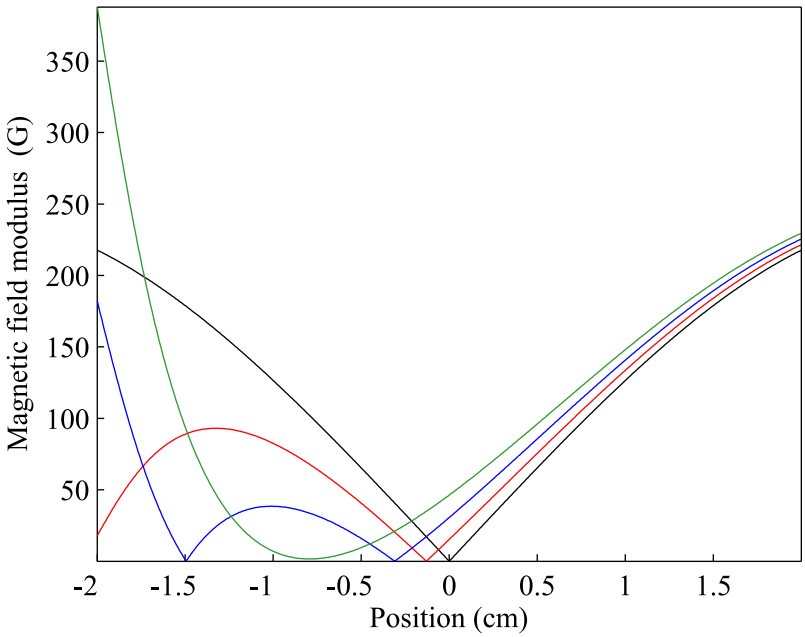

FIGURE 3.16: Calculation of the modulus of the magnetic field in a QUIC trap along the symmetry axis of the Ioffe coil as the current through the Ioffe coil is increased. The field is initially that provided by the quadrupole coils (black), then the current I_{Ioffe} is increased to 1/3 the quadrupole current I_{quad} (red), 2/3 I_{quad} (blue), and finally when the same current runs through all three coils (green). In this case the total quadrupole current was set to 25.7 A. The Ioffe coil is located to the left, with its front edge sitting at approximately -2 cm.

lost from the trap. The window of safety is somewhat narrow, given we choose to run the IP trap with a bias field on the order of one Gauss so as to maintain a steep trap (see section 3.3.2). To persist on the theme of preserving the trap geometry, the coils in the QUIC trap dissipate a sufficient amount of power that they need to be cooled, and this must be accounted for in their design. Clearly, as the coils heat up due to the current, they expand and thus the sensitive cancelation of field gradients can be lost.

Coil construction

To achieve efficient cooling, the coils are wound in layers, separated by thin spacers and submersed in flowing, chilled water. Water flows into one side of the coil assembly, flows between the layers, passes over the top of the coil, then is forced down between the windings on the other side of the coil on its way out. The trap is based on a design by the group of Mark Raizen at the University of Texas at Austin [62]. A schematic diagram showing the assembled coils in their final positions around the science cell is shown in figure 3.17. The coils were wound according to the results of computer simulations where the positions and dimensions of each winding were

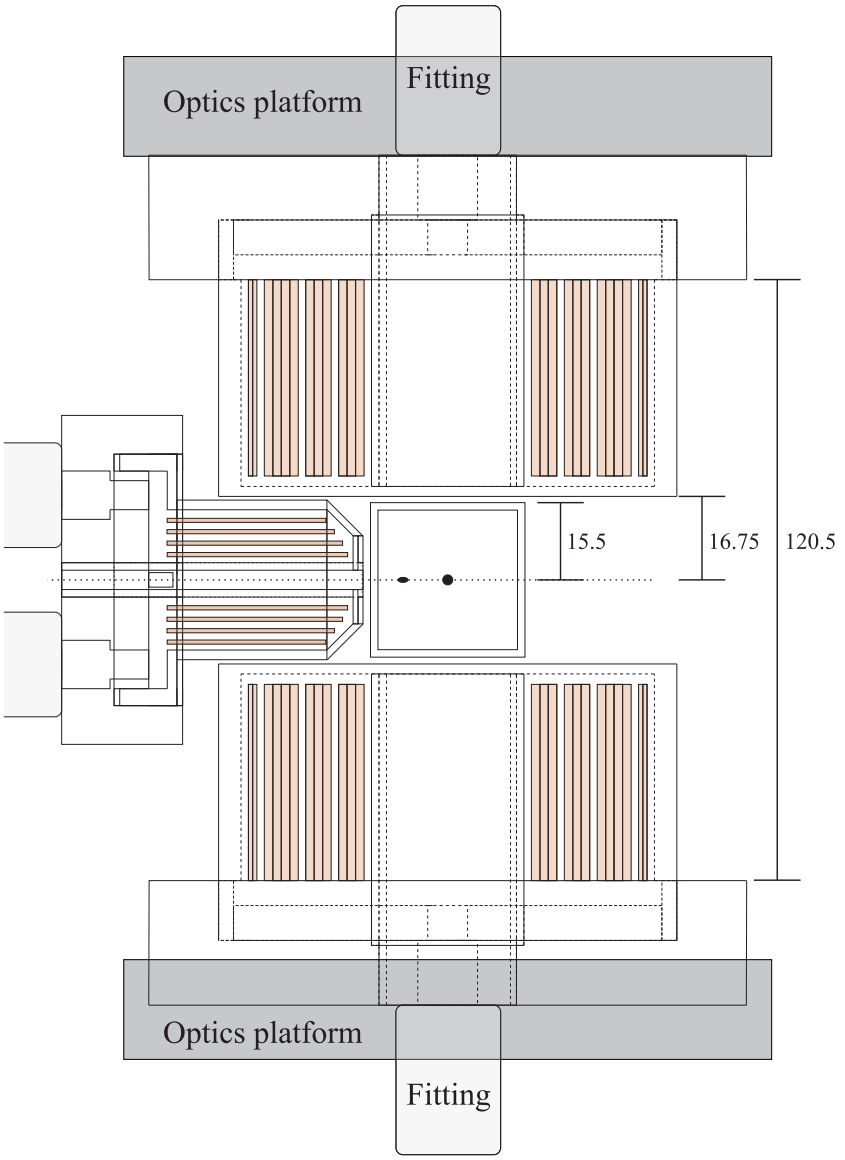

FIGURE 3.17: Schematic diagram of the coils comprising the magnetic trap in their assembled positions about the science cell. The view is from the front, looking up to the loading chamber. The innards of the coils are shown, with the different layers of windings represented by rectangles. There are holes in the quadrupole coils of 24.6 mm diameter for the vertical MOT and imaging beams. There is a hole along the symmetry axis of the Ioffe coil of 4 mm diameter.

modelled so as to achieve an accurate picture of the final field. The coil holders are made of Poly Vinyl Chloride (PVC), and are made water tight by standard PVC glue that is used in household plumbing; they were machined by Niels Lindegaard in the mechanical workshop at NBI. Each coil consists of three main parts: a central rod

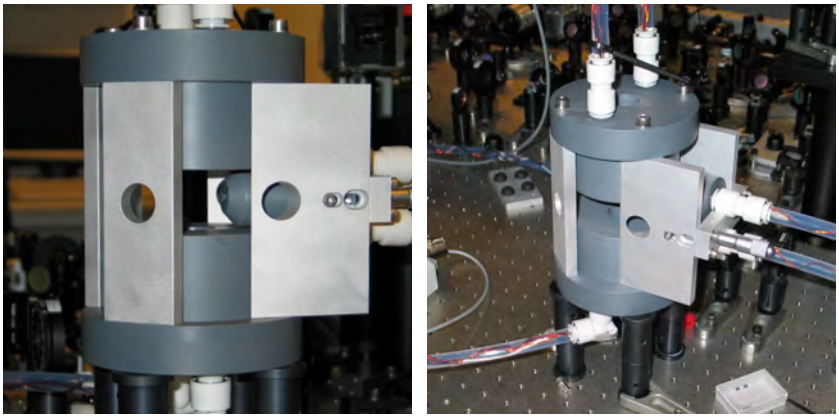

FIGURE 3.18: Pictures of the magnetic trap before its introduction around the science cell. The three PVC coils are mounted with aluminium supports; the supports are sandblasted to limit stray reflections from the metal, and have holes cut in them for the horizontal MOT beams to pass through. The plumbing fittings are visible, as is the wire passing out through the tubes. The micrometers used to position the Ioffe coil are visible in the picture to the right.

on which the coils are wound, a base containing holes for the water, and a lid. The coils were wound by hand on a lathe with the help of several purpose machined teflon winding blocks. Each layer is secured by quick drying glue, and when the entire coil is wound, an appropriate electrically insulating and water proof hard epoxy is used to glue the coils. Each of the quadrupole coils consists of 216 windings, divided into approximately 10 layers of 22 windings. There are four groupings of layers, each grouping separated by a layer of 1.5 mm spacers. The first three groupings contain three layers each, the final grouping contains four layers. The Ioffe coil contains 159 windings divided into approximately four layers of 42 windings, with a conical shape at the front edge to allow optical access for the horizontal MOT beams. Each layer of the Ioffe coil is separated by spacers. Both coils are wound with insulated copper wire, where the quadrupole coils are wound with 1.7 mm diameter wire, and the Ioffe coil by 0.864 mm diameter wire. The quadrupole coils have two additional layers (wound with 0.864 mm diameter wire) for the generation of additional homogeneous or quadrupole fields. The wire passes out thought the plumbing hoses and is connected to the outside world though home-made electrical feed-throughs based on stainless steel T-fittings.

Given that it is desirable that the same current run through all three coils in the full IP configuration, and that once the coils are sealed it is not possible to add more windings, the field geometry is determined by the positioning of the coils. Two pictures of the assembled coils before they were put into position about the science cell are shown in figure 3.18. The quadrupole coils are secured by rather bulky aluminum supports with holes cut in them for the horizontal MOT beams. It is not

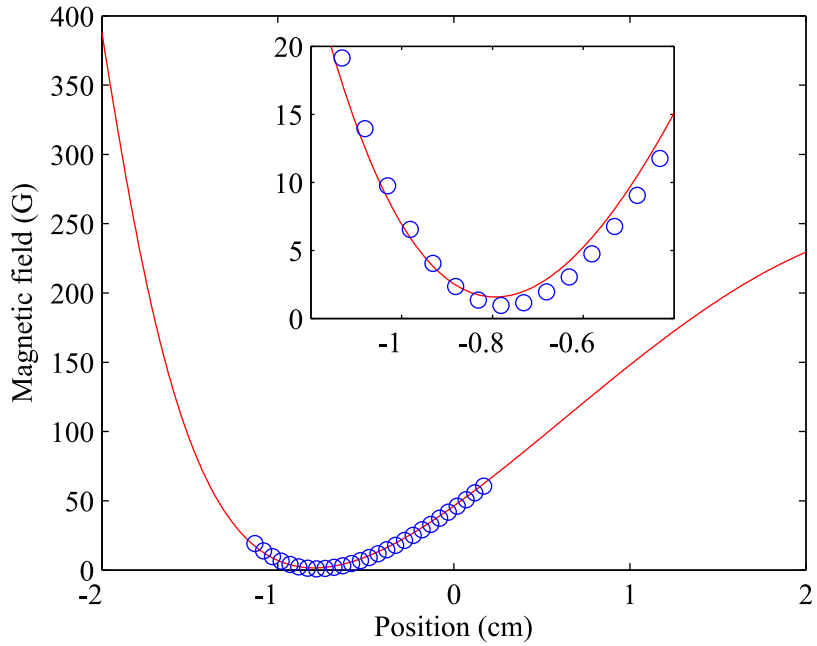

FIGURE 3.19: Calculated and measured (circles) magnetic field along the symmetry axis of the Ioffe coil. The inset shows a close-up of the main figure around the trap minimum.

possible, nor desirable, to move these coils other than by machining these supports; clearly, it is vital that the entire construction is as stable as possible (so aesthetics were reluctantly ignored in this instance). The Ioffe coil is sandwiched between two of these supports, such that it can be pushed backwards and forwards to achieve the right field geometry. It is secured by screws that pass through counter-sunk slots cut into the supports. The tapped holes in the Ioffe coil are not cut directly into the PVC because it is too soft; instead a metal thread is secured in the hole, meaning that one can properly tighten the mounting screws. During set-up, a temporary plate was added behind the Ioffe coil through which two micrometers were mounted. By loosening the Ioffe screws and turning the micrometers, once can very accurately adjust the position of the Ioffe coil.

The assembled coils generate the correct field and thermalize on a short time scale. Before the coil assembly was put into position, the field was measured with a Hall probe, and the result is shown in figure 3.19. The quadrupole trap by itself generates a gradient along the symmetry axis of 10.2 G/cm/A. The full magnetic trap running at 25 A dissipates approximately 600 W. When a single quadrupole coil is cooled with the maximum available cooling water (held at 15°C), at 25 A the coil rises in temperature by about 5°C within a few seconds. The Ioffe coils shows similar performance. When the cooling water is distributed between the coils as it

is in the experiment, the cooling is less efficient due to the reduction in flow to the individual coils, but nonetheless, the system only takes on the order of two complete BEC production cycles to thermalize.

Magnetic trap frequencies

While the simulated and measured values of the total magnetic field agree very well in figure 3.19, it is necessary to measure them *in situ*[6]. This is achieved by displacing a cold cloud in the magnetic trap and mapping out its centre of mass oscillations, otherwise known as sloshing motion. As we have seen, the trap can only be considered harmonic for cold clouds. Thus, a small displacement was induced by applying a suitable magnetic field gradient along the chosen direction, whereupon the atoms were allowed to oscillate in the trap for a variable time. The trap frequencies were found by fitting a sinusoid to the observed motion. In practice, it is often necessary to introduce a small exponential decay and/or drift term to the sinusoid. Furthermore, because the amplitude of oscillation within the trap is very small compared to our imaging resolution, we measure the atoms after a time of flight. In this way, we probe the sinusoidal variation in the velocity of the cloud, and make use of the time of flight to resolve this spatially. The displacement or velocity of the cloud is given by a rather generic damped sinusoid:

$$A(t) = A_0 e^{-t/\tau} \cos(\omega t + \theta) + \text{const.} \tag{3.36}$$

The results of the procedure are shown in figures 3.20 and 3.21. Data points over many oscillation periods were recorded to ensure good sampling of the oscillations. The measurements were performed at a current of 17.7 A through the magnetic coils, corresponding to the 'weak' trap in which the final stage of evaporation occurs (see section 3.7.1). The axial and radial trap frequencies were found to be $\omega_z = 2\pi \times 11.38$ Hz and $\omega_\rho = 2\pi \times 116.0$ Hz respectively. The trap bottom was measured before both measurements to be 1.085 $\pm$0.01 G.

The error estimates for the trap frequencies are on the per mil level, but to quote these would most likely be unrealistic, at least for use over an extended period. The main concern is the variation of trap bottom over extended periods, and the way this influences the radial trap frequency (see (3.13)). This relates to the magnetic environment around the science cell; for instance, one needs to be aware of this point when introducing new pieces of equipment (containing ferromagnetic materials) close to the cell. On the other hand, the axial trap frequency should depend only on the relative positions of the coils, and these have been constant (or at least not adjusted) since their installation two and a half years ago.

[6] Indeed, it was necessary to disassemble the coils as shown in figure 3.18 for their mounting around the science cell. This was a safety precaution given the small clearance between coils and cell and the torque exerted on the coils by the hoses for the cooling water.

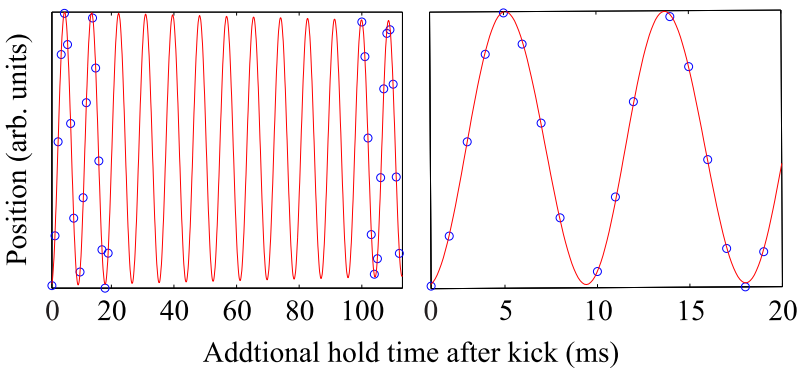

FIGURE 3.20: Radial trap frequency measurement. A BEC was displaced and then held within the magnetic trap for a variable time, whereupon the trap was switched off and the centre position of the cloud after time of flight was measured. Data points are blue circles superimposed on the sinusoidal fit, yielding $\omega_\rho = 2\pi \times 116.0$ Hz.

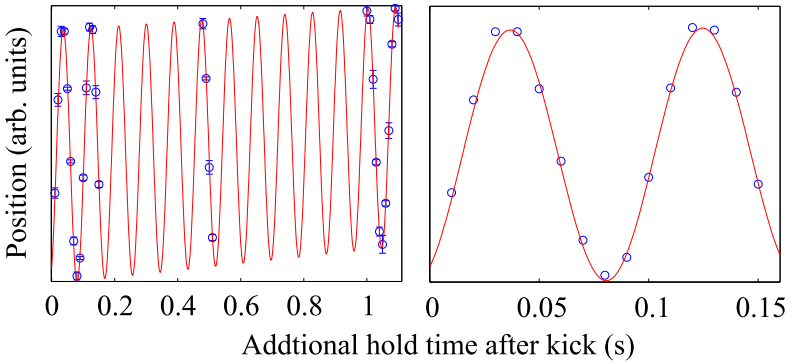

FIGURE 3.21: Axial trap frequency measurement. Data points are blue circles superimposed on the sinusoidal fit, yielding $\omega_z = 2\pi \times 11.38$ Hz. A linear offset was added to the fitting function to account for the drift over long time. The errorbars denote the standard error of the mean for three realizations.

Cooling water

The cooling water is provided by a recirculating chiller that has a flow of 5 l/min. The flow is divided between the three coils and the switchbox that will be described in the following section. On the return line, the chiller is buffered by a large tank that holds about 180 l of water. The chiller and buffer tank are located in a small room next to the lab with other noisy equipment; this closet has its own air-conditioning unit, which often works much harder then the lab units because of the presence of the chiller and a power supply to a laser used by the adjacent lab (this laser arguably

functions better as a heater than its intended purpose). Large tubes carry the water from the closet to underneath the optical table where it is branched off for the coils and switchbox; this minimizes the length of narrow tubing through which the cooling water must travel. The recirculating chiller is a Neslab model M33 PD1.

Guided by the chiller's manual, we use deionized water with a resistivity of approximately 3 MΩ·cm. Deionized water of this resistivity is used because the cooling system contains several types of metals. No anti-algal substance is added to the water as the tubing to the coils (at least according to the vendor) does not support algal growth. The cooling water should be changed and the chiller filter cleaned on a half-yearly basis.

The flow through the path to the switchbox is measured by a flow-wheel. The flow-wheel (McMillan model 101 flo-sensor) produces a voltage proportional to the flow. This voltage is monitored by a homebuilt comparator and if the flow moves outside a user-defined interval, the chiller is switched off and coil power supply is put into 'protect mode' where no current is emitted. See [34] for a schematic of the inter-lock circuit. This inter-lock is crucial to the safe running of the lab.

Power supply

The magnetic trap is powered by a high quality power supply capable of producing 0-30 A, 0-80 V, with a maximum power of 2100 W. The supply is an Agilent model E4356A, 'Telecom DC Power Supply'. We use the supply in constant current mode. The output current may be controlled remotely: we use an analogue 0-10 V output from the computer that is buffered by a homebuilt circuit. The buffer uses a linear opto-coupler to ensure the control computer is electrically insulated from the power supply. This analogue control is used to ramp the total current through the different stages of an experimental run.

Switchbox

Fast switching of the magnetic trap, and the conversion from quadrupole to full Ioffe-Pritchard trap is achieved through a homebuilt 'switchbox'. A schematic diagram of the main features of the switchbox is shown in figure 3.22. Switching of the magnetic field in either configuration is performed with the main switch. To use just a pure quadrupole trap, the shunt resistance is set to its minimum, and the Ioffe switch is left open.

To convert to a Ioffe Pritchard trap, the Ioffe switch is first engaged and then the current though the Ioffe coil is gradually ramped up by increasing the resistance of the shunt. The shunt resistance is comprised of a bank of power Mosfets, connected in parallel. The purpose of this is to reduce the resistance of the branch by sharing the current between three to five Mosfets, thereby reducing the dissipated power. The Mosfets and switches are mounted on an aluminium block that is cooled by water

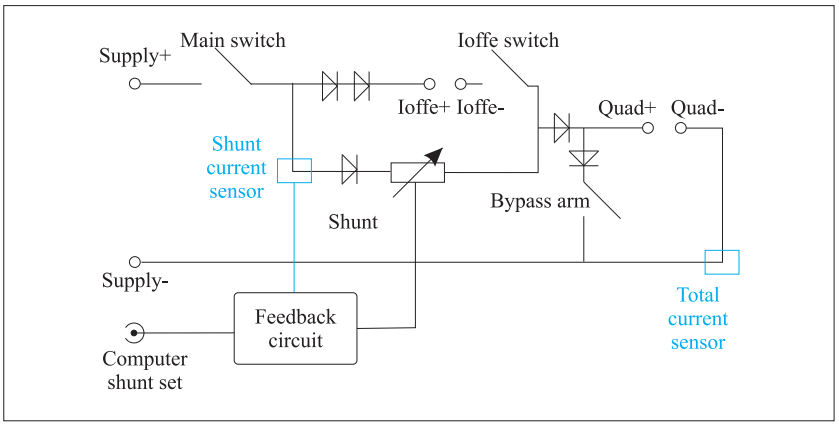

FIGURE 3.22: Schematic diagram of the switchbox used to effect fast switching of the magnetic field and the current sharing required for a conversion from quadrupole to Ioffe Pritchard magnetic trap.

from the recirculating chiller. The Ioffe switch is necessary because the resistance of the Mosfets bank is not negligibly small, and therefore without the Ioffe switch, some current would pass through the Ioffe coil. For the ramping up of the Ioffe current, we require a feedback circuit that takes the 'analogue' signal from the computer and compares it with the measured shunt current. We write 'analogue' because the signal needs filtering to remove the digital steps that make up the signal on a fine voltage scale. The shunt is driven by the output of a Proportional Integral feedback circuit (the board contains the components for a PID circuit, but the PI configuration was sufficient). The feedback circuit needs careful attention given the strongly non-linear response of the Mosfets to applied voltage.

The bypass arm is used to tailor the non-adiabatic turn on of the magnetic trap. The purpose of using such a sudden switching of the coils is to catch the atoms in the quadrupole trap after the MOT light is extinguished, given that they begin to fall due to gravity. This is achieved by instructing the supply to send out a large current (by the interface described in the previous section) while keeping the main switch open, leading to a build up of charge on the output capacitors of the supply; when the switch is closed, the current through the coils increases very steeply over a period of a few milliseconds. Inevitably, this leads to an overshoot of the current before it settles on the correct value. As we describe in section 3.6.2, it is best to keep the non-adiabatic turn on to as small a change in magnetic field as possible. Therefore, we employ a bypass arm to direct some of the excess current away from the quadrupole coils during the turn on so as to limit the overshoot.

The switchbox required a considerable amount of work before it worked in a satisfactory way. In particular, we experienced difficulties in making the feedback loop work as we wanted. Complicating the debugging process was the propensity to

burn out Mosfets in the shunt bank. Initially, the shunt bank was soldered together, making it a messy and somewhat time consuming process to locate and replace the abused mosfet. This was replaced by a system that works much better but still far from perfectly: the pins of the Mosfets are connected by pressure to copper rails. Nonetheless, the performance of the switchbox only improved after a complete rebuilding of the feedback circuit, and a tidying up of the layout of the box. One can certainly learn a lot about good electronic practices from such a piece of equipment that combines high power switching (of inductive loads) and feedback electronics. Since the rebuild and improvements, the switchbox has worked very well. Nonetheless, if the user programs something 'unreasonable' (i.e., stupid) in an experimental sequence, (s)he can expect to spend some time changing Mosfets.

3.5.5 RF evaporation

The RF evaporation described in section 3.3.3 requires a coil driven by an RF synthesizer. In fact, we use two RF coils: one centred around the quadrupole trap and one approximately centred on the position of the cloud in the IP trap. The first coil is circular, 29.5 mm in diameter, and comprised of two windings using 0.45mm total diameter wire. This coil is mounted to the bottom top quadrupole coil and centred around the optics hole in the coil. The rationale is that this coil is best suited to provide uniform RF radiation for evaporation in the quadrupole trap. The other coil is rectangular, 40 mm $\times$ 25 mm, comprised of two windings with the same gauge lacquered copper wire. This coil is mounted off-centre on the top of the lower quadrupole coil, so that the centre of the coil lies approximately under the minimum of the IP trap. The rectangular shape and its size accommodate this goal and the coil does not obscure the vertical MOT beam. Both coils are secured with Kapton tape, chosen for its thinness. The coils were tested for resonances *in situ* using an RF spectrum analyzer, but none such were found. However, the coils showed a general increase in radiated power with decreasing frequency.

The coils are driven by an RF synthesizer, with a primary output that can produce phase continuous frequency ramps in the range 0-20 MHz, and a second 'back-panel' frequency tripled output that is not as spectrally pure. The synthesizer is an HP 3325B. We use the back panel output for some coarse evaporation in the quadrupole trap, performed in 40 steps from 50 MHz to 20 MHz over a period of 9.6 s. The back panel output produces RF at a fixed power of 0 dBm, and is thus amplified (using the same components as those used for an AOM): an RF attenuator (used at a fixed level), digital switch and a 1 W RF amplifier. In an effort to protect the RF amplifier, the output is terminated by a 50Ω resistor and then the coil connected in series. The high frequency steps are sent to the synthesizer in 'real time' via a General Purpose Interface Bus (GPIB) during the experimental run. From 20 MHz down to condensation, the lower, rectangular RF coil is used, taking the signal di-

rectly from the front panel output which can produce up to 24 dBm. The amplitude is controlled by an analogue signal from the computer, and in general is reduced as we approach trap bottom so as to reduce the power broadening of the RF knife. The ramp is broken up into about 10 exponential ramps, approximated by several phase continuous linear sweeps; the initial and final frequencies and the duration of each ramp are produced in Matlab, read in by Labview and downloaded into the synthesizer via GPIB outside an experimental run.

3.5.6 Computer control

A computer is used to control the timing and administer the various remotely controlled pieces of equipment. The user interface is provided through Labview. The 'control computer' is augmented by several boards so that it can produce the wide variety of signals with precise timing that are required for the generation and probing of a BEC. The set-up is similar to that described in [54].

The central board that controls the timing of the experiment is a Viewpoint DIO-64. It contains 64 digital channels, 62 of these are used to produce the various required digital signals (TTL - Transistor-Transistor Logic). At present, only about half of these are used in the experiment. The channel values and the timing are stored in the output buffer of the DIO-64 board at the start of an experimental sequence. The unique feature of the board is that fine time resolution may be obtained without an excessive use of the buffer because only updates of the digital channels are stored. The board has a 20 MHz clock that controls the timing of the time-critical elements in the experiment[7]. In principle, this leads to a timing resolution of 50 ns.

Analogue signals are produced with an additional board that is synchronized with the DIO-64. This 'analogue board' has eight analogue and eight digital ports. Analogue signals, such as VCO control voltages or the linear ramps used in the compression or relaxation of the magnetic trap, are programmed in the Labview front panel (with a user defined time resolution) and then loaded into the analogue board's output buffer upon the initiation of an experimental sequence. This board is synchronized with the main board through one of the DIO-64's two remaining digital channels: the output of the analogue board is updated by a trigger sent from the DIO-64 that is detected on one of the analogue board's digital ports. While the possible timing resolution of the DIO-64 is 50 ns, the settling time of an analogue port when changing value is 2 μs; as such, this sets the timing resolution of a the control computer. (At this stage, the final digital output of the DIO-64 carries an unused copy of the update signal that is sent to the analogue board.)

For other operations, such as the sending of GPIB or camera pre-trigger commands, where the required timing is not nearly as critical as the 2 μs described above, 'software timing' is used. That is, the computer system clock is essentially respon-

[7] In fact, the clock is 40 MHz, but must be used with two as the minimum divider

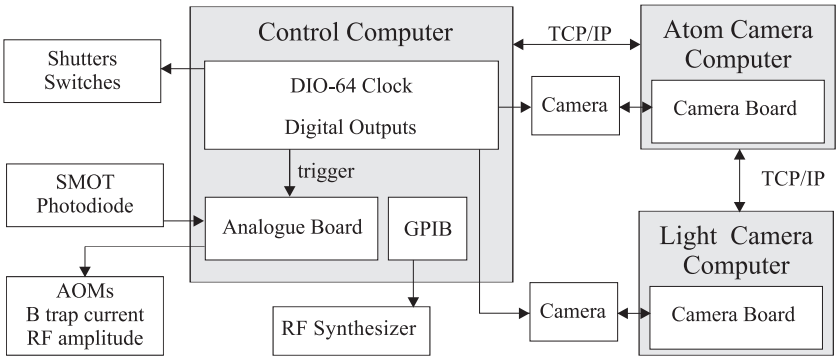

FIGURE 3.23: Schematic diagram of the control system of the experiment.

sible for the timing of such events, administered by Labview, although the loss of synchronization is guarded against within the Labview code by synchronizing the system clock with the DIO-64 clock shortly before such an event.

Several other computers are used to interface with the cameras and other detectors used in data taking. Different computers are used for these tasks so as to limit the burden on the control computer. One is dedicated to the absorption imaging camera, another to a CCD camera used to image light emitted by the atoms in light scattering experiments, and finally we use a high-quality digital oscilloscope (which is itself a computer) to monitor various other signals of interest in a given experiment. The two cameras are described in chapter 4. A schematic of the set-up is shown in figure 3.23.

3.6 An experimental sequence

3.6.1 Loading the science MOT

Atoms are pushed from a 2D loading MOT by radiation pressure to a 3D science MOT. As we have mentioned several times, the purpose of this arrangement is to collect as many laser cooled atoms as possible in the science chamber, whereupon we can begin evaporative cooling. We typically obtain approximately a few times 10^9 ^{87}Rb atoms in the science MOT in a time of 15 to 25 seconds. The loading is performed with constant experimental parameters. As the number of atoms in the SMOT increases, so does the fluorescence, and some of this is collected by a lens placed close to the cell that directs the light onto a photodiode. The signal from the photodiode runs into a comparator circuit: when the signal crosses some user-defined level, the comparator changes its output state and through a digital input (on the 'analogue board', see above), the computer is given the signal to continue with the rest of the sequence - namely, the loading into the magnetic trap and evaporation. The signal from the photodiode is shown in figure 3.24.

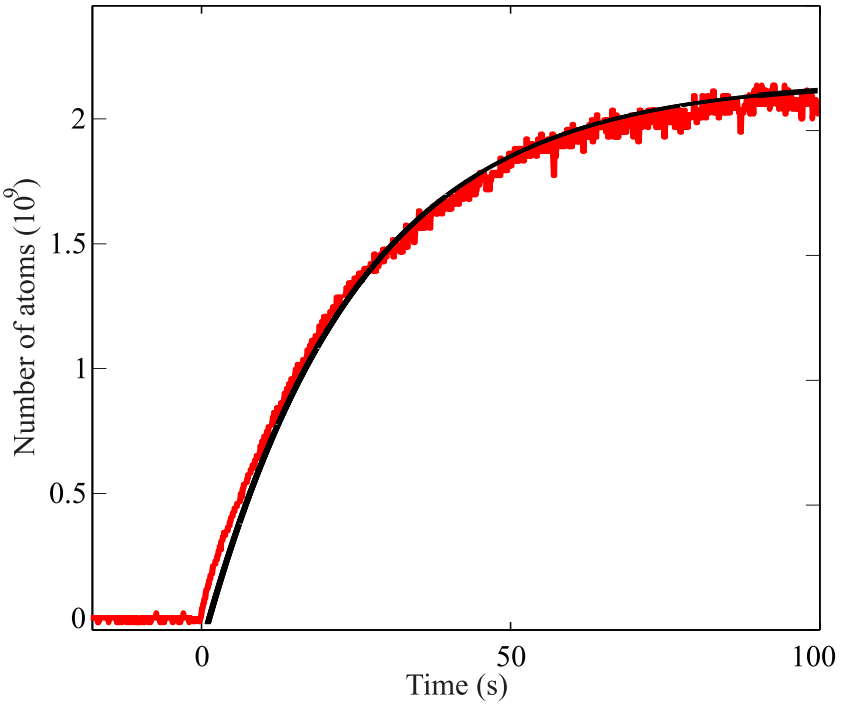

FIGURE 3.24: Time trace (red) of the output of the photodiode measuring the fluorescence of the science MOT. An inverted exponential fit to the trace is also shown (black) [34].

Provided the beam of cold atoms is well collected by the SMOT, the flux of atoms is given by the initial slope of the curve in figure 3.24, and this is approximately 10^8 atoms/s. This value for the flux is not unusual in the literature (e.g, [63]), but fluxes greater than 10^{10} atoms/s have also been achieved in variants of 2D MOTs [64, 65]. The initial loading rate shown in figure 3.24 reduces exponentially due to density dependent losses in the science MOT. The loading curve is fitted with $N(t) = N_0(1-\exp(-t/\tau))$, yielding a time constant for the loading of $\tau = 25$ s.

The transfer was optimized empirically, but the parameter space is rather large (several laser detunings and powers and magnetic field gradients), so inevitably it could benefit from numerical simulations, some of which are described in the cited references, and in general a more tailored approach. One point that could be addressed is the vapour pressure of the loading chamber; this is most likely kept too low because of conservative use of the dispensers (which probably derives from a healthy fear of vacuum problems). We attempted to make use of Ultra-Violet desorption to transiently increase the vapour pressure of the loading chamber [66], but the efforts were unsuccessful - the optical access is simply not sufficient to get enough UV light into the loading chamber to have an effect. If at some stage it is deemed necessary to greatly improve the transfer rate, in all likelihood this will require a

major overhaul, namely the replacement of the loading chamber with one of more appropriate size and shape, combined with several changes to the magnetic fields and beams.

3.6.2 Loading the magnetic trap

There are three main steps in loading the magnetic trap from the science MOT: a Compressed MOT (CMOT) phase, optical pumping and finally the switch-on of the magnetic trap. In general, the physical overlap of the cloud at the different stages from MOT to magnetic trap is crucial to the overall transfer efficiency. At each step, one must check this overlap; typically this is optimized through the power, polarization and alignment of the SMOT beams. At least in our set-up, the main disadvantage of loading a MOT from a cold atom beam is the precise alignment it requires. Although it is an iterative process, fortunately it is the case that the loading of the science MOT is dominated by the alignment of the loading MOT and push beam, whereas the SMOT can be optimized principally for its loading into the magnetic trap. Provided the optical molasses is well balanced and well centred on the minimum of the quadrupole field, the remaining optimization largely relates to the timing and parameter values used in the various steps. In our case, these settings are set in the computer sequence and lead essentially to global changes in the cloud.

As noted in section 3.5.4, the magnetic trap must be switched on quickly so as to catch the atoms against gravity. Additionally, the minimum of a weak magnetic trap is considerably offset by gravity, leading to sloshing motion of the loaded trap, and a decrease in phase space density. On the other hand, during the fast switch-on the atoms gain potential energy depending on their position, and again the cloud is heated. We can make a rough estimate of the energy gained in the non-adiabatic increase in the magnetic field: The quadrupole trap is switched on at 9 A, leading to a gradient of about 90 G/cm (see section 3.5.4), or in terms of Zeeman energy gained, expressed as a temperature, 3 mK/cm. Thus, it is clear that the best strategy is to make the cloud as small as possible before loading into the magnetic trap, and to make sure the cloud centres in the SMOT and quadrupole trap overlap. Furthermore, it is important that the turn-on of the magnetic trap is fast so that the atoms do not fall too much with respect to the quadrupole centre, leading to more sloshing.

Compressed MOT

As such, the goals of the CMOT phase are to reduce the size of the cloud and increase its density. As described in section 3.3.1, this is achieved by letting the atoms spend more time in a dark state ($F = 1$), thereby reducing the repulsion between atoms due to reabsorption of trap light. The main changes in the CMOT as opposed to a standard MOT are thus the reduction of repump power, and the increase in the detuning of the trap beams. The repump power is reduced by a factor of five, and the red detuning

of the trap beams increases from approximately 2.5Γ to 8Γ. At the same time, the coil supply is instructed to reduce its output, although this occurs slowly, over the 20 ms duration of the CMOT phase. The parameters of the phase were optimized iteratively, trying to strike the balance between cloud size and number of atoms.

At the end of the CMOT phase, there are 2 ms where the magnetic trap main switch is opened, thereby putting the experiment into a nominal 'polarization gradient cooling' phase. However, the primary objective is to begin charging up the output capacitors of the coil power supply, so as to achieve a fast switch-on: the supply is instructed to send out 24 A in this period.

Optical pumping

The atoms are optically pumped to the $F = 1$ manifold by switching off the repump beam. This simple form of optical pumping means that the atoms are distributed between the magnetic sublevels, leading to approximately a third of the atoms in the $F = 1, m_F = -1$ state. The optical pumping phase lasts 3 ms. The timing was chosen so that no discernable number of atoms were observed in the other states that can be magnetically trapped ($F = 2, m_F = 1, 2$); this was confirmed by imaging the cloud in the absence of repump light.

Magnetic trap switch-on

With the output capacitors of the coil power supply having charged up for 5 ms, the main switch is engaged and the quadrupole field attains its target value of 9 A within 2.5 ms. There are several parts to this process in order to avoid a significant overshoot of the current, where the bypass is engaged transiently and various other tricks are played.

Final numbers in the quadrupole trap

When optimized, we obtain a few times 10^8 atoms at approximately 150 μK in the quadrupole magnetic trap, which is more than enough given the obtainable tightness of the magnetic trap to ensure successful evaporation. Nonetheless, approximately an order of magnitude is lost in the transfer from the science MOT, where roughly one third is lost in each step. The loss in going from optical pumping to the magnetic trap is understandable given the atoms are approximately evenly distributed between the three magnetic sublevels in the $F = 1$ manifold. The losses in the other steps also seem reasonable given the much reduced loading rate of the CMOT, and the absence of trapping during optical pumping.

Transfer to QUIC trap

Over a period of 500 ms, the atoms are transferred adiabatically from the quadrupole trap to the full Ioffe-Pritchard configuration. This is achieved by linearly ramping up the current to the Ioffe coil, as described in section 3.6.2. As may be seen in figure 3.16, as the current through the Ioffe coil is increased, the minimum of the quadrupole trap is drawn towards to the Ioffe coil. When I_{Ioffe} is high enough, a second trap minimum approaches that of the quadrupole field, and the trapped atoms spill over into the double-well trap. Finally, the transfer is complete when $I_{\text{Ioffe}} = I_{\text{quad}}$, and the trap has a single non-zero local minimum. If performed correctly, this procedure leads to all the atoms being transferred to the IP trap at no loss of phase space density. If the procedure is reversed then the atoms are approximately divided between the two potential wells [60]. This adiabatic transfer requires that the ramping of the I_{Ioffe} is sufficiently slow, and that no (or little) noise is added to the current by the switchbox. Both would induce heating in the trap, either though the sloshing motion associated with too fast a transfer, or the shaking of the trapping potential due to a noisy current flowing through the coils. Initially, the transfer was performed at a reduced overall current ($\sim$ 16 A) because the feedback circuit could not cope with the non-linearity of the Mosfets, leading to a step in the Ioffe coil current. However, since the switchbox was reworked (see section 3.5.4), the transfer works well at the standard operating current.

3.7 Demonstration of BEC

3.7.1 Optimization of the evaporation sequence

The evaporation takes place primarily within the full QUIC trap, but there is an initial phase of cooling in the quadrupole trap. As mentioned in section 3.5.5, this initial phase makes use of the back panel output of the RF Synthesizer, where the evaporation is performed in 40 steps from 50 MHz to 20 MHz over a period of 9.6 s. The effect of this evaporation is to reduce the temperature from approximately 150 to 100 μK, and to reduce the atom number from approximately 3×10^8 to 1.5×10^8.

The main evaporation sequence in the Ioffe-Pritchard trap was optimized empirically according to equation (3.14). That is, the evaporation was broken up into sections and several frequency ramps were tried for each section; the ramp that produced the highest gradient $\ln(\rho_f/\rho_i)/\ln(N_f/N_i)$ was chosen. This was done graphically, and the results of the optimization are shown in figure 3.25. For each ramp, three pictures were taken of the thermal cloud after time of flight. Using a 2D Gaussian fitting routine, the cloud parameters were extracted from the processed images and used to evaluate the temperature and the number of atoms. The number of atoms

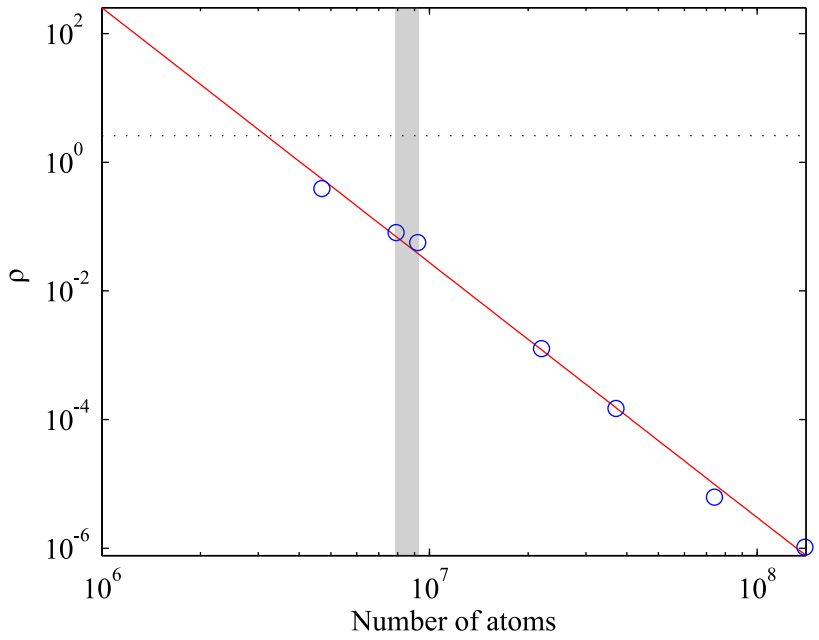

FIGURE 3.25: The increase in the phase space density as a function of the number of atoms for the optimal evaporation sequence. The blue circles are the mean of three realizations for the optimal evaporation time constant. Until $N \approx 10^7$, $\rho \approx 10^{-2}$, the optimal time constant was found to be $\tau = 12$ s. At this point, denoted by the grey stripe, the trap was relaxed to limit density dependent heating. From this point, a considerably faster evaporation was found to be optimal. The red line is a linear fit to the data points, corresponding to an efficiency parameter of $\gamma = 3.96$. The dotted line indicates $\rho = 2.612$ - the phase space density at which Bose-Einstein condensation begins.

was estimated by integrating the 2D fit. The temperature was measured along the long axis of the trap by using the fitted width in equation (3.30). This is not quite correct for the large initial clouds, because they are more than big enough to sample the trap outside the region where it is harmonic. The same is true in the radial direction. Nonetheless, both directions lie within 10 % of each other for the hot clouds, and within 3% for the cold clouds. Furthermore, the complications with the method do not change the results of the optimization, but rather the absolute numbers along the way.

There are two main parts to the evaporation sequence: the bulk of the evaporation takes place in a 'tight' trap so as to maximize the elastic collision rate, but the final phase occurs in a 'relaxed' trap, so as to limit the effects of 3-body recombination. The optimized evaporation ramp is shown in figure 3.26; the inset shows the period where the trap is relaxed - which the RF frequency follows - followed by a final phase with much reduced time constants. The RF coil was driven with the maximum power

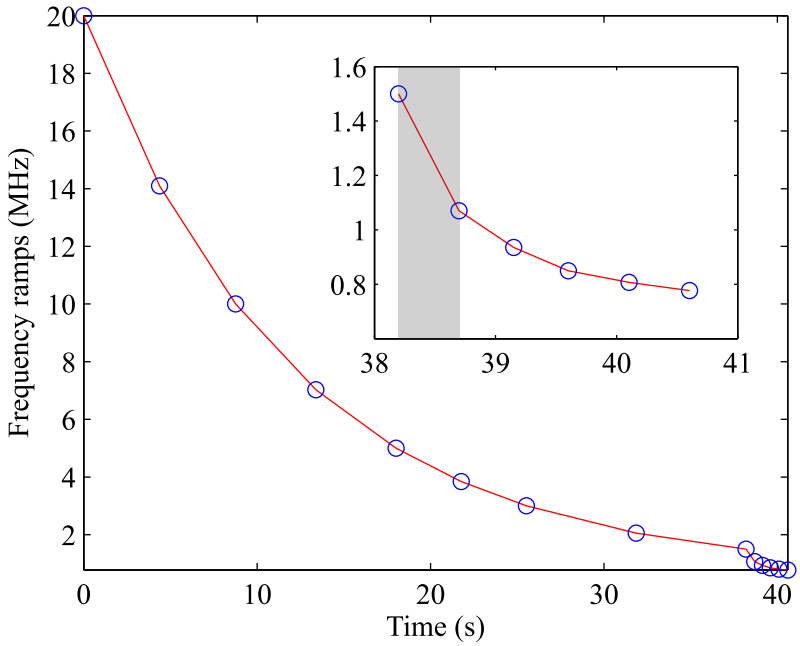

FIGURE 3.26: The frequency ramps produced by the RF synthesizer. For the first 38 s, the sections comprise an exponential ramp with constant $\tau = 12$ s. Subsequently, the trap is relaxed as the current is ramped down by a third over 500 ms. In this time, marked by a grey stripe, the frequency follows the lowering trap bottom and reducing temperature of the cloud. At the end of the sequence, much shorter ramps are used: $\tau \sim 1$.

available (24 dBm, see section 3.5.5) for all but the very end of the evaporation.

It was found that an exponential ramp with time constant $\tau = 12$ was optimal for the majority of the evaporation. In this time, the magnetic trap is driven at 26.7 A, leading to a trap bottom of 1.6 G and trap frequencies of $\omega_z \approx 2\pi \times 13.6$, $\omega_\rho \approx 2\pi \times 138$ Hz. These frequencies are calculated by the computer simulation used to design the trap - see section 3.5.4. The exponential ramp is approximated by linear sections, where the RF synthesizer sweeps the frequency in a phase continuous manner. At the start of the ramp - 20 MHz - $\eta \approx 9$.

At an RF frequency of 1.5 MHz, the magnetic trap is relaxed so as to limit the effects of density dependent heating. The heating rate in the stiff trap was measured to be approximately 190 nK/s, most likely due to three-body recombination; the heating rate dropped to approximately 50 nK/s when the trap was relaxed by reducing the current from 26.7 to 17.7 A. The relaxation occurs over 500 ms so as to be adiabatic, using a linear ramp. The trap frequencies at this current were measured to be $\omega_z = 2\pi \times 11.38$ Hz and $\omega_\rho = 2\pi \times 116.0$ Hz. As a result of the relaxation, the trap bottom changes from 1.6 G to 1.085 $\pm$0.01 G, as described in section 3.5.4. In order to maintain the same value of η after the relaxation, the RF knife frequency

Step	ν_{start} (MHz)	ν_{stop} (MHz)	τ (s)	Duration (s)	RF power (dBm)
1	20	10	12	8.76	24
2	10	5	12	9.26	24
3	5	3	12	7.51	24
4	3	1.5	12	12.67	24
5	1.5	1.07	0.649	0.500	24
6	1.07	0.85	1	0.903	24
7	0.85	0.777	1.5	1	10
8	0.777	5	-0.005	0.022	-56

TABLE 3.3: Experimental evaporation parameters. The time constant in the fifth step - the relaxation of the trap - is chosen to match the duration of the current ramp. The final step causes the RF knife to have a negligible effect on the experiments that follow by reducing the power and sending it to a non-resonant frequency.

is decreased. There are two modifications to consider: the bias field is 0.5 G lower, and the temperature of the sample has decreased with the lower trap frequencies: $T \propto \omega$, and $\omega \propto \sqrt{I}$. The current is reduced to two thirds of its initial value, so that the trap frequencies and hence the temperature are scaled by $\sqrt{2/3}$. Initially, $\nu = \nu_0 + \nu_\eta = 1120 + 380$ kHz where $\nu_0 = \mu B_0/h$ and ν_η denotes the frequency corresponding to η; after the relaxation $\nu_0 + \nu_\eta = 770 + (380 \times \sqrt{2/3}) = 1080$ kHz. The change in frequency during the relaxation is evident in the inset of figure 3.26.

The final phase of the evaporation uses considerably faster frequency ramps than the initial phase so as to counteract the heating and loss associated with three-body recombination [67, 68]. It was found that $\tau \approx 1$ gave the biggest condensates. However, we have experienced instability in the atom number and indeed in the position and orientation of the BEC if the final ramp is too fast and uses too much RF power. For this reason, the final evaporation phase uses a considerably reduced RF power, and a slightly shallower ramp.

Important values in the RF evaporation are shown in table 3.3, and absorption images at various stages in the evaporation are shown in figure 3.27.

As noted in sections 2.2.3 and 3.4, there are significant differences in the expansion of thermal and Bose condensed clouds, and these constitute an important factor in 'pronouncing BEC' for the first time. It is namely the inversion of the aspect ratio that allows one to unambiguously state that Bose-Einstein condensation has been achieved. In our case at least, the imaging system still required significant work at the time we reached BEC, making the atom numbers obtained from the absorption signal somewhat unreliable. To illustrate the differences in expansion, figure 3.28 shows the evolution of the aspect ratio of a thermal cloud and BEC.

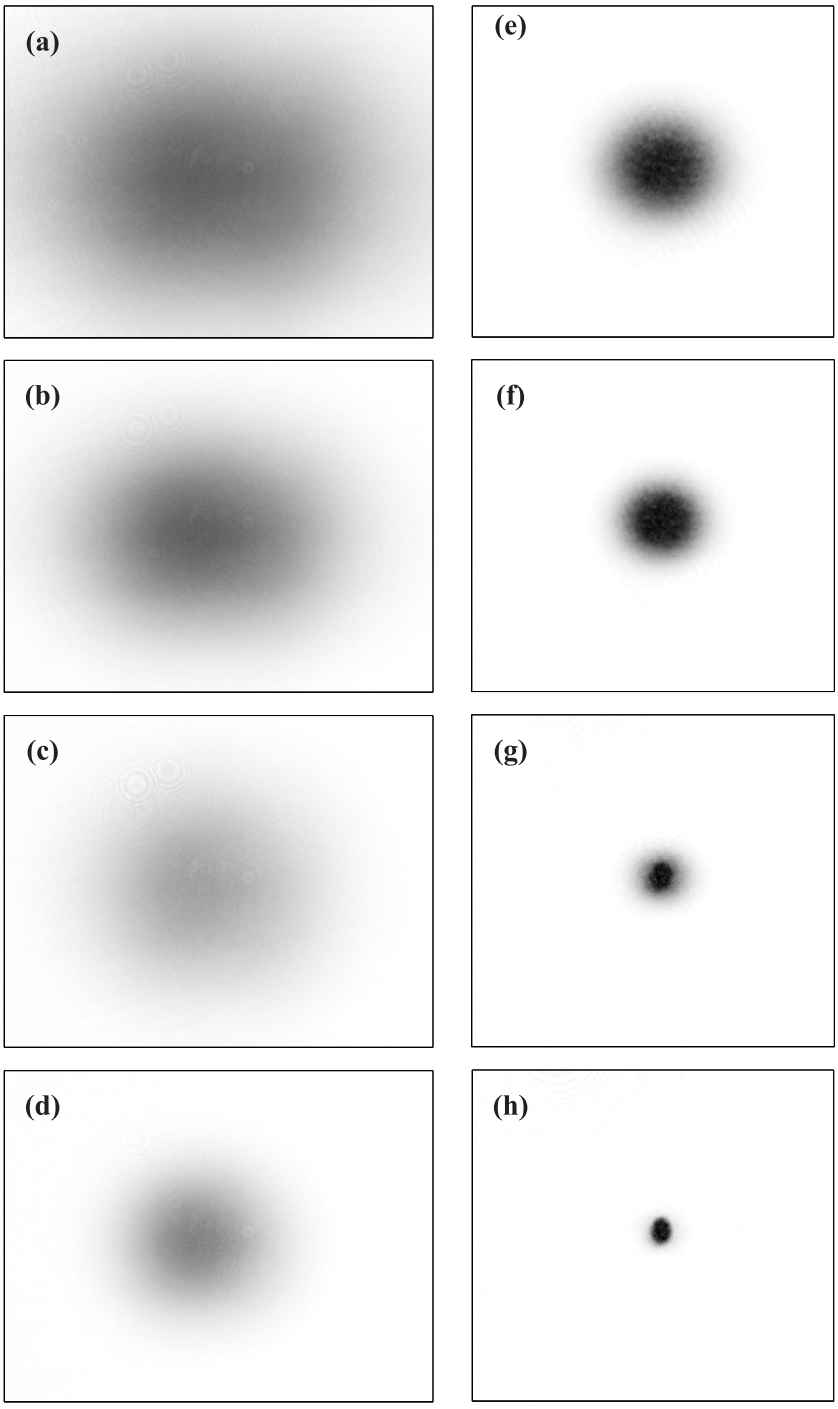

FIGURE 3.27: Absorption images taken under the optimization of the evaporative cooling. (a) the starting point of $\simeq 1.5 \times 10^8$ atoms at approximately 150 μK after 15 ms time of flight; (b) the cloud after RF evaporation from 20 $\rightarrow$ 10 MHz, this and all following images taken after 25 ms time of flight; (c) 10 $\rightarrow$ 5 MHz; (d) 5 $\rightarrow$ 3 MHz; (e) the cloud upon release from the relaxed trap after evaporation down to 1.07 MHz; (f) 1.07 $\rightarrow$ 0.85 MHz; (g) a bimodal cloud somewhat below T_c; (h) a near pure condensate.

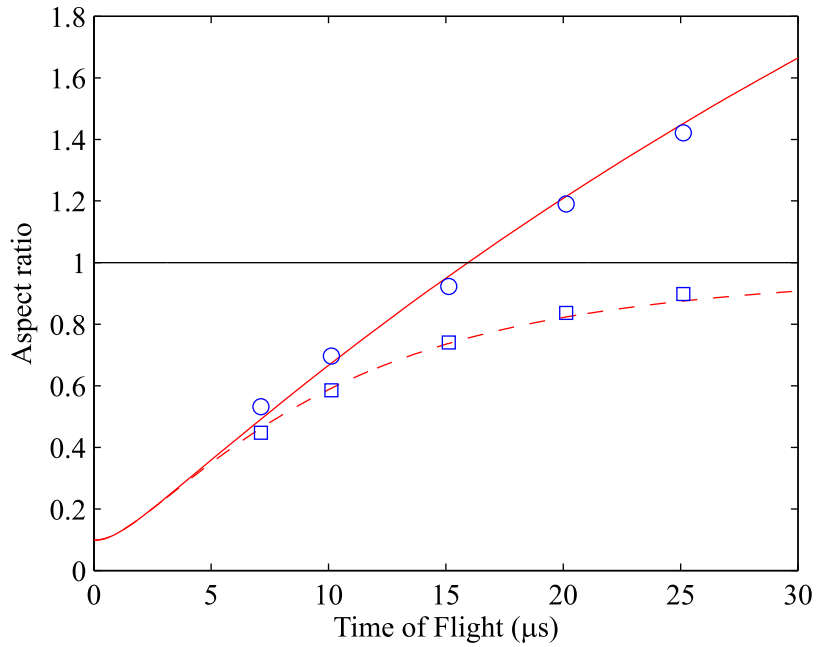

FIGURE 3.28: Illustration of the difference in evolution of the aspect ratio of a BEC and a thermal cloud in time of flight. Aspect ratios ($\rho_0(t)/z_0(t)$) for a BEC (circles, solid line) and a cold thermal cloud (squares, dashed line) are plotted with values calculated from equations (3.30) and (3.31).

Chapter 4

Atom and light detection

4.1 Introduction

The experiments in this work may be described quite simply as the process of shining light on a trapped BEC, and recording its 'response'. This chapter describes the techniques and equipment by which we measure the light that has interacted with the condensate. With our set-up, there are two main probes of the system: absorption images of the density distribution of the atoms after a time of flight, and the counting of photons emitted by the condensate. As mentioned in chapter 1, by shining quasi-resonant light on the condensate, a self-stimulated Raman process can occur whereby atoms co-operatively scatter pump photons primarily along the long axis of the BEC, leading to the emission of a pulse of light and recoiling atoms. We use time of flight absorption imaging to record the changes to the BEC's momentum distribution. We can measure the light pulse emitted by the BEC by two pieces of equipment: a home-built differential photodetector based on Silicon PIN diodes that gives us temporal resolution of the emitted pulse, and another CCD camera to image the spatial distribution of the emitted light. Figure 4.1 illustrates the different beams and orientations of the experimental set-up.

4.2 Absorption imaging

While a brief description of absorption imaging was presented in section 3.4, we give here a more detailed treatment. There are several very good resources that contain fairly comprehensive treatments of the absorption imaging of cold atomic samples, not surprisingly from the first two groups to achieve BEC [21, 54]. The purpose of the following is to give a cohesive treatment of what we consider to be the essential aspects.

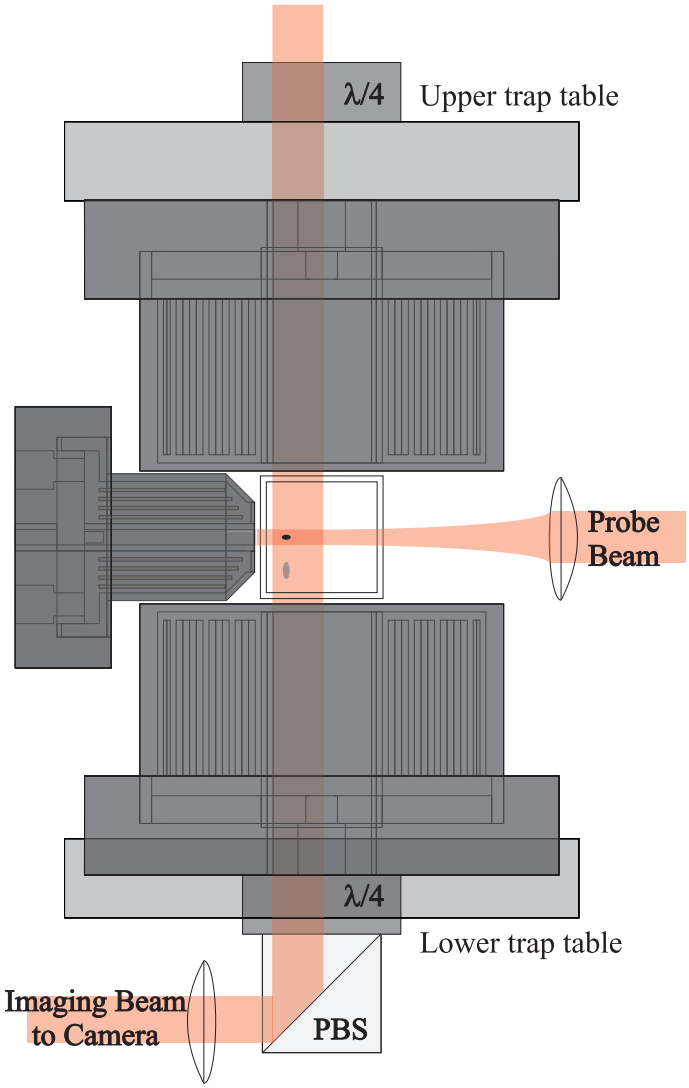

FIGURE 4.1: Schematic drawing illustrating the paths along which we interrogate the atoms with light. Absorption imaging occurs along the vertical axis, taking a shadow picture of a BEC that has been released from the magnetic trap and allowed to expand, falling due to gravity in the process. The shadow cast by the atoms on the beam is imaged on a CCD camera. The probe light is applied along the long axis of the condensate while it is still trapped. The back-scattered light is collected with the same lens used to focus the probe beam onto the BEC, and then directed onto polarization optics and either a time-resolved detector or CCD camera.

4.2.1 Lambert-Beer

The attenuation of the intensity of light passing through an ensemble atoms is given by the amount of scattered power per unit volume. For a laser beam travelling in the

z direction through a cloud of two-level atoms, this relationship is given by [36]:

$$\frac{dI'}{dz} = -\hbar\omega_l\Gamma\rho_{ee}n = -\hbar\omega_l\frac{\Gamma}{2I_s}\frac{1}{1+I'/I_s+(2\delta/\Gamma)^2}I'n, \tag{4.1}$$

where ω_l is the frequency of the laser and the remaining terms were defined in section 3.3. If one considers only the linear dependence in I, i.e., the case $I \ll I_s$, then such a relationship is known as the Lambert-Beer law (or some variation comprised of these names). From the definition of the saturation intensity $I_s = \pi hc\Gamma/(3\lambda^3)$, and defining $I'(L) = I$, $I'(0) = I_0$, the solution of the differential equation may be written:

$$\ln\left(\frac{I}{I_0}\right) + \frac{I-I_0}{I_s(1+(2\delta/\Gamma)^2)} = -\sigma_{\text{abs}}\tilde{n}(x,y), \tag{4.2}$$

where the absorption cross section is defined by:

$$\sigma_{\text{abs}} = \frac{3\lambda^2}{2\pi}\frac{1}{1+(2\delta/\Gamma)^2}, \tag{4.3}$$

and $\tilde{n}(x,y)$ is the column density, as defined in equation (3.25). In the absence of the inhomogeneous term on the left hand side of (4.2), this is equivalent to equation (3.24). The inhomogeneous term gives the non-linear intensity dependent component of the response of a two-level atom to applied light - the term responsible for the power broadening of a transition. It is worth noting that it is only the homogeneous part of (4.2) that is defined as the optical depth:

$$I(x,y) = I_0(x,y)e^{-OD(x,y)} \quad \Leftrightarrow \quad \ln\left(\frac{I}{I_0}\right) = -OD(x,y). \tag{4.4}$$

The inhomogeneous term is then treated as a correction to the true optical depth, but we now consider this within the more general context of extracting the column density from realistic absorption images, which always suffer from some level of experimental imperfection.

4.2.2 Extracting the column density

As described in section 3.4, one requires three pictures to obtain high quality absorption images of the column density distribution: a shadow image I_{sh} with the atomic cloud of interest, a background image I_{bg} of the imaging beam in the absence of atoms, and a bias image I_{bia} taken under the same conditions but with no imaging light. Figure 4.2 shows I_{sh}, I_{bg} and the final processed image of a cold thermal cloud. It is worth looking at the various terms contained in a shadow image [21]:

$$I_{\text{sh}}(x,y) = I_0^{\text{sh}}\left[P(x,y)e^{-OD(x,y)} + S^{\text{sh}}(x,y)\right] + I_{\text{bia}}^{\text{sh}}(x,y). \tag{4.5}$$

We write $I_0^{\text{sh}}(x,y) = I_0^{\text{sh}}P(x,y)$ to separate the maximum intensity and the spatial profile of the imaging beam. In general, the imaging beam profile is far from clean

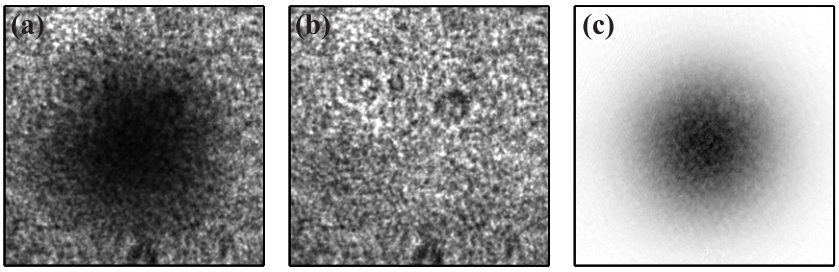

FIGURE 4.2: Absorption imaging of a cold thermal cloud. (a) Shadow picture $I_{\rm sh}$, (b) background picture $I_{\rm bg}$, and (c) the final processed image.

due to imperfections and dirt on the optical elements it passes through on its way to the atoms, as is evident in figure 4.2(b), and this information is included in $P(x,y)$. $S^{\rm sh}(x,y)$ represents any feature in the shadow image deriving from the imaging beam that is not related to $\sigma_{\rm abs}\tilde{n}(x,y)$. There are two main components to this term: light that is not resonant with the atoms, and light that is scattered from optical surfaces after the atoms that somehow finds its way onto the CCD chip. This will be discussed further, but for the moment we consider it a general spatially dependent piece of additive noise on the signal. $I^{\rm sh}_{\rm bia}(x,y)$ is a spatially dependent offset term that accounts for any non-ideal feature in a shadow image that is not related to the imaging beam. Typically this is due to offsets produced in the camera, for instance in the conversion of photon number to pixel counts or fixed pattern noise on the CCD chip [69]. (In fact, it is desirable to have a positive offset to the images so that negative values of the noise are not clipped in the analogue to digital conversion of the photoelectron charge to counts.) Similarly, the background image may be written:

$$I_{\rm bg}(x,y) = I_0^{\rm bg}\left[P(x,y) + S^{\rm bg}(x,y)\right] + I^{\rm bg}_{\rm bia}(x,y). \tag{4.6}$$

With these definitions, we proceed in forming the left hand side of equation (4.2); let us call the argument of the natural logarithm the transmission T:

$$T = \frac{I_{\rm shd}(x,y) - I_{\rm bia}(x,y)}{I_{\rm bg}(x,y) - I_{\rm bia}(x,y)} = \frac{I_0^{\rm sh}\left[P(x,y)e^{-OD(x,y)} + S^{\rm sh}(x,y)\right]}{I_0^{\rm bg}\left[P(x,y) + S^{\rm bg}(x,y)\right]}. \tag{4.7}$$

Experimentally, one produces shadow and background pulses that are nominally the same, but that often differ slightly in overall intensity. In our case, the imaging pulses are produced by an acousto-optic modulator, and these have the tendency to increase in diffraction efficiency by 1-2% over subsequent pulses after a period of inactivity. In any case, this difference can be accounted for after the fact by analysing both shadow and background images in a region where there are no atoms, comparing the mean values of these regions and multiplying the background image by the appropri-

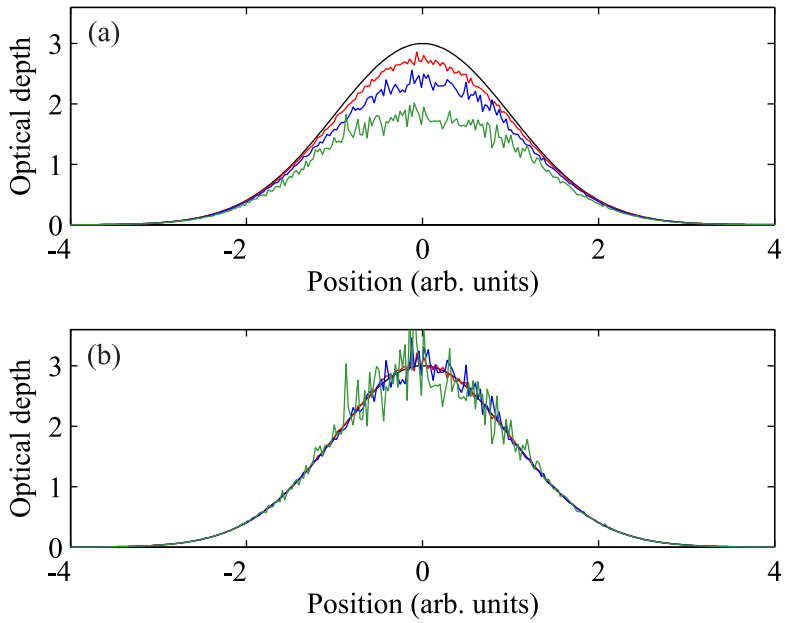

FIGURE 4.3: Illustration of the effect of increasing values of $S(x,y)$ on a reconstructed absorption image given by $-\ln(T)$. The cloud has peak optical depth 3, and the level of additional noise on the images is characterized by the maximum possible optical depth the system can detect OD_{sat}. The curves are for $OD_{\text{sat}} = 100$ (black), 4 (red), 3 (blue), and 2 (green). (b) shows the processed images once the correction has been applied.

ate correction factor. Thus, $I_0^{\text{bg}} \rightarrow I_0^{\text{sh}}$, and (4.7) becomes:

$$T = \frac{e^{-OD(x,y)} + S^{\text{sh}}(x,y)/P(x,y)}{1 + S^{\text{bg}}(x,y)/P(x,y)}. \tag{4.8}$$

In order to proceed, we require a model for the noise terms $S^{\text{sh}}(x,y)$ and $S^{\text{bg}}(x,y)$. To motivate this model, let us consider the effect of the noise terms on a processed image, neglecting for the moment the power broadening term in (4.2). For flexibility in the following arguments, the data is computer generated with realistic parameters. Figure 4.3 (a) shows traces of a simulated reconstructed absorption image $-\ln(T)$ as $S^{\text{sh}}(x,y) = S^{\text{bg}}(x,y) = S(x,y)$ is varied. It is evident that the greater the value of $S(x,y)$ applied, the lower the observed peak optical depth. The data was simulated using:

$$S(x,y) = P(x,y)\exp(-OD_{\text{sat}}) + \text{noise}. \tag{4.9}$$

$P(x,y)$ is chosen as a broad Gaussian profile with multiplicative Gaussian noise that has root mean square variation (rms) $\sigma = 0.2 \times I_0$, consistent with experimental values - the goal is to simulate the imaging beam profile in figure 4.2(b). The

size of $S(x,y)$ relative to the signal of interest $I_0(x,y)e^{-OD(x,y)}$ is determined by a single number: the maximum optical depth one can observe in a given system, $OD_{\rm sat}$. The additive noise used in $S(x,y)$ is also Gaussian distributed, with rms width $\sigma\exp(-OD(x,y))$. It is this noise that is responsible for the increased fluctuations at high optical depth relative to $OD_{\rm sat}$ that is evident in figure 4.3.

With the choice of $S(x,y)$ given in (4.9) (ignoring the noise), it is possible to correct for the saturation of optical depth. It is a simple matter to solve for the true optical depth in equation (4.7), and identifying T with the measured optical depth $T=\exp(-OD_{\rm meas}(x,y))$, we obtain an expression for the corrected optical depth which we call $OD_{\rm mod}$:

$$OD_{\rm mod}(x,y) = -\ln\left(e^{-OD_{\rm meas}(x,y)}\left[1+e^{-OD_{\rm sat}}\right]-e^{-OD_{\rm sat}}\right). \tag{4.10}$$

Often an approximation to this result in the limit of small $\exp(-OD_{\rm sat})$ is quoted in the literature:

$$OD_{\rm mod}(x,y) \approx \ln\left(\frac{1-e^{-OD_{\rm sat}}}{e^{-OD_{\rm meas}(x,y)}-e^{-OD_{\rm sat}}}\right). \tag{4.11}$$

The two expressions agree when the measured optical depth is far less than the saturated value, but (4.11) overestimates the value of $OD_{\rm mod}$ when $OD_{\rm meas}\sim OD_{\rm sat}$. Given both are equally straightforward to program, it is preferable to use equation (4.10). Figure 4.3 (b) shows the implementation of the correction to the observed optical depth in (4.10). The correction cannot do anything about the noise, but it does reproduce the correct form of the simulated cloud.

With the observed optical depth corrected for saturation of optical depth, equation (4.2) may now be written:

$$-OD_{\rm mod}(x,y)+\frac{I_0(x,y)[e^{-OD_{\rm mod}(x,y)}-1]}{I_{\rm s}(1+(2\delta/\Gamma)^2)} = -OD_{\rm actual}(x,y) = -\sigma_{\rm abs}\tilde{n}(x,y). \tag{4.12}$$

This equation gives the correction to the observed optical depth for power broadening of the optical transition. With the assumption that $S^{\rm sh}(x,y)=S^{\rm bg}(x,y)=S(x,y)$, the noise term $S(x,y)/P(x,y)$ present in $I_{\rm sh}$ and $I_{\rm bg}$ is cancelled in the inhomogeneous term $\propto I_{\rm sh}-I_{\rm bg}$. Figure 4.4 shows the effect on the standard optical depth term $-\ln(T)$ of power broadening (the second term on the left hand side of (4.12)); with the correction, the true optical depth is observed. Our typical intensity for imaging is approximately $I_{\rm s}/10$, leading to a minor correction, on the order of a couple of per cent. Of course, it is desirable to keep this correction as small as possible given the experimental likelihood of different spatial noise on the shadow and background images.

It is apparent from the above discussion that the ability to generate high quality processed absorption images requires that the noise term $S(x,y)$ is small and as constant as possible between the taking of pictures. The primary task then is to experimentally reduce and stabilize the contributions to $S(x,y)$.

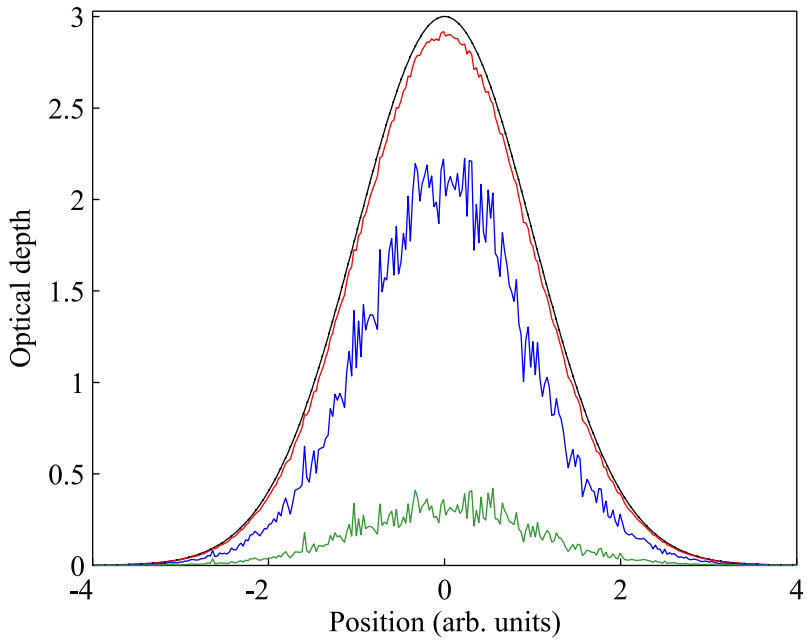

FIGURE 4.4: The correction for power broadening of the optical transition in absorption imaging. The figure shows the optical depth $-\ln(T)$ that is uncorrected for power broadening for several values of the intensity; the saturation of optical depth is assumed to be negligible (i.e., $OD_{\mathrm{sat}} \to \infty$). The curves show $I_0/I_{\mathrm{s}} = 0.0001$ (black), 0.1 (red), 1 (blue), and 10 (green). With the correction in (4.12) applied, the curves coincide with the black curve.

4.2.3 Set-up

The atoms are imaged along the vertical direction after a time of flight. With this arrangement, we obtain pictures showing the axial and a radial axis of the BEC, and as we have seen in previous chapters, this is important for the demonstration of Bose-Einstein condensation. The imaging light shares a common axis with the vertical beams of the science MOT, which are mixed and separated with polarization optics on either side of the science cell. From the previous section, it is clear we wish to minimise the amount of stray light when taking shadow images: absorption imaging never occurs with the MOT or any other light on. For most of the images in this work, the time of flight is 45 ms, meaning that the cloud has dropped by 10 mm when the image is taken; and, in the case of an unperturbed BEC, the aspect ratio has inverted. The imaging light is produced by the injection locked slave laser RBS4; this light is pulsed with an AOM, and is spatially filtered and transported to the upper trap table by a polarization maintaining single mode (PM) fibre. Polarizing beamsplitters are used in transmission before and after the fibre to ensure a clean polarization. We use 50 μs imaging pulses, that have a rise and fall time on the order of 100 ns. Before

the imaging pulse, the atoms are optically pumped out of the $|F = 1, m_F = -1\rangle$ state by a dedicated repump beam. The shadow cast by the atoms is imaged approximately one-to-one on a CCD camera that sits below and to the left of the lower trap table (seen from the view in figure 4.1). The imaging light is typically resonant with the $F = 2 \rightarrow F = 3$ transition. A small magnetic field is applied along the vertical axis to help align the atoms so they experience a uniform polarization during repumping and imaging. In general, we have tried to make the set-up as stable as possible: solid plates and supports are used, the imaging beam has good pointing stability, and stray light shielding is employed. We now describe the salient points in some more detail.

Imaging beam spectral characteristics

The frequency of the imaging light is checked *in situ* before any important experimental run. In principle, one can work out the frequency very accurately with knowledge of the frequencies sent to the AOMs, but these can change slightly on a daily basis and clearly the magnetic environment in which the atoms reside can also modify their internal structure. For these reasons, we perform an *imaging lineshape measurement* before any significant experimental run. This consists of taking pictures of identically prepared cold thermal clouds with several different detunings, and thereby mapping out the lineshape of the imaging light [54]. We use a cold thermal cloud that has resonant optical depth no greater than 2.5 so that saturation of optical depth is not an issue. Figure 4.5 illustrates the results of the procedure.

The fact that the fitted linewidth is very close to the expected linewidth in figure 4.5 indicates that the frequency of the imaging beam is reasonably well-known and controlled. However, referring to the spectrum of the slave laser used for imaging in figure 3.12, there is a concerning 'hump' in the spectrum at 775 nm where the laser is free-running. As noted in 3.5.2, a numerical integration of the spectrum suggests the non-resonant light comprises up to 2.3% of the overall power. This is consistent with the observed maximum optical depth $OD_{\text{sat}} \simeq 5$.

Camera

The camera used for absorption imaging is a model Chroma C3 made by DTA Scientific Instrument. The CCD chip is a Kodak KAF3200ME, with pixel size $6.8 \times 6.8\ \mu\text{m}^2$ and dimensions of 2184×1472 square pixels (14.9 mm$\times$10 mm). The analogue to digital converter is 14 bit, and the camera is run at the maximum gain setting of approximately 0.8 photoelectrons per analogue to digital unit (ADU, also called 'pixel count'). The CCD chip has a quantum efficiency at 780 nm of approximately 59%. We generally do not cool the camera chip, which would reduced the dark current, but given we clean the chip shortly before an image and the short exposure time to take an image, the dominant contribution to the noise is from the readout. The read-out noise is about 11 e^- rms, or in terms of pixel counts approximately 13.4.

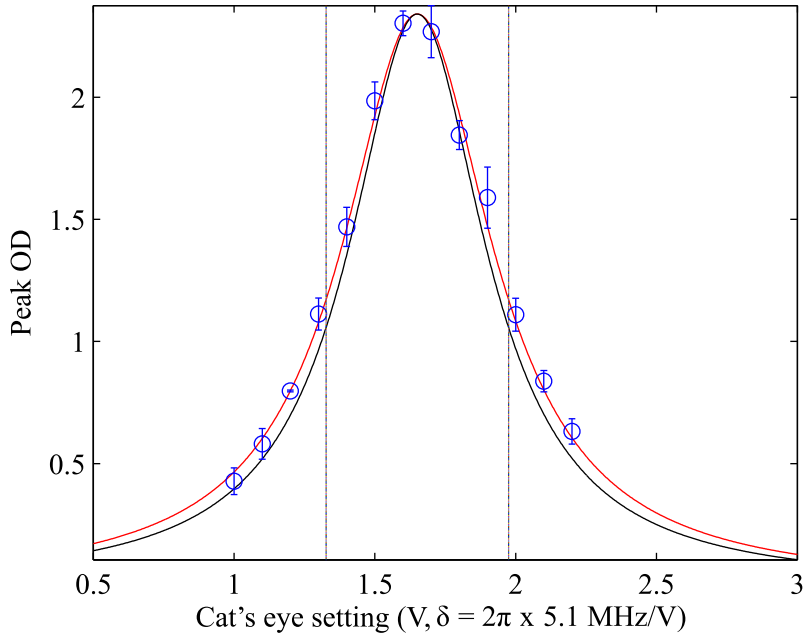

FIGURE 4.5: An imaging lineshape, used to identify the frequency of the imaging light. Several pictures are taken of a cold thermal cloud at several detunings, controlled by the voltage to the cat's eye VCO. Blue circles indicate the mean of three data points, and errorbars the standard error of the mean. The red curve is a Lorentzian fit to the data, and the black curve is the natural lineshape. The two vertical lines indicate the fitted linewidth $\Gamma_{\text{fit}} = 6.69$ MHz, compared to the natural linewidth of $\Gamma = 6.07$ MHz. However, imaging at $I/I_s \approx 0.1$ leads to a power broadened linewidth of $\Gamma\sqrt{1+I/I_s} \approx 6.4$ MHz.

A read-out of the full chip takes 2.6 s although we in standard operation use much smaller regions of interest; the read-out time can be reduced further with binning at the expense of spatial resolution but we do not use this option. To be able to make the correction for power broadening of the transition in (4.12) we need to know the response of the camera for an applied intensity of light. (Note that the conversion factor from photons falling on the chip to pixel counts drops out in the homogeneous part $\ln(T)$.) Under standard operating conditions, the camera was measured to produce 0.738 counts/photon.

While the specifications listed above are satisfactory, the camera has required a lot of work to function reliably. In particular, the Labview programs and the Digital Link Libraries (DLLs) that came with the camera did not function well initially. Mechanically, the camera also has its problems. The most obvious is that the camera has a single M6 tapped hole for mounting (and this hole is about 3 threads deep!). As such, to secure the camera, we sandwich it between an additional pair of mounts. A noisy cooling fan that came mounted to the back of the camera was removed and

mounted separately on a shutter mount (see 3.5.2). Finally, the camera's mechanical shutter is very noisy, and the poor software has meant that to date we have not implemented an imaging procedure in kinetics mode that might improve the image quality: greatly reducing the time between different raw images mitigates the effects of acoustic noise and other slow fluctuations.

Camera objective and magnification

For the images presented in this work, the atoms were imaged on the camera chip with a high quality multi-element lens. The model was Rodenstock Apo-Rodagon N, with focal length f=105 mm. This lens contains 7 elements, has a maximum clear aperture of 22 mm, and is optimized for use at approximately 460 and 540 nm. It was mounted on a lens tube that was connected to the camera by a modular focus device. The lens and camera are positioned such that the atoms are imaged with a magnification measured to be 1.07. The transmission through the objective was measured to be 0.957.

Imaging parameters

The main goal in choosing the imaging parameters is to obtain an integrated photon count on the camera that optimizes the signal to noise ratio of the raw images while staying well below the saturation intensity at the position of the atoms. As mentioned above, we typically aim for an intensity of about $I_s/10$ at the atoms, corresponding to 0.166 mW/cm^2. Additionally, we would like to make good use of the dynamic range of the camera; a mean value of 10^4 counts out of the possible 1.6×10^4 per pixel integrated over the imaging pulse duration is a safe value, given the intensity fluctuations over the imaging beam profile. Given the response of the camera, and that the transmission from the position of the atoms to the camera chip is approximately 0.61, an imaging pulse of 50 μs is a reasonable compromise, leading to an estimated intensity at the atoms of 0.2 mW/cm^2 or $\sim 0.12 \times I_s$. After 45 ms time of flight, the atoms drop by 20 μm during a 50 μs imaging pulse; for the standard condensates we produce, this drop corresponds to less than 5% of their length at the time, and the depth of focus of the imaging system is much larger than this value.

The noise properties of the detection system become more important as the optical depth of the atomic cloud increases. Quite simply, the greater the attenuation of the imaging light, the closer the signal comes to the noise floor of the detection system. The goal is to have the shot noise of the light dominating over the other sources of noise in the system; that is, the electronics noise of the camera and the noise represented by $S(x,y)$ that in general will exhibit spatial correlations between different pixels. Assuming the imaging light is well described by a coherent state, the noise on the photon number is Poissonian, which - scaled by the quantum efficiency of the camera chip - leads to the observed noise on the photoelectrons, and thus the final

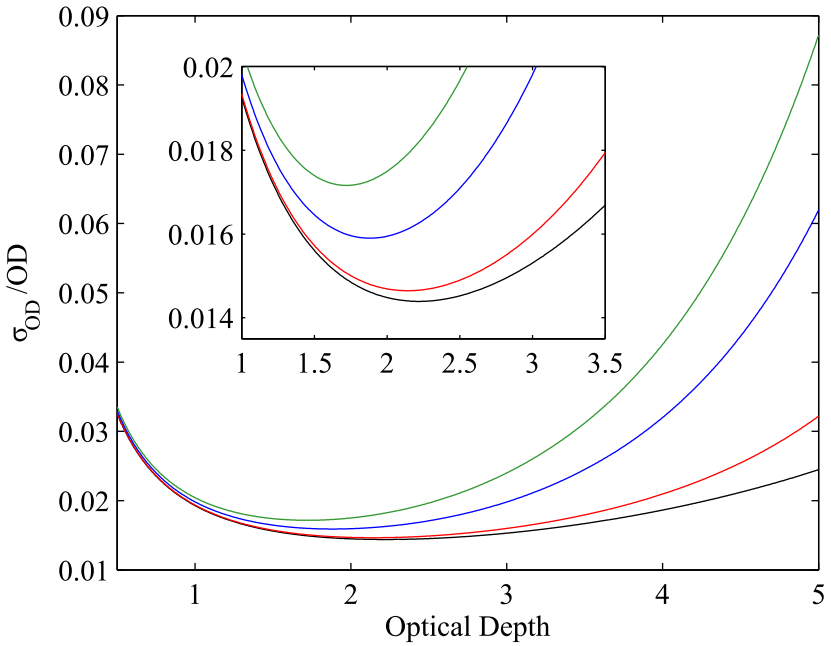

FIGURE 4.6: Relative error of the optical depth for several values of camera noise. The curves are generated using equation (4.15). The curves correspond to $\sigma_{\text{cam}} = 0$ (black), 5 (red), 13.4 (blue) - the experimental value, and 20 (green). The inset shows the same curves around their minima.

raw image. Through an error analysis, one can deduce the optimal optical depth that minimizes the relative error of the processed signal. For simplicity, we consider the low intensity limit where the optical depth is given by $\ln(T)$. Furthermore, we work in terms of the integrated intensities observed on the camera chip, that is in terms of pixel counts. Then,

$$OD = \ln\left(\frac{N_{\text{bg}} - N_{\text{bia}}}{N_{\text{sh}} - N_{\text{bia}}}\right) \quad \text{and} \quad N_{\text{sh}} = N_{\text{bg}} e^{-OD}. \tag{4.13}$$

We model the noise present on the images as follows:

$$\sigma_{\text{sh}}^2 = N_{\text{bg}} e^{-OD} + \sigma_{\text{cam}}^2, \quad \sigma_{\text{bg}}^2 = N_{\text{bg}} + \sigma_{\text{cam}}^2 \quad \text{and} \quad \sigma_{\text{bia}}^2 = \sigma_{\text{cam}}^2, \tag{4.14}$$

where N_{bg} is the shot noise of the imaging light, and σ_{cam}^2 represents the variance of the total camera noise. From the standard formula for error propagation one obtains:

$$\sigma_{\text{OD}}^2 = \frac{N_{\text{bg}}(1 + e^{OD}) + 2\sigma_{\text{cam}}^2(1 - e^{OD} + e^{2OD})}{N_{\text{bg}}^2}. \tag{4.15}$$

Figure 4.6 shows the relative error in the optical depth calculated with (4.15) for several values of camera noise. The relative error is minimized for values of the

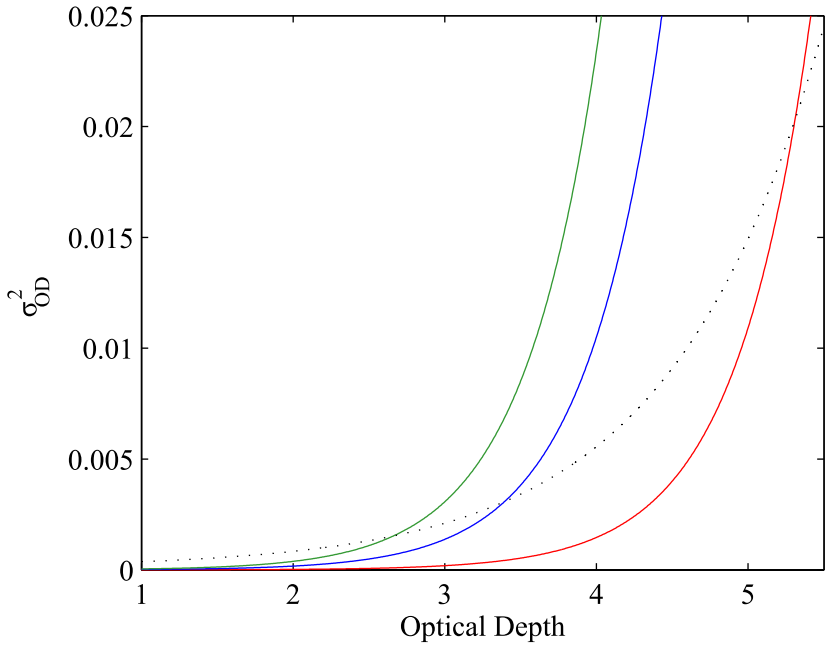

FIGURE 4.7: The size of the two components of (4.15). The dotted line shows $(1+e^{OD})/N_{\mathrm{bg}}$. The solid curves show $2\sigma^2_{\mathrm{cam}}(1-e^{OD}+e^{2OD})/N^2_{\mathrm{bg}}$ for $\sigma_{\mathrm{cam}} = 5$ (red), 13.4 (blue) - the experimental value, and 20 (green). It is desirable to operate at optical depths so that the shot noise of light predominates over technical noise.

optical depth $OD \approx 2$. The two contributions to the noise - the shot noise of the imaging light, and the camera noise - are shown in figure 4.7.

4.2.4 Optical pumping and effective absorption cross-sections

In order to obtain correct absolute values of the density distribution inferred from absorption imaging, we need to take into account the multilevel structure of ^{87}Rb. There are two main points to consider: the optical pumping of the atoms from $|F=1, m_F=-1\rangle$ to the $F=2$ manifold, and how quickly the atoms are then optically pumped during imaging into an extreme state from which they are driven on the $F=2 \rightarrow F'=3$ cycling transition. Additionally, the heating induced by the scattering of photons in either repumping or imaging should not significantly alter the density distribution we are trying to measure. By simulating the master equation for a ^{87}Rb atom interacting with a laser field we can obtain the deviations in the real system from the assumed dynamics. The simulations were written by Marco Koschorreck.

With the dedicated repump beam, the optical pumping from $|F=1, m_F=-1\rangle$ to the $F'=2$ manifold takes on the order of 2 μs and scatters at most two photons in

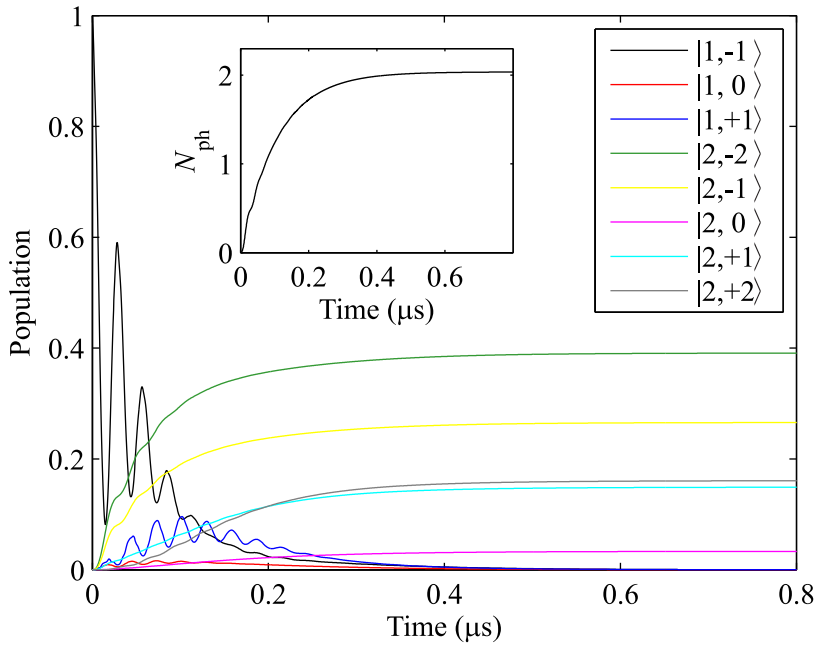

FIGURE 4.8: Simulation of the optical pumping of the atoms from the $|F=1,m_F=-1\rangle$ state to the $F=2$ manifold. The populations in the various atomic states are shown as a function of time. The oscillations at the beginning are due to the high intensity - the curves become smooth for lower powers. The inset shows the number of photons scattered v. time.

the process.

The repump beam approaches from the front of the cell - from the direction of view in figure 4.1. The beam is transported to the trap table by a PM fibre and is outcoupled from the fibre so that it is approximately collimated with a waist of 1 mm. The fibre is oriented such that the polarization of the output beam has maximum transmission through a polarizing beamsplitter. The beam is then directed into the cell, approximately 10 mm below the position of the trapped cloud for a 45 ms time of flight. The beam has total power of 6.5 mW, which, given its small waist, provides a very high intensity at the atoms. The repump pulse is applied for 2 μs (which is the smallest possible time we can produce directly from the computer control system). Experimentally, no increase in imaging signal was observed with longer repumping times. Furthermore, the repumping appeared insensitive to modest misalignment of the beam. Apart from the fact that a dedicated repump beam is necessary in the set-up to optically pump the atoms in a sensible time frame, it has the additional benefit that, with the use of a cylindrical lens, the repump light can take the form of a 'sheet' so that only a slice of the atoms is imaged.

The result of the simulation of optical pumping from the $|F=1,m_F=-1\rangle$ state

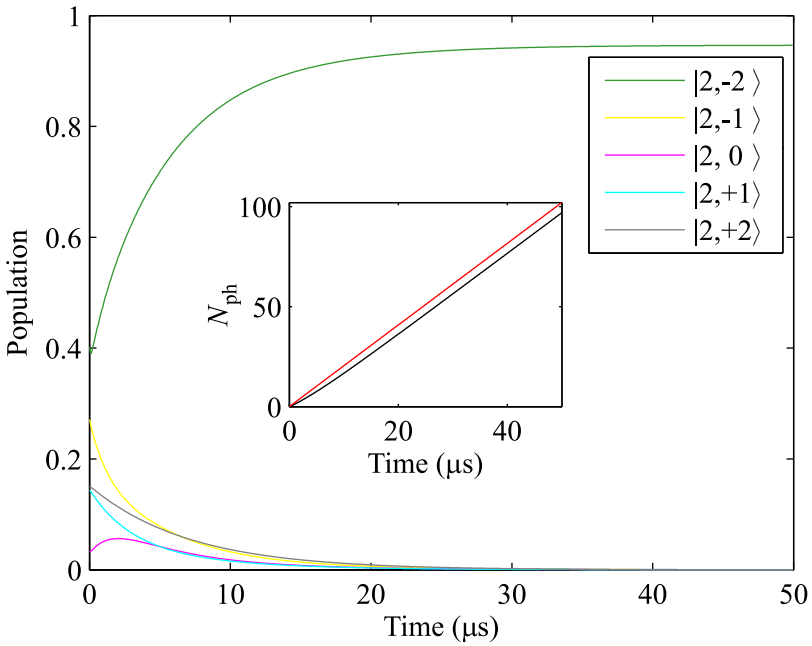

FIGURE 4.9: Simulation of imaging on the $F = 2 \rightarrow F' = 3$ transition driven with σ_- resonant light using the nominal experimental intensity $I = 0.12 I_s$ with $I_s = 1.66$ mW/cm^2. The initial populations are those produced by the repumping (see figure 4.8). As time proceeds, the atoms not already in $|F = 2, m_F = -2\rangle$ are optically pumped to the extreme state. Once there, the atoms scatter on the cycling transition corresponding with a rate given by that for a two level atom (see equation (4.1)). The inset shows the integrated number of photons scattered v. time from the simulations (black) and from the expression for a two level atom (red).

to the $F = 2$ manifold is shown in figure 4.8. With the experimental repump intensity and polarization, within half a microsecond an atom has with probability one been transferred to the upper ground state and emitted on average two photons in the process. After the optical pumping, an ensemble of atoms is thus distributed among the $F = 2$ magnetic sublevels, where the exact nature of the distribution depends on the polarization of the repump light. Note that the simulation describes the behaviour of the density matrix of a single ^{87}Rb atom: it does not include any information about the physical density of the cloud or thus the attenuation as the light passes through the sample. Nonetheless, the result is consistent with experiment.

Simulation of the imaging procedure reveal that fewer photons are scattered in the true multi-level system of ^{87}Rb relative to that of a two level atom. Figure 4.9 shows the populations of the various sublevels as imaging proceeds, where a σ_- polarization and the nominal experimental intensity have been used, and the initial population distribution is the output of the repump simulation. It is evident that atoms not in

$|F=2, m_F=-2\rangle$ are optically pumped into the extreme state over a period of several tens of microseconds. This leads to a reduction in the number of scattered photons as compared to the two-level atom scattering rate used in equation (4.1)). This can be seen in the inset figure: the number of photons scattered v. time according to the simulations is shown together with the number from the nominal two-level atom expression. According to the simulations, 5% fewer photons are scattered than in the ideal case; if instead we image with σ_+ light, the reduction is 10%.

Accordingly, we must modify equation (4.3) to take account of this: we can define an effective scattering cross-section that produces the final results in figure 4.9.

Finally, we note that the number of photons scattered in the imaging procedure does not significantly modify the density distribution of the atomic cloud. An atomic sample exposed to a laser beam changes its velocity along the direction of beam propagation by $N_{\rm ph} v_{\rm rec}$ and its transverse velocity increases by $v_{\rm rec}\sqrt{N_{\rm ph}/3}$. The longitudinal change is irrelevant as the camera and lens position are set so to have the cloud in focus; however the induced heating and thus observed larger cloud width are of importance. The transverse heating leads to an increase in width of displacements $v_{\rm rec}\sqrt{N_{\rm ph}/3}\Delta t$ in a time Δt [21, 70]. Thus, during the 50 μs imaging flash in which on the order of 100 photons are scattered, the cloud is increased in width by ~ 2 μm which is at worst approximately a 2% increase.

4.2.5 Absorption imaging checks and balances

It is possible to check that the absorption imaging is giving sensible results by comparing the properties of the observed clouds with theory; there are two main methods.

In the first, one scans the evaporation sequence for the first sign of a condensed fraction, and compares the observed temperature and number of atoms in the cloud with those expected from theory. The fitting procedures were discussed in section 3.4, and the scaling of the critical temperature with the number of atoms is the content of equation (2.7). Corrections to T_c due to several factors such as finite particle number and interactions between atoms are on the per cent level [19]. We observe that the pair of measured critical temperature ($\sim$ 380 nK) and number of atoms ($\sim 4\times10^6$) agrees to within 10% of what is expected from theory.

The second method consists of comparing the atom number inferred by the measurement of the chemical potential with that using the widths and the peak optical depth in the observed cloud. This was described in section 3.4.3. Briefly, one can infer the chemical potential from the width of the expanded cloud, and from this one can obtain the atom number with knowledge of the trap frequencies, mass of the atom, and the scattering length. Alternatively, one makes use of all the fitted parameters: the widths, and the peak optical depth and, via the scattering cross-section, one obtains the 2D density distribution and thereby the total atom number. Figure 4.10 shows a comparison of the two methods using on-resonance absorption imaging. The

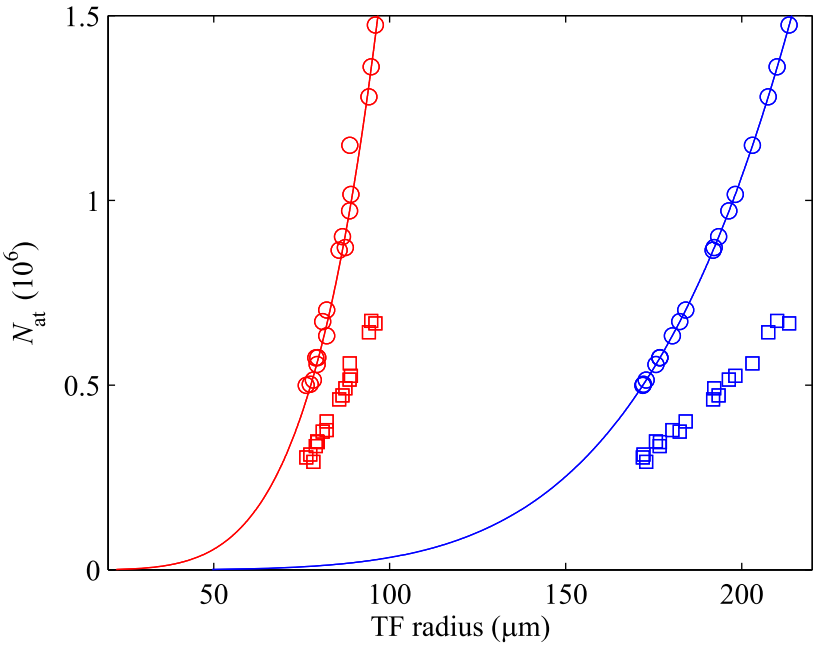

FIGURE 4.10: Comparison of atom number measurement of a BEC using two methods. We generate BECs with a range of sizes using extra-hold time in trap and an aggressive RF shield (see 6.4); the time of flight was 45 ms. By using the Thomas Fermi radii to infer the chemical potential, we obtain the number of atoms (circles). The chemical potential is obtained from the radial width (blue) (hence the perfect agreement), but the axial widths agree very well with theory. When we use all fitted parameters to obtain the number of atoms (squares), the agreement is out by a factor of about two. The disagreement illustrates the present technical limitations of the imaging set-up - the expanded Thomas Fermi profiles have an optical depth of about 15 and the resonant absorption imaging cannot resolve this given the technical noise of the system.

atom numbers and Thomas Fermi radii comprise a self-consistent data set, whereas the numbers obtained using all the fitted parameters do not. In fact, the atom numbers derived from all the fitted parameters are too low by a factor of order two. The resolution to this disagreement lies in the fact that the observed peak optical depth of the expanded BEC is limited by technical noise in the imaging. The peak optical depth of such a cloud is about 15, whereas the fitted peak optical depth is on the order of 7, depending on the atom number. This is not surprising, given the above discussion of technical limitations in absorption imaging.

We therefore conclude that the imaging system performs in a way that is consistent with our understanding. Nonetheless, there are obvious limitations that might be improved upon. If we continue with absorption based imaging and it is important to image clouds of high optical depth, then a form of anti-trapped expansion could be employed to reduce the observed optical depth [54]; however this would require the

development of microwave technology in the lab. Alternatively, selective repumping could be used to limit the cloud to a slice of atoms. In general, off-resonant absorption imaging seems frowned upon, given the lensing effects that can occur in such a high density sample. However, we have never observed any variation in the width when using a detuned imaging beam. Nonetheless, off-resonant absorption imaging essentially throws away signal, which is never a good solution. Furthermore, birefringence due to impure polarization in the imaging beam becomes more likely with off-resonant light, and it would require a careful analysis of the effect of the polarization optics in the imaging set-up. If off-resonant imaging was chosen, then it would make sense to move to an imaging method based on dispersion such as phase contrast imaging.

4.3 Light detection

4.3.1 Time-resolved differential integrating photodetector

To measure the time development of light that has interacted with the trapped atoms, we use a homemade differential integrating photodetector. Much of the group's work relates to the generation and measurement of spin squeezing in atomic ensembles and quadrature squeezing of light fields. The detector we use is one of four built within the group in the last few years with the obvious goal of advancing the group's scientific goals, but it has also served to increase the knowledge base within the group on the techniques and technology related to ultra-sensitive detection of light - no single commercially available device can match the characteristics of this detector. The detector is designed to provide shot noise limited measurement of light pulses that have passed through an atomic ensemble. In order to cancel the classical noise on a laser signal, the detector should be used in a balanced configuration: i.e., equal (mean) intensity in both arms. However, to date we have used the detector unbalanced to measure the photon flux from the BEC, rather than the noise properties of this light. Here we give a brief summary of the properties of the detector; it was developed and tested primarily by Patrick Windpassinger, with guidance from Jörg Helge Müller, and built by Axel Boisen; further details may be found in [71].

The operation of the detector is described in the schematic diagram 4.11. The difference of the signals from two reverse-biased PIN photodiodes is AC coupled to an integrating circuit, whereupon near Gaussian pulses are produced by sending the signal through sequential high and low-pass filters. The PIN diodes have a good quantum efficiency of $\simeq 87\%$. The detector is shot-noise limited for photon fluxes greater than $\sim 10^5/\mu$s; i.e., the shot noise of the light predominates over the technical noise of the detector for fluxes over this value. While using the detector unbalanced means that classical fluctuations on the light are not cancelled, this does not affect the technical noise of the detector. As such, even if the detector is completely imbalanced

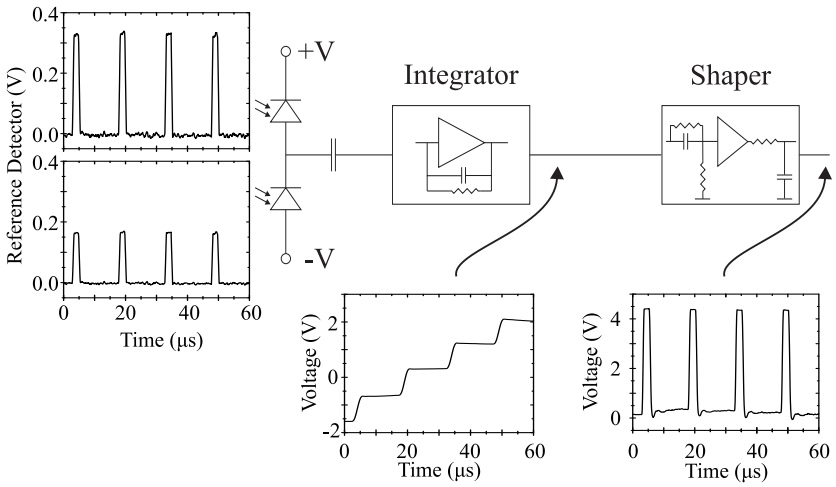

FIGURE 4.11: Schematic diagram of the differential, integrating photodetector. The difference signal between two PIN photodiodes is AC coupled to an integrating circuit. The signal is then shaped to produce approximately Gaussian pulses [71].

(i.e., all the light in a single port), the numbers quoted above hold true.

Photodetector pointspread punction

In order to use the detector to measure the time development of light scattered by the BEC, we need to quantify how the detector modifies the shape of an incident pulse. Figure 4.12 shows the time traces from a monitor photodiode and the detector of a pulse used to calibrate the response of the detector. The first thing to note is that the pulse measured by the photodetector has a rise and fall time on the order of 1 μs. More precisely, the detector pulse was fitted using a double error function model, yielding a fitted rms width of 315 ns for the underlying Gaussian. This agrees well with the theoretical response of the detector to an applied delta function: the pointspread calculated using the real component values is given by a Gaussian of width $\simeq$ 333 ns. Thus, measured pulses will be slightly broadened and delayed by approximately 1 μs. As we shall see in, the pulses we wish to measure are generally tens of microseconds long and exhibit reasonable shot to shot fluctuations, so the change is not of great significance. Another non-ideal feature of the detector is the slight overshoot at the top and bottom of the pulse. However, this overshoot is on the order of a percent and is most pronounced for step-functions which are never observed in experiment.

Photodetector calibration

The detector was calibrated by measuring its response to incident light pulses of known power. The result of the calibration is shown in figure 4.13. A calibrated

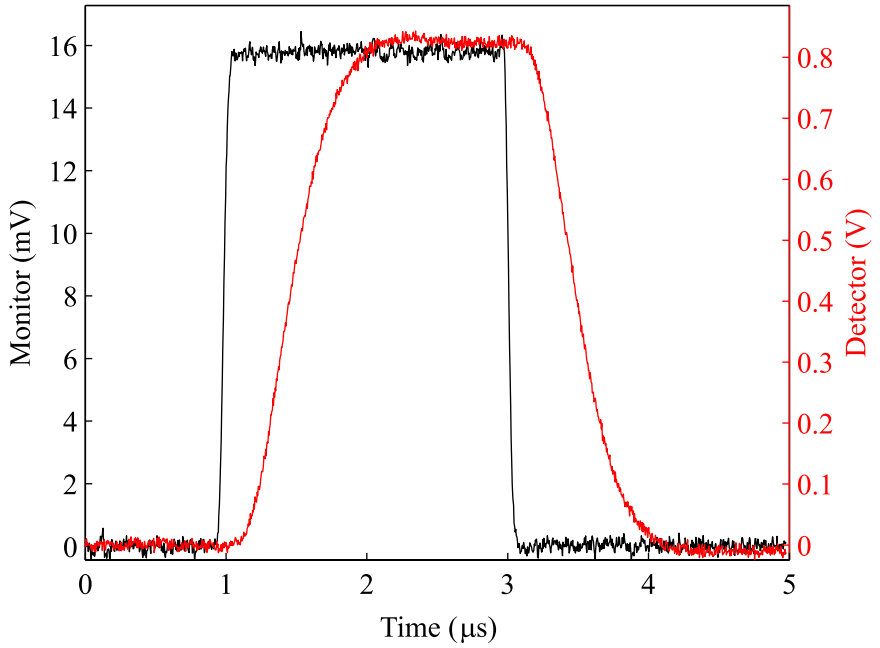

FIGURE 4.12: The pulse-shaping effect of the photodetector. A rectangular pulse recorded on a calibrated 'monitor' photodiode (black) is plotted with the response of the photodetector (red). The detector signal has a rise and fall time of $\simeq 1$ μs, and there is a slight overshoot of the voltage on the way up and the way down.

Newport model 840-C with detector head 818-SL was used as the power reference, with quoted accuracy of $\pm 1\%$ (at the 2 standard deviation level i.e., $\approx 95\%$ of measurements fall within this error interval).

4.3.2 CCD Camera

A CCD camera can be used as an alternative to the differential photodetector: clearly, it provides spatial resolution of the light scattered by the condensate, but under the right circumstances it can also offer a better signal to noise ratio if one's goal is to count photons. The camera is an Andor Ikon-M DU-934BRDD. The camera is well suited to our purposes: it is designed to offer very high quantum efficiency in the Near Infra-Red (NIR) with very low technical noise. The CCD chip is a back-illuminated, 'deep depletion' device centred on 800 nm. With cooling, the camera chip can reach temperatures as low as -100°C, but even without cooling fluid the operating temperature can at least reach -70°C. We typically use the camera at -60°C without any forced cooling fluid; for stability it is preferable to have the camera working well within its cooling range. At this temperature the chip produces less than $1e^{-}$/pixel/s in dark current. Instead, the read-out noise dominates given we

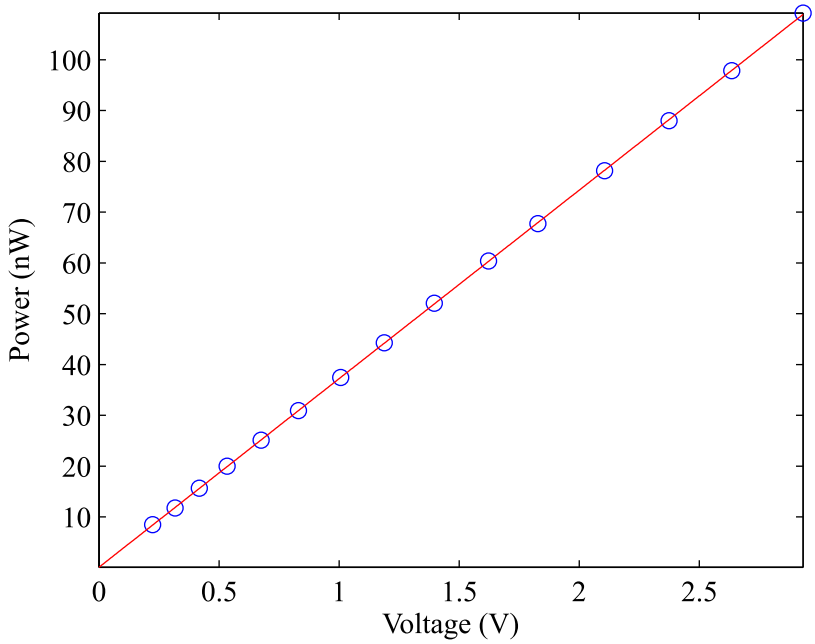

FIGURE 4.13: Calibration of the photodetector. Light pulses of known power were directed onto the detector and its response was measured. The calibration yielded a response of $37.12 \pm 1\%$ nW/V.

use the camera at its highest analogue to digital conversion rate of 2.5 MHz at 16 bit. The sensitivity at the highest gain setting of approximately $g^{-1} = 1.2\mathrm{e}^-/(\mathrm{A/D\ count})$, with a read-out noise of $9.7\mathrm{e}^-$ and a base level of 3348 counts. The CCD chip has 1024×1024 square pixels of area 13 $\mu\mathrm{m}^2$. The chip has nominally 94% quantum efficiency at 800 nm.

The camera is run on a third lab computer, taking its trigger from a TTL signal from the computer that controls the experiment. The software interface for this camera works very well, and did so more or less immediately. We use short programs coded in the Andor Basic language to control detection sequences containing several pictures.

CCD Calibration

The camera was calibrated at several different temperatures, and figure 4.14 shows the result for the CCD chip cooled to -60°C. The calibration yielded a total gain of $G = 1.24 \pm 1\%$ photon/(ADU).

It is possible to isolate the quantum efficiency of the camera chip by combining the above measurement with another measurement that relies on taking several flat-field pictures and making use of the statistical properties of the light. The observed

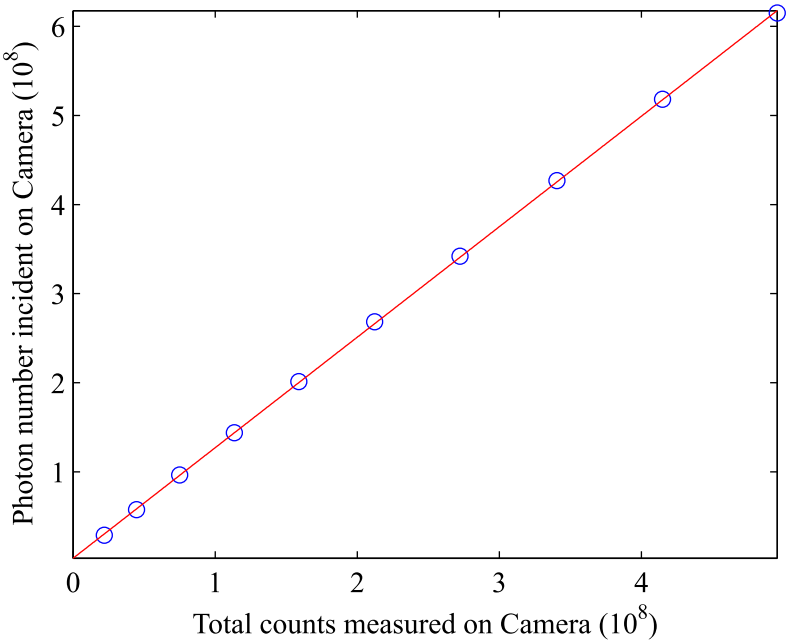

FIGURE 4.14: Calibration of the Andor CCD camera with chip cooled to -60°C. Light pulses of known power were directed onto the camera and its response was measured. The calibration yielded a response of $G = 1.24 \pm 1\%$ photon/(ADU).

number of counts of a given frame is given by $F = G\,N_{\text{ph}} = g\,Q_{\text{eff}}\,N_{\text{ph}}$, where Q_{eff} is the quantum efficiency of the CCD chip and N_{ph} is the number of photons incident on the chip. After taking two frames F_1 and F_2 where the intensity distribution is uniform and large compared to the technical noise and base level, one forms the quotient:

$$M = \frac{\text{var}(F_1 - F_2)}{\langle F_1 + F_2 \rangle} = \frac{\text{var}(F)}{\langle F \rangle}, \tag{4.16}$$

where the second equality follows from the fact that F_1 and F_2 are independent realizations taken under identical conditions so that $\langle F_1 F_2 \rangle = \langle F_1 \rangle \langle F_2 \rangle$, and that $\text{var}(F_1) = \text{var}(F_2) \equiv \text{var}(F)$ and $\langle F_1 \rangle = \langle F_2 \rangle \equiv \langle F \rangle$. (Note that in practice, one has to account for the technical noise of the camera in (4.16); therefore the variance of the readout noise was subtracted from the numerator and twice the base level was subtracted from the denominator.) If the light that illuminates the camera has Poissonian photon statistics, then the variance of the photoelectrons in the CCD chip is given by: $\text{var}(F) = g^2 \text{var}(Q_{\text{eff}} N_{\text{ph}}) = g^2 Q_{\text{eff}} \langle N_{\text{ph}} \rangle$. Thus, $M = g$ and the quantum efficiency may be obtained from the overall gain G of the camera determined above. Five flat field frames were taken, leading to 10 independent permutations. The mean inferred value of the gain and the standard error of the mean over the 10 realizations

was $g^{-1} = 1.219 \pm 0.007$ in agreement with the nominal value. The quantum efficiency at 795nm was found to be $Q_{\text{eff}} = 98.2 \pm 1\%$ (where again, the dominant error derives from the calibration of the power meter).

Chapter 5

Superradiance

5.1 Introduction

In a dense atomic ensemble, light scattered by an atom can interact with other atoms in the sample. This effect was noted in connection with the limiting density in a Magneto-Optical Trap in section 3.3.1, but it is also the general physical idea of the experimental results in the following chapters. Superradiance is a process whereby one or more initially unoccupied electromagnetic field modes first become weakly populated through spontaneous emission, and then amplified with the highest gain along the direction of greatest optical depth. This implies that the emission can be highly directional in elongated atomic ensembles, as opposed to normal spontaneous emission where atoms emit independently into approximately 4π. Furthermore, instead of exponential decay of the light at the natural decay rate Γ as one would expect from standard spontaneous emission, it is a characteristic feature of superradiance that the emission comes as a pulse of width $\propto 1/\Gamma N_{\mathrm{at}}$ and with a peak intensity $\propto N_{\mathrm{at}}^2$ where N_{at} is the number of atoms in the sample. These features are depicted in figure 5.1.

Superradiance has enjoyed periods of considerable interest since Dicke's seminal paper on the subject in 1954 [10]. Dicke considered the evolution of a system of two-level atoms where initially each atom was in the electronic excited state. Accordingly, we shall refer to this as 'Dicke superradiance' or 'superradiance in electronically inverted samples'; note that in the literature this form of superradiance is often called *superfluorescence* [72]. One might say that this form of superradiance had its heyday in the 1970s and early 1980s, with the bulk of experimental results coming in this period. The first realization was a pencil shaped sample of Hydrogen Fluoride in 1973 [73]. In general, such experiments involve optically pumping an elongated atomic sample to an electronically inverted state and recording the light emitted along the long axis of the sample with a photodetector (using an appropriate frequency filter to discriminate the longitudinal mode of interest).

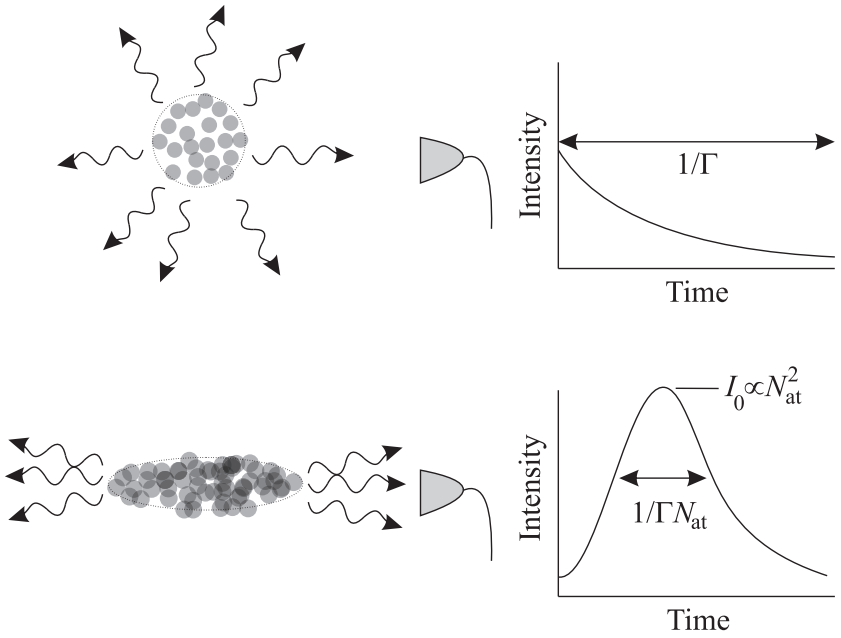

FIGURE 5.1: Illustration of the differences between standard spontaneous decay from a dilute atomic sample, and Dicke superradiance from a dense and asymmetric sample. Light within a certain solid angle is detected by a photodetector and the time-trace of the intensity in both cases is shown in the accompanying figures. Under the right conditions in a sufficiently dense sample, light is emitted as a superradiant pulse of width $\propto 1/\Gamma N_{at}$ and with a peak intensity $\propto N_{at}^2$ [74].

There are several aspects to superradiance that make it a very rich topic in physics. First and foremost, superradiance is the process whereby quantum fluctuations in the form of spontaneous emission are amplified by an atomic gain medium. In this way, the process is very similar to that in a laser, where the initial photon number statistics in a given mode are those of a thermal field but as the system evolves the statistics become Poissonian [75]. As such, it is often the case in treating superradiance that one is forced to break up the treatment into two parts: first one considers an initial 'quantum' phase whereby given modes of light are first populated, and then 'semi-classical' evolution where the populated modes are amplified according to the gain properties of the atomic medium. It is namely in the amplification phase that complications arise due to the need to consider the propagation of scattered light through the atomic medium. Another element in the mix is that, at first sight, the concept of 'coherence in spontaneous radiation processes' can be somewhat confusing because it appears to question cherished concepts like stimulated and spontaneous emission. As noted in [74], this confusion to a large extent arises from whether one chooses to analyse the system in the Schrödinger or Heisenberg pictures. In the Schrödinger

picture - as Dicke used - one seeks to solve for the state of the system in an N-atom generalization of the Wigner-Weisskopf theory of spontaneous emission for a single atom, whereas in the Heisenberg picture one focusses on a small number of atom and light field variables. Given the latter picture lies much closer to semi-classical treatments, we shall argue in these terms.

Superradiance has experienced a renaissance in recent years with the realization of Superradiant Light Scattering (SLS) in ultra-cold atomic ensembles. The first observation of SLS was reported in 1999 by Wolfgang Ketterle's group at the Massachusetts Institute of Technology (MIT) [76]. In this experiment, a cigar-shaped BEC confined in a magnetic trap was illuminated by a pulse of off-resonant light perpendicular to the long axis of the trap with the appropriate polarization to induce (primarily) Rayleigh scattering; i.e., the internal state of the atom after the scattering was left unchanged, but its motion changed due to the recoil associated with absorption and emission of a photon. As well as time-traces and pictures of the emitted superradiant pulses, time of flight images of the atomic density distribution were used to study the process. This experiment has led to many subsequent investigations by several groups [77, 78, 79, 80, 81, 82].

In this chapter, we introduce superradiant light scattering by an ultra-cold atomic sample. Where possible, it is our goal to draw comparisons between superradiant light scattering and superradiance in inverted samples. As such, we begin the chapter with a brief treatment of Dicke superradiance. This includes arguments justifying the use of a semi-classical approach in such problems, and gives the framework within which we can model fluctuations. Following an introduction to the physics of SLS, we present 1D Maxwell-Schrödinger equations that describe on a semi-classical level the time development of superradiant scattering by a BEC.

5.2 Dicke superradiance - the pendulum model

A useful way to view Dicke superradiance is through the motion of the ensemble's collective state on the Bloch sphere. For simplicity, we consider a 1D mean field model, such that we assume that neither the electric field amplitude or the atomic polarization varies over the length of the pencil-shaped sample. Furthermore, we consider emission into a single transverse mode. Following reference [74], the equations describing the evolution of the system are:

$$\frac{d\sigma_+}{dt} = i\omega_0\sigma_+ + \Gamma\sigma_+\sigma_3, \quad \frac{d\sigma_3}{dt} = -\Gamma\sigma_+\sigma_-. \tag{5.1}$$

ω_0 is the resonance frequency of the two-level atoms with excited and ground states given by $|e\rangle$ and $|g\rangle$, and decay from the excited state occurs at the rate Γ. The diagonal Pauli operator for the jth atom is given by:

$$\sigma_{3,j} = \frac{1}{2}(|e\rangle\langle e|_j - |g\rangle\langle g|_j). \tag{5.2}$$

The atomic raising and lowering operators are defined by:

$$\sigma_{+,j} = |e\rangle\langle g|_j \quad \text{and} \quad \sigma_{-,j} = |g\rangle\langle e|_j. \tag{5.3}$$

Equations (5.1) are expressed in terms of the collective raising, lowering, and diagonal Pauli operators, that are defined by:

$$\sigma_q = \sum_j \sigma_{q,j}, \quad \text{for} \quad q = +,-,3. \tag{5.4}$$

It is possible to simplify the solution of (5.1) by treating the operators as classical variables with initial values sampled from appropriate probability distributions. This idea corresponds to the fact that a thermal state of the electromagnetic field can be represented by a fluctuating classical field with given statistics. The term that initiates the dynamics in the (5.1) is $\Gamma\sigma_+\sigma_-$ - it represents the spontaneous emission of a photon. It turns out that statistics governing a measurement of $\sigma_\pm$ (through its quadratures) are those consistent with a Gaussian phase space distribution of the two variables α and ϕ. That is, $\langle\sigma_-(t=0)\rangle = \alpha\exp(i\phi)$, with the respective probability distributions given by:

$$Q(\phi) = \frac{1}{2\pi}, \tag{5.5}$$

$$P(\alpha^2) = \frac{\mathrm{e}^{-\alpha^2/N_{\mathrm{at}}}}{N_{\mathrm{at}}}. \tag{5.6}$$

Note that $\langle\alpha^2\rangle = N_{\mathrm{at}}$. With these designations, and denoting the now classical variables by σ_-^{cl} etc, the equations (5.1) describe the rotation of the Bloch vector, while preserving its length: $\sigma_+^{\mathrm{cl}}\sigma_-^{\mathrm{cl}} + (\sigma_3^{\mathrm{cl}})^2$.

With this motivation, we introduce the new variables θ and ϕ by:

$$\mathrm{e}^{-i\omega_0 t}\sigma_+^{\mathrm{cl}}(t) = \frac{N_{\mathrm{at}}}{2}\sin(\theta(t))\mathrm{e}^{i\phi}, \tag{5.7}$$

$$\sigma_3^{\mathrm{cl}}(t) = \frac{N_{\mathrm{at}}}{2}\cos(\theta(t)), \tag{5.8}$$

which upon substitution into (5.1) yield:

$$\frac{d\theta}{dt} = \frac{\Gamma N_{\mathrm{at}}}{2}\sin(\theta), \tag{5.9}$$

$$\frac{d\phi}{dt} = 0. \tag{5.10}$$

A diagram representing the Bloch sphere is shown in figure 5.2. The initial condition θ_i may be obtained from expressing $\langle\sigma_-\rangle$ in terms of the new variables via (5.6) and (5.7); the mean 'tipping angle' is given by $\bar{\theta}_i = 2/\sqrt{N_{\mathrm{at}}}$. Equation (5.9) may be

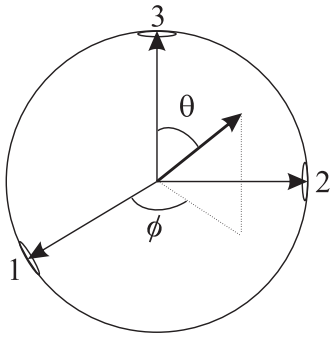

FIGURE 5.2: The Bloch sphere, where an arbitrary collective atomic state is represented as a vector in an abstract space identified by the axes $1,2,3$. The ensemble in the fully excited state $|e,e,\ldots,e,e\rangle$ corresponds to the vector pointing upwards, and $|g,g,\ldots,g,g\rangle$ corresponds to the vector pointing down. If the dynamics is 'coherent', the length of the vector does not change.

integrated directly to give:

$$\begin{aligned}\int_{\theta_i}^{\theta}\frac{d\theta'}{\sin\theta'} &= \int_0^t \frac{\Gamma N_{\rm at}dt'}{2}\\ \tan\left(\frac{\theta}{2}\right) &= \tan\left(\frac{\theta_i}{2}\right)e^{\Gamma N_{\rm at}t/2},\end{aligned} \tag{5.11}$$

and the radiated intensity is given by:

$$\begin{aligned}I(t) &= -\hbar\omega_0\frac{d\sigma_3^{\rm cl}}{dt} = \frac{\hbar\omega_0\Gamma N^2}{4}\sin^2(\theta)\\ &= \frac{\hbar\omega_0\Gamma N^2}{4}\cosh^{-2}\left[\frac{\Gamma N_{\rm at}}{2}(t-t_D(\theta_i))\right],\end{aligned} \tag{5.12}$$

with the delay time of the pulse given by:

$$\tau_P(\theta_i) = -\frac{2}{\Gamma N_{\rm at}}\ln\left(\frac{\theta_i}{2}\right). \tag{5.13}$$

The mean delay time is given by:

$$\langle\tau_P\rangle = \frac{1}{\Gamma N_{\rm at}}\ln(N_{\rm at}). \tag{5.14}$$

Equation 5.11 has the features noted in figure 5.1: a bell-shaped curve with a peak intensity proportional to the square of the number of atoms, and a width inversely proportional to the number of atoms multiplied by the spontaneous emission rate. Physically, we can view it as the irreversible falling of a pendulum through a viscous fluid. The non-zero initial condition θ_i, representing the effect of spontaneous emission on the atomic polarization, is necessary to instigate the evolution. It

is interesting to note the initial exponential growth of θ in (5.11); this is characteristic of the amplification of light through a gain medium where propagation effects are not accounted for.

5.3 Superradiant light scattering by a BEC

Superradiant light scattering from an ultra-cold atomic sample is self-stimulated Raman scattering that is initiated by spontaneous emission. Like superradiance in electronically inverted samples, it is a process whereby an initially unoccupied electromagnetic field mode becomes weakly populated through spontaneous emission, and then amplified by stimulated scattering within a dense atomic medium. In SLS, the electronically inverted sample is replaced by an atomic ensemble 'dressed' by a pump beam. Initially, the pump is spontaneously scattered by the atoms, and subsequently it acts as a reservoir as photons are coherently scattered from the pump into the superradiant mode(s). Note the strong connection with superradiance in inverted samples, except that the natural decay rate Γ is replaced by the spontaneous scattering rate, which we shall refer to as R:

$$R = \frac{\Gamma}{2I_s} \frac{I}{1 + I/I_s + (2\delta/\Gamma)^2}. \tag{5.15}$$

Again, some kind of geometrical asymmetry in the sample plays a role in determining which transverse mode sees the most gain. Typical experimentally produced BECs are cigar-shaped so that the dominant modes are along the long axes where the optical depth is greatest; these are the so-called 'endfire modes'. We use 'Raman scattering' in the general sense that the states before and after a scattering event are different - whether by the fact that only the external degrees of freedom change in the scattering process, or that the internal state of the atom also changes. In the literature, the former process is referred to as Rayleigh superradiance and the latter as Raman superradiance.

Given that the process is instigated through spontaneous scattering of pump photons, several modes compete for gain in the atomic medium. Figure 5.3 shows a cartoon of a common experimental configuration where a BEC is pumped from the side by a beam that is uniform in intensity over the sample; although the results we present pertain to an end-pumped BEC, it is useful to consider the side-pumped configuration first because the pump and superradiant modes are clearly distinct. Photons are scattered out of the pump beam according to their dipole emission patterns, and the polarization of the pump is chosen so as to drive σ-transitions (choosing the natural quantization axis along the direction of the bias field). It is evident that σ-transitions are most probable along the long axis of the condensate. Thus, photons are spontaneously scattered predominately within a cone centred on the long axis of the condensate. As such, several transverse modes within this cone are weakly populated

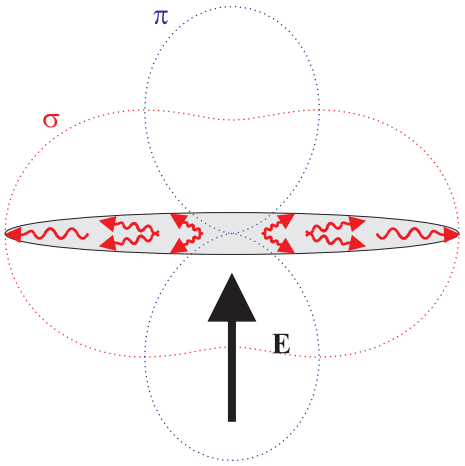

FIGURE 5.3: Cartoon depicting how SLS is initiated. A pump beam **E** that is uniform over the spatial extent of a prolate BEC is applied, causing photons to be spontaneously scattered according to the dipole emission patterns for circularly (σ) and linearly (π) polarized light with respect to a quantization axis that is oriented along the long axis of the BEC (i.e., along the bias field). Given the polarization of the pump is chosen so as to drive σ-transitions with respect to this quantization axis, photons will be predominantly scattered within a cone centred on the long axis of the trap. Gain competition between these modes determines the observed far field intensity distribution.

at random times by this process. Under the right conditions, the intensity of light that arises from stimulated scattering increases exponentially as it propagates through the atomic medium [83]. Thus, the physical picture is one where the final light intensity distribution is strongly dependent on gain competition between an initially small and random population of several transverse modes.

Clearly, the diffraction properties of the BEC play a role in the far-field intensity distribution we observe in experiment. The Fresnel number of the sample is a useful figure of merit for qualifying the diffraction properties of the sample. It is given by:

$$F = \frac{\pi w^2}{\lambda L}, \tag{5.16}$$

where w and L are the radius and length respectively of the (assumed cylindrical) atomic sample, or alternatively w gives the radius of an aperture or waist of a Gaussian beam and L the distance to the plane of observation. If $F \ll 1$, the scattered light is confined to a narrow cone in the forward direction but this comes with the complication of introducing a strong radial dependence on the transverse modes[1]. Alternatively, if $F > 1$, the axial modes have little radial dependence but non-axial modes are supported [84].

[1]Note that $F \ll 1$ marks the region of applicability of Fraunhofer diffraction.

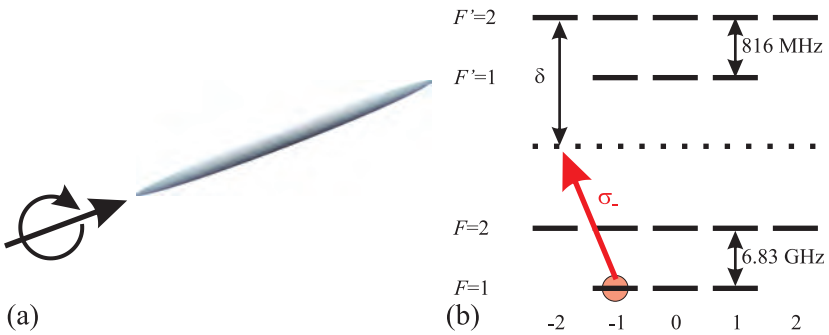

FIGURE 5.4: Coupling scheme used to induce SLS. (a) A circularly polarized pump beam is applied along the long axis of a trapped BEC. (b) The light drives the $F = 1, m_F = -1 \rightarrow F' = 2, m_F = -2$ transition and is detuned by δ.

It is clear from the above discussion that SLS is in general a multi-mode process, and the appearance of a predominant intensity peak in elongated samples is the result of complex dynamics. Indeed, the study of SR without an *a priori* single mode assumption is the subject of on-going research [85, 86]. As mentioned in 5.1, the standard approach to study superradiance or superradiant light scattering in extended samples is to consider an initial 'quantum' phase followed by a one-dimensional 'semi-classical' evolution whereby an assumed single mode of light is amplified [83, 87]. In our experimental realization of SLS, the results are well-described by such an approach, and we now describe the general experimental configuration so as to motivate the associated 1D model. We defer the discussion of the early phase of superradiance, and its measurable consequences, to chapter 7.

5.4 Experimental configuration

The trapped BEC is illuminated by a pulse of off-resonant light applied along the long axis of the condensate. The light is right-hand circularly polarized and drives the σ_- transition between $F = 1$, $m_F = -1$ and $F' = 2$, $m_F = -2$; it is detuned by a frequency δ from this transition. Figure 5.4 shows these features. This choice of transition and detuning approximates very well a two-level atom driven coherently by an applied laser field. The single particle spontaneous scattering rate R lies in the range $1 - 16 \times 10^3$ s^{-1} for the experimental parameters considered. An atom in the excited to $F' = 2$, $m_F = -2$ may decay to three levels $F = 2$, $m_F = -2, -1$ and $F = 1$, $m_F = -1$ with probabilities $1/3$, $1/6$ and $1/2$ respectively.

With the condensates used in experiments, the Fresnel number of the sample is approximately one, implying that the main aspects of the system's dynamics may be described by a one dimensional theory. Such a choice means that light scattered within the sample retains its general transverse distribution along the length of the

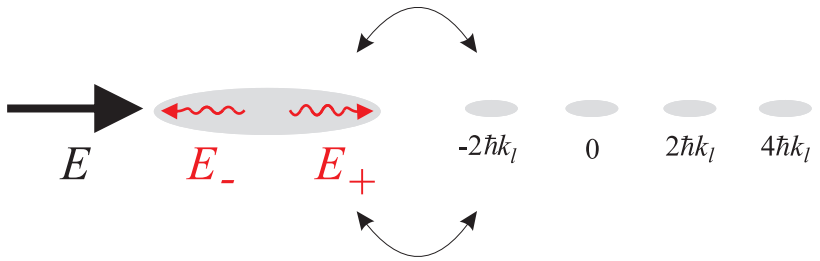

FIGURE 5.5: A BEC end-pumped by laser field E exhibits two endfire modes E_+ and E_-. Scattering of a pump photon into E_- leads to the atom gaining $2\hbar k_l$ in momentum, and because the atom returns to the same internal ground state after the scattering - Rayleigh scattering - sequential scattering can occur leading to the populating of several forward momentum orders. If the pump is sufficiently intense, the Kapitza-Dirac regime can arise where atoms in the zeroth momentum order absorb back-scattered light and re-emit into the forward direction.

sample, and furthermore that this distribution has little transverse variation; i.e., the light within the sample is well-described by a single, approximately flat, transverse mode.

In the end-pumped geometry, light is predominantly backscattered by the atomic ensemble leading to the concomitant scattering of atoms into forward momentum orders separated by $2\hbar k_l$. As can be inferred from figure 5.5, an atom with momentum $2\hbar k_l$ arises from the destruction of a pump photon E and the creation of a backscattered photon E_-. Because an atom returns to its initial internal state after scattering a photon, the process can repeat and with appropriate parameters one can generate several diffracted orders in the forward direction. For single particle scattering rates much smaller than the recoil frequency $\omega_r = 2\pi\times 3.6$ kHz, scattering to higher atomic momentum orders occurs sequentially on a time scale $\sim \tau_r = 2\pi/\omega_r$. When $R \sim \omega_r$, there is sufficient gain for atoms to be back-scattered into negative momentum orders, i.e., the Kapitza-Dirac regime where atoms absorb back-scattered light and re-emit into the forward direction, as shown in figure 5.5.

5.5 Maxwell-Schrödinger equations

The starting points are the Schrödinger equation for the ground state of a two level atom in the presence of an off-resonant light field, and the wave equation with a polarization source term [88, 89]:

$$i\hbar\frac{\partial\psi}{\partial t} = -\frac{1}{2M}\nabla^2\psi + \frac{1}{\hbar\delta}(\mathbf{d}\cdot\mathbf{E}^{(-)})(\mathbf{d}\cdot\mathbf{E}^{(+)})\psi, \tag{5.17}$$

$$c^2\nabla^2\mathbf{E}^{(\pm)} - \frac{\partial^2\mathbf{E}^{(\pm)}}{\partial t^2} = \frac{1}{\varepsilon_0}\frac{\partial^2\mathbf{P}^{(\pm)}}{\partial t^2}, \tag{5.18}$$

where the total electric field is given by $\mathbf{E} = \mathbf{E}^{(+)} + \mathbf{E}^{(-)}$, $\mathbf{d}$ is the atomic dipole moment, M the mass, and the polarization is given by:

$$\mathbf{P}^{(+)}(\mathbf{r},t) = -\frac{\mathbf{d}\,|\psi(\mathbf{r},t)|^2\,\mathbf{d}\cdot\mathbf{E}^{(+)}(\mathbf{r},t)}{\hbar\delta}, \quad \mathbf{P}^{(-)} = \mathbf{P}^{(+)*}. \tag{5.19}$$

The excited electronic state has been adiabatically eliminated given the assumed low rate of real excitations. These equations give a self-consistent description of an ensemble of two-level atoms interacting with a classical electric field. The applied field polarizes the atoms according to quantum mechanics, the dipole moments of these atoms are summed to give the macroscopic polarization $\mathbf{P}(\mathbf{r},t)$, and this enters the wave equation as a source term [90]. We assume that the polarization of the atoms is linear in the applied electric field, and therefore that there is no saturation of the atomic transition - a point which needs to be confirmed as a matter of self-consistency in the solution of the problem. Indeed, for the parameters considered in this work, this condition is always fulfilled. At this stage, we neglect the harmonic trapping potential and the mean field interaction term representing collisions between atoms.

In order to solve the above equations, we need to make some approximations. Based on the discussion of the previous section, it is reasonable to ignore the transverse spatial variation of the condensate wavefunctions and electric fields. As such, we make the ansatz:

$$\psi(z,t) = \sum_{m=2n} \psi_m(z,t)\mathrm{e}^{-i(\omega_m t - m k_l z)}, \tag{5.20}$$

and

$$\mathbf{E}^{(+)}(z,t) = \mathbf{e}_{+1}\left[E_+(z,t)\mathrm{e}^{-i(\omega t - k_l z)} + E_-(z,t)\mathrm{e}^{-i(\omega t + k_l z)}\right]. \tag{5.21}$$

$\psi_m(z,t)$ is the *slowly varying amplitude* for the atomic momentum order $m = 2n$ for integer n; the concomitant recoil frequency is given by $\omega_m = m^2\omega_r$, with the recoil frequency $\omega_r = \hbar k_l^2/(2M)$. E_+ and E_- are slowly varying amplitudes for the forward and backward travelling electric fields, and $\mathbf{e}_{+1}$ denotes the unit polarization vector for right-hand circular light. Note that in this formalism, we cannot distinguish between incident and forward scattered light - E_+ contains both components. Such an identification is necessary in a 1D treatment, which assumes that the incident and scattered fields occupy the same light mode. This identification is supported somewhat by the fact that the pump is partially mode matched to the BEC, as we describe in 6.2.

Upon substitution of equation (5.20) into (5.17) we look for terms that oscillate at $(\omega_m t - m k_l z)$. Similarly we substitute (5.21) into (5.18) and look for terms with the common phase $(\omega t \pm k_l z)$. For the light fields, we make the Slowly Varying Envelope Approximation (SVEA). The content of the approximation is to neglect derivatives of the slowly varying envelopes E_+, $E_-$with respect to terms involving the derivatives

of the fast oscillating exponentials. That is, we assume:

$$\left|\frac{\partial E_\pm}{\partial t}\right| \ll |\omega_l E_\pm| \qquad \left|\frac{\partial E_\pm}{\partial z}\right| \ll |k_l E_\pm|\,. \tag{5.22}$$

To simplify the ensuing equations, we rescale the position and time variables such that $\xi = k_l z$ and $\tau = 2\omega_r t$. The light field amplitudes are rescaled according to:

$$E_\pm = e_\pm \sqrt{\hbar\omega_l k_l / 2\varepsilon_0 A},$$

with A the cross-sectional area of the (assumed cylindrical) BEC. Finally, we obtain:

$$\begin{aligned} i\frac{\partial \psi_m(\xi,\tau)}{\partial \tau} = &-\frac{1}{2}\frac{\partial^2 \psi_m(\xi,\tau)}{\partial \xi^2} - im\frac{\partial \psi_m(\xi,\tau)}{\partial \xi} \\ &+\Lambda e_-^*(\xi,\tau)e_+(\xi,\tau)\psi_{m-2}(\xi,\tau)\mathrm{e}^{+2i(m-1)\tau} \\ &+\Lambda e_+^*(\xi,\tau)e_-(\xi,\tau)\psi_{m+2}(\xi,\tau)\mathrm{e}^{-2i(m+1)\tau} \\ &+\Lambda(|e_+(\xi,\tau)|^2 + |e_-(\xi,\tau)|^2)\psi_m(\xi,\tau), \end{aligned} \tag{5.23}$$

$$\begin{aligned} \frac{\partial e_+(\xi,\tau)}{\partial \xi} = &-i\frac{\Lambda}{\chi}\sum_{m=2n} e_-(\xi,\tau)\psi_m(\xi,\tau)\psi_{m-2}^*(\xi,\tau)\mathrm{e}^{-2i(m-1)\tau} \\ &+e_+(\xi,\tau)\,|\psi_m(\xi,\tau)|^2\,, \end{aligned} \tag{5.24}$$

$$\begin{aligned} \frac{\partial e_-(\xi,\tau)}{\partial \xi} = &+i\frac{\Lambda}{\chi}\sum_{m=2n} e_+(\xi,\tau)\psi_m(\xi,\tau)\psi_{m+2}^*(\xi,\tau)\mathrm{e}^{+2i(m+1)\tau} \\ &+e_-(\xi,\tau)\,|\psi_m(\xi,\tau)|^2\,, \end{aligned} \tag{5.25}$$

with the coupling constants $\Lambda = |\mathbf{d}|^2\,\omega_l k_l / 4\omega_r \hbar\delta\varepsilon_0 A$ and $\chi = ck_l/2\omega_r$. Retardation effects have been neglected in equations (5.24) and (5.25) given the length of the condensate $L = 130\ \mu$m, which allows us to discard a time derivative term. However, it is worth noting that with the definition of a retarded time (in unscaled quantities): $t' = t - z/c$, the result can be made exact [74].

5.6 Four wave mixing

Equations (5.23), (5.24) and (5.25) describe a Raman interaction where a ladder of momentum states are coupled by two counter-propagating light fields. The first two terms in (5.23) describe the quantum diffusion and the momentum displacement induced by recoil respectively of the wavefunction envelopes. In our parameter regimes and interaction times, and given by construction these envelopes are slowly varying, these terms contribute very little to the dynamics. Terms three and four describe the coupling to the nearest momentum states via exchange of photons between e_+ and e_-. The final terms in (5.23) account for phase rotation of the matter wave due to the

light shift. Equations (5.24) and (5.25) have terms equivalent to the coupling terms in (5.23). Specifically, the growth of e_- occurs with the corresponding growth of recoiling atoms ψ_{m+2} and the decrease of e_+ photons and ψ_m atoms. The last terms in equations. (5.24) and (5.25) describe the effect on light of the slowly varying refractive index due to the large scale atomic density distribution. If one disregards the quantum diffusion and the momentum displacement terms in equation (5.23), these equations demonstrate the symmetry of a four wave mixing process.

The equations (5.23)-(5.25) describe a non-linear process: the scattering of atoms depends on the local intensity of light, and correspondingly the scattering of photons depends on the local atomic density. In general, a standing wave of light will arise with spatial period $\lambda/2$, but comprised of several frequency components shifted by multiples of $4\omega_r$ - these are represented by the exponential terms $\exp(\pm 2i(m\pm 1)\tau)$ in (5.24) and (5.25). Given that the effect on wavelength of these frequency changes is insignificant over the spatial extent of the condensate, these changes will manifest themselves as amplitude and phase modulation of the standing wave along the length of the sample that will change dynamically. A similar picture arises on the atomic side: condensates with different momenta interfere, and given we consider Rayleigh scattering where the internal state of the atoms remains unchanged, this leads to a density modulation[2]. In general, this matter-wave grating is comprised of as many spatial periods and oscillating frequencies as there are populated momentum orders. In the regime of weak excitation, corresponding to a low single particle scattering rate R, only ψ_0 and ψ_2 become significantly populated leading to a spatial period of $\lambda/2$. This leads to the very appealing physical picture of the atomic density modulation comprising a Bragg mirror from which light is 'reflected'.

This point of view is supported by figure 5.6, which shows time of flight absorption images of an unperturbed BEC and a BEC exposed to pump beam aligned with its long axis. In this case, the pump beam was approximately collimated and much broader than the BEC. It is evident that it is primarily atoms centred around zero transverse momentum that are diffracted into the $2\hbar k_l$ momentum state. Note that it is reasonable to relate the transverse density distribution after time of flight to the in-trap momentum distribution because the expansion along the radial direction is ballistic; such a statement about expansion in the axial direction would need qualification given the effects of mean-field repulsion, as noted in section 3.4.2. In a simple picture, for incident plane waves, the Bragg condition for light to be backscattered is fulfilled for those atoms with close to zero transverse momentum. One can draw the analogy to diffraction by an acousto-optic modulator: typically maximum diffraction

[2]It is perhaps questionable to call the diffracted orders 'condensates', but it has been shown that the different momentum orders generated in such a process are phase coherent [91]. In principle in the cited reference the component shifted in momentum arose from a seeded process - rather than one instigated by spontaneous emission - but this was only necessary to provide a phase reference for the colliding condensates.

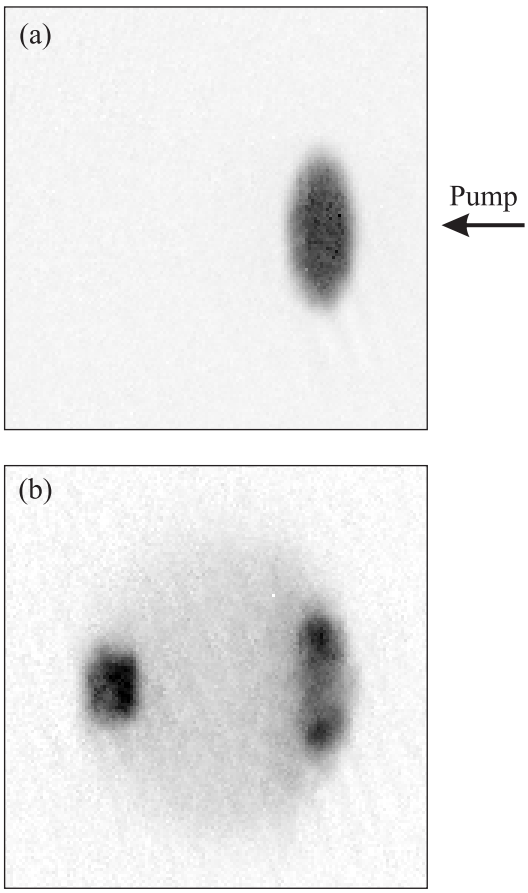

FIGURE 5.6: Illustration of a Bragg condition in superradiant scattering for weak pumping ($R \ll \omega_r$). A pump beam that was much broader than the transverse extent of the BEC was flashed on the magnetically trapped atoms; the trapping potential was extinguished immediately after the interaction. (a) shows the unperturbed BEC, (b) shows a BEC that was dressed by the pump beam; both are absorption images taken after 45 ms time of flight. With the pump well-aligned, the diffraction to $2\hbar k_l$ occurs primarily for atoms centred around zero transverse momentum.

efficiency into one of the first orders occurs with the appearance of a narrow stripe missing from the zero-order beam.

Chapter 6

Coupled wave dynamics in superradiant light scattering

6.1 Introduction

Here we present experimental results relating to the semi-classical evolution of superradiant light scattering from a Bose-Einstein condensate, and using the 1D Maxwell-Schrödinger equations of section 5.5, we simulate the system and find very good agreement with experiment over a wide parameter range. Whereas most earlier experimental studies of superradiant light scattering have largely drawn on time of flight images of the atomic density distribution, we study the process primarily through the time-resolved detection of superradiant pulses emitted by the sample [76, 79, 77, 78, 81, 82].

While the general configuration of the experiment was described in the previous chapter, we begin with a more practical account of the experimental set-up, and the forms of data we obtain. Subsequently we present results relating to some general features of superradiant light scattering. As noted in 5.1, it is a characteristic feature of superradiance that the peak intensity of the first superradiant scales with the square of the number of atoms in sample; we begin with this feature. We then present a systematic study of the effects of pump detuning on the process while the single particle scattering rate is kept constant. In this way, we investigate the effect of the detuning of the pump beam in the process, and move between the case where the pump beam remains essentially undepleted by the scattering, to the situation where superradiant scattering is 'clamped' by a lack of photons in the pump beam. Crucial to these dynamics is the structure that builds up along the long axis of the condensate, demonstrating characteristics from Dicke superradiance from extended samples [92]. Through experiments and simulations we show that collective atom light coupling leads to the self-organized formation of dynamic Bragg gratings within the sample. These gratings lead to an efficient back-scattering of pump photons and

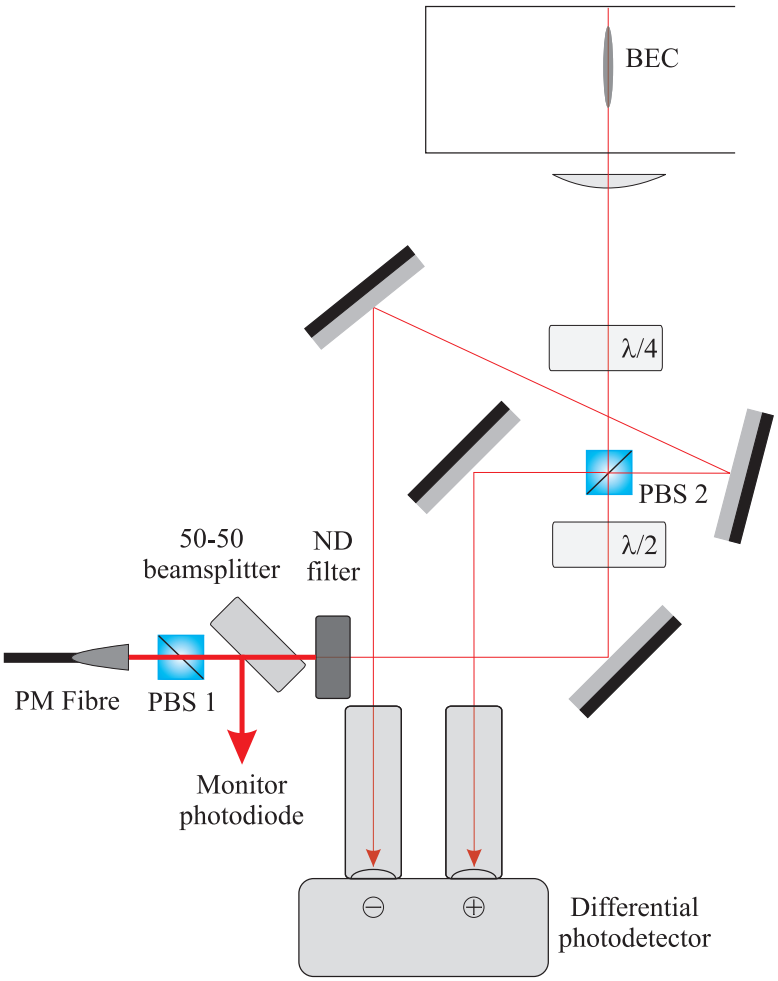

FIGURE 6.1: Schematic probing set-up for superradiant light scattering experiments (not to scale!). Pulses from a PM fibre with a pure circular polarization are focussed onto a magnetically trapped BEC. The superradiant pulse is back-scattered with the same polarization and is thus reflected by the polarizing beam splitter PBS 2, then directed on to a differential integrating photodetector. To minimise this background scattered light recorded by the photodiode, a portion of the input beam is directed onto the 'subtracting' port of the differential photodetector so as to cancel this background signal.

optical resonator structures within the BEC.

6.2 Experimental set-up for SLS

Here we provided a brief summary of the experimental set-up followed by a more detailed description of the important features that have not been covered in earlier chapters.

Superradiant Rayleigh scattering is induced in a trapped BEC by flashing it with a pulse of off-resonant light along the long axis of the condensate, as shown in figure 6.1. The BEC is generated by evaporatively cooling a cloud of ^{87}Rb atoms in the $|F = 1, m_F = -1\rangle$ hyperfine state in a Ioffe-Pritchard magnetic trap. Except for experiments where the number of atoms is intentionally varied, cigar shaped condensates contain 1.35×10^6 atoms, with in-trap Thomas Fermi radii of $\rho_0 = 6.4$ and $z_0 = 65$ μm in the radial and axial directions respectively and with no discernible thermal fraction. The pump light is detuned by a variable amount from the $|F = 1, m_F = -1\rangle \rightarrow |F = 2, m_F = -2\rangle$ transition on the D1 line of ^{87}Rb at 795 nm, and circularly polarized with respect to the long axis of the trap (see figure 5.4). All data presented is for red detunings ($\delta = \omega_l - \omega_0 < 0$); rectangular pump pulse envelopes; and where the atoms are interrogated in-trap, with the trapping potential extinguished immediately after the end of the pump pulse. The pulses are produced by an acousto-optic modulator before the fibre, and the beam was focused to a waist of 13 μm at the center of the condensate with negligible change of beam size over the length of the BEC. Light is back-scattered by the sample in the same polarization as the input beam, and thus the backward travelling light is reflected by the polarizing beamsplitter PBS 2, then directed onto a sensitive PIN diode photodetector. The detector, with a bandwidth of 400kHz, is shot-noise limited for photon fluxes greater than 10^5 photons/μs. To avoid back reflections from optics and cell windows that seed the process, the pump beam is inserted at a slight angle (less than 2°). Pictures of the atoms are obtained after 45ms time of flight by resonant absorption imaging.

The pump beam is shaped, filtered and directed onto the BEC from a solid breadboard mounted next to the SMOT platforms. The pump beam is spatially filtered by a single-mode, polarization maintaining fibre, and outcoupled to form a very weakly diverging beam with waist ~ 0.65 mm. The polarization of the beam is filtered by a polarizing beamsplitter (PBS 1) straight after the fibre. Approximately half the beam power is split using a 50-50 beamsplitter and directed onto a calibrated, fast-photodiode used to monitor the input pulses. The power in the beam is considerably reduced using a collection of Neutral Density (ND) filters. The beam is directed through a second polarizing beamsplitter (PBS 2), oriented so as to minimise the reflected component for P-polarized light. Before PBS 2, the beam passes through a half-wave plate mounted in a precision rotation stage so that a well-controlled portion of the beam can be split from the beam. This light is directed onto the 'subtracting' port of the differential photodetector, and is set in the absence of atoms to cancel stray light scattered by the science cell and other optics the pump beam passes through. The pump beam passes through a zero-order quarter wave-plate oriented so as to maximize superradiant Rayleigh scattering. Finally, the light is focused onto the BEC using an AR-coated achromat with nominal focal length f=60 mm. The lens is mounted such that it can be tilted arbitrarily and translated in three directions. With the exception of a Newport 25 mm linear translation stage used to adjust the position

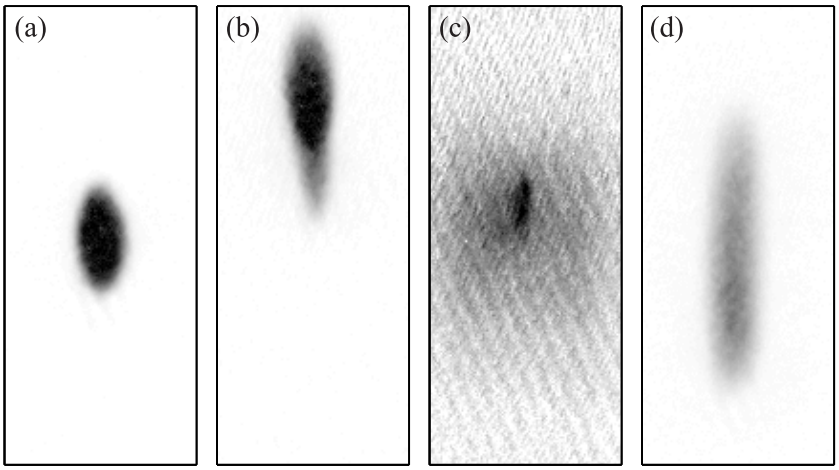

FIGURE 6.2: Time of flight absorption images from the initial alignment of the pump beam, which propagated in the images from right to left. A far red-detuned beam (830 nm) was directed onto the BEC in the magnetic trap leading to a modification of the trapping potential. The bare BEC is shown in (a); the effects of poor alignment of the dipole beam led to displacement of the trap centre (b) and excessive heating (c) given the non-adiabatic turn-on of the dipole beam. (d) shows the beam well-aligned leading to the trapping of the BEC in a potential that was much tighter transversely, leading to an exaggerated expansion after time of flight. (Note that for clarity the greyscale was modified in (c) given the much reduced optical depth of the strongly heated cloud.)

of the focus along the long axis of the BEC, all of the optics mounts used in transporting the pump beam to the BEC are made by S.Maier GmbH and are of a very high quality: it has never been necessary to realign the pump beam unless changes were made to the set-up.

We note a few points that are pertinent to the above description.

Given it is not possible to measure the beam waist at the position of the atoms using standard methods, it was measured using a nominally identical lens (i.e., the same model) at approximately the same position in the beam path as it is used in practice. The results agreed very well with predictions from Gaussian beam optics. The beam waist was measured to be 13.2 μm by recording the beam's intensity profile on the Andor CCD camera at several positions around the focus; given that this is not an *in situ* measurement, we quote 13 μm as above.

Due to the sensitivity of superradiant light scattering to seeding from stray scattered light, maximizing SLS it is not necessarily an accurate measure of good alignment, so instead we employed a method using a far red detuned laser to perform the initial alignment of the pump beam to the BEC. The light was provided by a laser diode free running at 830 nm that was coupled through the pump fibre and optics. Given that the focusing lens is an achromat, the focal point of the dipole beam was very close to the pump beam. By turning the dipole beam on non-adiabatically, we

obtained a sensitive probe of the beam's alignment. First, we optimized the position of the lens to see the greatest possible (destructive) effect: given the non-adiabatic turn-on, if the dipole beam is in the same general neighborhood as the magnetic trap bottom, the shift in effective trapping potential shifts leads to heating of the trap. This is evident in figure 6.2. Once the dipole beam was well-aligned, so that the two trap centres overlapped, the effective trapping potential was much tighter in the transverse direction. A such, the BEC expanded more quickly in the transverse direction and this effect was easily detected in time of flight absorption imaging.

Given the sensitivity of the superradiant process to atom number, this was monitored closely during experiments. Clearly, it was important to have the experiment cycling so that the set-up was 'thermalized'. Typically, five realizations of a given set of experimental parameters were performed, and the size of the BEC (using the 'real-time' fitting of Thomas Fermi profiles within the Labview program controlling the absorption imaging camera), and hence the number of atoms in the condensate (see 3.4.3), was monitored before and after. At times, the final cut of the RF evaporation were be changed by a few kHz to achieve the desired size of BEC.

6.3 Forms of data and simulations

Figure 6.3 illustrates the different forms of data and the level of agreement we obtain between experiment and simulations.

Figure 6.3(a) shows experimental and simulated time traces for high and low pump powers, with the corresponding atomic distributions shown in (c) and (d). As a reference, the time of flight absorption image of an unperturbed BEC is shown in (b).

Figure 6.3(d) shows the low pump power case case, with single particle scattering rate $R = 2.2 \times 10^3$ s^{-1}, where the transfer is limited to the first order. At such low values of R, it is observed experimentally that scattering to subsequent orders occurs on a slow time scale, so that in principle the appearance of the next diffraction order coincides with a second superradiant pulse. In general, however, there is not a one-to-one correspondence between multiple light pulse emission and cascading transfer to higher momentum states in extended sample Rayleigh SLS because one part of the sample can be driven by light from another part. This *ringing* behaviour is a general feature of superradiance in extended samples [92].

When the pump is strong, that is when $R \sim \omega_r$, there is sufficient gain for atoms to be scattered into negative momentum orders. This is the Kapitza-Dirac regime where atoms absorb back-scattered light and re-emit into the pump beam. This is shown in figure 6.3(c). An asymmetry in distance between forward and backward scattered atoms and the center of the original condensate after time of flight is also visible; this has been observed previously in the side-pumped geometry [77, 88]. This asymmetry

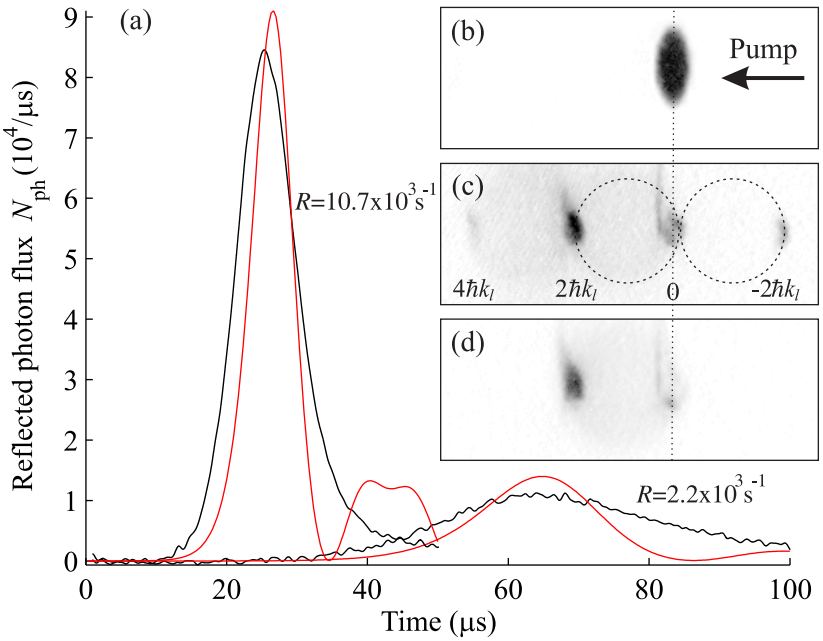

FIGURE 6.3: Illustrations of the different forms of data we obtain and of the agreement between simulations and experiment. (a) Traces from the photodetector are shown for high and low pump powers at a detuning of $\delta = -2\pi \times 2.6$ GHz. Simulations for the same parameters are presented as red lines. Absorption images after 45ms time of flight (TOF) of the corresponding atomic distributions are shown in (c) (high power $R = 10.7 \times 10^3$ s^{-1}, pump pulse duration 50 μs) and (d) (low power $R = 2.2 \times 10^3$ s^{-1}, pump pulse duration 200 μs). An unperturbed BEC is shown (b). Circles indicating the separation of adjacent momentum orders after 45 ms TOF are shown in (c); note that they originate from the input light end ($z = \xi = 0$) of the BEC. (The greyscale has been changed for the different absorption images so that the important features in each image are visible.)

can be traced back to the spatial inhomogeneity of superradiant scattering favouring the input end of the condensate, where the amplitude of the reflected light E_- is highest. The spatial dimensions of the condensate and the slow expansion upon release from the trap along the long axis are such that this spatial feature of the scattering is evident after 45 ms time of flight. For this reason, the circles in figure 6.3(c) marking the possible forward and backward momentum exchange between the matter and light fields coincide at the input end of the BEC. The spatially dependent dynamics within the BEC will be discussed in section 6.6.

The momentum distributions are somewhat distorted due to the input angle of the beam. When the beam is aligned parallel to the long axis of the BEC, the Bragg condition is satisfied for the atoms centered around zero transverse momentum as shown in figure 5.6. However, at the slight incident angle used, the patterns become more complicated.

To compare experimental results with simulations, the equations (5.23), (5.24) and (5.25) were solved numerically for experimental parameters.

We describe briefly the implementation of the 1D Maxwell-Schrödinger equations. The first attempt made use of several differential equation solvers in Matlab©. This gave sensible results but the computation time was somewhat long. A more tailored approach was implemented by Dirk Witthaut, where the dynamics of the atoms is simulated with a split operator technique [93]. This method is based on a splitting of the time evolution operator:

$$\begin{aligned} U(t+dt,t) &= \exp(-i/\hbar \int_t^{t+dt} T + V(t')dt') \\ &= \exp(-i/\hbar T dt/2)\exp(-i/\hbar \int_t^{t+dt} V(t')dt')\exp(-i/\hbar T dt/2) + O(dt^3) \end{aligned}$$

where T is the time-independent kinetic energy operator and V is the time-dependent coupling to the light field, and when included, the trapping potential and mean-field. V is diagonal in real space, so that it can be directly applied to the real space wave function. In contrast, T is diagonal in momentum space so that one can apply it to the momentum space wave function and flip between the two representations using the fast fourier transform. For the moderate number of discrete grid points used here, however, it is also possible to evaluate $\exp(-i/\hbar T dt/2)$ numerically in real space. For a set of standard experimental parameters, a complete simulation takes on the order of a minute. The number of required momentum orders clearly depends on the strength of the interaction and is chosen so that the outermost orders are negligibly populated.

The initial wavefunction ψ_0 was taken to be a 1D Thomas-Fermi profile normalized to the number of atoms in the trap N_{at}. The boundary conditions for the light fields were typically taken to be $e_+(0,\tau) = e_i$ and $e_-(k_l L,\tau) = 0$, with e_i a constant derived from the experimental pump photon flux and the (assumed) geometrical overlap of the BEC and the Gaussian intensity distribution of the pump beam. Note that $|e_-(0,\tau)|^2$ is proportional to the back-scattered light intensity measured in experiment, and that the total photon flux is conserved:

$$|e_+(0,\tau)|^2 = |e_-(0,\tau)|^2 + |e_+(k_l L,\tau)|^2 . \tag{6.1}$$

As equations (5.23), (5.24) and (5.25) contain no explicit noise term to instigate superradiant scattering, we seed the process by taking a non-zero first order momentum component $\psi_2 = \psi_0/\sqrt{N_{\mathrm{at}}}$, corresponding to a single delocalized atom in the first side-mode [89]. The random nature of the initiation of superradiant scattering may be modelled in the present formalism by using random initial conditions sampled from a physically motivated probability distribution [84], and we return to this in section 7.1.

The simulations describe well the arrival times and amplitudes of the first superradiant light pulse. The agreement arises in part from a careful calibration of the experimental detection system, but we should note that the nominal field amplitudes e_i derived from experimental parameters have been scaled up by a global factor of 10.5% in simulations to better capture the essential features of the experimentally observed superradiant pulses. That is, in all simulations shown in this work, the experimental pump photon flux (as measured on the calibrated monitor photodiode $\propto |e_i|^2$; see figure 6.1) is scaled up by a global factor of 22%.

Clearly, there are limits as to how well one can expect a 1D semi-classical model to describe a 3D quantum system. It is evident from 6.3(a), that while the amplitudes and arrival times of the experimental pulses are well described by the simulations, the agreement of the widths of the first superradiant pulses and the subsequent ringing behaviour is not as good. This is consistent with similar modeling of superradiance in inverted samples: experimentally one observes much less ringing than is predicted by 1D numerical simulations [72]. Nonetheless, it is clear that the simulations capture the general features of the evolution of the first superradiant pulse well, and are primarily useful to help our understanding, rather than to provide a comprehensive model.

6.4 Dependence on atom number

It is interesting to check experimentally and with the 1D model that we can reproduce the quadratic dependence on the number of atoms N_{at} of the peak intensity of the first superradiant pulse. Furthermore, in the subsequent experiments presented, we keep the atom number nominally constant, so it is pertinent to investigate how sensitive the signals we measure are to fluctuations in the atom number. It is most likely obvious to the reader, that it is much easier to produce smaller condensates than bigger ones! As such, experimentally we can test the dependence only over a limited range before the detection of light and atoms becomes problematic.

One can generate smaller condensates by simply lowering the RF further, but we have found the most reproducible method is to simply the leave the BEC in the trap with the RF knife at the position of the final cut. Essentially, this is just an (aggressive) RF shield, so that as hot atoms are produced through inelastic collisions - which we take to be three-body recombination - they are removed from the trap as the cross the RF knife. By varying the hold time in the trap by up to several seconds, one can realize arbitrarily small condensates.

However, varying the atom number in a BEC changes its size and therefore the coupling to the pump beam. This is in contrast to experiments in superradiance by inverted samples, where the effective number of atoms participating in the process may be varied by the degree of population inversion, without changing the sample

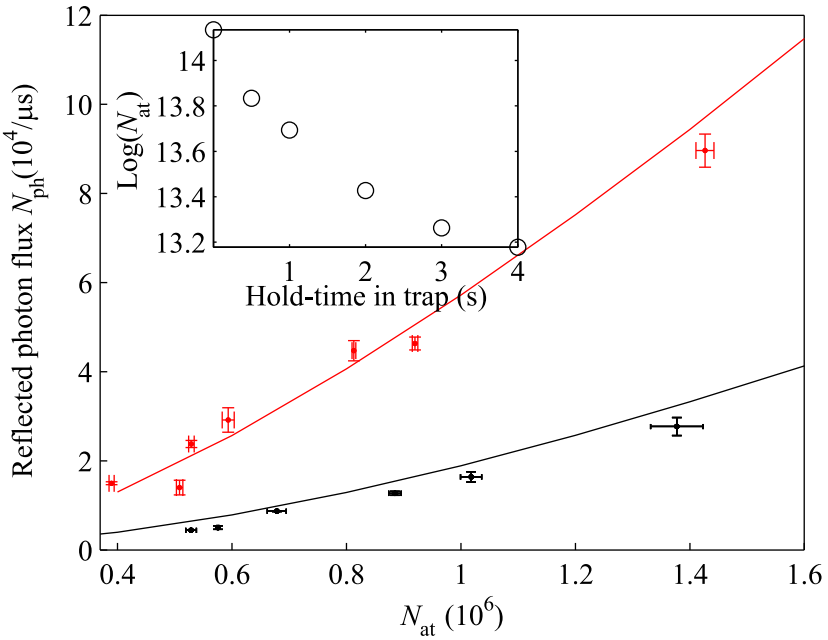

FIGURE 6.4: The atom number dependence of the peak value of the first superradiant pulse. Experimental data (points) and simulations (solid curves) are shown for two values of the single particle scattering rate: 4.3 (black) and 10.7 (red) $\times 10^3$ s^{-1}. The atom number for each point was obtained by fitting the unperturbed BEC with a Thomas-Fermi profile and using the widths to infer the chemical potential. The errorbars represent the standard error of the mean of three realizations for each setting. The inset shows the logarithm of the number of atoms v. hold-time: the 'super-exponential' character indicates the decay mechanism is not related to background gas collisions.

geometry [73]. To simulate SLS from a BEC, one evaluates the chemical potential from the assumed number of atoms using (3.33) and obtains the in-trap dimensions of the BEC using expressions in table 3.2; these dimensions are used in the BEC and light field normalizations, and in evaluating the effective number of photons interacting with the BEC from its overlap with the pump beam.

Experimental and simulated results where the number of atoms in the BEC is varied are shown in figure 6.4. After a given hold time in the magnetic trap after condensation (the maximum was five seconds), three realizations of the unperturbed BEC followed by three realizations of superradiant scattering were performed. The atom number was obtained from fitting Thomas-Fermi profiles to the expanded clouds and inferring the chemical potential as described section 3.4.3. The inset figure shows $\log(N_{at})$ v. time to demonstrate that the decay is consistent with three-body recombination [48, 94]. The fact that these data do not fit on a straight line indicates that the decay is not due to background gas collisions, but rather two or three body collisions.

Indeed, the decay is two orders of magnitude faster than that expected from the level of vacuum. There is good overall agreement between the simulations and the data, and it is evident that the peak scattering rate has a weak quadratic dependence in this parameter range.

We can see how this quadratic dependence on the atom number arises by manipulating the 1D Maxwell-Schrödinger equations. For simplicity, we consider the case where only the zeroth and first order atomic modes are populated. Recalling figure 6.3, this corresponds well to the low pump power case $R = 2.2 \times 10^3$ s^{-1}. In this parameter range, and neglecting the wavefunction kinetic energy and displacement terms and suppressing the explicit position and time dependence, equations (5.23), (5.24) and (5.25) become:

$$\frac{\partial \psi_0}{\partial \tau} = -i\Lambda \left[e_+^* e_- \psi_2 \mathrm{e}^{-2i\tau} + (|e_+|^2 + |e_-|^2)\psi_0 \right], \tag{6.2}$$

$$\frac{\partial \psi_2}{\partial \tau} = -i\Lambda \left[e_-^* e_+ \psi_0 \mathrm{e}^{+2i\tau} + (|e_+|^2 + |e_-|^2)\psi_2 \right], \tag{6.3}$$

$$\frac{\partial e_+}{\partial \xi} = -i\frac{\Lambda}{\chi} \left[e_- \psi_2 \psi_0^* \mathrm{e}^{-2i\tau} + e_+(|\psi_0|^2 + |\psi_2|^2) \right], \tag{6.4}$$

$$\frac{\partial e_-}{\partial \xi} = +i\frac{\Lambda}{\chi} \left[e_+ \psi_0 \psi_2^* \mathrm{e}^{+2i\tau} + e_-(|\psi_0|^2 + |\psi_2|^2) \right]. \tag{6.5}$$

Given that the growth of e_- depends on the coherence - or polarization term - $\psi_2\psi_0^*$ we consider:

$$\frac{\partial(\psi_2\psi_0^*)}{\partial \tau} = i\Lambda e_-^* e_+ \mathrm{e}^{+2i\tau}(|\psi_2|^2 - |\psi_0|^2). \tag{6.6}$$

The first feature of note is that the growth of the coherence that drives the creation of e_- photons depends on the population difference between the two momentum orders. In this way, we can regard superradiant Rayleigh scattering as inversion in momentum space, as opposed to population inversion in Dicke superradiance. Evidently, the growth of the coherence $\psi_2\psi_0^*$ is proportional to the number of atoms in the sample, and given this term appears in the expression for the growth of the field amplitude e_-, it follows that the intensity of the emitted light in the back-scattered mode has the expected quadratic dependence on the number of atoms. We note further that the time development of the atomic coherence depends on the light field coherence $e_-^* e_+$. This is consistent with the physical picture that the both the local amplitude and phase of the matter and light wave coherences determine the evolution of the system.

6.5 Pump depletion

In the superradiance of inverted samples, all the qualitative features depend on just the number of atoms N_{at} and the natural decay rate Γ, and comparisons of superradiant light scattering and superradiance in inverted samples rely on the identification

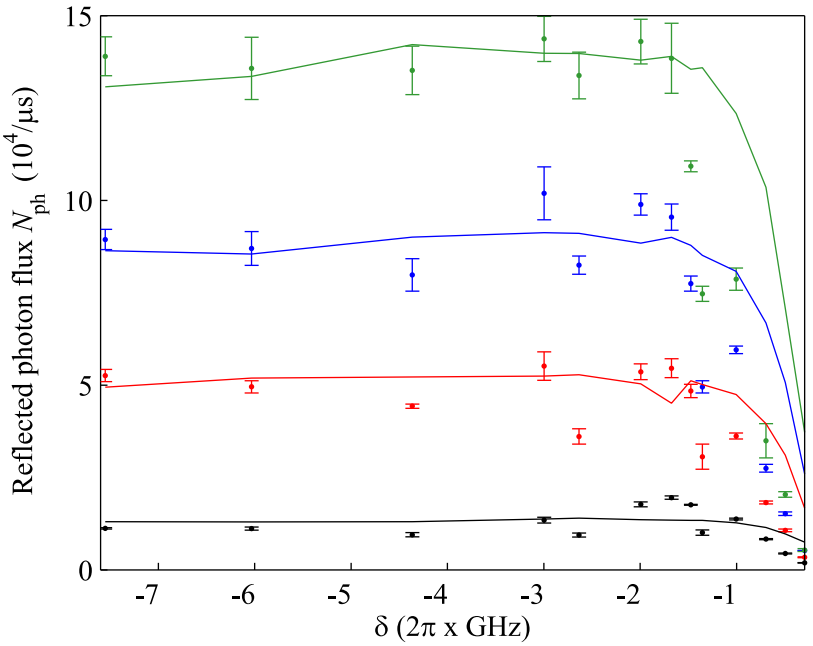

FIGURE 6.5: Experimental (points) and simulated (lines) peak photon flux of the first superradiant pulse as a function of detuning for R =2.2 (black), 6.4 (red), 10.7 (blue), 15.9 (green)$\times 10^3 s^{-1}$. Errorbar limits are the standard error of the mean for five realizations.

of the single particle scattering rate R as playing the role of Γ. However, we now explore how this identification breaks down by simultaneously varying the detuning and intensity of the pump beam so as to keep R constant. From physical grounds, it is obvious that the peak back-scattered photon flux must drop with the detuning, so that the reflectivity of the sample does not exceed one. This may be seen by rewriting (5.15) as $R = CN_{\text{pump}}/\delta^2$, with C a constant, and N_{pump} the photon flux of the pump beam. Accordingly, the reflectivity may be written as $N_{\text{ph}}/N_{\text{pump}} = CN_{\text{ph}}/(R\delta^2)$. Given the constancy of R in the following experiments, it is clear that the peak back-scattered photon flux must decrease as the detuning is decreased so as to maintain an upper bound (of one) for the reflectivity.

Figure 6.5 shows experimental data (points) and simulations (lines) of the peak value of the first superradiant pulse as the detuning of the pump beam is varied while keeping the single particle scattering rate R constant. Results are shown for four values of R in the range $R \ll \omega_r$ to $R \sim \omega_r$. For a large portion of the graph, the peak value is essentially independent of the detuning, and there is excellent agreement between simulations and data. For lower detunings, the peak value of the emitted pulse falls away, and the experimental data reaches our detection resolution for $\delta \approx -2\pi \times 300$ MHz, while the simulations show the same qualitative behaviour.

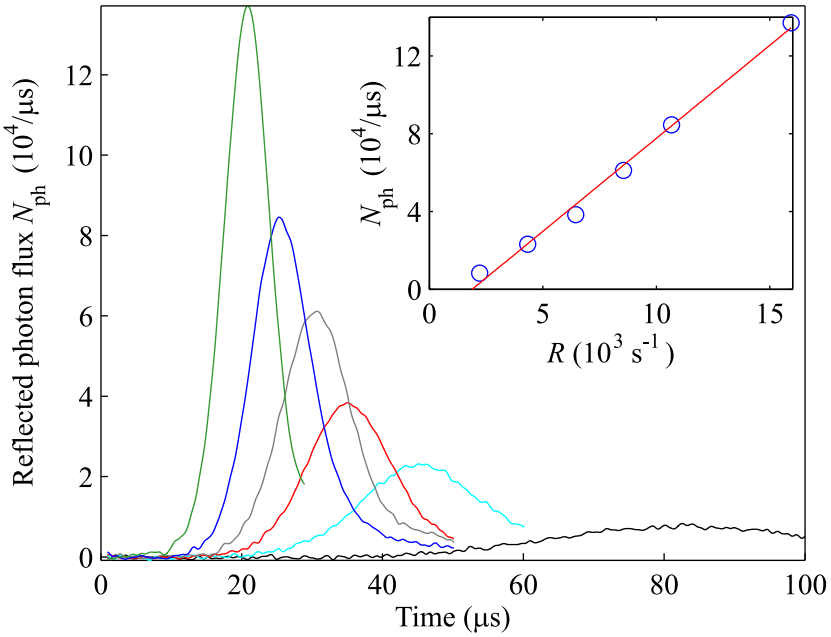

FIGURE 6.6: Experimental superradiant light pulses for several values of the single particle scattering rate in the high detuning regime ($\delta = 2\pi \times 2.6$ GHz). The curves correspond to R =2.2 (black), 4.3 (light blue), 6.4 (red), 8.6 (grey), 10.7 (blue), 15.9 (green)$\times 10^3 s^{-1}$. For clarity, the traces have been clipped after the first superradiant pulse. The inset figure shows the peak value of the pulse v. R. The data (circles) are well described by a linear fit (red line).

As the (red) detuning is increased, one observes experimentally that the atomic density distributions become more transversely elongated after time of flight. This is simply the effect of the dipole force: it begins to play more of a role as the power of the pump beam is increased to compensate for the increased detuning, so as to maintain the same single particle scattering rate. Note that the spontaneous scattering rate scales as I/δ^2 whereas the dipole force scales as I/δ (cf. (5.15) and (5.17)). Given that we use red detunings in the experiment, the atoms are attracted to the intensity maximum of the pump beam, and because the beam is focused to a moderate waist of 13 μm at the position of the atoms, the effect is to make the effective trapping potential much tighter transversely. This is the same effect that was used to align the pump beam to the BEC described in section 6.2.

To further study the two regimes, figure 6.6 shows experimental time traces for several different values of R at a high detuning, and figure 6.7 shows experimental traces for four low detunings while R is kept constant.

Figure 6.6 shows that in the high detuning regime, the superradiant peaks arrive earlier and are more sharply peaked the higher the pump power. From the inset figure, it is evident that the peak intensity increases linearly with the pump power, as one

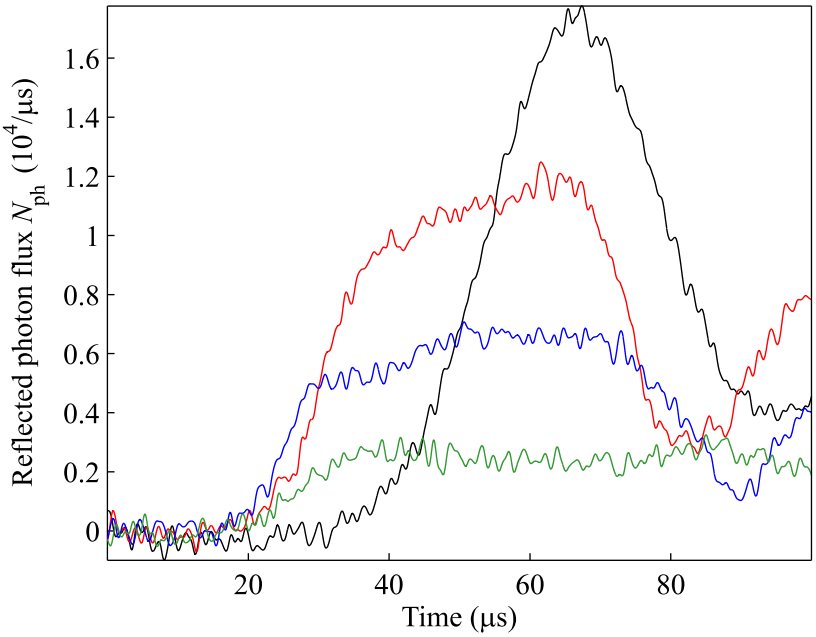

FIGURE 6.7: Traces corresponding to the decaying portion in figure 6.5, illustrating the clamping of the superradiant pulse due to depletion of the pump beam. For $R = 2.2 \times 10^3 \mathrm{s}^{-1}$ and detunings $\delta = -2\pi\times$ 2.0 (black), 1.0 (red), 0.7 (blue), 0.5 (green) GHz.

would expect from (6.6). This equation generalizes to to the multiple order case in a straightforward way, given that each momentum order only couples to its nearest neighbours. The inset figure also indicates a kind of threshold behaviour in that the data and fit do not pass through the origin; this is consistent with [76].

Figure 6.7 shows how the superradiant pulse intensity is clamped at low detunings. The lower amplitudes can be traced back to the lower incident photon fluxes and increasingly important pump depletion in the low detuning case. The transition from high detuning behaviour to the pump-depletion regime occurs in the experimental data at points where the incident photon flux is approximately 10 times the peak reflected photon flux. Above this point, while the amplitude of the reflected pulses drops, the observed peak reflectivity of the sample increases sharply, up to values of $\sim 30\%$. The simulations show the same qualitative behaviour in this regime, and we attribute the loss of quantitative agreement to the incoherent losses that are not captured by the model: i.e., emission into different modes. The spatial dependence of the light and matter waves plays a critical role here, and to gain more insight into the behavior of the system, we explore the light and matter wave dynamics inside the sample through simulations.

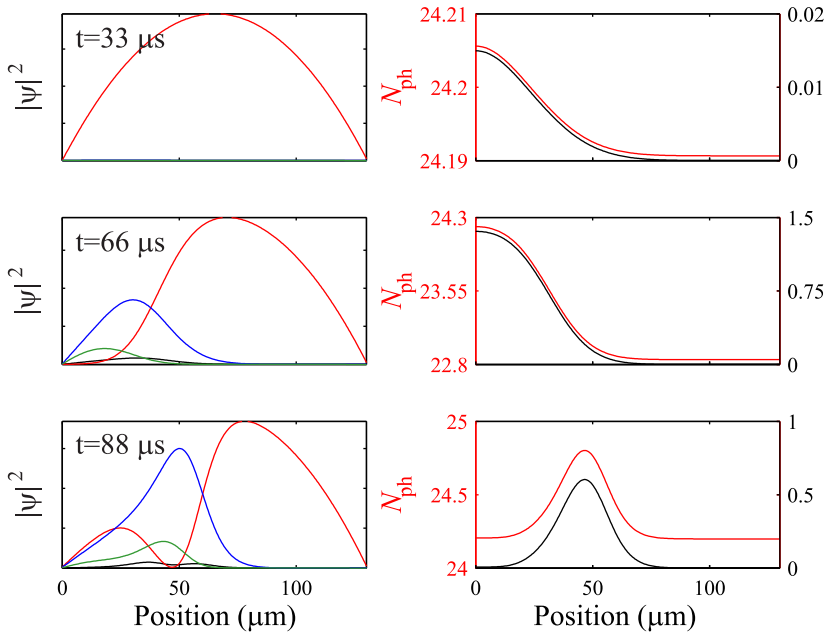

FIGURE 6.8: Simulated low power dynamics within the BEC at high detuning $\delta = -2\pi \times 2$ GHz. To the left, the density of the different momentum components of the BEC is shown: ψ_{-2} (black), ψ_0 (red), ψ_2 (blue), ψ_{+4} (green). In the right column, the light field fluxes for the forward e_+ (red line) and backward e_- (black line) travelling waves are shown. Note for each of the light intensity figures, the left (red) scale pertains to e_+ and the right hand scale (black) pertains to e_- using the standard unit of $10^4/\mu$s. The position scale within the condensate (length $L = 130\mu$m) is the same for all the subfigures.

6.6 Spatially dependent dynamics

To gain understanding of the fundamental elements of the dynamics, we consider simulations for the low power case of $R = 2.2 \times 10^3 \mathrm{s}^{-1}$ where - at least experimentally - only the first order diffracted atomic mode becomes populated. Figure 6.8 shows the results of simulations for $\delta = -2\pi \times 2$ GHz so as to explore the high detuning regime. For three relevant times during the interaction, atomic density distributions along the long axis of the BEC are shown in the left column, and the scaled intensities $\propto |e_+|^2$ and $|e_-|^2$ are shown in the right column. The general dynamics for low input power, high detuning are as follows: The back-scattered light intensity in the sample builds up at the input end because there it sees gain from approximately the entire length of the BEC; this is the time shown in the uppermost row. It is this spatial inhomogeneity in the scattering that was referred to in connection with figure 6.3. At this point, the rate of transfer of atoms from ψ_0 to ψ_2 concurrent with the growth of e_- and reduction in e_+ begins to increase steeply. At the time shown in the

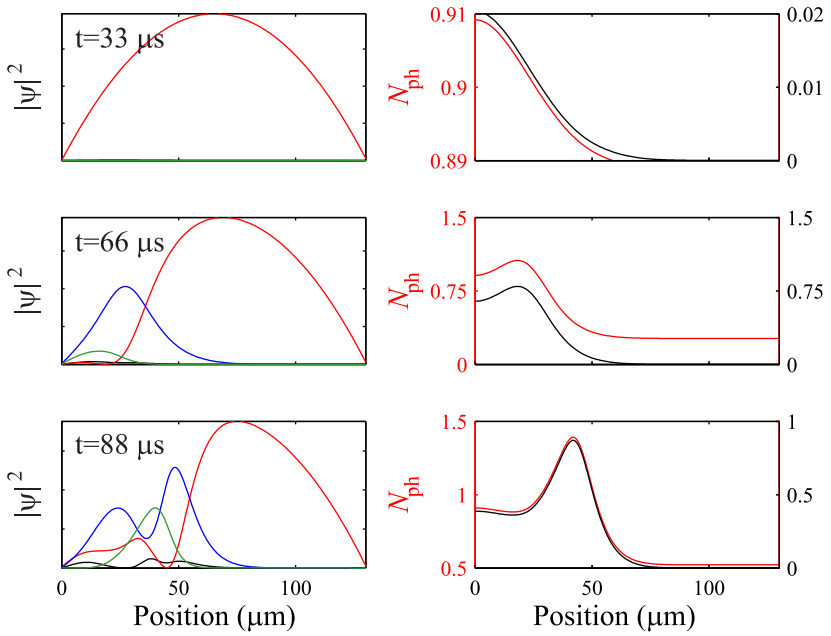

FIGURE 6.9: Simulated low power dynamics within the BEC at low detuning. Again, in the left column the density of the different momentum components of the BEC is shown: ψ_{-2} (black), ψ_0 (red), ψ_2 (blue), ψ_{+4} (green). In the right column, the light field fluxes for the forward e_+ (red line) and backward e_- (black line) travelling waves are shown. Note for each of the light intensity figures, the left (red) scale pertains to e_+ and the right hand scale (black) pertains to e_- using the standard unit of $10^4/\mu$s; the right hand scales are the same for each of the corresponding subfigures in figure 6.8. The position scale within the condensate (length $L = 130\mu$m) is the same for all the subfigures.

second row, the population in ψ_0 is sufficiently depleted at the input edge of the BEC so that the process slows down and then stops. However, the light field envelopes then move towards the centre of the condensate, where $|\psi_0|$ is still large, and the exchange between the two light fields continues; this is the time shown in the bottom row, identified by $t = 88$ μs. At this time, $|\psi_0|$ grows again at the input end of the condensate, driven there by the destruction of e_- photons generated further inside the sample, and ψ_2 atoms. In this way, the back-scattered photon flux out the input end of the condensate stops, and the first superradiant pulse has been emitted. The basis of 'ringing' behaviour - the emission of subsequent superradiant pulses - is merely a repetition of the dynamics described above. Furthermore, a fascinating implication of the above dynamics, visible in the light intensity subfigure at $t = 88$ μs, is that at times the light intensity within the BEC is higher than outside - the interaction leads to the formation of an optical resonator, where partially reflecting mirrors are formed by the density modulation due to the interference of stationary and recoiling

matter-waves. These Bragg gratings are centered where ψ_0 and ψ_2 cross.

The dynamics in the low detuning case is similar, but with two significant differences. Due to the increased light scattering cross-section at low detunings, the pump light is significantly depleted in its passage through the BEC, as is evident in the right hand column of figure 6.9, which shows the same quantities as figure 6.8 except at a low detuning: $\delta = -2\pi \times 294$ MHz. Accordingly, the build up of back-scattered light is accelerated and even more localized at the input end of the BEC, so that the scattering of ψ_0 to ψ_2 atoms is limited to a very narrow region of atoms at the input end. This narrowness is reflected at later times in the length of the 'resonator'. Thus, the spatial dependence of the pump depletion and hence the size of the scattering region leads to the reduced amplitude of the back-scattered pulses in figure 6.7. The second main difference is that the ψ_4 mode becomes significantly populated at low detunings. This means that the first SR pulse is not stopped by a lack of ψ_0 atoms, but rather can continue due to the scattering from ψ_2 to ψ_4 via the destruction of a pump photon. This can be seen in the bottom light subfigure, where there is more light 'leaking' from the resonator compared to the corresponding subfigure in 6.8; and in figure 6.7, where the low detuning pulses are broader, and show a secondary peak soon after the first. In general, the dynamics become complicated as the number of significantly atomic orders and hence number of timescales in the problem increases.

It is important to note that the reflectivity of the sample is much greater in the low detuning case than it is for high detunings. By comparing the light figures in 6.8 and 6.9, one can see that the peak reflectivity in the high detuning case is on the order of 5%, whereas it attains a value in excess of 80% for low detunings.

It is evident that the light intensities of the forward and backward travelling waves have the same spatial form at each point in time but offset from each other. This can be understood by a simple energy conservation argument that is valid within the approximation that retardation of the fields is unimportant; i.e., the relevant time scales are much greater than the transit time of light through the length of the BEC L/c. The rate of change of energy in a given slice $\Delta\xi$ of the BEC is given by the net flux of photons into the slice:

$$\frac{d\rho}{dt} = K\left[|e_+(\xi,\tau)|^2 - |e_+(\xi+\Delta\xi,\tau)|^2 - |e_-(\xi,\tau)|^2 + |e_-(\xi+\Delta\xi,\tau)|^2\right], \quad (6.7)$$

where ρ is the linear energy density, and K is a constant. Given the neglect of retardation so that we do not consider the transient build-up of light intensity within the sample but instead assume that it is infinitely quick, (6.7) must equal zero. Therefore,

$$\begin{aligned} \lim_{\Delta\xi\to 0} \frac{|e_+(\xi+\Delta\xi,\tau)|^2 - |e_+(\xi,\tau)|^2}{\Delta\xi} &= \lim_{\Delta\xi\to 0} \frac{|e_-(\xi+\Delta\xi,\tau)|^2 - |e_-(\xi,\tau)|^2}{\Delta\xi}, \\ \frac{\partial\,|e_+(\xi,\tau)|^2}{\partial\xi} &= \frac{\partial\,|e_-(\xi,\tau)|^2}{\partial\xi}, \end{aligned} \quad (6.8)$$

and the desired relation is obtained. In the limit where $\Delta\xi \to k_l L$, equation (6.7) reduces to the photon flux conservation law of (6.1). However, as we have seen, the light intensity can attain a local maximum within the BEC, and we now explore this feature.

6.7 Bragg mirrors and resonator structures

It is an interesting feature of superradiant Rayleigh scattering that one may interpret the coherence terms like $\psi_0\psi_2^*$ that drive the scattering from one light field to the other as a density grating. In the end pumped geometry, this density grating - like the total light intensity - has a spatial period of half a wavelength, meaning that the Bragg condition for back-scattering photons is fulfilled; this supports the analogy of this structure with a dielectric mirror. Figure 6.10 shows the spatial distribution of light intensity and atomic density within the sample for the lower power, high detuning case shown in figure 6.8, with the fast time and space dependence inserted (i.e., equations (5.20) and (5.21)). The total light intensity has its maximum between the two main 'Bragg mirrors'.

A useful way to understand the dynamics is thus through the light and density gratings: the local amplitudes and phases of these gratings determine the dynamics of the sample. To motivate this idea, above the main figure of 6.10 we have plotted close-ups of the gratings at, and to either side, of the intensity maximum. It is evident that the phase between the the light and matter wave gratings shows symmetric behaviour either side of the intensity maximum, whereas at the peak intensity, the nodes of the density grating coincide with the anti-nodes of the light standing wave. The dynamics are complicated somewhat by the fact that condensate components other than ψ_0 and ψ_2 are populated, leading to several frequency components making up the matter-wave grating. This can be seen clearly in the close-up figure at the intensity maximum whereas to either side, the grating is dominated by the overlap of ψ_0 and ψ_2 components, leading to a single, dominant, spatial period.

With this in mind, it is interesting to analyse the spatial dependence of the back-scattered light intensity. By straightforward manipulation of (5.24) and (5.25), we obtain:

$$\frac{\partial |e_-|^2}{\partial \xi} = -2\frac{\Lambda}{\chi}\sum_m \mathrm{im}\left\{e_-^* e_+ \psi_m \psi_{m+2}^* \mathrm{e}^{2i(m+1)\tau}\right\}, \tag{6.9}$$

and expressing the two coherences in terms of their modulus and phase, we may

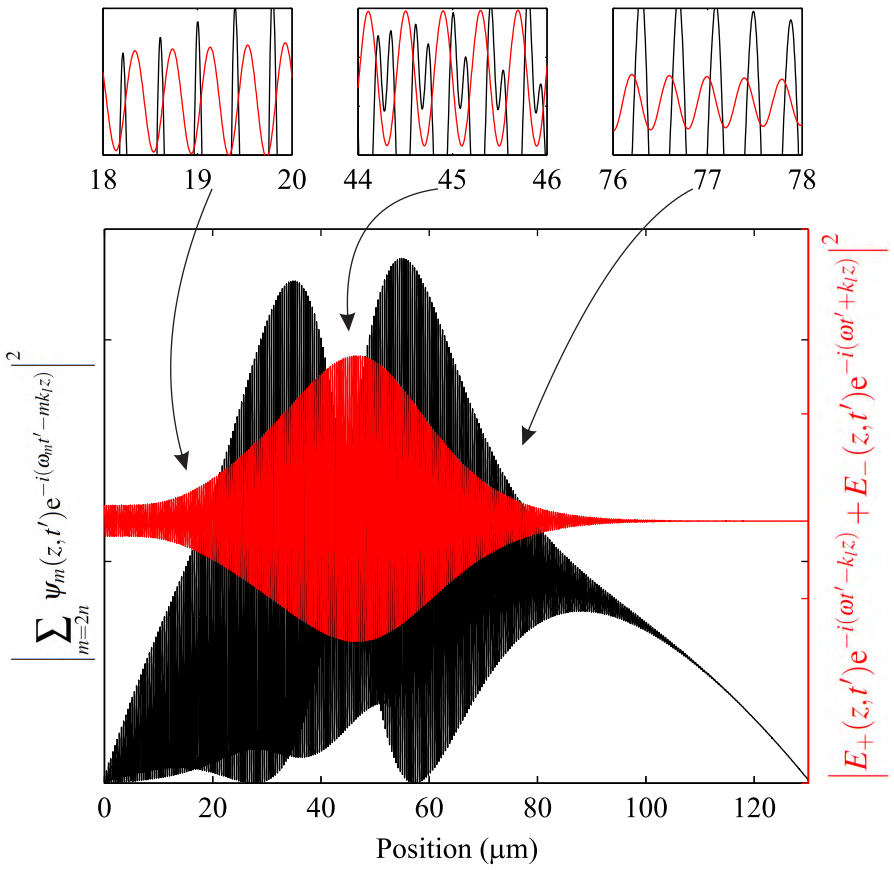

FIGURE 6.10: Simulation of the total electric field intensity and matter wave density distributions for the low power, high detuning case considered in figure 6.8 at time $t' = 88\ \mu$s. The interfering matter waves form Bragg mirrors that partially reflect the light, and at the chosen interaction time there are two such mirrors, leading to an intensity maximum within the sample. Above the main figure are close-ups at different points within the sample, illustrating that the phase between the light and matter-wave gratings shows symmetric behaviour about the intensity maximum.

write:

$$\begin{aligned}\frac{\partial |e_-|^2}{\partial \xi} &= -2\frac{\Lambda}{\chi}\sum_m \mathrm{im}\left\{\left|e_-^* e_+\right|\left|\psi_m \psi_{m+2}^*\right| e^{i(\phi_1+\phi_{at}+2i(m+1)\tau)}\right\} \\ &= -2\frac{\Lambda}{\chi}\sum_m \left|e_-^*(\xi,\tau)e_+(\xi,\tau)\right|\left|\psi_m(\xi,\tau)\psi_{m+2}^*(\xi,\tau)\right| \times \\ &\qquad \sin\left(\phi_1(\xi,\tau)+\phi_{at}(\xi,\tau)+2(m+1)\tau\right),\end{aligned} \tag{6.10}$$

where the explicit space and time dependence has been included in the final line.

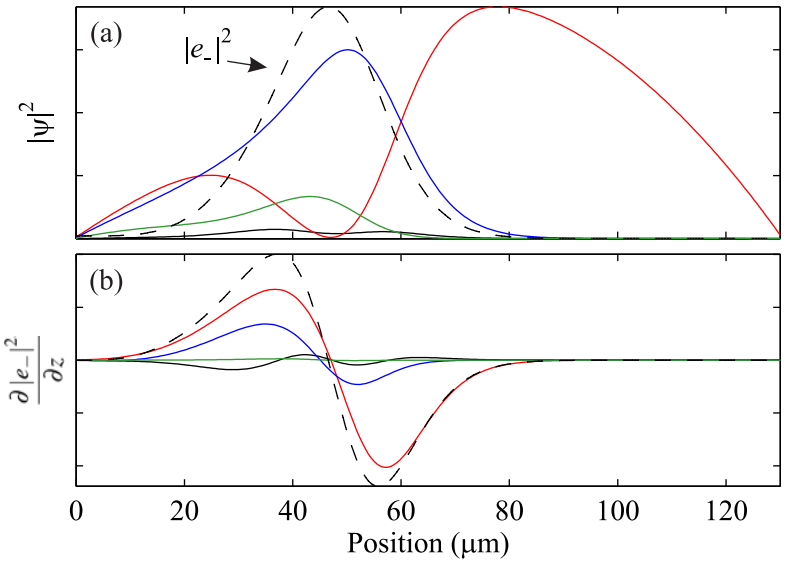

FIGURE 6.11: Interpreting the growth in back-scattered light intensity in terms of overlap of the light and matter wave gratings. (a) As in figure 6.8, simulated low power dynamics within the BEC at high detuning $\delta = -2\pi \times 2$ GHz. The density of the different momentum components of the BEC is shown at time $t = 88\mu$s: ψ_{-2} (black), ψ_0 (red), ψ_2 (blue), ψ_{+4} (green); and $|e_-|^2$ is shown (black dashed line). (b) Equation (6.9) (expressed in terms of unscaled position z) is shown for the different terms in the sum: $\psi_{-2}\psi_0^*$ (black), $\psi_0\psi_2^*$ (red), $\psi_2\psi_{+4}^*$ (blue), $\psi_{+4}\psi_{+6}^*$ (green). The sum of all the terms is shown as a black dashed line.

This equation summarizes the ideas discussed above: the local growth in space of the back-scattered light intensity depends on the amplitude and the phase of the light and matter-wave gratings. Figure 6.11 illustrates this, where (6.9) (expressed in terms of unscaled position z) is plotted underneath the squared modulus of the slowly varying envelopes for atoms and light. It is clear that the back-scattered light intensity reaches its maximum when (6.9) equals zero, and is the case in the figure. The different frequency components serve to shift slightly the zero crossing of the overlap of the two gratings. Finally, the observed 90° phase shift between light and matter-wave gratings in figure 6.10 at the intensity maximum can now be understood within the framework implied by equation (6.10)[1].

In summary, the growth in the back-scattered light intensity is the result of phase-sensitive gain determined by the overlap of the light and matter wave gratings. In the limiting case of atoms being scattered from a red-detuned optical lattice, one can view the atoms as being pulled towards the anti-nodes of the lattice. In the more general situation considered above, it is not a matter of one grating being pulled

[1]Figure 6.10 shows the total intensity $|e_+ + e_-|^2$, while the present discussion relates to $|e_-|^2$. However, the two lie within a fraction of the standing wave spatial period of eachother.

towards the other, but instead more complex dynamics where both light and matter wave gratings exert a comparable mechanical effect on each other, and this occurs because they are interacting quantum systems of similar sizes.

Chapter 7

Fluctuations in superradiant light scattering

We now shift our focus from 'mean values' in superradiance to fluctuations and correlations between atoms and photons. As we noted in connection with the superradiance of inverted samples in section 5.2, the state of light in the initial phase of the process is thermal. The same is true in superradiant light scattering, and the random nature of the spontaneous emission that initiates the process is also manifest at much longer times [95, 96]. To some extent, one can view SLS from a cold atomic sample as being analogous to a photomultiplier: the initial detection of a photon occurs in a probabilistic way, but the subsequent amplification of that signal evolves as a 'classical process'.

In this chapter, we present three main results in the regime of high detuning, so that the pump depletion effects of the previous chapter are not significant.

First, we study the fluctuations in arrival times and amplitudes of the superradiant light pulses that are induced by the random nature of the way the process is initiated. For a high and low scattering rate R and using the time resolved photodetector, we performed many realizations with nominally the same experimental conditions. There are several results from Dicke superradiance that may be applied to help our understanding. Furthermore, we show that the simulations with initial conditions sampled from a thermal distribution, produce the same distributions.

The second result relates to the way the state of light and atoms changes as the superradiant process evolves. Analogous to a laser, the state of the emitted light evolves from a thermal state to one well described by a coherent state. Using the data mentioned above, we obtain the cumulative number of photons emitted as a function of time, and compare this with a result from Dicke superradiance.

Finally, we study the number correlations between recoiling atoms and photons. Conservation of momentum guarantees that such atoms and photons are created in pairs according to the generic parametric down conversion Hamiltonian $\propto \hat{a}^\dagger \hat{b}^\dagger$,

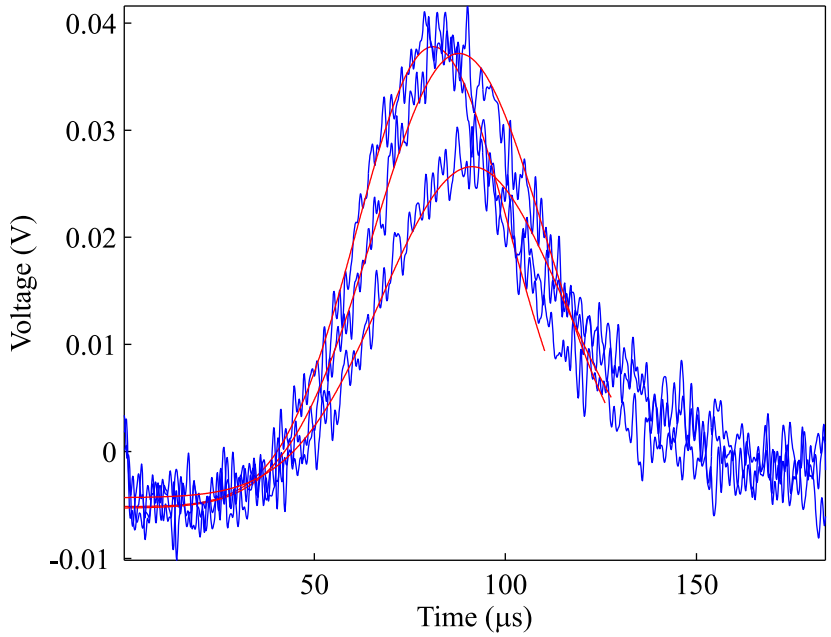

FIGURE 7.1: Illustration of the variations in the first superradiant pulse in three realizations with a low value of the single particle scattering rate ($R = 2.2 \times 10^3 \mathrm{s}^{-1}$, $\delta = 2.6$ GHz). The output of the time-resolved differential photodetector is shown (blue) along with Gaussian fits (red) to the first portion of the trace so as to capture the essential properties of the pulse (amplitude, arrival (peak) time τ_P, and the width). The time over which the pulse was fitted was $1.4 \times \tau_P$.

where here $\hat{a}^\dagger$ denotes the creation of a photon in the appropriate mode, and $\hat{b}^\dagger$ does the same for an atom in a given momentum order.

7.1 Timing Fluctuations

Figures 7.1 and 7.2 show time traces from the differential photodetector for three realizations using respectively low and high single particle scattering rates. Given that the noise on the traces is quite prominent for the low value of R, in order to obtain good estimates of the peak value and arrival time of the first superradiant pulse, we fit the first portion of the traces with a Gaussian. The region of fitting is abbreviated because, as we saw in the previous chapter, the extended length of the sample leads to ringing behaviour that is a result of complex dynamics. Furthermore, it is likely that mean-field effects begin to play a role as the process proceeds, as strong ringing is not evident in either of the figures. As such, we focus on the first superradiant pulse and use the Gaussian fitting procedure as an empirical model to obtain quantities of interest. Clearly, the agreement between the data and the fits is

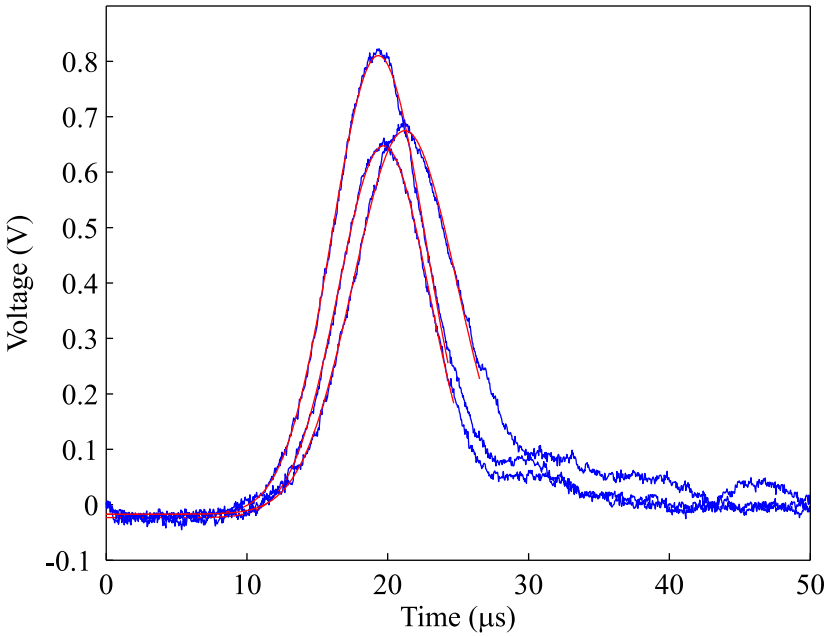

FIGURE 7.2: As in figure 7.1 but for a high value of the single particle scattering rate ($R = 15.9 \times 10^3 \mathrm{s}^{-1}$). The time over which the pulse was fitted was $1.25 \times \tau_P$.

very good. Finally, it is evident that the different realizations show variations in the amplitude, time to peak τ_P and width.

Figures 7.3 and 7.4 show histograms of the arrival time τ_P for low and high values respectively of the single particle scattering rate. The histograms have been fitted with a time-delay distribution that arises in superradiance in inverted samples; it is essentially an extreme value distribution.

To see how the distribution comes about, we revisit the analysis of section 5.2, but this time include the effects of propagation within a 1D model. The following treatment is based on references [74, 92, 97]. The analogue of (5.9) with propagation included is known as the Sine-Gordon equation:

$$\frac{\partial^2 \theta}{\partial z \partial t'} = \frac{\Gamma N_{\mathrm{at}}}{2L} \sin(\theta), \tag{7.1}$$

where L is the length of the sample, and $t' = t - z/c$ is the retarded time. Given the discussion of 5.5, we neglect retardation and set $t' = t$. The term ΓN_{at} defines the natural time-scale of the problem, and we thus define:

$$T_{\mathrm{R}} = \frac{1}{\Gamma N_{\mathrm{at}}}. \tag{7.2}$$

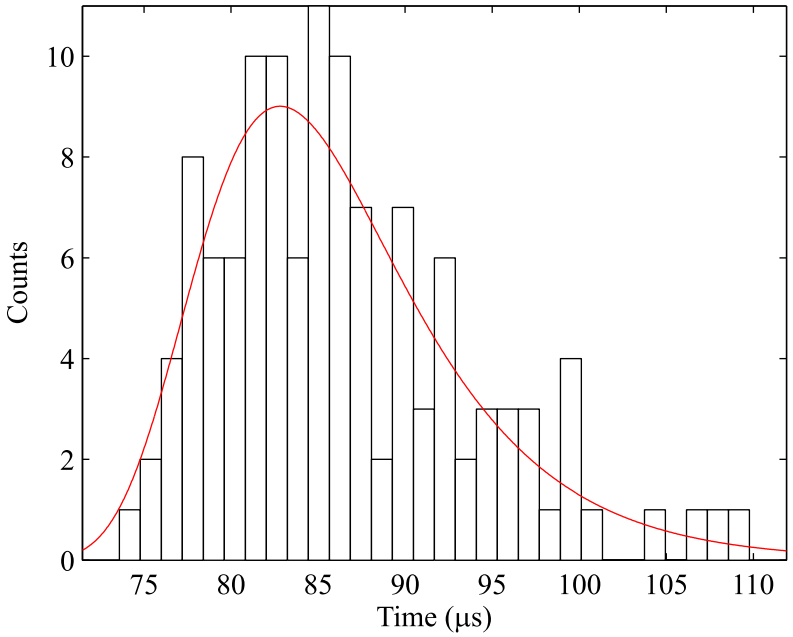

FIGURE 7.3: Histogram of arrival times τ_P of the first superradiant pulse for 120 realizations of a low single particle scattering rate $R = 2.2 \times 10^3 \mathrm{s}^{-1}$. The histogram uses 30 bins, and is fitted with equation (7.11). The result of the fit was $\langle \tau_P \rangle = 82.8\ \mu$s, and $\Delta\tau_P = 5.96\ \mu$s.

Equation (7.1) may be rewritten in terms of the single variable given by:

$$q = 2\left(\frac{z}{L}\frac{t}{T_{\mathrm{R}}}\right)^{1/2}, \tag{7.3}$$

so that the Sine-Gordon equation becomes:

$$\theta''(q) + \frac{1}{q}\theta'(q) - \sin(\theta(q)) = 0, \tag{7.4}$$

with the boundary conditions:

$$\theta(0) = \theta_i \quad \text{and} \quad \theta'(0) = 0. \tag{7.5}$$

One can now associate ringing behaviour - the emission of several superradiant pulses - with the oscillatory behaviour of this equation: instead of the irreversible decay associated with (5.9), the 'pendulum' in this model overshoots π and continues up towards 2π, whereupon the process repeats in an oscillatory fashion. Note that in the previous model, $0 \leq \theta \leq \pi$ and $0 \leq \phi \leq 2\pi$, so that we may understand values of $\theta > \pi$ as corresponding to a π change in ϕ; that is, the polarization and emitted electric field undergo a π phase shift between subsequent superradiant emissions [74].

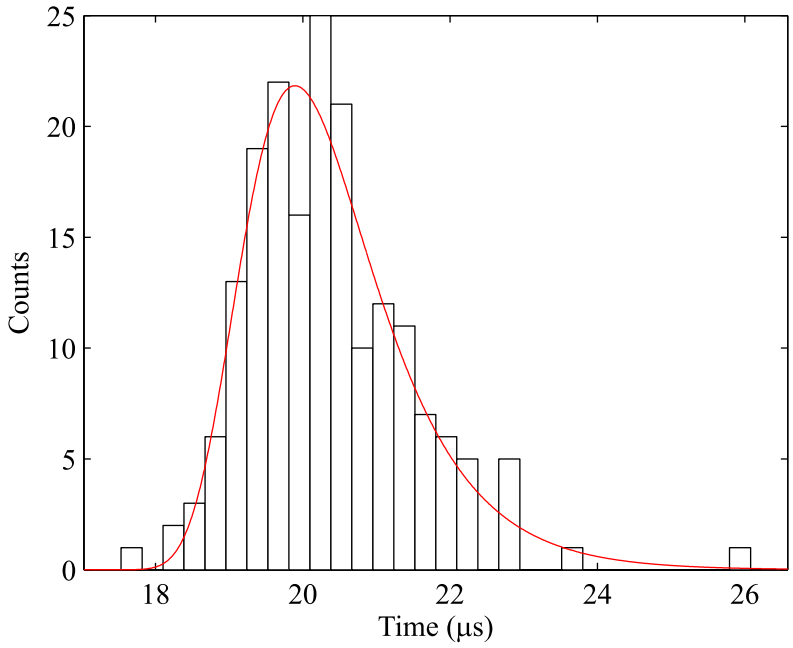

FIGURE 7.4: Histogram of arrival times τ_P of the first superradiant pulse for 186 realizations of a high single particle scattering rate $R = 15.9 \times 10^3 \mathrm{s}^{-1}$. The histogram uses 30 bins, and is fitted with equation (7.11). The result of the fit was $\langle \tau_P \rangle = 19.9\ \mu$s, and $\Delta\tau_P = 0.896\ \mu$s.

One can obtain an expression for the mean time delay and the fluctuations about this mean starting from equation (7.4). To proceed, we note that for the vast majority of the delay time to the peak of the first superradiant pulse, θ is very small; this is intuitively clear of a pendulum or rigid rotor displaced by a minute amount from pointing directly upwards: for a long time it is slow moving and limited to small angles, but by the time it crosses ($\theta(z = L, t = \tau_P) = \pi/2$) it is moving very quickly. As such, we may assume that the first pulse achieves its maximum at $\theta \approx 1$, because given the speed of the pendulum at that point, the time difference between this point and $\pi/2$ is very small. Accordingly, we may approximate $\sin(\theta)$ with θ. Equation (7.4) then becomes Bessel's modified equation, and has the following solution for small input angles θ_i [98]:

$$\theta(q) = \theta_i I_0(iq), \tag{7.6}$$

where I_0 is the zeroth order modified Bessel function, so that the delay time may be written:

$$I_0\left(2i\left[\frac{\tau_P}{T_\mathrm{R}}\right]^{1/2}\right) \approx \frac{1}{\theta_i}. \tag{7.7}$$

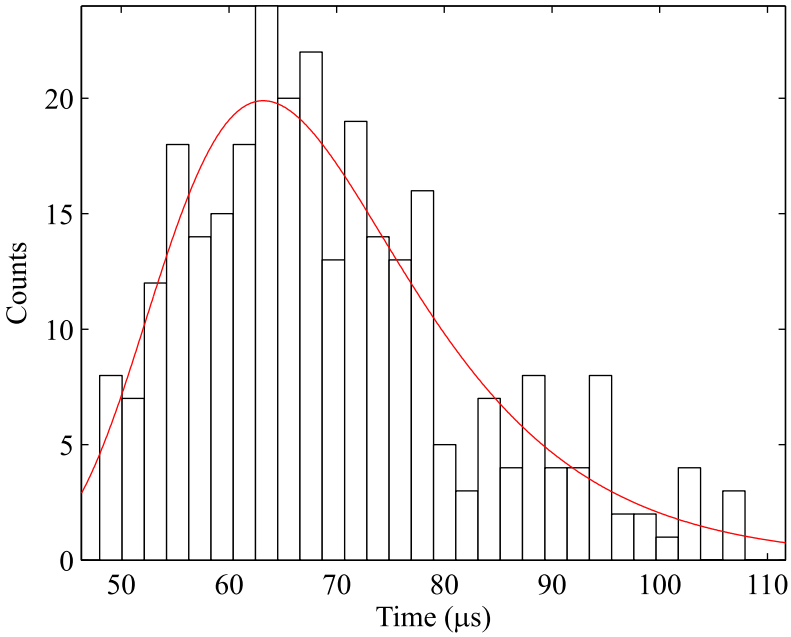

FIGURE 7.5: Histogram of the simulated arrival times τ_P of the first superradiant pulse for 300 realizations of a high single particle scattering rate $R = 2.2 \times 10^3 \mathrm{s}^{-1}$. The histogram uses 30 bins, and is fitted with equation (7.11). The result of the fit was $\langle \tau_P \rangle = 63.2\ \mu$s, and $\Delta\tau_P = 11.4\ \mu$s.

In general, the delay time is many times greater than T_R (see (5.14)) so to a very good approximation we may replace I_0 by its asymptotic value [99]:

$$I_0(iq) \to \frac{1}{\sqrt{2\pi q}} \mathrm{e}^q. \tag{7.8}$$

Solving for the delay time:

$$\tau_P = \frac{1}{4} T_\mathrm{R} \left[\ln \left(\frac{(16\pi^2 \tau_P / T_\mathrm{R})^{1/4}}{\theta_i} \right) \right]^2. \tag{7.9}$$

This expression is rather complex, but we note that the logarithm is dominated by the initial tipping angle $\theta_i \sim 2/\sqrt{N}$ so that the effect of τ_P in the argument is rather small. To simplify matters, we make use of equation (5.14) and approximate the argument in (7.9) as $A = (16\pi^2 \ln(N_\mathrm{at}))^{1/4} \approx 6.9$ for $N_\mathrm{at} = 1.35 \times 10^6$. With this simplification, the mean delay becomes:

$$\langle \tau_P \rangle = \frac{1}{4} T_\mathrm{R} \left[\ln \left(\frac{A\sqrt{N_\mathrm{at}}}{2} \right) \right]^2. \tag{7.10}$$

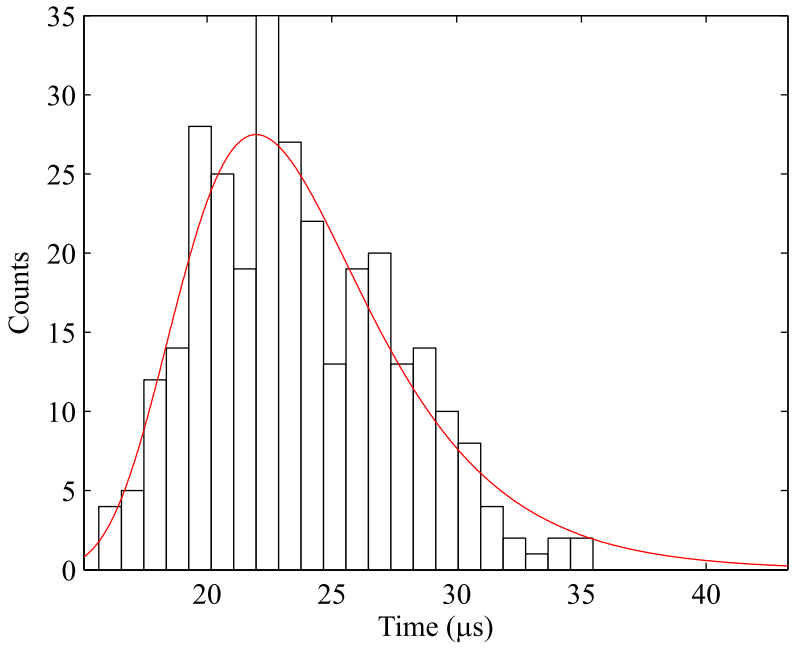

FIGURE 7.6: Histogram of the simulated arrival times τ_P of the first superradiant pulse for 300 realizations of a high single particle scattering rate $R = 15.9 \times 10^3 \mathrm{s}^{-1}$. The histogram uses 30 bins, and is fitted with equation (7.11). The result of the fit was $\langle \tau_P \rangle = 22.0\ \mu$s, and $\Delta\tau_P = 3.7\ \mu$s.

and transforming the thermal statistics of θ into those of the new random variable τ_P, we obtain [74]:

$$P(\tau_P - \langle \tau_P \rangle) = \exp\left[-\left(\frac{\tau_P - \langle \tau_P \rangle}{\Delta\tau_P}\right)\right] \exp\left[-\exp\left[-\left(\frac{\tau_P - \langle \tau_P \rangle}{\Delta\tau_P}\right)\right]\right], \qquad (7.11)$$

with the fluctuations given by:

$$\Delta\tau_P = \frac{1}{2}\sqrt{T_\mathrm{R} \langle \tau_P \rangle}. \qquad (7.12)$$

The histograms in figures 7.3 and 7.4 are well described by the extreme value distribution of equation (7.11) but in general the fitted parameters do not agree particularly well with those predicted by the preceding treatment. For instance for the low power case, (7.10) predicts a value $\langle \tau_P \rangle = 123\ \mu$s for the mean delay, and (7.12) predicts $\Delta\tau_P = 12\ \mu$s, whereas the fit gives the corresponding values $\langle \tau_P \rangle = 82.8\ \mu$s, and $\Delta\tau_P = 5.96\ \mu$s[1], so it seems that we can only take the analogy between the two systems so far. Clearly, there is a significant difference between Dicke superradiance

[1]Note that Γ must be scaled by an appropriate factor in (7.10) and (7.12) so as to use the number

and superradiant Rayleigh scattering, in that in the latter, atoms can scatter multiple times and populate many momentum orders, whereas in Dicke superradiance an atom can only decay once before requiring re-excitation from light emitted somewhere else in the extended sample. Nonetheless, the general applicability of (7.11) seems justified and gives insight into how the statistical properties of the instigating process manifest themselves at long times.

To elaborate on this, it is interesting to examine fluctuations in the simulations. Following equations (5.5) and (5.6), the simulations were run with a random polarization source sampled from a thermal distribution and with a random phase. The fluctuating polarization source is easiest to implement within the simulations because the electric field is described by first order differential equations of the longitudinal spatial variable, and therefore it is natural to specify the field in each case at either end of the sample (see section 6.3), whereas the wavefunctions are naturally solved in (5.23) by defining the total wavefunction at time zero in addition to boundary conditions. Given the electric field is in a thermal state due to spontaneous emission, the corresponding effect on the initial wavefunction is taken to be a random number sampled from a thermal number distribution in the first order diffraction mode. The thermal distribution was taken to have mean one, so as to be consistent with the simulations of the previous chapter.

The results of simulations for the two single particle scattering rates considered in experiments are shown in figures 7.5 and 7.6. The histograms are again well described by the extreme value model in (7.11), and show the same trends as the data - the higher the pump power, the earlier the pulse and the narrower the spread in τ_P. The agreement of the fitted parameters between simulations is fair, particularly for the high power case, although there is a discrepancy in the mean arrival time for the low power case. We reiterate that the simulations are most useful for understanding general features of the evolution, as opposed to being a comprehensive model of the system. For both high and low power cases, the width $\Delta\tau_P$ of the simulations is larger than the experimental data. It is also interesting to note that the 'noise' on the experimental data is smaller than for the simulations (i.e., the residual is greater for the simulations), despite the fact that one would expect the opposite given more realizations of the simulations were performed.

---

of photons spontaneously scattered into the assumed endfire mode. This factor is given by:

$$\mu = \frac{3}{16\pi}\left(\frac{4}{3} - \cos(\vartheta) - \frac{1}{3}\cos(\vartheta)^3\right),$$

where $\vartheta = \lambda/(\pi\rho_0)$ is the far-field diffraction angle (alternatively, the geometric angle ρ_0/z_0 could be used given the choice of Fresnel number $F \approx 1$). This expression is simply the solid angle of emission implied by ϑ weighted by the circular dipole emission pattern. If one takes account the Thomas Fermi profile then the effective scattering angle increases, leading to an increase in μ and hence a decrease in $\langle\tau_P\rangle$ [100]. An additional factor of 1/2 is included so that only decay into the the initial state $F = 1, m_F = -1$ is considered (see 5.4).

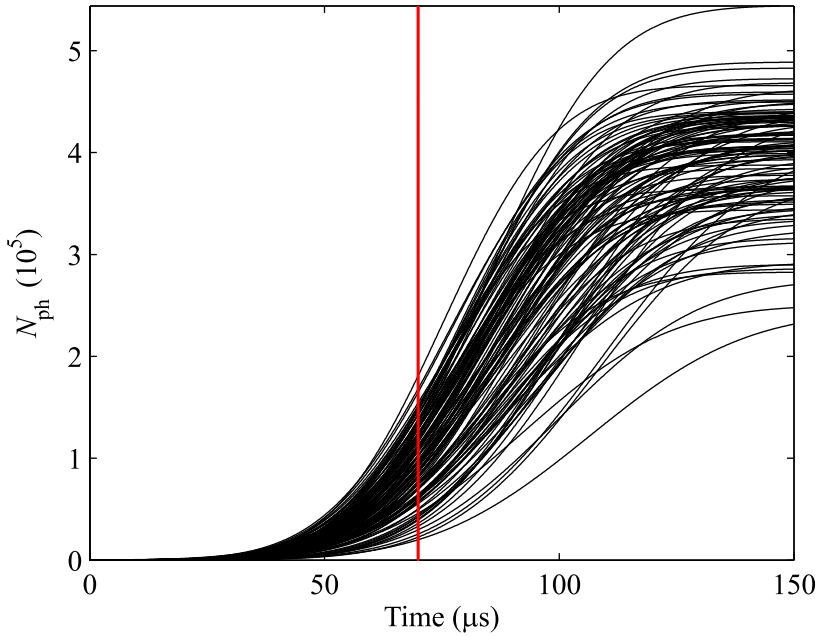

FIGURE 7.7: Cumulative integral of the Gaussian function fitted to the first superradiant pulse in the low pump power regime for the same data set as in figure 7.3. The red line indicates the time at which we show the photon statistics in figure 7.8.

7.2 Evolution of light field statistics

The change from spontaneous to stimulated scattering in superradiant light scattering is manifest in the evolution of the emitted light. Initially, the number distribution of the light field, and hence the atomic polarization, is in a thermal state. As we saw in the previous chapter, as the number of backscattered photons in the BEC volume increases, the intensity of backscattered light increases at the input end of the condensate leading to the emission of the first superradiant pulse. This means that the photon statistics of the endfire mode evolve throughout the process.

This is closely related to the transient evolution of photon statistics when a Continuous Wave (CW) laser is switched on [75, 101]. There, the light field evolves from a thermal distribution to one well described by Poisson statistics. It is important to note, however, that the process can only achieve CW emission because of continuous repumping of the gain medium. In the case of superradiant scattering in a BEC, the gain is achieved through the density and physical extent of the atomic medium, rather than a resonator cavity. Most importantly, however, the process never achieves a steady state of emission because of local depletion of the atoms, as evident in figure 6.8.

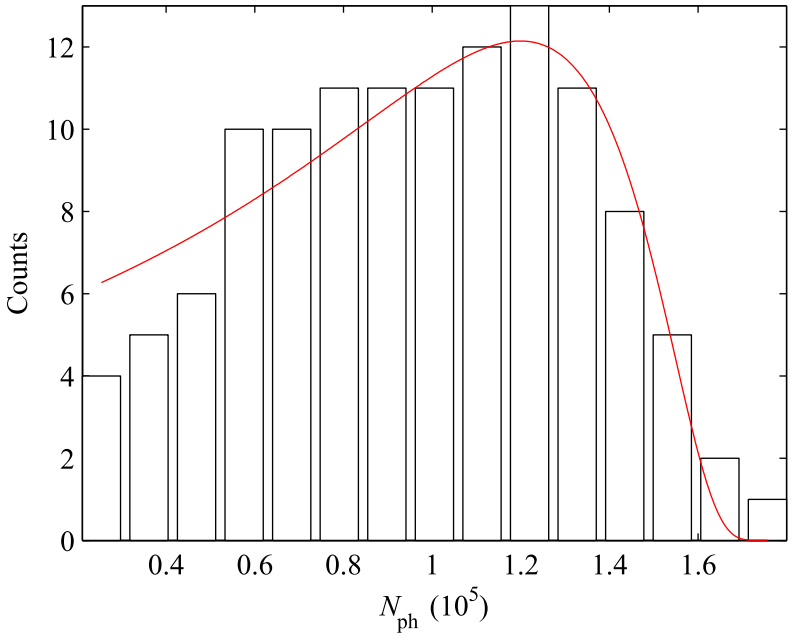

FIGURE 7.8: Histogram giving the photon number distribution at a time shortly before the peak of the superradiant pulse (indicated by the red line in figure 7.7).

We can probe these time dependent photon statistics (somewhat indirectly) with the data of the previous section. Figure 7.7 shows the cumulative integral of the Gaussians fitted to experimental pulses in the low pump power regime. As noted in the discussion of figures 7.1 and 7.2, the Gaussian is only a reasonable model up to approximately the peak of the first superradiant pulse. Accordingly, we limit our use of the cumulative integrals that derive from the fits to the point of inflection, corresponding to the peak of the pulse. Each cumulative integral gives the number of photons emitted at a given time for that realization; by considering several realizations, we may build up a picture of the photon statistics. We use the fits rather than the traces themselves to avoid spurious results arising from the noise. At early times, one can observe the thermal number distribution by this method, but the methodology is questionable at this early phase because the numbers are so small and depend strongly on the choice of model and the quality of the fitting, rather than corresponding to a direct measurement. However, at longer times, for instance close to the peak of the pulse, there is no question that the detector signal and corresponding fit is an accurate measurement of the photon flux. Nonetheless, in a forthcoming work [13], we will present more complete measurements of the evolution of the light state by using the direct counting of photons by the Andor camera.

Figure 7.8 shows the photon number distribution inferred by this method at a

time shortly before the mean arrival time $\langle \tau_P \rangle$ for the data set. This time is indicated by the red line in figure 7.7. Superimposed on the histogram is a fit to the following equation [102, 103]:

$$P_n(t) = \left(\frac{N_{\rm at}}{N_{\rm at} - n} \right)^2 \exp\left(-\frac{t}{T_{\rm R}} \right) \exp\left[-\frac{N_{\rm at} n}{N_{\rm at} - n} \exp\left(-\frac{t}{T_{\rm R}} \right) \right]. \tag{7.13}$$

This gives the emitted number of photons as a function of time into a single electric field mode. The experiment of [102] studied the superradiance of Rydberg atoms in a moderate Q cavity, but the result holds in the absence of a cavity provided the emission is into a single mode. As we have discussed, this point is of course doubtful in our set-up, but nonetheless, the function recreates the correct general shape of the data. The steep edge to the right of the figure represents the exponential distribution of the initial thermal state. One can view the first phase of the process - well before $\langle \tau_P \rangle$ - as corresponding to a thermal state whose temperature is increasing. However, the point of inflection of the superradiant pulse marks the time when depletion of the atoms begins to slow down the process. Accordingly, the period of linear amplification ends leading to a flattening out of the photon number distribution. Subsequently, as depletion becomes more important, the distribution obtains an extended tail towards zero photons. The corresponding peak in the photon number distribution during the turn-on transient of a CW laser arises from non-linearity in the atom-field interaction due to the high intensity within the cavity [75]. Due to depletion of the BEC, the emitted light does not achieve Poissonian photon number statistics as this would imply steady-state operation. As we have seen, an extended sample leads to superradiant ringing behaviour, so that a better analogy to this process might be a pulsed laser.

7.3 Probing atom-photon correlations

To this point, we have used the superradiant light pulse to investigate the system experimentally, but we now describe progress towards a joint measurement of the scattered light and atoms. The results and discussion here represent a first attempt to demonstrate number correlations between and scattered light and photons at better than the shot noise level.

The motivation to perform such a measurement lies in the fact that the diffracted atoms and scattered photons are created in pairs. Considering a low pump power regime so that atoms predominantly occupy the zeroth and first order momentum modes, we may represent this process by the Hamiltonian (in the Fock representation):

$$H \sim \hat{a}_-^\dagger \hat{b}_2^\dagger \hat{a}_+ \hat{b}_0 + \hat{a}_+^\dagger \hat{b}_0^\dagger \hat{a}_- \hat{b}_2, \tag{7.14}$$

where $\hat{a}_-^\dagger$ denotes the creation of a back-scattered photon, and $\hat{b}_2^\dagger$ the creation of an atom in the diffraction order with momentum $2\hbar k_l$ etc. As we have seen, even in the

low pump power regime, in the appropriate limit of a high detuning the attenuation of the pump beam through the sample is negligible so that the pump mode may be represented by a complex number - i.e., as a coherent state. Similarly, in the early phase of superradiance, depletion of the mother condensate is negligible, and we may treat it as a large complex amplitude. In these limits, (7.14) reduces to a generic parametric down conversion Hamiltonian $\propto \hat{a}_-^\dagger \hat{b}_2^\dagger$, which is known to generate two mode squeezed states, or to use other terminology, Einstein-Podolsky-Rosen (EPR) entangled states. Entanglement in the ultra-low gain regime of such an interaction, when far less than one atom-photon excitation pair is generated on average, forms the basis for a quantum repeater [104] and has been studied extensively [1]. Here, we are interested in the high gain - superradiant - regime where the detection of entanglement requires in general the measurement of both the phase and amplitude of the light and matter waves at the sub-shot noise level [105].

A second motivation of the present work is to implement a calibration procedure of the counting of scattered light and atoms that is analogous to the use of correlated photons to calibrate single-photon detectors. The procedure in such a calibration is to use pairs of photons from parametric down conversion; one photon is used in a trigger channel, and the other is directed onto the detector one wishes to calibrate. The beauty of the method is that it does not rely on an external standard - the finite efficiency of the trigger detector is irrelevant, as one merely searches for coincidence events. Such an approach has a history dating nearly 40 years, such that the first reported use of the method was also the first demonstration of coincidences of parametric down-conversion photon pairs [106, 107].

The conditions for the experiment are very similar to those described earlier. We use a low single particle scattering rate ($R = 3.3 \times 10^3$ s^{-1}) so that typically only a single forward diffraction order is substantially populated. The number of diffracted atoms is counted directly using absorption imaging, and the number of back-scattered photons is counted on the Andor Camera; both methods are described in chapter 4. Given that diffracted atoms and back-scattered photons are created in pairs, we map out the linear dependence by using a few different pump pulse durations (50 and 55 μs) and make use of the inherent variation in pulse arrival times to populate an appropriate range of $N = N_{\mathrm{at}} = N_{\mathrm{ph}}$.

Figure 7.9 shows a standard absorption image under these conditions superimposed with regions that are important in data processing. The four square regions at each edge of the picture are those used in the background and raw images to eliminate slight intensity differences between the two (section 4.2.2). This difference is typically on the several per mil level. Clearly, the larger the regions and the closer they are to the relevant data in the image, the better one can cancel this effect. The red rectangle indicates the region over which the signal is summed to obtain the number of atoms diffracted into the first order, and the blue square gives the corresponding region for the small number of atoms transferred to the second forward order; each

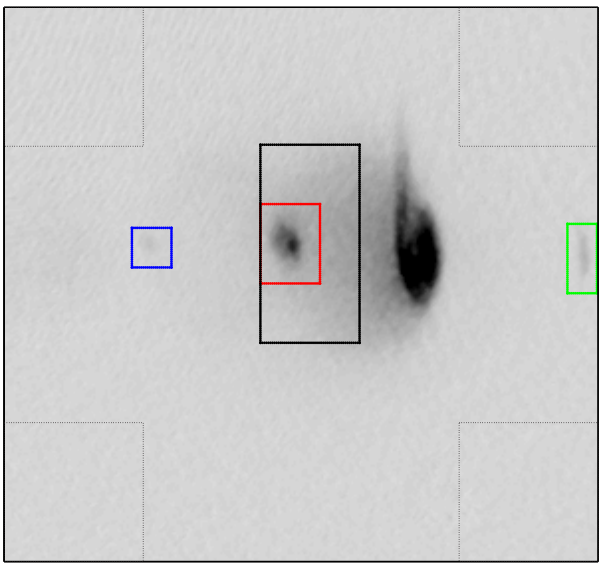

FIGURE 7.9: Absorption image of a BEC after exposure to a pump pulse illustrating important regions to the extraction of the number of diffracted atoms. The black dotted squares in each corner indicate the regions in the background (I_{bg}) and raw images (I_{sh}) used to eliminate slight intensity differences between the two. The red rectangle indicates the region over which the signal is summed to obtain the number of atoms diffracted into the first order. The blue square gives the corresponding region for the small number of atoms transferred to the second forward order, and the green square covers the atoms in the first negative order. A considerable pedestal of scattered atoms is visible between the 0 and $2\hbar k_l$ components. In the event where collisions between these components scatter $2\hbar k_l$ atoms into this 'halo', the black rectangle gives the region over which the atom number is summed. The greyscale was chosen to highlight the background structure.

atom in the $4\hbar k_l$ order corresponds to two emitted photons. The green rectangle covers the region over which $-2\hbar k_l$ atoms are found.

Figure 7.10 shows the corresponding data for the back-scattered light. The figure is a background subtracted image showing the relevant region of the camera chip. The red rectangle denotes the region over which we sum the recorded counts in order to count the number of back-scattered photons. The same procedure to that used in the shadow images is used to ensure that the data and background images have the same integrated count in regions where there are no SR photons.

However, there is a large amount of stray reflection from various optical elements - particularly the back window of the science cell - and this makes it difficult to differentiate between the desired signal and the background. By tilting the pump beam slightly it is possible to separate the two signals at the position of the camera, but in the data presented here, this separation is imperfect. There is a prominent circle next to the region of interest in figure 7.10 where this problem is evident. Indeed,

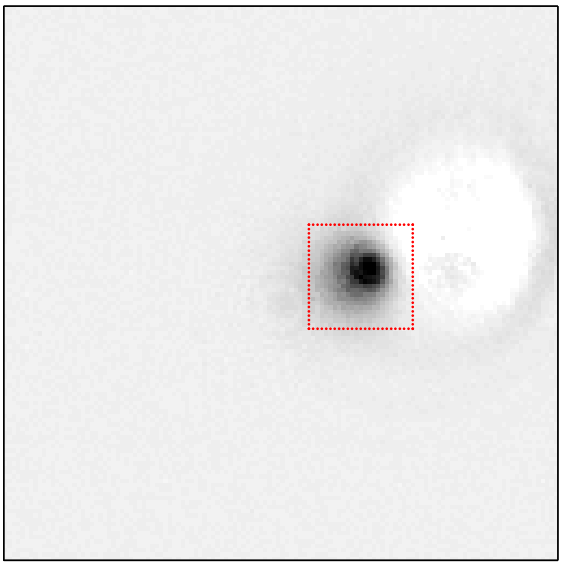

FIGURE 7.10: Background subtracted image of the superradiant light. The red square indicates the region over which the frame is summed to arrive at the photon count. The background is flat except for the large circular region next to the signal of interest. In this region, the background subtraction is complicated by the fact that stray reflections from the far cell wall is affected by the BEC.

in the background-subtracted image, the circle appears to have a lower background count than regions far away from the atoms. This derives from the effect that the atoms have on the pump beam that is scattered from the far wall of the cell. In general, given the extremely high optical depth and parabolic density profile, the BEC acts as a lossy, graded index fibre to the pump light - even in the absence of superradiance, it has a significant effect on the passage of light through the cell. As such, the scattering of light from the far cell wall is significantly affected by the presence of the BEC, thereby causing the image and background frames to differ in the region where this light is concentrated. The end result is that the background subtracted image becomes negative in this region, which, given its proximity to the superradiance signal, compromises somewhat the ability to accurately count photons in this region. The same effect is evident in figures 7.1 and 7.2, where the time trace of the detector has an initial dip at the time the pulse begins.

The superradiant light pulse moves around slightly from shot to shot, thereby placing a limit on the size of the region over which we count. This may be seen in figure 7.11, where one can see small variations - on the order of a few pixels - in the central position of the pulse on the camera chip. The lens in front of the camera

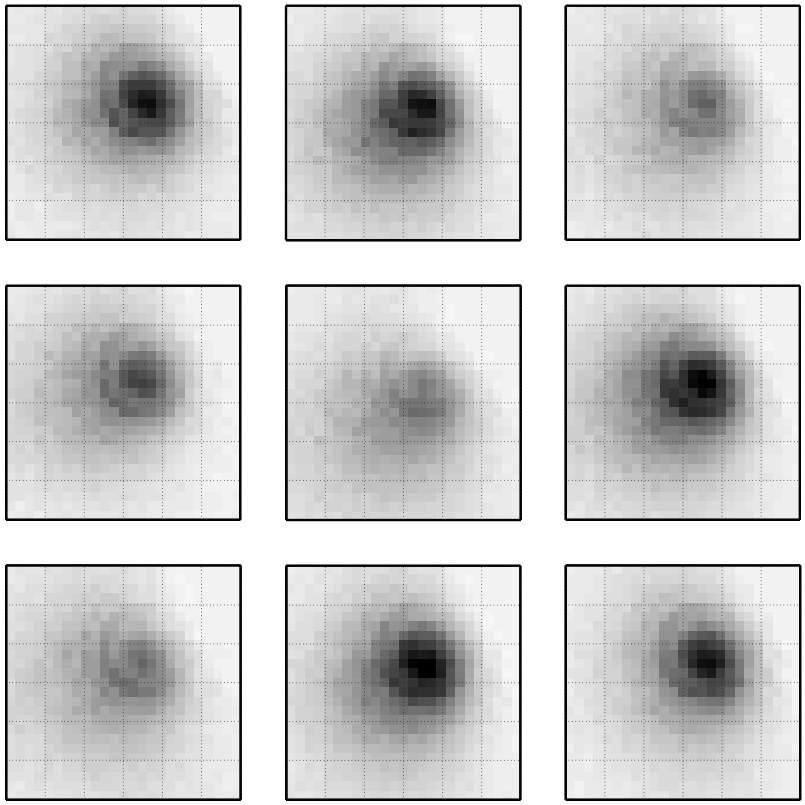

FIGURE 7.11: Background subtracted images of the SR pulses for different realizations of the experiment. A slight variation in the central position of the back-scattered light on the order of one or two pixels is visible.

was set so as to image the focal plane of the achromat used to focus the pump beam and collimate the back-scattered light. As such, the set-up is arranged to image the angular distribution of the back-scattered light.

We observe correlations in the number of atoms and photons, but the fluctuations are at a considerably higher level than that of $\sqrt{N}$. Preliminary experimental results towards demonstrating correlations at the shot noise level are shown in figure 7.12. The first point to note is that the slope of the figure is not one: summing atoms in the first and second orders, and subtracting the number if the minus first order, the observed atom number is approximately one quarter the number of measured photons. The second point is that the fluctuations about the linear fit are on the level of a few 10^4 whereas shot noise $\sqrt{N}$ fluctuations are on the order of several hundred. We address each issue separately.

The observed gradient can be caused by the under-counting of atoms, the over-

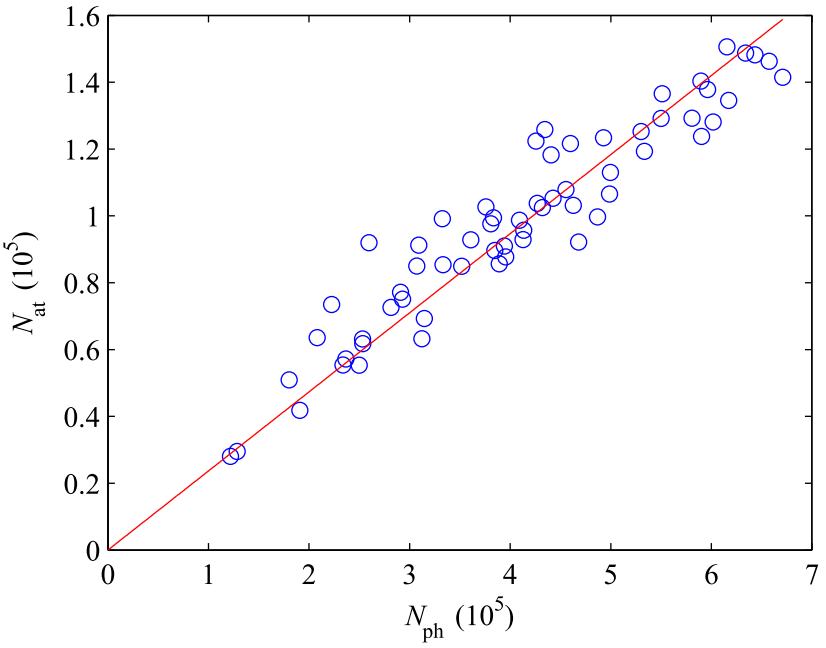

FIGURE 7.12: Plot of N_{at} v. N_{ph}. The data was fitted with a straight line constrained to pass through the origin. The slope of the line was found to be 0.24.

counting of photons, or a combination of the two. Given the results of section 4.2.5, and the low observed optical depth ($\lesssim 2$) in the regions where we count, there is no obvious reason to believe that the atom counting is at fault. A second factor could be inter-atomic collisions between the moving atoms that scatter atoms out of the $2\hbar k_l$ component [108]. In this way, photons may be detected correctly but subsequent collisions could disrupt the atom measurement. If one takes into account half the halo visible in figure 7.9, and uses the larger region shown in black, then the gradient doubles. However, the fluctuations about the mean increase by a factor of three. Finally, despite the problems in the overlap of signal and background, it seems unlikely that we overcount the number of photons in the superradiant pulse.

Given the more complex procedure to obtain the number of atoms, we believe the excessive noise visible in figure 7.12 derive primarily from the atom counting. Of course, the success of both methods depends on the ability to produce a clean signal on top of a flat background, but the transformations used to obtain an absorbtion image are more susceptible to noise. In particular, the fine structures visible in the processed image in figure 7.9 that derive from imperfect overlap of shadow and background images cause significant problems for the direct counting of atoms.

The task of improving the results is a technical one.

First, we note that a reduction of the number of scattered pairs will improve

matters. Given that shot noise scales as $\sqrt{N}$ and that classical noise scales as N, one can come closer to the regime where shot noise where shot noise predominates by going to lower values of N. However, this strategy only carries us so far, because at some point we approach the technical noise floor.

Second, we might reduce the influence of the technical noise in the images by moving to smaller regions of interest by reduction in the magnification, or in the case of atom pictures, changing to smaller times of flight. The advantage of this is twofold. The lower the number of pixels over which we sum the smaller the influence of the technical noise of the camera. As noted in sections 4.2.3 and 4.3.2, the technical noise values of the cameras lie at around 10 e^-/pixel. Thus, we must detect more than 100 photons or atoms per pixel in order to be shot noise limited. Additionally, the smaller the region over which we sum leads a smaller contribution of the imperfectly cancelled background.

In the case of absorption images, the fine spatial structures associated with imperfect overlap of the shadow and background images play an important role in increasing the observed noise when counting pixels. A study of several hundred processed images in the absence of atoms revealed persistent, non-white spatial structures. These are an additional and more complex source of noise on the absorption images. As such, moving to smaller regions of interest will help, but direct efforts to improve the stability of the absorption imaging set-up are also required. These relate to the mechanical stability of all the components, and the frequency stability of the imaging light.

Chapter 8

Summary and outlook

This thesis describes the construction of a machine to generate Bose Einstein condensates in ^{87}Rb and the first experiments performed with this machine on superradiant Rayleigh scattering.

Bose Einstein condensates of ^{87}Rb are produced by evaporatively cooling atoms in a magnetic trap of the quadrupole-Ioffe configuration. The atoms are loaded into the magnetic trap from a Magneto-Optical trap in a region of ultra-high vacuum. In order to load this MOT, we generate a cold beam of atoms using another form of Magneto-Optical trap in a second part of the vacuum chamber; to ensure an intense beam of atoms, this part of the chamber is held through differential pumping at a higher vapour pressure of ^{87}Rb. The two chamber arrangement is a standard approach to obtain a sufficient number of atoms in the magnetic trap, at a level of vacuum that is good enough to ensure that evaporative cooling reaches the runaway regime. The evaporative cooling is achieved by selectively driving radio frequency transitions to untrapped magnetic substates. After approximately 15 seconds of loading in the second MOT, 50 seconds of evaporative cooling leads to pure, prolate condensates containing up to a few million atoms. During the evaporation, the magnetic trap is relaxed so that density dependent heating does not substantially reduce the number of atoms in the condensate.

The application of an off-resonant beam of light along the long axis of the condensate leads to a form of collective Rayleigh scattering analogous to the superradiance that occurs in electronically inverted samples. One can think of this process as the amplification of quantum noise: photons are spontaneously scattered out of the pump beam, and due to the extended optical depth along the long axis of the BEC, the modes that propagate along this axis see the most gain. In the end-pumped geometry, the strongest superradiant mode is the one where photons are back-scattered by the atoms. The overlap of stationary and recoiling atoms recoil produces a density modulation - a Bragg grating - which amplifies the back-scattering. We have performed a systematic study of the effects of pump detuning on the process while keeping the

single particle scattering rate constant. In this way, we move between the case where the pump beam functions as a reservoir of photons to the situation where superradiance is clamped by a lack of photons in the pump beam. Our experimental results are strongly supported by simulations of the system based on 1D Maxwell-Schrödinger equations. We demonstrate that the dynamics result from the structures that build up in the light and matter fields along the long axis of the condensate. In particular, we find that the emission of the first superradiant pulse may be understood in terms of the overlap of light and matter wave gratings. Finally, the random nature of the spontaneous scattering that initiates the collective scattering is manifest at later times in the distribution of arrival times and photon numbers of the first superradiant pulse.

In chapter 7 we noted the difficulties in demonstrating correlations between back-scattered photons and recoiling atoms; subsequent efforts have focussed on bridging the gap between the observed noise and shot noise. As suggested in chapter 7, the absorption imaging set-up has received the most attention. Given the suspicion that vibrations associated with the camera shutter were causing differences between shadow and background images, a variety of measures have been taken to mitigate this. In particular, the camera objective has been changed to a single Gradium© lens, mounted independently of the camera on a 3D translation stage. Furthermore, the camera has been mounted on a linear translation stage, so that focussing the images is more straightforward and that we can take images at different times of flight in a reproducible way. This has proven to be useful as we have moved to a reduced time of flight so as to obtain a smaller region over which to sum the diffracted atoms. Recent efforts have been directed at the frequency stability of the imaging light: a narrow-band interference filter of width ~ 0.2 nm has been added to limit the thermal background on the imaging beam (section 4.2.3); an additional saturated absorption set-up has been added to monitor the frequency stability of the imaging light; and a different slave laser is now used to provide the imaging light. The effect on the frequency stability of the imaging light due to vibrations transmitted through the table from the camera shutter and the turn-off of the magnetic trap has been investigated, and at present the locking mechanism of the trap laser is being reworked so as to provide a tighter lock (3.5.2).

However, the changes to date have not brought a substantial improvement to the data shown in figure 7.12 - the noise is still far in excess of $\sqrt{N}$ - suggesting that some physics might be getting in the way of a good measurement. As noted, collisions between atoms in different momentum orders are a possible cause of an observed number of scattered atoms that is lower than that expected from the photon count, and increased fluctuations in the number that is measured. Furthermore, it is likely that collisions will constitute a significant decoherence mechanism in future work where we seek to make use of the external degrees of freedom. Therefore, a significant experimental and theoretical study of these collisions is required. However, this also motivates the use of the internal atomic degrees of freedom in pursuing the goal of

coherent control in the atom-light interface.

To this end, a crossed dipole trap will soon be added to the set-up, opening up the ability to trap the atoms independently of their magnetic substate. The benefits of such a trap are clear, as it gives full access to the internal degrees of freedom. With appropriate ambient magnetic field stabilization and such a set-up, we can obtain strong coupling and long coherence times between light and the spin degree of freedom.

The next experiment will be to observe the Faraday rotation of a linearly polarized beam due to the macroscopic spin of the BEC, as represented by equation (1.1). The experiment can be performed in either the existing magnetic trap or the coming dipole trap. The light is again focussed onto the long axis of the BEC, and the scattered light will be detected through the hole in the Ioffe coil. The physical mechanism by which the polarization rotates is circular birefringence: the two circular polarizations that comprise the input linear polarization have different coupling strengths (due to different Clebsch-Gordon coefficients) and hence experience a different phase shift. The strength of the interaction then depends on the spin polarization of the sample, and at least in a magnetically trapped BEC, all of the atoms are oriented along the bias field. As such, the degree of rotation is a quantum non-demolition measurement of the spin polarization and hence the number of atoms in the sample. This will be the first step towards a 'traditional' measurement for the group in the context of BEC, and paves the way for measurements where the rotation occurs due to fluctuations in the collective spin [3]. It is important to note that the work presented here forms the basis of our understanding of how to experimentally avoid the regime where superradiance occurs.

In the longer term, we have the important goal of demonstrating a long-lived quantum memory for light [4] in a Bose Einstein condensate. Other experiments, in a similar vein, relate to the demonstration of spin squeezing in the BEC. Furthermore, it would be interesting to combine interactions that make use of both the internal and external degrees of freedom; for instance Raman superradiance where we extend the two-mode squeezing to make use of different internal levels. Finally, it could also be interesting to study superradiant dynamics with the atoms stored in a tight optical lattice, thereby frustrating the external degree of freedom.

Bibliography

[1] H. Kimble, "The quantum internet," *Nature (London)*, vol. 453, pp. 1023–1030, 2008.

[2] K. Hammerer, A. S. Sørensen, and E. S. Polzik, "Quantum interface between light and atomic ensembles," *Submitted to Rev. Mod. Phys.*, 2008.

[3] B. Julsgaard, A. Kozhekin, and E. S. Polzik, "Experimental long-lived entanglement of two macroscopic objects," *Nature (London)*, vol. 413, p. 400, 2001.

[4] B. Julsgaard, J. Sherson, J. I. Cirac, J. Fiurášek, and E. S. Polzik, "Experimental demonstration of quantum memory for light ," *Nature (London)*, vol. 432, p. 482, 2004.

[5] M. H. Anderson, J. R. Ensher, M. R. Matthews, C. E. Wieman, and E. A. Cornell, "Observation of Bose-Einstein Condensation in a Dilute Atomic Vapor," *Science*, vol. 269, no. 5221, pp. 198–201, 1995.

[6] K. B. Davis, M. O. Mewes, M. R. Andrews, N. J. van Druten, D. S. Durfee, D. M. Kurn, and W. Ketterle, "Bose-Einstein Condensation in a Gas of Sodium Atoms," *Phys. Rev. Lett.*, vol. 75, no. 22, pp. 3969–3973, 1995.

[7] C. C. Bradley, C. A. Sackett, J. J. Tollett, and R. G. Hulet, "Evidence of Bose-Einstein Condensation in an Atomic Gas with Attractive Interactions," *Phys. Rev. Lett.*, vol. 75, no. 9, pp. 1687–1690, 1995.

[8] A. E. Kozhekin, K. Mølmer, and E. Polzik, "Quantum memory for light," *Phys. Rev. A*, vol. 62, no. 3, p. 033809, 2000.

[9] O. S. Mishina, D. V. Kupriyanov, J. H. Müller, and E. S. Polzik, "Spectral theory of quantum memory and entanglement via Raman scattering of light by an atomic ensemble," *Phys. Rev. A*, vol. 75, no. 4, p. 042326, 2007.

[10] R. H. Dicke, "Coherence in Spontaneous Radiation Processes," *Phys. Rev.*, vol. 93, no. 1, p. 99, 1954.

[11] A. Hilliard, F. Kaminski, R. le Targat, C. Olausson, E. S. Polzik, and J. H. Müller, "Rayleigh superradiance and dynamic Bragg gratings in an end-pumped Bose-Einstein condensate," *Phys. Rev. A*, vol. 78, no. 5, p. 051403(R), 2008.

[12] A. Hilliard, F. Kaminski, R. le Targat, E. Polzik, and J. H. Müller, "Collective Rayleigh scattering in a Bose Einstein Condensate," *In preparation*, 2008.

[13] A. Hilliard, F. Kaminski, R. le Targat, E. Polzik, and J. H. Müller, "Fluctuations in superradiant light scattering," *In preparation*, 2008.

[14] S. Bose, "Plancks Gesetz und Lichtquantenhypothese," *A. Phys*, vol. 26, no. 178, 1924.

[15] A. Einstein, "Quantentheorie des einatomigen idealen Gases: Zweite Abhandlung," *Sitzungsber. Kgl. Preuss. Akad. Wiss.*, 1925.

[16] C. Pethick and H. Smith, *Bose-Einstein Condensation in Dilute Gases*. University Press, Cambridge, first ed., 2002.

[17] F. Dalfovo, S. Giorgini, L. P. Pitaevskii, and S. Stringari, "Theory of Bose-Einstein condensation in trapped gases," *Rev. Mod. Phys.*, vol. 71, no. 3, pp. 463–512, 1999.

[18] A. J. Leggett, "Bose-Einstein condensation in the alkali gases: Some fundamental concepts," *Rev. Mod. Phys.*, vol. 73, no. 2, pp. 307–356, 2001.

[19] M. J. Davis and P. B. Blakie, "Critical Temperature of a Trapped Bose Gas: Comparison of Theory and Experiment," *Phys. Rev. Lett.*, vol. 96, no. 6, p. 060404, 2006.

[20] V. Bagnato, D. E. Pritchard, and D. Kleppner, "Bose-Einstein condensation in an external potential," *Phys. Rev. A*, vol. 35, no. 10, pp. 4354–4358, 1987.

[21] W. Ketterle, D. S. Durfee, and D. M. Stamper-Kurn, "Making, probing and understanding Bose-Einstein condensates," in *Proceedings of the International School of Physics of Enrico Fermi,Course CXL: Bose-Einstein condensation in gases* (M. Inguscio, S. Stringari, and C. E. Wieman, eds.), 1998.

[22] J. Dalibard, "Collisional dynamics of ultra-cold atomic gases," in *Proceedings of the International School of Physics of Enrico Fermi, Course CXL: Bose-Einstein condensation in gases* (M. Inguscio, S. Stringari, and C. E. Wieman, eds.), Italian Physical Society, 1998.

[23] L. P. Pitaevskii, "Vortex lines in an imperfect Bose gas," *Zh. Eksp. Teor. Fiz.*, vol. 40, 1961.

[24] E. P. Gross, "Hydrodynamics of a Superfluid Condensate," *J. Math. Phys.*, vol. 4, no. 2, pp. 195–207, 1963.

[25] C. C. Bradley, C. A. Sackett, and R. G. Hulet, "Bose-Einstein Condensation of Lithium: Observation of Limited Condensate Number," *Phys. Rev. Lett.*, vol. 78, no. 6, pp. 985–989, 1997.

[26] D. G. Fried, T. C. Killian, L. Willmann, D. Landhuis, S. C. Moss, D. Kleppner, and T. J. Greytak, "Bose-Einstein Condensation of Atomic Hydrogen," *Phys. Rev. Lett.*, vol. 81, no. 18, pp. 3811–3814, 1998.

[27] A. Robert, O. Sirjean, A. Browaeys, J. Poupard, S. Nowak, D. Boiron, C. I. Westbrook, and A. Aspect, "A Bose-Einstein Condensate of Metastable Atoms," *Science*, vol. 292, no. 5516, pp. 461–464, 2001.

[28] F. Pereira Dos Santos, J. Léonard, J. Wang, C. J. Barrelet, F. Perales, E. Rasel, C. S. Unnikrishnan, M. Leduc, and C. Cohen-Tannoudji, "Bose-Einstein Condensation of Metastable Helium," *Phys. Rev. Lett.*, vol. 86, no. 16, pp. 3459–3462, 2001.

[29] G. Modugno, G. Ferrari, G. Roati, R. J. Brecha, A. Simoni, and M. Inguscio, "Bose-Einstein Condensation of Potassium Atoms by Sympathetic Cooling," *Science*, vol. 294, no. 5545, pp. 1320–1322, 2001.

[30] T. Weber, J. Herbig, M. Mark, H.-C. Nagerl, and R. Grimm, "Bose-Einstein Condensation of Cesium," *Science*, vol. 299, no. 5604, pp. 232–235, 2003.

[31] Y. Takasu, K. Maki, K. Komori, T. Takano, K. Honda, M. Kumakura, T. Yabuzaki, and Y. Takahashi, "Spin-Singlet Bose-Einstein Condensation of Two-Electron Atoms," *Phys. Rev. Lett.*, vol. 91, no. 4, p. 040404, 2003.

[32] A. Griesmaier, J. Werner, S. Hensler, J. Stuhler, and T. Pfau, "Bose-Einstein Condensation of Chromium," *Phys. Rev. Lett.*, vol. 94, no. 16, p. 160401, 2005.

[33] D. Steck, "Rubidium 87 D Line Data." Online, 2003.

[34] C. Olausson, "A Rubidium Bose-Einstein Condensate: Toward the BEC-Light Quantum Interface," Master's thesis, University of Copenhagen, 2007.

[35] W. H. Wing, "On neutral particle trapping in quasistatic electromagnetic fields," *Progress in Quantum Electronics*, vol. 8, 1984.

[36] H. J. Metcalf and P. van der Straten, *Laser Cooling and Trapping*. Springer, first ed., 1999.

[37] C. Cohen-Tannoudji, "Atomic motion in laser light," in *Les Houches 1990, Session LIII, Fundamental sysytems in quantum optics* (J. Dalibard, J.-M. Raimond, and J. Zinn-Justin, eds.), 1992.

[38] W. D. Phillips, "Laser cooling, optical traps and optical molasses," in *Les Houches 1990, Session LIII, Fundamental sysytems in quantum optics* (J. Dalibard, J.-M. Raimond, and J. Zinn-Justin, eds.), 1992.

[39] H. J. Metcalf and P. van der Straten, "Laser cooling and trapping of atoms," *J. Opt. Soc. Am. B*, vol. 20, no. 5, p. 887, 2002.

[40] J. Dalibard and C. Cohen-Tannoudji, "Laser cooling below the Doppler limit by polarization gradients: simple theoretical models," *J. Opt. Soc. Am. B*, vol. 6, no. 11, p. 2023, 1989.

[41] A. Aspect, E. Arimondo, R. Kaiser, N. Vansteenkiste, and C. Cohen-Tannoudji, "Laser Cooling below the One-Photon Recoil Energy by Velocity-Selective Coherent Population Trapping," *Phys. Rev. Lett.*, vol. 61, no. 7, pp. 826–829, 1988.

[42] M. Kasevich and S. Chu, "Laser cooling below a photon recoil with three-level atoms," *Phys. Rev. Lett.*, vol. 69, no. 12, pp. 1741–1744, 1992.

[43] H. Katori, T. Ido, Y. Isoya, and M. Kuwata-Gonokami, "Magneto-Optical Trapping and Cooling of Strontium Atoms down to the Photon Recoil Temperature," *Phys. Rev. Lett.*, vol. 82, no. 6, pp. 1116–1119, 1999.

[44] C. G. Townsend, N. H. Edwards, C. J. Cooper, K. P. Zetie, C. J. Foot, A. M. Steane, P. Szriftgiser, H. Perrin, and J. Dalibard, "Phase-space density in the magneto-optical trap," *Phys. Rev. A*, vol. 52, no. 2, pp. 1423–1440, 1995.

[45] W. Ketterle, K. B. Davis, M. A. Joffe, A. Martin, and D. E. Pritchard, "High densities of cold atoms in a dark spontaneous-force optical trap," *Phys. Rev. Lett.*, vol. 70, no. 15, pp. 2253–2256, 1993.

[46] O. J. Luiten, M. W. Reynolds, and J. T. M. Walraven, "Kinetic theory of the evaporative cooling of a trapped gas," *Phys. Rev. A*, vol. 53, no. 1, pp. 381–389, 1996.

[47] D. W. Snoke and J. P. Wolfe, "Population dynamics of a Bose gas near saturation," *Phys. Rev. B*, vol. 39, no. 7, pp. 4030–4037, 1989.

[48] E. A. Burt, R. W. Ghrist, C. J. Myatt, M. J. Holland, E. A. Cornell, and C. E. Wieman, "Coherence, Correlations, and Collisions: What One Learns about Bose-Einstein Condensates from Their Decay," *Phys. Rev. Lett.*, vol. 79, no. 3, pp. 337–340, 1997.

[49] J. Schuster, A. Marte, S. Amtage, B. Sang, G. Rempe, and H. C. W. Beijerinck, "Avalanches in a Bose-Einstein Condensate," *Phys. Rev. Lett.*, vol. 87, no. 17, p. 170404, 2001.

[50] W. Ketterle and N. van Druten, "Evaporative cooling of trapped atoms," *Adv. At. Mol. Phys.*, vol. 37, no. 181, 1996.

[51] M. Yamashita, M. Koashi, and N. Imoto, "Quantum kinetic theory for evaporative cooling of trapped atoms: Growth of Bose-Einstein condensate," *Phys. Rev. A*, vol. 59, no. 3, pp. 2243–2249, 1999.

[52] P. Valkering, "Optimization of evaporative cooling of rubidium atoms in a magnetic trap," Master's thesis, University of Utrecht, 1999.

[53] R. deCarvalho and J. Doyle, "Evaporative cooling at low trap depth," *Phys. Rev. A*, vol. 70, no. 5, p. 053409, 2004.

[54] H. J. Lewandowski, D. M. Harber, D. L. Whitaker, and E. A. Cornell, "Simplified System for Creating a Bose Einstein Condensate," *J. Low Temp. Phys.*, vol. 132, no. 5-6, 2003.

[55] Y. Castin and R. Dum, "Bose-Einstein Condensates in Time Dependent Traps," *Phys. Rev. Lett.*, vol. 77, p. 5315, 1996.

[56] F. Dalfovo, C. Minniti, S. Stringari, and L. Pitaevskii, "Nonlinear dynamics of a Bose condensed gas," *Physics Letters A*, vol. 227, p. 259, 1997.

[57] W. Petrich, M. H. Anderson, J. R. Ensher, and E. A. Cornell, "Stable, Tightly Confining Magnetic Trap for Evaporative Cooling of Neutral Atoms," *Phys. Rev. Lett.*, vol. 74, no. 17, pp. 3352–3355, 1995.

[58] G. Bjorklund, M. Levenson, W. Lenth, and C. Ortiz, "Frequency Modulation (FM) spectroscopy," *Appl. Phys. B*, vol. 32, p. 145, 1983.

[59] J. Appel, *A Light-Atom Quantum Interface based on Electromagnetically Induced Transparency*. PhD thesis, University of Calgary.

[60] T. Esslinger, I. Bloch, and T. W. Hänsch, "Bose-Einstein condensation in a quadrupole-Ioffe-configuration trap," *Phys. Rev. A*, vol. 58, no. 4, pp. R2664–R2667, 1998.

[61] T. Bergeman, G. Erez, and H. J. Metcalf, "Magnetostatic trapping fields for neutral atoms," *Phys. Rev. A*, vol. 35, no. 4, p. 1535, 1987.

[62] T. Meyrath, *Experiments with Bose-Einstein Condensation in an Optical Box*. PhD thesis, The University of Texas at Austin, 2005.

[63] W. Wohlleben, F. Chevy, K. Madison, and J. Dalibard, "An atom faucet," *Eur. Phys. J. D.*, vol. 15, 2001.

[64] K. Dieckmann, R. J. C. Spreeuw, M. Weidemüller, and J. T. M. Walraven, "Two-dimensional magneto-optical trap as a source of slow atoms," *Phys. Rev. A*, vol. 58, no. 5, pp. 3891–3895, 1998.

[65] J. Schoser, A. Batär, R. Löw, V. Schweikhard, A. Grabowski, Y. B. Ovchinnikov, and T. Pfau, "Intense source of cold Rb atoms from a pure two-dimensional magneto-optical trap," *Phys. Rev. A*, vol. 66, no. 2, p. 023410, 2002.

[66] C. Klempt, T. van Zoest, T. Henninger, O. Topic, E. Rasel, W. Ertmer, and J. Arlt, "Ultraviolet light-induced atom desorption for large rubidium and potassium magneto-optical traps," *Phys. Rev. A*, vol. 73, no. 1, p. 013410, 2006.

[67] M. Yamashita, M. Koashi, T. Mukai, M. Mitsunaga, N. Imoto, and T. Mukai, "Optimization of evaporative cooling towards a large number of Bose-Einstein-condensed atoms," *Phys. Rev. A*, vol. 67, no. 2, p. 023601, 2003.

[68] T. Mukai and M. Yamashita, "Efficient rapid production of a Bose-Einstein condensate by overcoming serious three-body loss," *Phys. Rev. A*, vol. 70, no. 1, p. 013615, 2004.

[69] J. H. Müller. Private communication.

[70] M. A. Joffe, W. Ketterle, A. Martin, and D. E. Pritchard, "Transverse cooling and deflection of an atomic beam inside a Zeeman slower," *J. Opt. Soc. Am. B*, vol. 10, no. 12, p. 2257, 1993.

[71] P. Windpassinger, *Non-Destructive Quantum State Measurements and Spin Squeezing*. PhD thesis, University of Copenhagen, 2008.

[72] M. F. H. Schuurmanns, Q. Vrehen, D. Polder, and H. M. Gibbs, *Advances in Atomic and Molecular Physics*, vol. 17, ch. Superfluorescence, pp. 168–226. Academic Press, 1981.

[73] N. Skribanowitz, I. P. Herman, J. C. MacGillivray, and M. S. Feld, "Observation of Dicke Superradiance in Optically Pumped HF Gas," *Phys. Rev. Lett.*, vol. 30, no. 8, pp. 309–312, 1973.

[74] M. Gross and S. Haroche, "Superradiance: an essay on the theory of collective spontaneous emission," *Physics Reports*, vol. 93, no. 5, pp. 301–396, 1982.

[75] F. T. Arecchi, V. Degiorgio, and B. Querzola, "Time-dependent statistical properties of the laser radiation," *Phys. Rev. Lett.*, vol. 19, no. 20, pp. 1168–1171, 1967.

[76] S. Inouye, A. P. Chikkatur, D. M. Stamper-Kurn, J. Stenger, D. E. Pritchard, and W. Ketterle, "Superradiant Rayleigh Scattering from a Bose-Einstein Condensate," *Science*, vol. 285, no. 5427, pp. 571–574, 1999.

[77] D. Schneble, Y. Torii, M. Boyd, E. W. Streed, D. E. Pritchard, and W. Ketterle, "The Onset of Matter-Wave Amplification in a Superradiant Bose-Einstein Condensate," *Science*, vol. 300, no. 5618, pp. 475–478, 2003.

[78] D. Schneble, G. K. Campbell, E. W. Streed, M. Boyd, D. E. Pritchard, and W. Ketterle, "Raman amplification of matter waves," *Phys. Rev. A*, vol. 69, no. 4, p. 041601(R), 2004.

[79] L. E. Sadler, J. M. Higbie, S. R. Leslie, M. Vengalattore, and D. M. Stamper-Kurn, "Coherence-Enhanced Imaging of a Degenerate Bose-Einstein Gas," *Phys. Rev. Lett.*, vol. 98, no. 11, 2007.

[80] Y. Yoshikawa, Y. Torii, and T. Kuga, "Superradiant Light Scattering from Thermal Atomic Vapors," *Phys. Rev. Lett.*, vol. 94, no. 8, 2005.

[81] Y. Yoshikawa, T. Sugiura, Y. Torii, and T. Kuga, "Observation of superradiant Raman scattering in a Bose-Einstein condensate," *Phys. Rev. A*, vol. 69, no. 4, p. 041603(R), 2004.

[82] J. Li, X. Zhou, F. Yang, and X. Chen, "Superradiant Rayleigh scattering from a Bose-Einstein condensate with the incident laser along the long axis," *Phys. Lett. A*, vol. 372, no. 26, pp. 4750–4753, 2008.

[83] M. G. Raymer and J. Mostowski, "Stimulated Raman scattering: Unified treatment of spontaneous initiation and spatial propagation," *Phys. Rev. A*, vol. 24, no. 4, pp. 1980–1993, 1981.

[84] F. Haake, H. King, G. Schröder, J. Haus, and R. Glauber, "Fluctuations in superfluorescence," *Phys. Rev. A*, vol. 20, no. 5, pp. 2047–2063, 1979.

[85] J. P. Clemens, L. Horvath, B. C. Sanders, and H. J. Carmichael, "Collective spontaneous emission from a line of atoms," *Phys. Rev. A*, vol. 68, no. 2, p. 023809, 2003.

[86] M. W. Sørensen and A. S. Sørensen *In preparation*, 2008.

[87] H. Uys and P. Meystre, "Theory of coherent Raman superradiance imaging of condensed Bose gases," *Phys. Rev. A*, vol. 75, no. 3, p. 033805, 2007.

[88] O. Zobay and G. M. Nikolopoulos, "Dynamics of matter-wave and optical fields in superradiant scattering from Bose-Einstein condensates," *Phys. Rev. A*, vol. 72, no. 4, 2005.

[89] O. Zobay and G. M. Nikolopoulos, "Spatial effects in superradiant Rayleigh scattering from Bose-Einstein condensates," *Phys. Rev. A*, vol. 73, no. 013620, p. 013620, 2006.

[90] A. Icsevgi and W. E. Lamb, "Propagation of Light Pulses in a Laser Amplifier," *Phys. Rev.*, vol. 185, no. 2, pp. 517–545, 1969.

[91] E. W. Hagley, L. Deng, M. Kozuma, M. Trippenbach, Y. B. Band, M. Edwards, M. Doery, P. S. Julienne, K. Helmerson, S. L. Rolston, and W. D. Phillips, "Measurement of the Coherence of a Bose-Einstein Condensate," *Phys. Rev. Lett.*, vol. 83, no. 16, pp. 3112–3115.

[92] J. C. MacGillivray and M. S. Feld, "Theory of superradiance in an extended, optically thick medium," *Phys. Rev. A*, vol. 14, no. 3, pp. 1169–1189, 1976.

[93] M. D. Feit, J. Fleck, J. A., and A. Steiger, "Solution of the Schrödinger equation by a spectral method," *J. Comput. Phys.*, vol. 47, 1982.

[94] J. Söding, D. Guéry-Odelin, P. Desbiolles, F. Chevy, H. Inamori, and J. Dalibard, "Three-body decay of a rubidium Bose-Einstein condensate," *Appl. Phys. B*, vol. 69, pp. 257–261, 1999.

[95] M. M. Cola, M. G. A. Paris, and N. Piovella, "Robust generation of entanglement in Bose-Einstein condensates by collective atomic recoil," *Phys. Rev. A*, vol. 70, no. 4, p. 043809, 2004.

[96] P. Meystre, *Atom optics*. Springer, 2001.

[97] D. Polder, M. F. H. Schuurmans, and Q. H. F. Vrehen, "Superfluorescence: Quantum-mechanical derivation of Maxwell-Bloch description with fluctuating field source," *Phys. Rev. A*, vol. 19, no. 3, pp. 1192–1203, 1979.

[98] D. C. Burnham and R. Y. Chiao, "Coherent Resonance Fluorescence Excited by Short Light Pulses," *Phys. Rev.*, vol. 188, no. 2, pp. 667–675, 1969.

[99] M. R. Spiegel, *Mathematical Handbook of Formulas and Tables*. Schaum's Outline Series, McGraw-Hill, 1997.

[100] J. H. Müller, P. Petrov, D. Oblak, C. L. G. Alzar, S. R. de Echaniz, and E. S. Polzik, "Diffraction effects on light-atomic-ensemble quantum interface," *Phys. Rev. A*, vol. 71, no. 3, p. 033803, 2005.

[101] D. F. Walls and G. J. Milburn, *Quantum Optics*. Springer, 1995.

[102] J. M. Raimond, P. Goy, M. Gross, C. Fabre, and S. Haroche, "Statistics of millimeter-wave photons emitted by a rydberg-atom maser: An experimental study of fluctuations in single-mode superradiance," *Phys. Rev. Lett.*, vol. 49, no. 26, pp. 1924–1927, 1982.

[103] V. Degiorgio and F. Ghielmetti, "Approximate solution to the superradiance master equation," *Phys. Rev. A*, vol. 4, no. 6, pp. 2415–2418, 1971.

[104] L.-M. Duan, M. D. Lukin, J. I. Cirac, and P. Zoller, "Long-distance quantum communication with atomic ensembles and linear optics," *Nature (London)*, vol. 414, p. 413, 2001.

[105] C. A. Muschik, E. S. Polzik, and J. I. Cirac, "Detecting entanglement in two mode squeezed states by particle counting," *arXiv:0806.3448*, 2008.

[106] M. Ware and A. Migdall, "Single-photon detector characterization using correlated photons: the march from feasibility to metrology," *Journal of Modern Optics*, vol. 51, no. 9-10, pp. 1549–1557, 2004.

[107] D. C. Burnham and D. L. Weinberg, "Observation of simultaneity in parametric production of optical photon pairs," *Phys. Rev. Lett.*, vol. 25, no. 2, pp. 84–87, 1970.

[108] Y. B. Band, M. Trippenbach, J. P. Burke, and P. S. Julienne, "Elastic Scattering Loss of Atoms from Colliding Bose-Einstein Condensate Wave Packets," *Phys. Rev. Lett.*, vol. 84, no. 24, pp. 5462–5465, 2000.